UNIVERSITY OF OKLAHOMA

GRADUATE COLLEGE

THERMOPHOTOVOLTAIC DEVICES AND INFRARED PHOTODETECTORS BASED ON INTERBAND CASCADE STRUCTURES

A DISSERTATION

SUBMITTED TO THE GRADUATE FACULTY

in partial fulfillment of the requirements for the

Degree of

DOCTOR OF PHILOSOPHY

By

WENXIANG HUANG
Norman, Oklahoma
2020

THERMOPHOTOVOLTAIC DEVICES AND INFRARED PHOTODETECTORS BASED ON INTERBAND CASCADE STRUCTURES

A DISSERTATION APPROVED FOR THE
HOMER L. DODGE DEPARTMENT OF PHYSICS AND ASTRONOMY

BY THE COMMITTEE CONSISTING OF

Dr. Rui Yang, Chair

Dr. Michael Santos, Co-chair

Dr. Kieran Mullen

Dr. Bruno Uchoa

Dr. Arne Schwettmann

Dr. Bin Wang

To my parents, Caijin Huang and Feng Cheng

Acknowledgements

It would not have been possible to write this dissertation without the help and support of the kind people around me, only some of whom will be given special mention here.

Above all, I would like to express my sincere gratitude to my advisor Prof. Rui Q. Yang for his selfless support, for prompt and useful advice on my Ph.D. study and research, and for sharing his motivation and immense knowledge. He assigned me both theoretical and experimental topics that were interesting and meaningful, as well as beneficial for improving my analytical skills and hands-on abilities. It has been wonderful to work with him and I have had a lot of fun interacting with him all the time. I also want to thank him for the travel support he provided for me to attend several conferences and share our research results with community members. Besides my advisor, I would like to thank Prof. Mike Santos for chairing my committee, and for his support and assistance since the start of my graduate career. He provided the resources for our group to grow our material, nominated me for several awards, and helped me improve my presentations.

I am grateful to Dr. Kieran Mullen, Dr. Bruno Uchoa, Dr. Arne Schwettmann and Dr. Bin Wang for serving on my dissertation committee and squeezing out time to review my general exam and dissertation.

I would also like to thank the current and former members of the Quantum Device Laboratory at the University of Oklahoma. During my first year in the lab, I was fortunate to work closely with Dr. Lin Lei. Many thanks go to him for teaching me the characterization measurements and data analysis of the devices. Many thanks go to Dr. Lu Li who performed the fabrication of most of the devices studied in this dissertation. I want

to extend sincere thanks to Dr. S.M. Shazzad Rassel. He was helpful in carrying out the dark current measurements for many laser devices. I also want to thank Dr. Hossein Lotfi for long discussions on band structure modeling and the device theory. Many thanks go to Dr. Hao Ye for growing some of the structures presented in this work. I want to thank the current group member Jeremy Massengale for MBE growth and material characterization of most of the structures presented in this work. I am grateful to Yuzhe Lin for the fabrication of some devices in this work.

I am also appreciative of our group's collaborators. Particularly, I would like to thank Prof. Matthew Johnson for providing our group with both resources and expertise in device fabrication and material characterization. I would like to thank Dr. James Gupta of the National Research Council of Canada who performed the MBE growth of some laser structures for our research group.

I would also like to acknowledge the sources that have provided me with funding during my Ph.D. career. I am grateful for funding from the NSF (Award Nos. ECCS-1202318, DMR-1229678, DMR-1608224, and IIP-1640576) and the AFOSR (Award No. FA9550-15-1-0067).

Last, but definitely not least, I am greatly indebted to my parents. It is their unconditional love, care, and tolerance that made the hardship of finishing my Ph.D. career worthwhile. Without their support, I would not have been able to overcome the difficulties during these years.

Table of Contents

List of Tables

List of Figures

Abstract

Mid-infrared (IR) optoelectronic devices form the basis for many practical applications such as thermophotovoltaic (TPV) energy conversion, gas sensing, thermal imaging, medical diagnostics, free-space communications, infrared countermeasures and IR illumination. The mid-IR device family based on interband cascade (IC) structures includes IC lasers (ICLs), ICTPV cells and IC infrared photodetectors (ICIPs). These are special types of multistage devices whose operation is made possible by the unique properties of the 6.1 Å material system: InAs, GaSb and AlSb, and their related alloys. One of the key properties is the type-II broken-gap alignment between InAs and GaSb.

In multistage ICTPV cells and ICIPs, electrons must undergo multiple interband excitations in order to travel between the electrical contacts. This means that the transport of a single electron requires multiple photons, which reverses the situation in ICLs where a single electron can generate multiple photons. Counterintuitively, this transport feature in ICTPV cells and ICIPs is conducive to improving device performance by enhancing the open-circuit voltage in ICTPV cells and suppressing the noise in ICIPs. Furthermore, the collection efficiency of photo-generated carriers in multistage IC devices can be significantly improved by thinning the absorbers in individual stages. Collectively, these advantages make IC structures an attractive choice for narrow bandgap optoelectronic devices, especially for operation at high temperatures. One focus of this dissertation is to outline and demonstrate the advantages provided by IC structures, both in theory and experiment. Another focus of this dissertation is to obtain a better understanding of the physics of IC devices and gain insights into their operation.

Theoretical studies of single-absorber and multistage ICTPV cells are presented.

The limitations in efficiency are understood by considering several important practical factors. These factors are identified to be closely associated with a short carrier lifetime, high dark saturation current density, small absorption coefficient, and limited diffusion length. The multistage IC architecture is shown to be able to overcome the diffusion length limitation that is responsible for the low quantum efficiency (QE) in single-absorber TPV cells. This ability of the IC architecture offers the opportunity to enhance conversion efficiency by about 10% for wide ranges of αL (product of absorption coefficient and diffusion length) and bandgaps, resulting in a particle conversion efficiency approaching 100%.

The illustrated theoretical advantage of multistage IC structures is confirmed experimentally in a comparative study of three fabricated TPV devices, one with a single absorber and two that are multistage IC structures. The bandgap of the InAs/GaSb type-II superlattices (T2SLs) in the three devices is close to 0.2 eV at 300 K. The extracted collection efficiency is considerably higher in multistage IC devices than in the single-absorber device. To further investigate the prospects of IC TPV cells, detailed characterization and performance analyses of two sets of four IC devices with similar bandgaps are performed. The four different configurations enable a comparative study that shows how device performance is affected by material quality variations, as well as by current mismatch between stages and collection efficiency.

The carrier lifetime advantage of IC devices over another family of cascade devices, namely quantum cascade (QC) devices, is manifested in the saturation current density (J_0). The values of J_0 extracted using a semi-empirical model, are more than one order of magnitude lower in IC devices than in QC devices. The significance of J_0 on the

performances of IR detectors and TPV cells is apparent in a comparison of the measured detectivity (D^*) and the estimated open-circuit voltage (V_{oc}). To extract the carrier lifetime in IC devices, a simple and effective electrical method is developed. This method is more generally applicable and considers the parasitic shunt and series resistances found in practical devices. It provides a simple way to extract the carrier lifetime in InAs/GaSb T2SLs in a wide range of operating temperatures.

The effect of current mismatch on the performance of ICIPs is investigated using two sets of devices with current-matched and noncurrent-matched configurations. It is shown that current matching is necessary to achieve maximum utilization of absorbed photons for an optimal responsivity. The detectivities of both sets of devices are comparable largely due to the occurrence of a substantial electrical gain in noncurrent-matched ICIPs. The electrical gain is shown to be a ubiquitous property for noncurrent-matched ICIPs through the study of another three devices. To unlock the mechanism underlying electrical gain, a theory is developed for a quantitative description and the calculations are in good agreement with the experimental results.

Chapter 1: Introduction

1.1 Infrared radiation

Infrared radiation (IR) is a type of electromagnetic wave with wavelength longer than for visible light. The wavelength range for IR is between about 700 nm and 1mm, equivalent to a frequency range of approximate 430 THz to 300 GHz. IR radiation is commonly divided into several sub-divisions [1]: near-infrared (NIR, 0.7-1.4 μm), short wavelength (SWIR, 1.4-3.0 μm), mid wavelength infrared (MWIR, 3-8 μm), long wavelength (LWIR, 8.0-15 μm) and far infrared (FIR, 15-1000 μm). There are various uses of infrared radiation in the areas of military, environment, industry, astronomy, climatology and many more. For example, SWIR is extensively used in fiber-optic communication wherein pulses of SWIR light are sent though an optical fiber. MWIR is of main interest in gas sensing areas since many molecules and trace gasses have strong absorption lines in this band. One of the most useful applications of LWIR is thermal imaging that translates thermal energy into image in order to analyze an object or scene. A specific example of thermal imaging is shown in Figure 1-1(a) in which an infrared camera is used to screen passengers in the airport to prevent virus spread [2]. To implement these applications, one essential component is the infrared detector. One focus of this dissertation is a special type of semiconductor infrared detector. The other focus of this dissertation is a thermophotovoltaic (TPV) cell that is the core element in a TPV system [3]. As shown in Figure 1-1(b), a complete TPV system includes a heat source, radiator, emitter, set of TPV cells and cooling system. TPV technology [4-5] has been proposed for applications such as portable power sources, heat conversion of concentrated solar energy and cogeneration in remote locations.

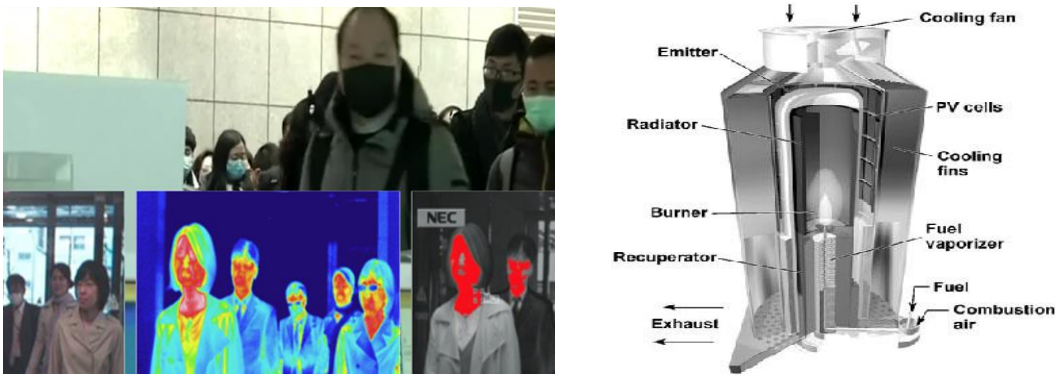

Figure 1-1: (a) Infrared thermography is applied for virus screening in an airport [2], (b) Schematic illustration of a TPV system consisting of a heat source, radiator, emitter, set of TPV cells and cooling system. Figure is from [3].

According to thermodynamic laws, all objects with temperatures higher than absolute zero emit electromagnetic radiation. Ideally, if the object is a perfect blackbody, the spectral radiance follows Planck's law. In this case, the power emitted per unit area, per unit solid angle and per unit frequency of a blackbody is given by:

$$B_\lambda(\lambda, T) = \frac{2hc^2}{\lambda^5} \frac{1}{exp\left(\frac{hc}{\lambda k_b T}\right) - 1}, \tag{1-1}$$

where h is the Planck's constant, c is the speed of light, λ is wavelength, k_b is Boltzmann constant, and T is temperature. The net power per unit area radiated outward from an ideal blackbody, considering the temperature difference with the ambient, can be obtained by integrating Planck's radiation formula:

$$\frac{P}{A} = 2hc^2 \left[\int_0^\infty \frac{d\lambda}{\lambda^5 exp\left(\frac{hc}{\lambda k_b T}\right) - 1} - \int_0^\infty \frac{d\lambda}{\lambda^5 exp\left(\frac{hc}{\lambda k_b T_{amb}}\right) - 1} \right] \tag{1-2}$$

where A is the surface area and T_{amb} is the ambient temperature. This integration gives the final form of Stefan-Boltzmann law that is written as:

$$\frac{P}{A} = \sigma(T^4 - T_{amb}^T) \tag{1-3}$$

where σ is the Stefan-Boltzmann constant, equal to 5.6704×10^{-8} $W \cdot m^{-2} \cdot K^{-4}$.

Illustrations of blackbody spectral radiation at various temperatures are shown in Figure 1-2. The marked regions are linked with several specific technologies: solar cells, thermophotovoltaics and infrared detectors. The surface temperature of the Sun is around 5800 K; the strongest output of the solar radiation spectrum is in the visible range. Therefore, the semiconductor materials used in solar cells typically have a wide bandgap (E_g) such as 1.1 eV for Si, the most common material for commercial solar cells [6-7]. By comparison, the temperature of the heat source in a TPV system is in a lower temperature regime, ranging from 1000-2000 K [4-5]. The radiation of the heat source mainly falls in the NIR and SWIR spectra. On this account, narrower bandgap materials are preferred for TPV cells. For example, the most prevalent material for TPV cells is GaSb with a 0.7 eV bandgap [4-5]. Thermal imaging targets usually have a temperature approaching the ambient; the radiation is mainly distributed over the MWIR and LWIR bands. Hence, the infrared photodetectors fitted in infrared cameras are typically made of semiconductors whose bandgaps are lower than 0.4 eV, e.g. InSb with a bandgap of 0.18 eV [8-9].

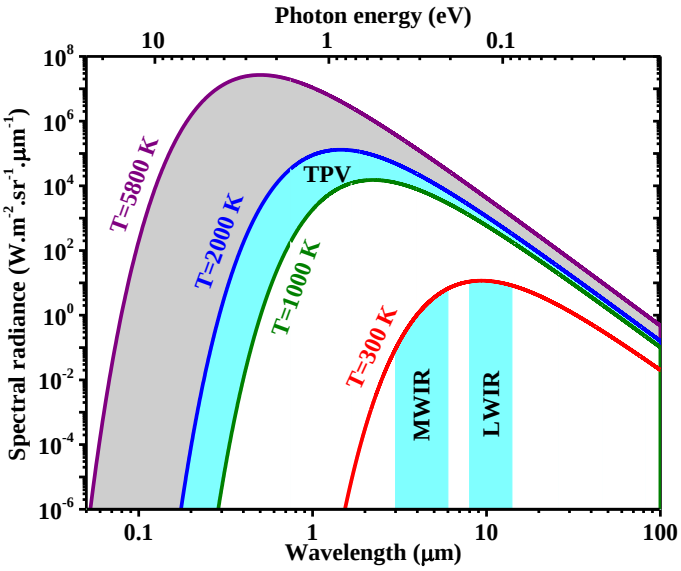

Figure 1-2: Spectral radiation for blackbodies at various temperatures. The shaded regions are of interest for applications such as solar cell, thermophotovoltaics and thermal imaging.

An important feature of infrared radiation is that it is mostly blocked out by the atmosphere. The two natural greenhouse gases in Earth's atmosphere ─ water vapor and carbon dioxide, absorb most of the infrared light. Only a few infrared wavelength ranges are likely to travel through the atmospheric window, as shown in Figure 1-3 [10]. Hence, the better view on the infrared world from ground-based infrared cameras is at infrared wavelengths with a high atmospheric transmittance. The atmospheric window is also an important consideration in free space optical communication (FSO) [11]. Because of this, unlike the earlier mentioned division scheme, a more commonly recognized categorization framework in the detector community is [10]: NIR (0.7-1 μm), SWIR (1-3 μm), MWIR (3-5 μm), LWIR (8-14 μm), very long wavelength IR (VLWIR, 14-30 μm), and far IR (FIR, 30-100 μm) bands.

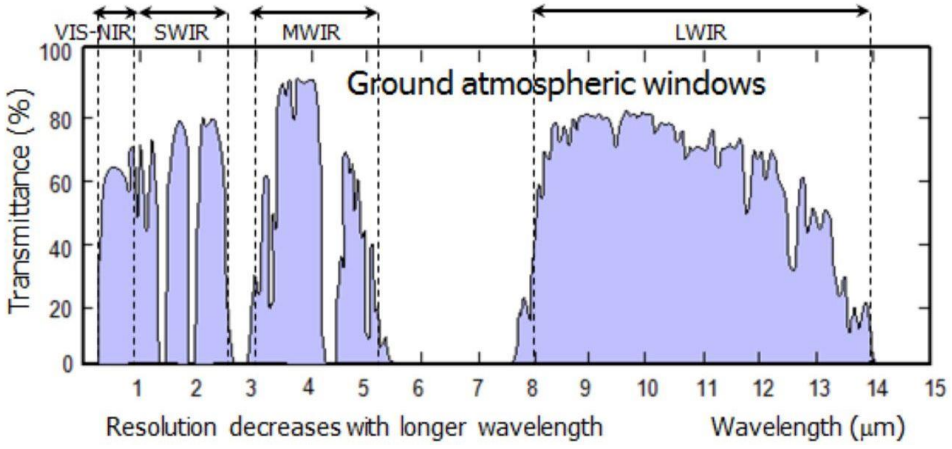

Figure 1-3: Atmospheric transmittance spectrum of infrared radiation. The figure is from [10].

1.2 Overview of infrared thermophotovoltaic energy conversion

1.2.1 Background

In modern society, the overuse of diminishing fossil fuels has driven humanity to develop alternative non-fossil energy source as well as ways of efficient use of fossil fuels. TPV is a promising technology that can generate electricity from non-fuel resources such as radioactive energy and concentrated sunlight. Potentially, it is also a more efficient way to convert fossil fuel combustions with the ultimate efficiency approaching the Carnot limit [4-5]. Although the expected high efficiency has not been fulfilled at the current stage, fuel versatility still motivates further pursuit of this approach.

Early efforts on TPV were dedicated to developing military portable power sources until the 1970s [12]. After the US Army decided to choose thermoelectrics as the priority development project, TPV technology experienced a slow pace of development. However, it still significantly profited from the progress of solar photovoltaics (PVs), particularly from the rapid development of solar cells. Two examples are GaSb and InGaAs diodes that are now the two prevalent TPV cells, while they were originally explored as the subcells in multi-junction solar cells [13-14]. Besides, the experience in controlling the incident radiation gathered from concentrated solar PV also promotes the development of TPV. There was a regenerated interest in TPV in the 1990s for space, industry and military applications. In industry, the use of TPV for waste heat recovery was conceived as a prospective market niche. Over the same period, the near-field TPV concept started to emerge, which utilized a sub-micron vacuum gap between the radiator and TPV cells [15-17]. This method can appreciably improve the heat transfer between the radiator (or emitter) and TPV cell. Another benefit of this displacement is enhanced incident power

density and the resulting higher conversion efficiency.

Until now, TPV is still in a research and development phase, and has not reached commercial maturity, as it has been impeded by some research barriers. For example, in the past, the lack of suitable high efficiency TPV cells was the main obstacle. Currently, the main difficulty is the involvement of various areas of applied science. Unlike solar PVs, the realization of a TPV system relies on experience in various aspects including optics with filters, heat transfer over a small scale and materials tolerant of high temperature. Despite these obstacles, some prototype TPV system demonstrations were reported, as briefly summarized in Table 1-1.

Table 1-1: Summary of some demonstrated TPV system performance.

Heat source	Propane combustion	Propane combustion	Propane combustion	Butane combustion	JP8 combustion	Combined combustor-emitter	Radioisotope module	Sunlight	Sunlight
Emitter material	SiC	Si_xN_y	Si/SiO_2 photonic crystal	Yb_2O_3	tungsten on SiC	SiC	tungsten	tungsten photonic crystal	planar tungsten
Emitter temperature	1200 °C	770 °C	700 °C	1462 °C	1275 °C	1309 °C	1007 °C	1500 °C	1200 °C
Spectral control	dielectric filter on TPV cell	N/A	selective emitter	selective emitter	selective emitter, dielectric filter on TPV cell	surface reflective filter	dielectric filter on TPV cell	selective emitter	surface reflective filter
TPV cell	GaSb	GaSb	GaInAsSb	Si	GaSb	InGaAs	InGaAs	Ge	GaSb
Cell bandgap	0.7 eV	0.7 eV	0.55 eV	1.4 eV	0.7 eV	0.6 eV	0.6 eV	0.66 eV	0.7 eV
Cell temperature	75 °C	25 °C	water cooled	14 °C	25 °C	25 °C	50 °C	120 °C	water cooled
Output power	80 W	1 mW	344 mW	48 W	700 W	3.16 W	100 W	415 mW	9.2 W
Power density	0.4 W/cm^2	32 mW/cm^2	344 mW/cm^2	0.1 W/cm^2	1.5 W/cm^2	0.79 W/cm^2	0.5 W/cm^2	67 mW/cm^2	6.24 W/cm^2
System Efficiency	2.0%	0.08%	2.5%-	2.4%	16% projected	emitter/module 23.6%	20% projected	0.8%	6.2%
Institution	JX Crystal Inc.	MIT	MIT	UNSW	JX Crystals Inc.	Bechtel Bettis Inc.	Emcore	Barcelona University	UVA
Reference	[18]	[19]	[20]	[21]	[22]	[23]	[24]	[25]	[26]

1.2.2 Active components in a TPV system

Solar PV and TPV are similar technologies as they both use PV cells to generate electricity from high temperature radiation sources. One of the main differences between the two is the geometry. A TPV system typically consists of a heat source, absorber and emitter (or radiator), filter and TPV cells. Sometimes a cooling fan is included in the system to prevent overheating of the TPV cells. The general operating principle of a TPV system is illustrated in Figure 1-4. The radiation produced from the heat source (either radioisotope, or fuel combustion or concentrated sunlight) is absorbed by the absorber and subsequently radiated by the emitter. The filter then converts the broadband radiation spectrum into a narrowband emission spectrum tuned to the response of the TPV cell. Afterwards, the radiation is captured by the TPV cell and converted into electricity. In some cases, the absorber is coupled with a selective emitter with a narrow range of wavelength emission, thus the filter is no longer needed. Besides the filter, the other approach of spectral control is to reflect out-of-band photons back to the emitter via reflectors in front of or behind the TPV cell.

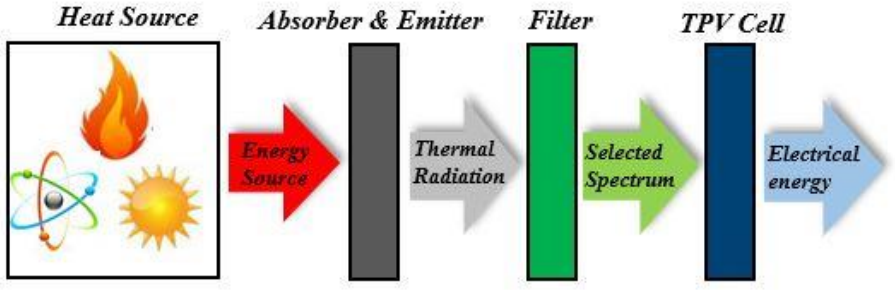

Figure 1-4: Schematic illustration of a TPV system.

The system efficiency is affected by the performance of the individual components as well as the interaction between them. To build a reliable TPV system, the operations of

the components need to be optimized. For example, since the heat source in a TPV system is generally at 1000-2000 K, the emitter should have high thermal stability. There are several suitable materials for emitters, classified as ceramics [18-19, 23], metals [22, 24, 26-28], metal oxides [21, 27, 29-30], or other novel materials [31-33]. Conventional metals and ceramics tend to have broadband emission. In contrast, the pure polished metal oxides (e.g. rare-earth oxides) can have narrow-band emission. Among these materials, tungsten is currently the most used, since its emission spectrum is well matched with the bandgap of GaSb [22, 24, 26-27]. Novel emitters based on artificial structures such as photonic crystals and metamaterials have the advantage of very narrow emission bands, but at the expense of more complex structures than conventional emitters [31-33].

1.2.3 Thermophotovoltaic cells

In the early period of development, investigations of TPV cells were mainly focused on Si [34] and Ge [35]. The low cost and mature production phase of Si made it a competitive material. However, the bandgap of Si is too wide for efficient conversion of IR radiation, because most of the photons possess energies lower than its bandgap and are unable to excite electron-hole pairs. Ge has a narrower bandgap than Si, but its crystal structure can be easily damaged at high temperatures. Also, the recombination losses in Ge cells are very high due to the large effective mass and high carrier concentration. Current generation of TPV cells are mainly made of GaSb [22, 36], InGaAs [23, 37-38], GaInAsSb [39-40] and InGaSb [41-42]. Among them, GaSb is often regarded as the most suitable choice for TPV generators. GaSb has a similar bandgap (~ 0.72 eV) with Ge, which allows it to respond to light with longer wavelengths. Under a perfectly filtered blackbody (T=1350 K), an efficiency of ~30% was projected for GaSb cells [36].

Up to now, without a filter, the best reported efficiencies for TPV cells are 24% for a 0.6 eV InGaAs cell on InP [23, 37] and 19.7% for a 0.53 eV GaInAsSb cell on GaSb [39]. These records were measured with a ~1000 °C broadband blackbody radiator and with a front surface reflector for recovering unabsorbed below-bandgap photons. The bandgap of a ternary InGaAs diode, exactly lattice matched to InP, is 0.74 eV, but it underperforms GaSb TPV cells [38]. By changing the ratio of Ga to In, the bandgap of InGaAs can be tuned from 0.55 to 0.6 eV with some strain from the InP substrate. The strained InGaAs cells generally outperform GaSb cells [23, 37]. Quaternary GaInAsSb alloys latticed-matched to GaSb have bandgaps theoretically ranging from 0.25 and 0.75 eV. The fabricated GaInAsSb cells on GaSb substrate have bandgaps from 0.5 to 0.6 eV [39-40]. The performance of these TPV cells generally falls behind InGaAs TPV diodes. Also, the manufacture of GaInAsSb cells is expensive and is not commercially available.

Aside from the above-mentioned materials, other TPV cell research interests are narrow bandgap (<0.4 eV) materials such as InAsSbP [43-44], InAs [45-46], InSb [47] and InAsSb [48]. These narrow bandgap cells have a low open-circuit voltage and fill factor, as well as a poor efficiency at room temperature as shown in Table 1-2. Even some studies are only for proof-of-concept demonstrations of potentials. To achieve optimal efficiency, they were cooled down to overcome some of the downsides [47]. The performance limiting factors in narrow bandgap TPV cells are identified theoretically and experimentally in Chapters 3 and 5, respectively. Nevertheless, theoretical calculations following the detailed balance principle showed that the optimal choice for TPV cell bandgap energy is between 0.2-0.4 eV [49-50]. In the next subsection, a similar bandgap range is calculated from the thermodynamic perspective. Additionally, up to now, relatively less research work has

been done towards narrow bandgap cells; there is still great potential in further development of them. Table 1-1summary some important device performances of various types of single-absorber TPV cells.

Table 1-2: Summary of various TPV technologies, classified by absorbing material.

InAsSbP	**InGaSb**	**GaInAsSb**	**GaInAsSb**	**InGaAs**	**InGAAs MIM**	**GaSb**	**GaSb**	**Ge**	**Si**
0.35	0.56	0.549	0.53	0.74	0.6	0.73	0.73	0.66	1.1
21 °C	27 °C	27 °C	27 °C	30 °C	25 °C	25 °C	25 °C	300 K	300 K
N/A	1373 K blackbody	arc lamp	950 °C SiC	3250 K blackbody	1039 °C tungsten	1350 K blackbody	1200 °C SiC	1100 °C tungsten	2300 °C radiator
without	without	without	front surface filter	front surface reflection	front surface filter	perfect band edge filter	front surface filter	front & back surface reflection	N/A
0.25	3.0	3.5	2.9	0.288	0.1	3.0	2.83	1.67	9.52
34%	61%	66%	67%	65%	66.2%	75%	73%	67%	N/A
120 mV	270 mV	313 mV	306 mV	405 mV	12.5 V	500 mV	477 mV	356 mV	N/A
0.024	0.49	0.723	0.58	0.08	0.79	1.26	0.98	0.4	10
0.18%	N/A	N/A	19.7%	12.4%	24%	projected 30%	21%	16%	26%
[44]	[42]	[40]	[39]	[38]	[23, 37]	[36]	[22]	[35]	[34]

Table 1-2 continued

Material	**InAsSb**	**InSb**	**InAs**	**InAs**
E_g (eV)	0.286	0.23	0.36	0.32
Cell *T*	27 °C	77 K	300 K	20 °C
Illumination source	1500 K blackbody	1248 K IR source	800 °C blackbody	950 °C blackbody
Spectral control	without	without	without	without
J_{sc} (A/cm^2)	39.88	7.2E-3	0.23	0.89
***FF* (%)**	N/A	64%	25%	37%
V_{oc}	162.8	83 mV	17.4 mV	60 mV
P_{out} (W/cm^2)	N/A	3.8E-4	1E-3	0.02
Efficiency	projected 16%	N/A	0.35%	3%
Reference	[48]	[47]	[46]	[45]

1.2.4 Thermodynamic analysis of thermophotovoltaic cell efficiency

In single-absorber TPV cells, without spectral control, the major energy loss arises from two mechanisms. The first mechanism is that photons with energies lower than the bandgap energy are not converted. The second mechanism is due to photons with energy higher than E_g. These photons contribute only E_g and the excess energy is released via hot carrier heating. Theoretically, both losses can be minimized by means of spectral control, but this would lead to low, often not acceptable, power densities, and low system efficiencies. Without spectral control, there is a tradeoff between the intensified below-bandgap loss and mitigated thermalization loss as the cell bandgap increases, implying an optimal choice of the bandgap to maximize cell efficiency. Several well-established models exist to identify the ideal cell bandgap, as well as to predict the upper limits of TPV efficiency and power density. The efficiencies predicted by different models are compared

in [51]. Some models are based on empirical values for the saturation current density [52-54]. Some models refer specifically to solar TPV conversion [55-57]. The usual assumption made in these models is full incident spectrum (no spectral control). Here, the ultimate efficiency and optimal bandgap are calculated by extending Shockley and Queisser's [58] limit for solar cells (also known as the detailed balance limit) to the TPV case.

In TPV systems, ideally, there is no radiation lost since the radiator and emitter are closely arranged. The solid angle subtended by TPV cell can be 4π sr compared to the 6.85×10^{-5} sr for conventional solar cells. Thanks to this arrangement, from the Stefan-Boltzmann law (Equation 1-3), the radiation density can reach 16-91 W/cm^2 incident on the TPV cell for a heat temperature at 1000-2000 K, while the average solar radiation on earth's surface is only 0.1 W/cm^2. To apply detailed balance analysis, several assumptions need to be made to simplify the scenario. First, there are no non-radiative channels in the TPV cell; carrier recombination and generation are exclusively radiative. Second, the bandgap is a sharp demarcation of absorption: photons with above-bandgap energy are completely absorbed, while below-bandgap photons are hardly absorbed. Third, when a bias voltage (V) is applied to the TPV cell, it will emit photons as a blackbody with a chemical potential of eV.

Under these assumptions, the current flowing in a TPV cell under a bias voltage (V) can be given by:

$$J(V) = \frac{2\pi q}{h^3 c^2}\int_{E_g}^{\infty}\left[\frac{E^2}{exp\left(\frac{E}{k_b T_s}\right)-1} - \frac{E^2}{exp\left(\frac{E-eV}{k_b T_{cell}}\right)-1}\right]dE \tag{1-4}$$

where q is electron charge, T_s and T_{cell} are the temperature of the source and cell, respectively. The first term in the integral stands for the photocurrent due to light

absorption. The second term represents the reverse dark current originated from electron recombination. Based on Equation 1-4, the calculated efficiencies of TPV cells for various source temperatures are shown in Figure 1-5. The inset within the figure is the optimal bandgap that maximizes the efficiency as a function of the source temperature. As can be seen, the optimal bandgap for a source temperature at 1000-2000 K is in the range of 0.18-0.37 eV, well less than the bandgap of current mainstream TPV cells made of GaSb, InGaAs and GaInAsSb. The corresponding maximum efficiency is between 22% and 33%, remarkably higher than the actual efficiencies of narrow bandgap TPV cells such as InAsSbP, InAs and InSb (See Table 1-2). This is because the detailed balance limit is a very idealized and an overestimated limit, as the analysis buries many practical factors. For example, in real narrow bandgap devices, non-radiative recombination such as Auger and Shockley-Read-Hall (SRH) tend to prevail over radiative recombination. These non-ideal factors will seriously limit overall device performance. In Chapter 3, the efficiency limits of narrow bandgap TPV cells will be re-evaluated by acknowledging some of the practical factors.

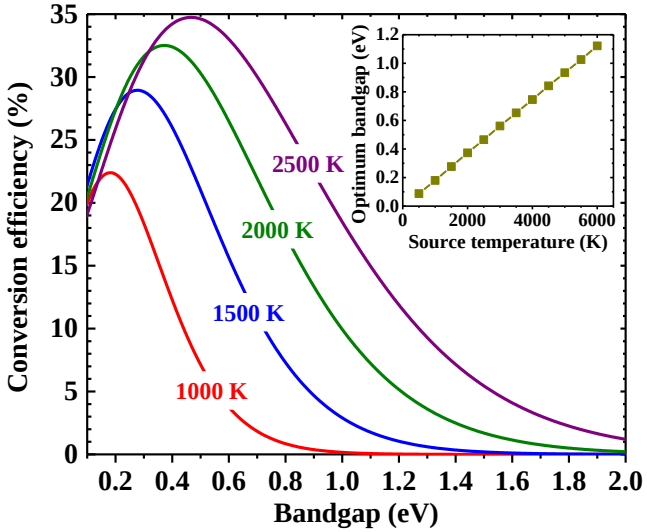

Figure 1-5: The calculated efficiencies based on Equation 1-4 for various blackbody temperatures. The inset shows the optimal bandgap that maximizes the efficiency.

1.3 Overview of infrared detectors

1.3.1 Background

The historical track record of modern infrared detectors (or systems) is shown in Figure 1-6. Modern development of infrared detector was possible after the discovery of lead salt family (PbSe and PbS) [59]. Thereafter, further researches launched the development of various detecting materials (or structures) including but not limited to: Ge [60], InSb [61], Si [62], HgCdTe [63], InGaAs [64], quantum well infrared detector (QWIP) [65], quantum dot infrared detector (QDIP) [66], barrier photodetector [67] and type-II superlattice (T2SL) [68], as shown in Figure 1-6. Also, there are three generations of IR detection systems that are generally considered in civil and defense applications. The first generation is scanning systems with single and linear units. The second generation includes focal plane array (FPA) technology with monolithic and hybrid detectors. Combined with the read-out circuit in the FPA, a multiplexing function can be achieved. The third generation has orders of magnitude more pixel elements than the second generation FPAs. In addition, a multicolor function and other superior on-chip features are possible in the third generation.

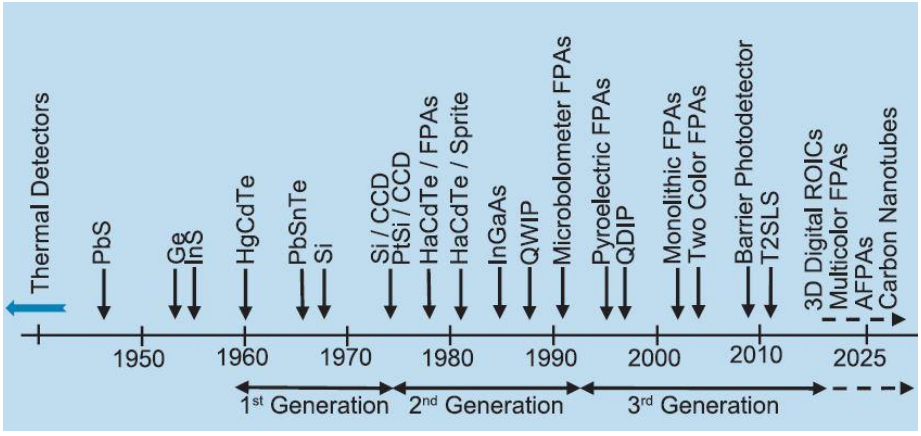

Figure 1-6: The development history of modern infrared detectors and systems.

As mentioned in Section 1.1, MWIR technology finds its application mainly in gas sensing. Specifically, there are three thriving civil application areas of mid IR gas sensors: environmental monitoring, industrial process control and medical diagnosis. Many molecules and gases exhibit strong absorption characteristics in the mid IR band, as shown in Figure 1-7 [69]. In addition, thanks to the much stronger absorption, gas sensing systems based on MWIR and LWIR optoelectronics have an inherent advantage over NIR counterparts in terms of sensitivity (or detection limit). For example, the detection limit for CH_4 at 3.26 μm is 1.7 ppb compared to 600 ppb at 1.65 μm. Another more contrasting example is CO_2. The detection limit for this greenhouse gas is 0.13 ppb at 4.23 μm, while it is 3000 ppb at 1.55 μm. Despite the real advantages, MWIR and LWIR optoelectronics had received considerably much less research attention than NIR optoelectronics. The main reason for this difference is the revolution of communication systems with the advent of optical fiber systems, which directly lead to the rapid development of NIR optoelectronics. Nevertheless, the impressive accomplishments in MWIR and LWIR lasers such as quantum cascade lasers (QCLs) [70-71] and interband cascade lasers (ICLs) [72-73] will significantly promote the research and development of MWIR detectors.

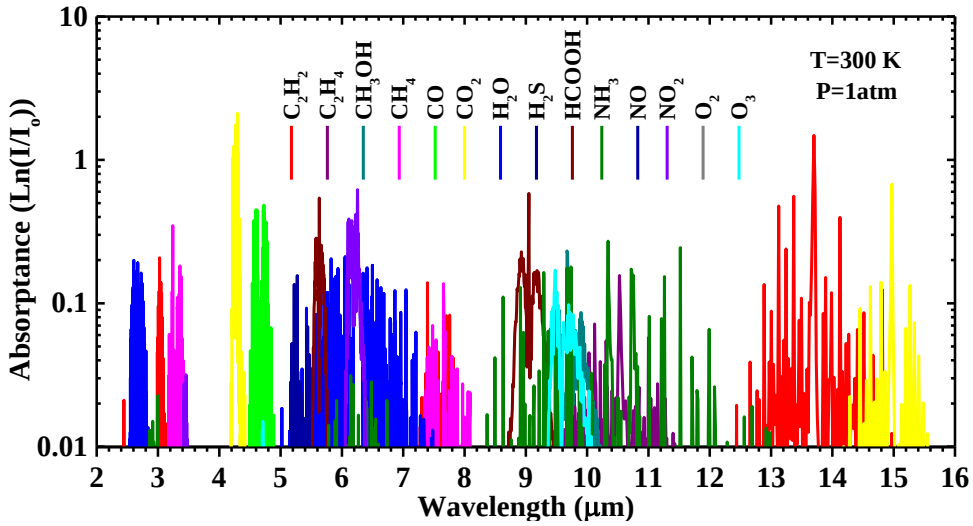

Figure 1-7: Mid infrared absorption spectra of some molecules and gases. Data were collected from [69].

1.3.2 Photon detection vs thermal detection

Most infrared detectors can be classified into two categories [9, 74-76]: photon detectors and thermal detectors. Photon detection occurs when incident photons, absorbed by the detecting material, excite free electron-hole pairs. In most instances, the material is a bulk semiconductor or a low dimensional material such as those mentioned in Subsection 1.3.1 (refer to Figure 1-6). The electrical signal arises from the change of electron distribution inside the detector. Thermal detection is defined as the mechanism that change some measurable property of the detecting material due to the temperature increase of that material resulting from the absorption of radiation, as illustrated in Figure 1-8 [76]. Among the various thermal mechanisms, the most important three are the thermoelectric effect, the resistive bolometric effect, the pyroelectric effect and its modification known as the ferroelectric bolometer [9, 74-76]. Although many other mechanisms were proposed, only these three have been shown to be practical to date. The electrical output in a resistive bolometer (typically made of VO_x) arises from the change of its electrical resistance as the

temperature rises. The pyroelectric effect is demonstrated with certain materials which could generate electrical polarization that can be measured as an electrical charge on the opposite face. The thermoelectric effect, i.e. Seeback effect, is the buildup of an electrical potential across a temperature gradient; the resulting voltage is proportional to the temperature difference between the hot and cold ends.

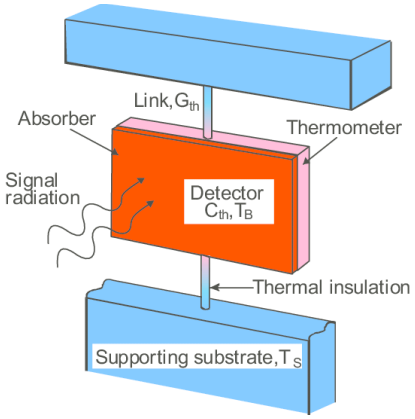

Figure 1-8: Block diagram of a thermal detector. Figure from [76].

In general, thermal detectors do not require cryogenic cooling, while the photon detectors in MWIR and LWIR regions are cooled to suppress thermal generation of carriers. The coolers are normally costly devices, making the detection system (e.g. an infrared camera) more expensive than uncooled systems. Also, the coolers make the systems bulky, and more steps are needed in manufacturing, therefore reducing the yields. In addition, photon detectors are selective in wavelength, while thermal detectors have no wavelength dependence. Nevertheless, cooled systems based on photon detectors are incredibly more sensitive than uncooled thermal systems, as illustrated in Figure 1-9. As can be seen, the image captured by a cooled infrared camera has a quality much better than that created by an uncooled camera. In addition, the imaging speeds of cooled systems are much higher than uncooled systems. The high-speed thermal imaging of cooled systems

allows capturing frame rates as high as 62000 fps.

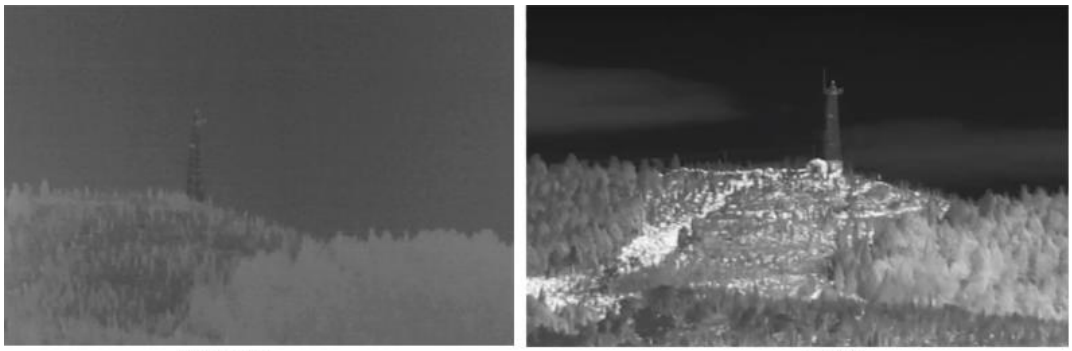

Figure 1-9: Images created by uncooled and cooled infrared cameras. The figures are from [77].

1.3.3 Examples of photon detectors

Photon detectors can be further subdivided into photoconductive (PC) and photovoltaic detectors according to satisfaction or violation of symmetry in the configuration. The simplest form of a symmetric PC photodetector consists of a slab of semiconductor, as shown in Figure 1-10(a). By contrast, the structure of a PV photodetector is asymmetric, in most cases, it is made of a p-n junction [See Figure 1-11]. Such an asymmetric structure enables the separation of photo-generated carriers without applying external bias. The resulting difference between PC and PV photodetectors is the operation bias: PV detectors can operate at zero bias, while PC detectors require an external bias to initiate the operation. In addition to the simplest semiconductor slab, a comparably more complex PC photodetector structure is a QWIP [65, 78], as illustrated in Figure 1-10(b). As can be seen, the basic elements of a QWIP are quantum wells (QWs) separated by wide barriers. The incident light is absorbed via intersubband transitions of electrons within the QWs. Once the electrons are optically excited into the continuous upper states, they will be measured as a signal current. However, to collect these electrons, an external bias needs

to be applied and the signal current responds in an almost linear fashion to the applied bias. Among various types of QWIPs, technology based on GaAs/AlGaAs multiple QWs is most mature [65, 78]. QWIP detectors have relatively low quantum efficiencies, generally lower than 10%, partially resulting from the selection rule of intersubband transitions in conduction band [79].

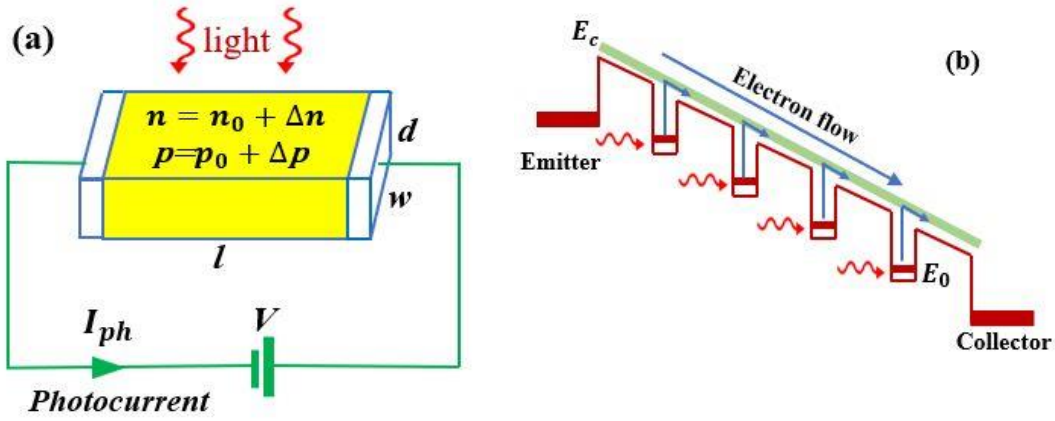

Figure 1-10: Schematic diagram of (a) a photoconductive photodetector made of a semiconductor slab, (b) a quantum well infrared photodetector based on bound-to-continuum transitions.

The most common configuration for PV detectors is a single p-n junction as shown in Figure 1-11. The optically excited electrons and holes are separated by the built-in electric field in the depletion region and then contribute to the signal current. One route to increase light absorption in a p-n junction is to sandwich a thick intrinsic layer between the p- and n- doped layers, forming the so-called p-i-n structure. Some p-i-n detectors can use avalanche multiplication but they must be reverse-biased [80].

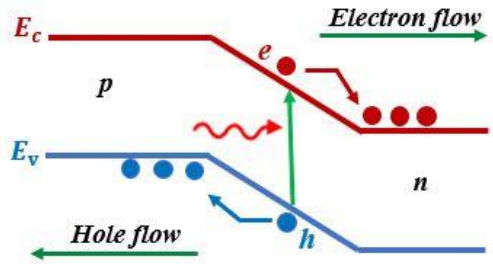

Figure 1-11: Schematic diagram of a PV detector made of a single p-n junction

Another simple but refined PV detector technology is the barrier photodetector [67, 81]. Among various types of barrier photodetectors, the most popular one is nBn detector as shown in Figure 1-12(a). Such a configuration is conducive to reducing majority-electron dark current, while the signal current from minority holes is unaffected. The barrier also takes a role to reduce the surface current, a benefit equivalent to self-passivation. In addition, the absence of a depletion region eliminates the excess dark current associated with the SRH process and trap-assistant tunneling. A special modification of the nBn detector is the complementary barrier infrared detector (CBIRD) [82] with an additional hole barrier introduced in the valance band, as shown in Figure 1-12(b). The electron and hole barriers complement one another to impede the flow of dark current. As with nBn detectors, the benefit of reduced dark current from elimination of a depletion region also extends to CBIRD detectors.

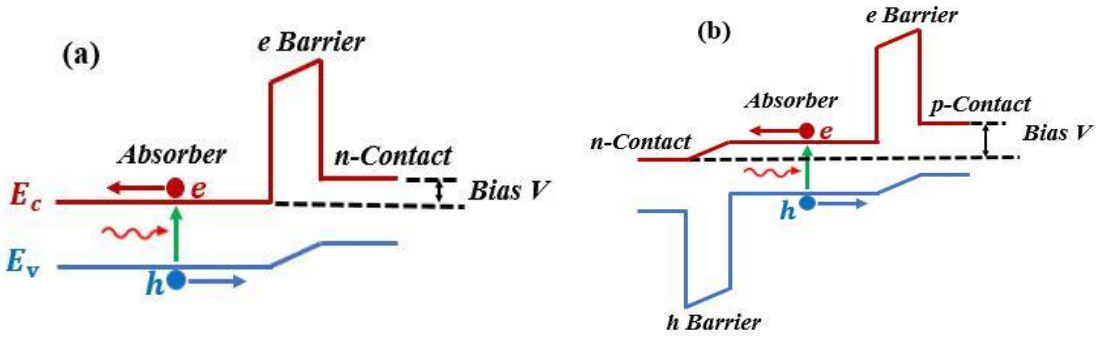

Figure 1-12: Schematics of (a) an nBn barrier detector and (b) a complementary barrier infrared detector; the biases are applied to improve carrier collection.

Apart from p-n junction and barrier structures, there is another more complex photodetector operating in PV mode: the quantum cascade detector (QCD) [83-84], as shown in Figure 1-13. As an intersubband detector, the QCD is a special variation from the standard QWIP structure. The QCD is configured to operate in PV mode to reduce the dark current present in a QWIP. However, despite this improvement, the dark current in QCDs is still relatively high due to the short carrier lifetime (~ ps at 300 K) in intersubband transitions. This fundamental problem severely undermines the ability to achieve a high detectivity for QCDs especially at high temperatures, which will be discussed in detail in Chapter 6. A brief summary of various photovoltaic photodetectors is presented in Table 1-3.

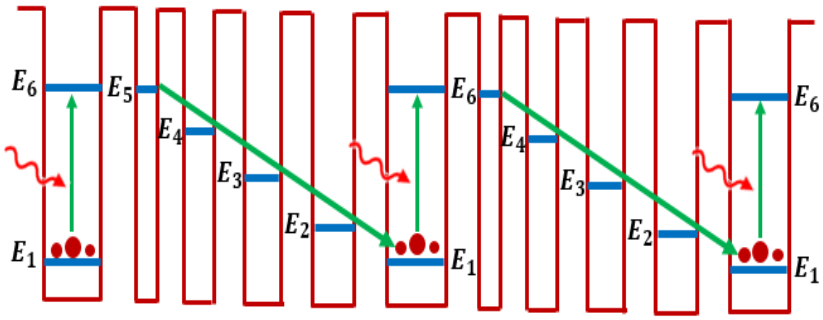

Figure 1-13: Schematic diagram of a quantum cascade detector.

Table 1-3: Summary of various photovoltaic photodetectors, classified by detecting material.

Material or Structure	λ_{cutoff} or λ_{peak} (μm)	T (K)	R_0A or J_d	R_i (A/W)	D^* (Jones)	Ref
Ge	1.55	300	10 A/cm^2	0.1	N/A	[60]
InGaAs	1.55	295	10 nA/cm^2	0.62	1.0×10^{12}	[85]
PbS	3.0	300	0.1 Ω·cm^2	1.22	3.0×10^{9}	[86]
PbSe	4.0	300	6.5 Ω·cm^2	1.6	1.0×10^{9}	[87]
InAs	3.4	295	8.1 Ω·cm^2	0.54	1.2×10^{10}	[88]
InSb	4.0	77	6.3E6 Ω·cm^2	N/A	1.0×10^{11}	[89]
InAsSb	4.0	300	0.19 Ω·cm^2	0.76	2.6×10^{9}	[90]
HgCdTe	3.0	300	1.0 Ω·cm^2	0.5	6.5×10^{9}	[91]
HgCdTe	5.0	300	0.01 Ω·cm^2	1.0	2.0×10^{9}	[91]
HgCdTe	8.0	230	2E-4 Ω·cm^2	0.8	4.0×10^{8}	[91]
HgCdTe	10.6	230	1E-4 Ω·cm^2	0.4	2.0×10^{8}	[91]
InAs/GaSb SL	2.2	300	15 Ω·cm^2	0.57	1.7×10^{10}	[92]
InAs/GaSb SL	4.2	150	5.1E3 Ω·cm^2	1.9	1.1×10^{12}	[93]
InAs/GaSb SL	9.9	77	1.4E4 Ω·cm^2	1.5	1.1×10^{11}	[82]
InAs/InAsSb SL	10.0	77	119 Ω·cm^2	4.47	2.8×10^{11}	[94]
InAs/InAsSb SL	14.6	77	0.84 Ω·cm^2	4.8	1.4×10^{10}	[95]
QCD	5.4	300	0.22 Ω·cm^2	7E-3	2.5×10^{10}	[96]
QCD	8	300	0.028 Ω·cm^2	1.7E-2	1.4×10^{7}	[97]

1.3.4 Performance metrics for infrared detectors

The most important performance coefficient for infrared detectors is the specific detectivity D^* that describes the smallest detectable signal. It equates to the reciprocal of noise-equivalent power (NEP, in unit of W) that is normalized per square root of frequency bandwidth and detector area. That is, the expression of D^* is given by:

$$D^* = \frac{\sqrt{\Delta f A}}{NEP} \tag{1-5}$$

where Δf is the bandwidth and A is the detector area. The unit of D^* is cm·Hz$^{1/2}$/W or more frequently it is expressed as Jones. The noise equivalent power NEP is the incident flux required to generate an output signal current/voltage equivalent to the noise current/voltage. For most photon detectors, the noise current is used to define NEP:

$$\mathrm{NEP} = I_n/R_i \tag{1-6}$$

where I_n is the noise current, and R_i is current responsivity that is equal to 1.24·QE/λ (QE is quantum efficiency). The noise sources in a photodetector include low-frequency noise, Johnson noise, shot noise and generation-recombination (G-R) noise. In some instances, the dominant noises are Johnson and shot noises. They occur as results of thermal fluctuation during carrier motion (Johnson noise) and statistical fluctuation of thermal generation of carriers (shot noise). Since the two noises are not coupled, the total mean square noise current is the sum of both noise currents:

$$i_n^2 = \frac{4k_bT}{R_0}\Delta f + 2eJA\Delta f \tag{1-7}$$

where R_0 is zero-bias resistance and J is the dark current density. The first term in this equation describes Johnson noise and the second term corresponds to shot noise. Substituting Equations (1-6) and (1-7) into Equation (1-5), one can obtain the expression of Johnson- and shot-noise limited detectivity:

$$D^* = \frac{R_i}{\sqrt{4k_bT/R_0A+2eJ}} \tag{1-8}$$

From this equation, the D^* can be improved either by reducing the noise or by increasing the QE. The most effective way to maximize D^* in conventional single-absorber detectors is to increase the QE. In contrast, the D^* can be effectively improved in multistage detectors via noise reduction, as will be described in Chapter 2.

1.4 Dissertation organization

Chapter 2 concentrates on the fundamentals of the interband cascade (IC) device family including IC lasers (ICLs), IC infrared photodetectors (ICIPs) and IC thermophotovoltaic (ICTPV) cells. The main purpose of this chapter is to explain the historic development, constituent materials, operation principles and basic theories of these quantum engineered devices. It commences with the introduction of the 6.1 Å material system: InAs, GaSb and AlSb and their unique properties. Subsequently, it presents the attractive features of IC structures when functioning as lasers, PV cells and detectors.

Chapter 3 presents the theoretical comparison between single-absorber and multistage ICTPV cells. The efficiency limits are calculated considering some practical factors that apparently violate the assumptions made in the idealized thermodynamic analysis in Subsection 1.2.4. This is in keeping with the relatively low efficiencies demonstrated for current narrow bandgap TPV technologies. Several limiting factors are identified, which turn out to be closely associated with short carrier lifetime, small absorption coefficient and high dark saturation current density.

After the theoretical comparison, experimental details and comparisons between single-absorber and multistage ICTPV cells are given in Chapter 4. A set of three TPV cells with single-absorber and multistage architectures are characterized and analyzed in detail. The experimental data confirmed the advantages of the multistage IC architecture for TPV cells. It is shown that a multistage IC structure can be successful in resolving the diffusion length limitation in single-absorber cells, and to achieve a collection efficiency approaching 100% for photogenerated carriers.

Speculatively, the performance should be better for ICTPV cells with more stages,

as will be shown in Chapters 3 and 4. The initial goal of the fabricated four ICTPV devices in Chapter 5 is to examine this speculation. However, the experimental study reaches the opposite conclusion that significantly increasing the number of stages may penalize device performance. Detailed device characterization and analysis are developed to explain this contradiction, as well as to identify and quantify three factors: current mismatch, material quality and collection efficiency.

Chapter 6 and 7 are mostly focused on the deep knowledge and strategies of IC infrared photodetectors. Chapter 6 first describes an effective and simple approach to extract carrier lifetime in the InAs/GaSb SLs. The developed method is applied to some ICIP devices to extract the carrier lifetime at high temperatures. This chapter then introduces a unified figure of merit for interband and intersubband devices, i.e. the saturation current density J_0. The significance of J_0 on the performances of detectors and PV cells is illustrated with measured D^* and calculated V_{oc}, respectively.

Chapter 7 first provides a comparative study of two sets of four ICIP devices with current-matched and noncurrent-matched configurations. This study demonstrated the necessity of current matching in ICIPs to maximize the utilization of absorbed photons for an optimal responsivity. Following this study, the universally observed electrical gain in noncurrent-matched ICIPs is explained with a unique mechanism. Furthermore, a theory is developed to quantitatively describe the electrical gain, and the calculations agree well with experimental data. Finally, Chapter 8 gives some prospective points for the future work arising from these studies.

Chapter 2: Sb-based interband cascade devices

2.1 6.1 Å Semiconductor family

Interband cascade (IC) optoelectronic device is an umbrella term that refers to IC lasers (ICLs) [72-73, 98], IC infrared photodetectors (ICIPs) [99] and ICTPV cells [100]. The materials that make up these devices are the 6.1 Å material system including InAs, GaSb, AlSb and their related alloys. The crystal structures of the three compounds are all zin blende. The main advantages of the three materials are small lattice constant mismatch and similar growth windows. Specifically, the lattice constants are respectively 6.0584, 6.0959 and 6.1355 Å for InAs, GaSb and AlSb. Thus, these binary materials can be incorperated together to the same heterostrucutre with low densities of defets and dislocations. The bandgaps of them and the related alloys are between 0.41 eV (for InAs) and 1.70 eV (for AlSb) as shwon in Figure 2-1(b). This bandgap range is of great interst for the design of optoeelctronic devices in the SWIR and MWIR spectral regimes.

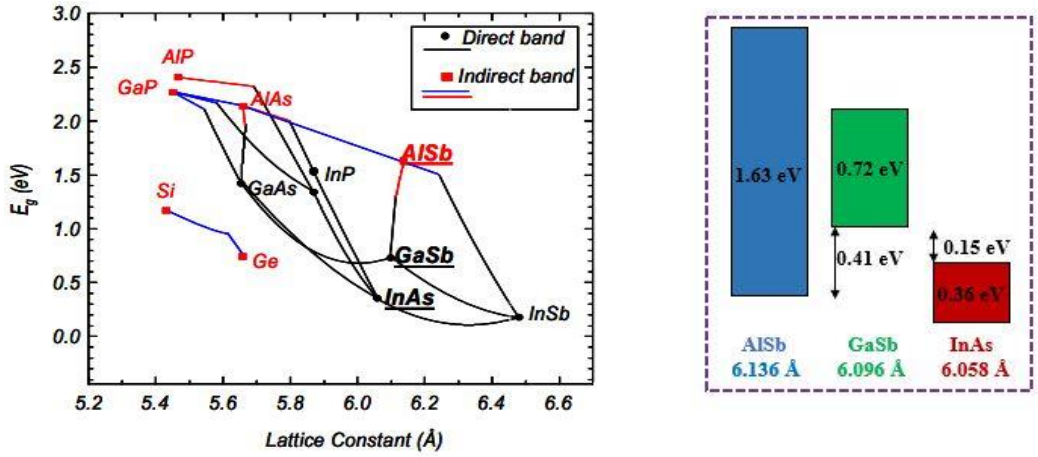

Figure 2-1: (a) Bandgap, lattice constant and (b) band alignment of the 6.1 Å semiconductor materials.

The operations of IC devices are possible due to the unique properties of the 6.1 Å materials. One of the key properties is the type-II broken-gap alignment between InAs and

GaSb. As shown in Figure 2-1(b), the conduction band edge of InAs is about 150 meV lower than the valence band edge of GaSb. The benefits of this type of misaligned structure are twofold. It enables smooth transition of electrons from valence band in GaSb layer to conduction band in InAs layer without energy loss [101-102]. Also, due to this alignment, the InAs/GaSb type-II SLs (T2SLs) have very flexible engineering capability [103-106] and can cover a wide range of infrared spectra from SWIR to VLWIR. On the other hand, the InAs/AlSb interface forms a type-II staggered alignment where the conduction band edge of InAs is slightly above the valence band edge of AlSb. This staggered alignment, tougher with the wide bandgap of AlSb, results in an extremely large conduction bandgap offset of nearly 1.45 eV. This enables the realizations of very deep quantum wells and very large tunneling barriers. Because of this feature, InAs/AlSb heterostructure has been frequently used in resonant interband tunneling diodes (RITDs) [107-108] and short-wavelength QCLs [109-110].

2.2 Interband cascade lasers-the historic origin

2.2.1 History and operation principle

Both ICIPs and ICTPV cells spring from ICLs, so for better understanding of their evolutions and operations, first a brief review of ICL is given before moving on to ICIPs and ICTPV cells. The concept of ICL was originally proposed in 1994 [98]. The main innovation behind the concept is the capability to manipulate electron transport to form an interband cascade scheme, whereby a single electron can generate multiple photons based on interband transitions, as shown in Figure 2-2. Prior to the proposal of ICL, another cascade laser, i.e. QCL, based on intersubband transitions was demonstrated in the same

year [70]. Both ICL and QCL consist of multiple cascade stages connected in series, and each cascade stage ideally acts as an individual photon generator. However, unlike QCLs in which the photons are generated via intersubband transition, ICLs use interband transitions for active generation of photons. The injected carriers in ICLs relax to the lower energy level at a rate much slower than in QCLs, so the threshold condition can be much easier to establish in ICL. This is because the interband transitions in ICLs are characterized by radiative, Auger and SRH processes, in which carrier lifetimes are on the order of nanosecond. In contrast, the intersubband relaxation in QCLs is accompanied with longitudinal phonon emission and has a picosecond time scale. The use of interband transition in ICLs makes the threshold current and input power much lower than that in QCLs. Even compared with other types of mid IR lasers such as Sb-based type-I QW diode lasers [18-19] and II-VI lead salt lasers [20-21], the threshold current and input power of ICLs are considerably lower. This makes them the preferred option for applications where low power consumption is strongly prioritized.

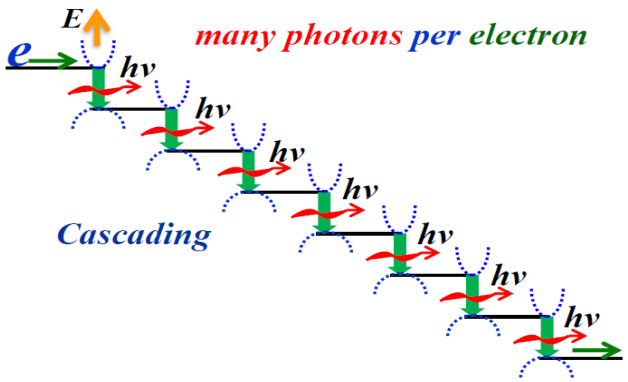

Figure 2-2: Illustration of the photon emission and cascading effect in an interband cascade laser. Figure from [115].

Compared to the conventional diode lasers, the cascade design requires a higher voltage to reach threshold. This is because each cascade stage needs to consume a voltage

to invert the population. Nevertheless, the current required to trigger the lasing action is significantly reduced, as multiple photons are generated for each injected electron. This tradeoff between voltage and current is in favor of reducing Ohmic losses from the series resistance, especially for high-power semiconductor lasers operating with high currents. In this regard, IC structures can be beneficial to improving the overall power efficiency by lowering the operating current.

The active core of an ICL is schematically shown in Figure 2-3. In each stage of an ICL, the active region is sandwiched between the electron and hole injectors. The active region, the electron injector and the hole injector are typically made of GaInSb-InAs “W” QW, multiple InAs/AlSb QWs and multiple GaSb/AlSb QWs, respectively. Under a forward bias, the electrons are injected from the injector into the conduction band of the active region. The injected electrons are confined in the active region by the AlSb barriers and transit to the valence band via photon emission. The transited electrons subsequently enter the electron injector in the next stage via interband tunneling through the broken gap between InAs and GaSb. This process is orders of magnitude faster than the interband transition (~1 ns) in the active region. Therefore, the electrons relaxed to valence band in the active region are efficiently swept out and population inversion can be readily achieved.

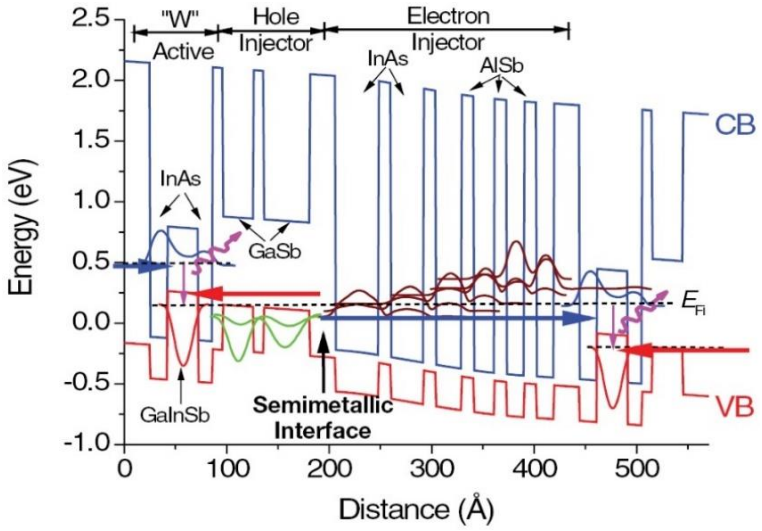

Figure 2-3: Band diagram of the active core for an interband cascade laser. Figure from [73].

2.2.2 Current status of ICL performance

Since its first demonstration, the performance/capability of ICL has been transformed a lot. In CW operation, ICLs can cover a broad range of wavelengths extending from 2.8 μm to 6.0 μm at room temperature (RT) or above [116-120]. Further preparation for high temperature operation with a longer wavelength is in progress [115, 121-124]. Typically, the epitaxy growth of ICL is done on either a GaSb [72-73, 116-118, 125-126] or InAs [115, 119-124] substrate. As wavelength increases, the InAs/AlSb SL cladding layers in GaSb-based ICLs need to be thick, in order to provide strong optical confinement. This is problematic for heat dissipation, as InAs/AlSb SLs have very low thermal conductivity (~2.7 W/m·K). Also, thick InAs/AlSb SLs are challenging in MBE growth due to many shutter movements. These issues can be readily resolved in InAs-based ICLs wherein the SL cladding layers are replaced with highly doped InAs layers [115, 119-124]. Besides, this approach offers another benefit: the low refractive index for highly

doped InAs layers increases the optical confinement. Figure 2-4 shows the room temperature threshold current densities for both InAs- and GaSb-based ICLs in the wavelength range of 2.7-7.2 μm. Most of the data are collected in pulsed modes at 300 K. As can be seen, the technology maturity for GaSb-based ICLs is well demonstrated in the 3-4 wavelength region. By comparison, InAs-based ICLs aim to cover wavelengths longer than 4 μm. In the 4-5 μm wavelength region, the two types of ICLs have comparable performances. However, as the wavelength goes beyond 6 μm, InAs-based ICLs outperform GaSb-based ICLs in terms of threshold current density.

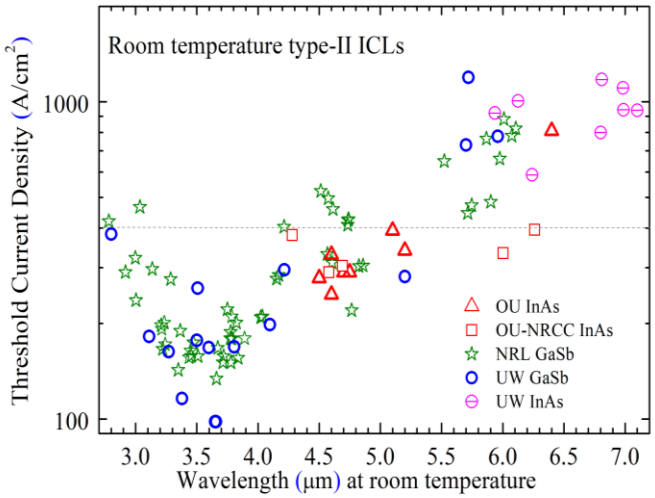

Figure 2-4: Room temperature threshold current density for both InAs- and GaSb-based broad-area ICLs. Figure is from [124].

2.3 Interband cascade thermophotovoltaic devices

2.3.1 InAs/GaSb type-II superlattices

The ideal of InAs/GaSb T2SLs was first introduced in 1977 [127]. Ten years later, it was proposed for detector application [68]. Since then, it has been recognized as a promising material for mid IR detectors due to the predicted reduction of Auger recombination rates [128-130]. Measurements of the Auger recombination coefficient by

pump-probe transmission likewise showed suppressed Auger rates compared to bulk materials [131]. Factors considered to contribute to this suppression include strain induced splitting in valence band, quantum confinement and off-resonance positions of the spin-orbit split-off band. On the other hand, as shown in Figure 2-5(a), the electrons and holes are confined separately in InAs and GaSb layers, which reduces the light absorption. The bandgap of InAs/GaSb SLs is the difference between the minibands for electrons and holes. The miniband for holes is very narrow since the effective mass of holes is large. Moreover, the energy level of hole is almost quasi-constant with GaSb well thickness. Hence, the bandgap of InAs/GaSb SLs is mainly controlled by conduction band level, via the change of InAs and GaSb layer thicknesses.

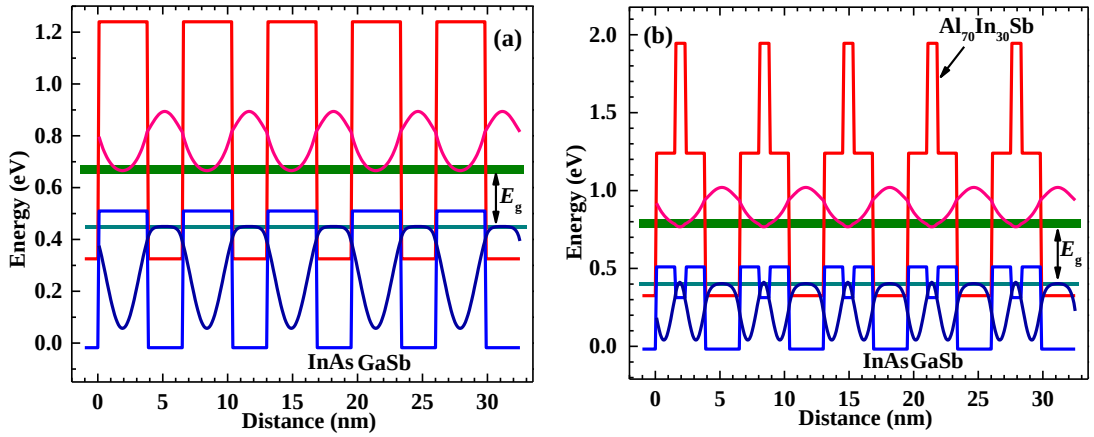

Figure 2-5: Band structure, minibands and wavefunctions of electrons and holes for (a) InAs/GaSb superlattice and (b) *M*-shape Al(In)Sb/GaSb/InAs/GaSb/Al(In)Sb SL.

When the bandgap is wide, the binary InAs/GaSb SL is not the preferred option. This is because a wide bandgap necessitates thin InAs layers, which can make the bandgap very sensitive to layer variations during growth. Also, it can cause interface mixing/roughness, as lower material and interface quality were reported in literature [132-133]. A solution to these issues is inserting thin Al(In)Sb layer in the middle of GaSb layers, forming the so-called *M* structure [104, 134-135]. The letter "M" stands for the shape of

the band alignment of the Al(In)Sb/GaSb/InAs/GaSb/Al(In)Sb layers, as shown in Figure 2-5(b). There are several potential advantages of the *M*-shape SL. First, the AlSb blocking barrier can reduce the dark current and improve the R_0A product of devices made from this structure [104]. Second, the AlSb layer can compensate the tensile strain induced by InAs layers. Third, it reduces the wavefunction penetration into barrier layers, thereby narrowing the minibands and allowing a sharp increase of absorption coefficient near bandgap. In addition to *M*-shape SL, there are other modifications of the normal InAs/GaSb SL, namely, the *W*- [105] and *N*-shape SLs [106]. These various modifications manifest the flexible heterostructure design of T2SLs based on InAs/GaSb/AlSb material system.

2.3.2 Operation principle of ICTPV cells

The photovoltaic operation of IC structures was first demonstrated with devices that were fabricated from ICL wafers [136]. The light absorption region was simply composed of a single pair of coupled quantum wells; small absorption was revealed by the measured low responsivity of the fabricated PV detectors. To address this problem, it is necessary to make some modifications to the structure. One prominent alteration is replacing the quantum well absorber with much thicker InAs/GaSb T2SLs [99-100]. This structural change was shown to be very effective to improve light absorption characteristics and overall device performance [99]. Further refinement of the structure was made on the hole injection region: additional QWs are added to better block intraband tunneling of electrons, thus reducing the dark current density [137].

Overall, the structure of an ICTPV cell is roughly similar with that of an ICL. Each stage of an ICTPV cell consists of an electron barrier (eB), a hole barrier (hB), and a T2SL absorber sandwiched between the two barriers, as shown in Figure 2-6. The electron and

hole barriers correspond to the hole and electron injectors in an ICL structure, respectively. They are assigned different names in ICLs and ICTPV cells to distinguish between their functions in the two structures. In ICTPV cells, the unipolar barrier plays a function as blocking the namesake carrier while allowing smooth transport of the otherwise carrier, as shown in Figure 2-6. The unipolar barriers work as intended because of the proper energy alignment at the interfaces. For example, the first electron miniband energy level of the T2SLs lies within the bandgap of GaSb layer in the electron barrier, therefore the photo-generated electrons can only move to the hole barrier. This provides a novel way for constructing PV devices with perfect current rectification without appealing to p-n junctions.

The basic operation principle of an ICTPV cell is illustrated in Figure 2-6(a). If the concept of hole is disregarded, the electron and hole barriers serve as the tunneling and relaxation regions for electrons, respectively. As shown, electrons optically excited in the absorber first travel to the hole barrier by diffusion. Following the diffusion process, the electrons then relax to the bottom state in the digitally grated QWs of the hole barrier. The transition in this energy ladder times on the order of picosecond, much faster than the interband excitation in the absorber region. As such, the photo-generated electrons can be transferred to the bottom of the energy ladder with very high efficiency. This mechanism allows efficient and quick removal of electrons in the absorber region. Finally, the electrons return to the valence band state in the adjacent absorber through interband tunneling facilitated by the broken gap alignment between InAs and GaSb.

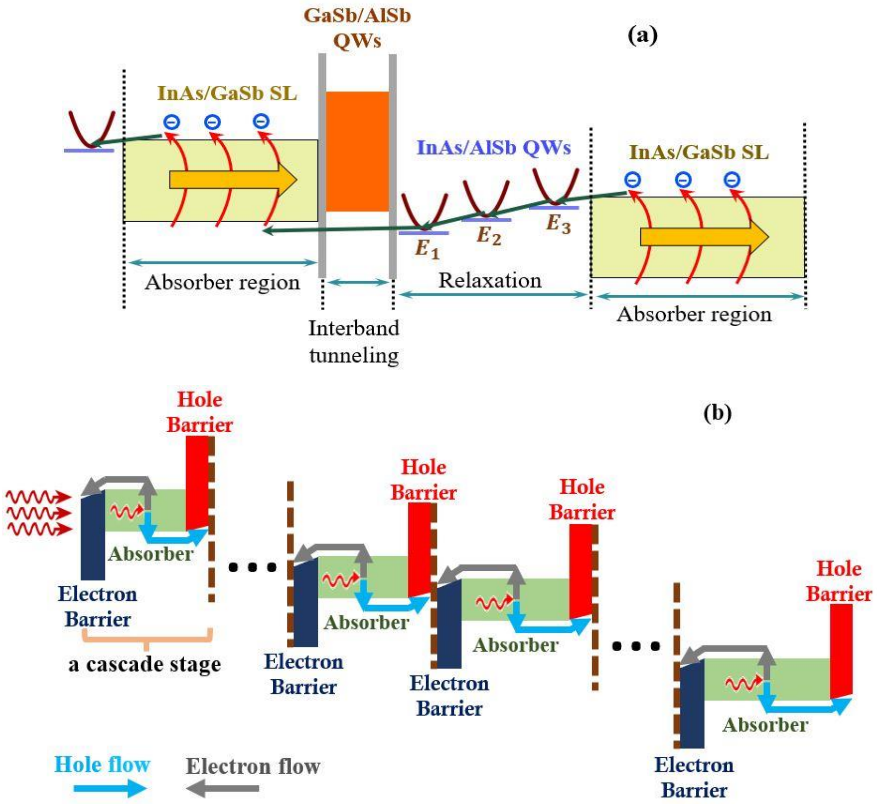

Figure 2-6: (a) Schematic band diagram of an ICTPV cell, (b) Schematic showing the operation of an ICTPV cell.

2.3.3 Enhancement of open-circuit voltage in ICTPV cells

The advantage of IC structure for light emission is apparent: one electron can be reused to generate multiple photons. In the reversing situation as in light-to-electron converting devices, generation of a single electron requires multiple photons. Given this situation, the achievable maximum quantum efficiency (or photocurrent) for ICTPV cells is reduced by a factor of $1/N_c$, where N_c is number of stages. This seems to make it counterintuitive to explore this type of TPV cells. To resolve this problem, one needs to really understand the benefits provided by multistage design. One of the key benefits is enhanced collection efficiency of photo-generated carriers. This benefit will be described in detail in next subsection, both physically and mathematically. Another important benefit

is the enhanced open-circuit voltage V_{oc}, as it is equal to the sum of the photovoltages created in every stage. As shown in Figure 2-6(b), the unipolar barriers repeat their roles to separate photo-generated electrons and holes in all stages. This yields an effective photovoltage in each individual stage. The recycling of electron across the device make them add up to the total open-circuit voltage of the device. This behavior is analogous to that seen in extensive study of multijunction solar cells [13-14]. As will be shown in Chapter 3, at high incident power densities, the V_{oc} of an ICTPV cell approximately scales with the number of stages.

Because of enhanced V_{oc}, the conversion efficiency of ICTPV cells can be higher than conversional single-absorber cells even though the photocurrent is lower, which will be shown in Chapter 3 and 4 in both theory and practice. From another perspective, like ICLs, the reduction of photocurrent can be beneficial for mitigating the Ohmic power loss in series resistances. In practice, TPV cells may experience significant Ohmic loss in cases such as power delivery in free space [138-139] and near-filed TPVs [15-17]. In these instances, the TPV cell often encounter an intensive illumination condition and generate a high photocurrent, consequently suffering a heavy Ohmic loss.

2.3.4 Improvement of carrier collection efficiency in IC structures

The QE of a TPV cell depends on both the absorption of incident photons and the collection of photo-generated carriers. The carrier collection probability $f_c(x)$ can be found using Green's function solution to the diffusion equation, as described in [140-141]. Its expression at distance x from the collection point (x=0) is given by:

$$f_c(x) = \frac{\cosh[(d-x)/L]}{\cosh(d/L)} \tag{2-1}$$

where d is the absorber thickness and L is the diffusion length. Here, the light is assumed to be incident from the collection point and travels through the absorber in a direction opposite to the flow of minority carriers. In the other case where light is incident opposite the collection point, most electrons are generated far from the collection point, therefore the QE is likely reduced [142]. In the subsequent discussion, only the regular illumination pattern will be treated. The calculated f_c (x) based on Equation 2-1 in a 3.3 μm absorber for various diffusion lengths is plotted in Figure 2-7. As shown, the f_c (x) is a strong function of diffusion length. Also, it decreases dramatically with x if the diffusion length is shorter than the absorber thickness. For example, given L=1 μm, f_c (x) is even lower than 0.4 when x is longer than L. Evidently, for a single-absorber device, increasing the absorber thickness enhances the absorption, but may fail to improve QE, especially when the diffusion length is short.

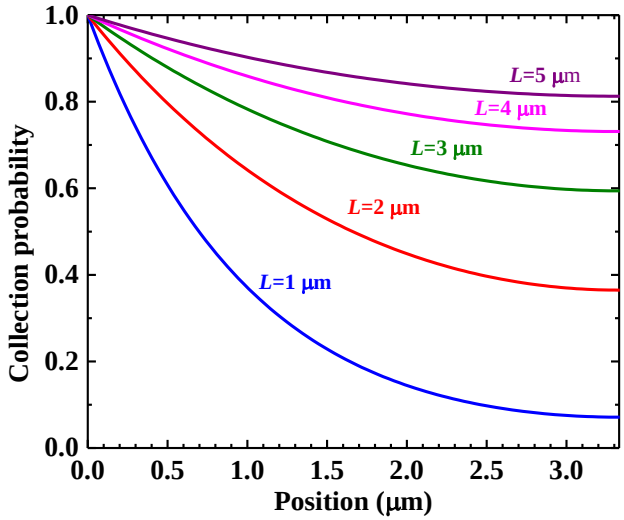

Figure 2-7: Collection probability of carriers as a function of the distance from the collection point. The absorber thickness is 3.3 μm. The number near the curve indicates the diffusion length.

The mechanism that affects collection probability also affect QE. Considering carrier collection probability, the QE of a single-absorber device is given by:

$$QE = \Phi^{-1} q \int_0^d f_c(x) g_{ph}(x) dx \tag{2-2}$$

where Φ is the incident photon flux density per unit area, and g_{ph} (x) is the photon generation rate per unit volume. Here, the top surface reflection is left aside, which is practically possible by adding a front anti-reflection layer. Note that Equation 2-2 can be used to calculate the effective QE in each stage of a multistage IC device as well. The g_{ph} (x) in Equation 2-2 exponentially deceases with position following the rule:

$$g_{ph}(x) = \Phi \alpha e^{-\alpha x} \tag{2-3}$$

where α is absorption coefficient. When applied to multistage IC device, Equation 2-3 needs to be modified to reconcile the light absorption in the optically upper stages. Based on Equations 2-2 and 2-3, the QE of a single-absorber TPV device is given as:

$$QE = \frac{\alpha L}{1-(\alpha L)^2} \times \left[\tanh(d/L) + \frac{\alpha L e^{-\alpha d}}{\cosh(d/L)} - \alpha L\right] \tag{2-4}$$

Likewise, the effective QE in the *N*th stage of a multistage IC device is given by:

$$QE_N = e^{-\alpha \sum_{m=1}^{N-1} d_m} \frac{\alpha L}{1-(\alpha L)^2} \times \left[\tanh(d_N/L) + \frac{\alpha L e^{-\alpha d_N}}{\cosh(d_N/L)} - \alpha L\right] \tag{2-5}$$

where d_{m} is the absorber thickness in the *m*th stage, and the term "$e^{-\alpha \sum_{m=1}^{N-1} d_m}$" represents light absorption in all the upper stages.

Based on the above equations, a numerical example is provided to illustrate the improvement of carrier collection in multistage architecture, as shown in Figure 2-8. It presents the calculated f_{c} (x)·g_{ph} (x) in single-absorber and four-stage IC devices for αL=0.4. The total absorber thicknesses (d) for both structures were set to be the absorption depth. Therefore, if no absorption occurs in the barrier regions (indicated by thick grey lines in Figure 2-8), the total absorption in the absorbers is equal in the two cases. The four-stage IC device has identical absorber thickness in each stage, meaning that the individual

absorber thickness is equal to $d/4$. According to Equation 2-2, the QEs of the two cells are marked by the shaded regions in Figure 2-8. As can be seen, the total effective QE of the four-stage IC device is appreciably higher than the single-absorber device. This result can be considered the equivalent of much higher total collection efficiency (η_c) in the four-stage IC device. Here, the η_c is defined as the ratio of the total effective QE in any of the stages to the total absorption of incident photons ($1-e^{-\alpha d}$). The calculated η_c for the single-absorber cell is only 46% due to the low collection probability at positions far from the collection point. At the right edge of the absorber, the carrier generated over there has a collection probability of only 16%. In contrast, since the absorbers are made thin, the collection probability is much higher in the four-stage IC device. For example, the collection probability is enhanced to 83% at the right edge of each individual absorber. This enables it to achieve a total η_c as high as 89%.

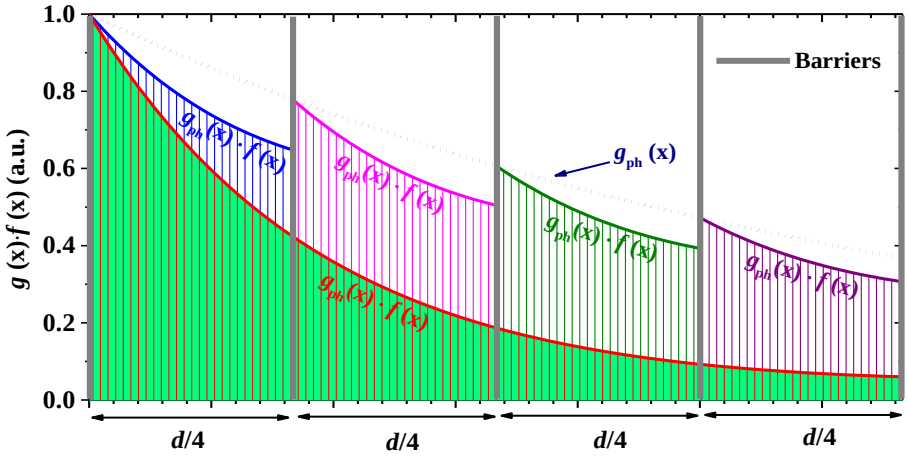

Figure 2-8: Comparison of collection process in single- and four-stage IC devices for a low αL product (αL=0.4). The thickness d of the single-stage device equates the absorption depth. The individual absorber thickness of four-stage IC device is $d/4$.

It should be commented that the above analysis ignored a couple of unfavorable factors that may affect collection efficiency. For example, TPV cells generally operate at

forward bias for performing power output. The applied external field may impede the collection of photo-generated carriers. To calculate η_c with accounting the external bias, it's going to be more complex and challenging whatever method one chooses. The experimental investigation of this subject is presented in Chapter 4, while the theoretical aspect will continuous to be one of future research focuses. Another neglected factor is the recombination at the absorber-electron barrier interface, characterized by surface recombination velocity. The complete calculation with consideration of interface recombination is described in [141].

2.4 Interband cascade infrared photodetectors

2.4.1 Operation principle of ICIPs

The configuration and operation principle of an ICIP are quite analogous to those of an ICTPV cell. In fact, there is no essential difference between them except operating bias voltage and light intensity encountered by them. As shown in Figure 2-9, like an ICTPV cell, each stage of an ICIP consist of an electron barrier, a hole barrier and a T2SL SL absorber. The constituent layers of the three components in each stage are same in the two different types of devices. Also, electrons almost undergo the same transport path in them. The only notable difference is the operating voltage as illustrated in Figure 2-6 and 2-9. To better differentiate them from an ICL, the detailed band profile of one stage of an ICIP is shown in Figure 2-9(b), which differs markedly in the absorber region from an ICL.

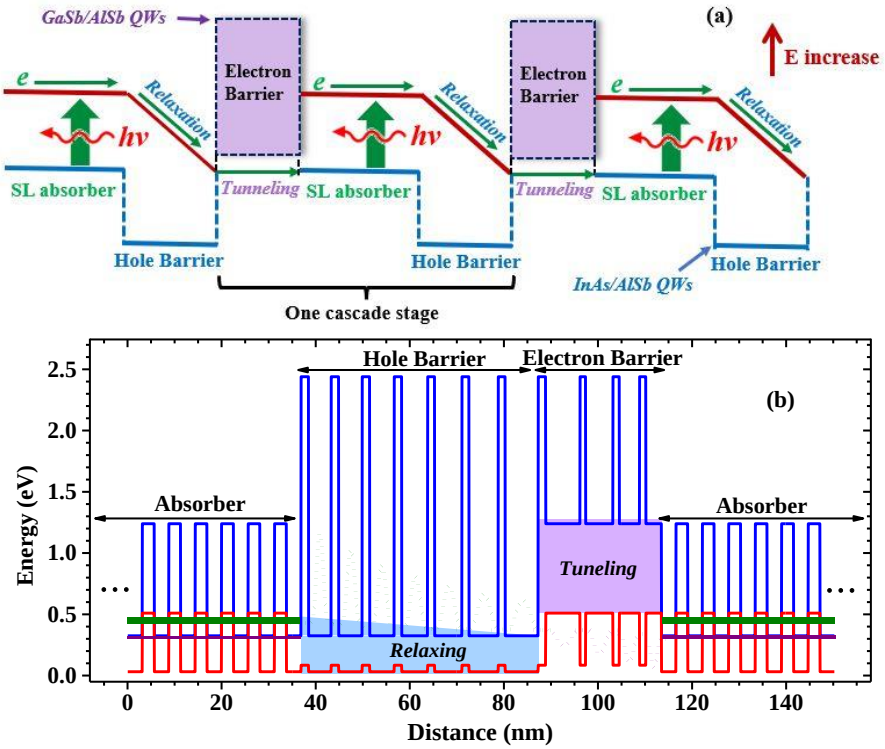

Figure 2-9: (a) schematic diagram of a multistage ICIP and (b) the band profile of one stage under zero bias. The olive and purples lines in the absorber represent the electron and hole minibands. The dotted olive wavefunction indicates the electron states in hole barrier while the dotted purple wavefunction represents the hole states in electron barrier.

Compared to ICTPV cells, ICIPs have relatively looser design requirement. For example, the individual absorber thickness in an ICTPV cell is better adjusted to keep current match between stages, as done elsewhere in multijunction tandem solar cells [13-14], otherwise the photocurrent will be largely reduced. However, such a requirement does not need to be fulfilled for ICIPs due to significant electrical gain, as will be descried in Chapter 7. Besides, ICIPs can operate at zero bias, so the device design is not concerned with the effect of external bias.

2.4.2 Noise reduction in ICIPs

As with an ICTPV cell, an ICIP also benefits from the high collection efficiency, but suffers from the relatively low achievable maximum QE. The other profit offered by multistage architecture in detectors is the reduced noise level. As shown in Figure 2-9(a), a single electron must undergo N_c interband excitations in an ICIP to travel across the contacts. This fact means that the noise is naturally reduced in ICIPs due to the averaging process. A similar example is quantum well infrared detector (QWIP) [65, 78]. The noise in these intersubband detectors is reduced by a factor of $1/N_w$ (number of quantum wells), provided that the emission and capture of electrons are uncorrelated in each QW. Another easy-to-understand example is the reduction of random error by increasing the sample size and averaging over all the samples.

There are various sources of noise that can affect a photodetector's detectivity. The dominant noise changes with the environment and the temperature of the detector. For example, when the signal is strong or the detector temperature is low, the dominant noise is from either the fluctuation of signal current or the fluctuation of current induced by background radiation. Conversely, when the signal is weak or the detector temperature is high, the detectivity is generally regulated by shot or Johnson noise. In realistic applications, the operation of detector is neither shot- nor Johnson-noise limited, since the performance is poor and does not satisfy application requirement. However, for most LWIR detectors such as MCT and T2SL detectors, the detectivity in this regime represents an ultimate limit for the detector operating at room temperature [130]. The focus here will only involve this situation. In addition, as mentioned before, the unipolar barriers allow ICIPs to operate in unbiased mode. This means that shot noise can be neglected in an ICIP,

and the detectivity will be exclusively limited by Johnson noise. The mean square Johnson noise current is inversely proportional to zero-bias resistance R_0, as seen from Equation 1-7. Hence, in order to proceed, the expressions of dark current and R_0 needs to be derived first.

Analogous to QE, the dark collection current (which has the same direction with photocurrent) in the *m*th stage in an ICIP can be calculated as:

$$J_{0m} = q\int_0^d f_c(x) g_{th} dx = q g_{th} L \tanh(d_m/L) \tag{2-6}$$

where g_{th} is thermal generation rate per unit volume. Unlike the optical generation, the thermal generation can be uniform across the device if the bandgaps of absorbers are made equal in each stage.

In addition, there is another contribution of dark current: the injection current. It has opposite direction with photocurrent and has a magnitude of $e^{V_m/k_bT} J_{0m}$ (V_{m} is the voltage that falls across the *m*th stage). Collectively, considering the two current components, the total dark current of an ICIP can be written as:

$$J_d(V) = q g_{th} L \sum_{m=1}^{N_c} \tanh(d_m/L)[exp(qV_m/k_bT) - 1] \tag{2-7}$$

Based on Equation 2-7, the R_0A of an ICIP can be extracted and expressed as:

$$R_0A = \frac{k_bT}{q^2 g_{th} L} \sum_{m=1}^{N_c} \frac{1}{\tanh(d_m/L)} \tag{2-8}$$

For an ICIP with identical stages, the expression of R_0A of can be simplified to:

$$R_0A = \frac{k_bT}{q^2 g_{th} L} \frac{N_c}{\tanh(d_m/L)} \tag{2-9}$$

Evidently, from Equation 2-8 and 2-9, the R_0A is larger for detectors with more stages and thinner absorbers. In other words, according to Equation 1-7, the Johnson noise is effectively reduced in ICIPs compared to single-absorber detectors.

2.4.3 Detectivity improvement in ICIPs

In principle, the device QE of an identical-stage ICIP is decided by the stage with minimum effective QE. This will be the last stage due to most significant light attenuation. However, to maintain current continuity, there is additional injection current induced to offset the higher photocurrent in other stages. This undermines some of the benefits provided by multistage architecture. Another design option to eliminate this downside is to make current-matched absorbers. In this revised design, the individual absorber thicknesses are increased from first stage to last stage to achieve equal photocurrent in each stage. In practice, perfect current match is hard to accomplish unless the diffusion length and absorption coefficient are accurately grasped. Nevertheless, even with inexact match in photocurrent, the device QE in principle can still be improved. Here, only current-matched ICIPs will be considered while ICIPs with identical absorbers will be detailed in Chapter 7.

The detectivity enhancement in ICIPs has been covered in [141], a brief review of the calculation results is provided here. Substituting Equation 2-8 into Equation 1-8, one can obtained the expression of Johnson-noise limited detectivity for an ICIP:

$$D^* = \frac{\lambda}{hc}\frac{QE\sqrt{\sum_{m=1}^{N_c} 1/tanh(d_m/L)}}{\sqrt{4g_{th}L}} \tag{2-11}$$

The current match condition in the ICIP is first obtained using an iterative process by varying the thickness of each stage so that the contribution of QE is equal. The absorber thicknesses are then determined by selecting the optimal photocurrent-matched absorber sequence that maximizes detectivity. In this way, the calculated detectivity enhancement as a function of αL for ICIPs with two, eleven and thirty stages are shown in Figure 2-10

[141]. The detectivity enhancement is defined as the D^* (N_c) of the optimized multistage ICIP normalized to the value D^* (1) of the optimized single-absorber detector. As can be seen, the detectivity enhancement is pronounced when $\alpha L<1$ for different designs. Also, the detectivity is raised as the number of stages increases since the noise is further suppressed, although the signal current is slightly reduced. At larger αL, multistage ICIPs do not make obvious advantage, but there is still a small advantage can be gained. For example, for optimized ICIPs with many stages, the upper limit improvement is about 1.1 times higher than single-absorber detectors [141]. This conclusion can be derived from Figure 2-10 where the platform value of detectivity enhancement is slightly higher than unity at large αL.

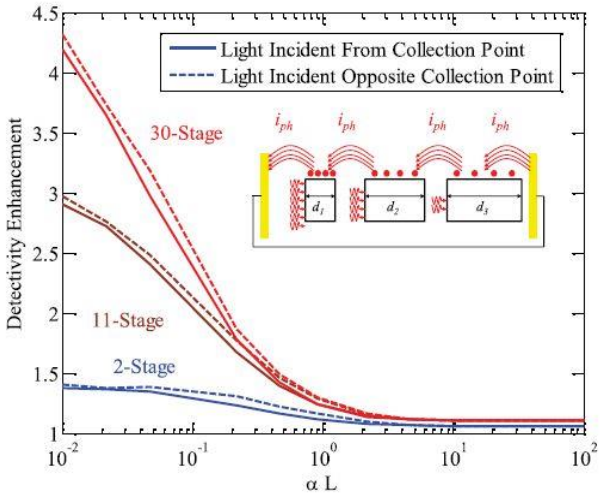

Figure 2-10: Johnson-noise limited detectivity enhancement for current-matched ICIPs with two, eleven and thirty stages. Figure is from [141].

2.4.4 Comments on detectivity improvement in ICIP

The above calculations clearly quantify the possible detectivity enhancement when $\alpha L<1$ for current-matched ICIPs. In realistic, for InAs/GaSb T2SLs, the absorption coefficient near bandgap is about 3000 and 2000 cm^{-1} in MWIR [143-145] and LWIR [145-

147] regimes, respectively. The diffusion length is shorter than 1.5 μm at RT, as estimated from the temperature or bias dependence of responsivity for the detectors made of InAs/GaSb T2SLs [149-151]. Taken together, the product αL can be smaller than unity at high temperatures (> 200 K), especially for LWIR T2SL detectors. Hence, the prospect of detectivity enhancement in ICIPs is real at high temperatures. At lower temperatures, the diffusion length is appreciably increased as carrier lifetime is extended. For example, the diffusion length can be far longer than 6 μm at 77 K, as evaluated in [152]. The increased diffusion length is very likely to make αL larger than unity, therefore it will be bootless to use ICIP structure at low temperatures. However, in applications where the response speed is prioritized over sensitivity, ICIP is still the better option. For single-absorber detectors, high response speed requires a thin absorber, which compromises light absorption and thus sacrifices the detectivity. However, for ICIPs, they have been demonstrated with high frequency operation (higher than 1.3 GHz) as well as decent detectivity [153-154].

2.5 Growth and fabrication of interband cascade devices

The IC devices are relatively complex structures; some devices even have thousands of layers. This complexity rules out the possible growth by conventional growth techniques as well as some epitaxy growth techniques such as chemical vapor deposition (CVD), physical vapor deposition (PVD) and liquid phase epitaxy (LPE). The only reliable and feasible growth method is molecular beam epitaxy (MBE) [75-76]. Up to present, almost without exception the reported IC devices were grown by MBE systems. Compared to other epitaxy growth techniques, MBE is better able to grow sophisticated structures with high degree of success. This is due to its nature of utilizing atomic layer-by-layer

growth, which is accomplished through a good monitor of molecular or atomic beams onto a heated substrate in ultrahigh environments. In this dissertation, all the devices involved were grown by the two MBE systems in the University of Oklahoma as shown in Figure 2-11. The first one is an Intevac Gen II that has been operational since 1994. The system is equipped with two Sb and As crackers, three In, Ga and Al effusion cells, as well as two Si and Be doping cells. The second one is a new Veeco Genxplor MBE system launched in 2015, which has many new and improved features. For example, all the group-III cells are comprised of dual-filament heaters to generate more stable flux. This new MBE system has ten cells including two In and two Ga cracked cells, two Al Sumo cells, one cracked As cell, one cracked Sb cell and three Si, Te and Be doping cells.

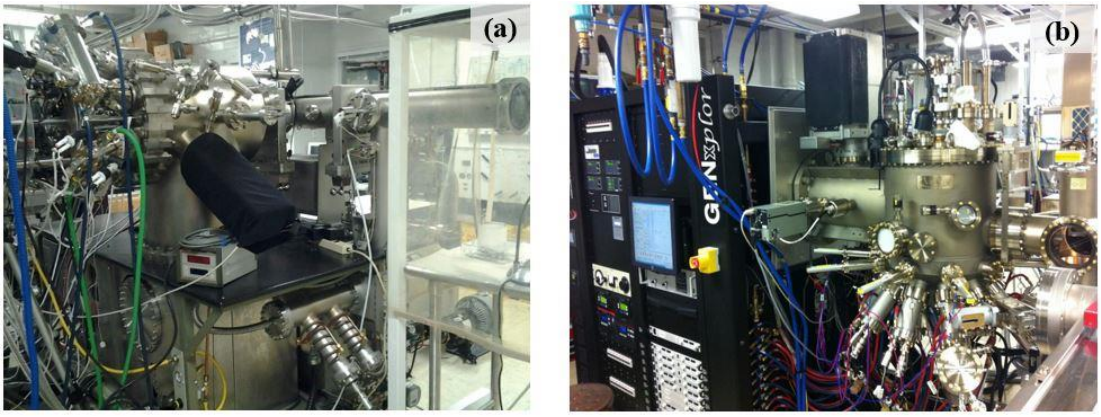

Figure 2-11: (a) Intevac GEN II MBE system (1993) and (b) Veeco GENxplor MBE system (2013).

Manufacture of IC devices involves various fabrication processes. The general processing flow of IC devices (e.g. ICTPVs and ICIPs) include: (1) standard cleaning, (2) mesa etching, (3) insulating layer deposition, (4) contact opening, (5) top contact deposition, (6) lapping, (7) bottom contact deposition, and (8) mounting and wire bonding. Specifically, after cleaning and standard contact photolithography, wet chemical etching is used to define a mesa structure by etching deep down below the active region. Then, a ~

200 nm thick silicon nitride followed by ~ 200 nm silicon dioxide is sputter deposited as an insulating layer. This step is followed by reactive ion etching (RIE) to open a window on top of mesa. This window is opened to deposit 30/300 nm of Ti/Au layer by sputtering technique as top metal contact. The schematic of a typical fabricated 3-stage ICTPV device is shown in Figure 2-12(a). The cross-sectional scanning electron microscope image of the 3-stage ICTPV device is presented in Figure 2-11(b) [157].

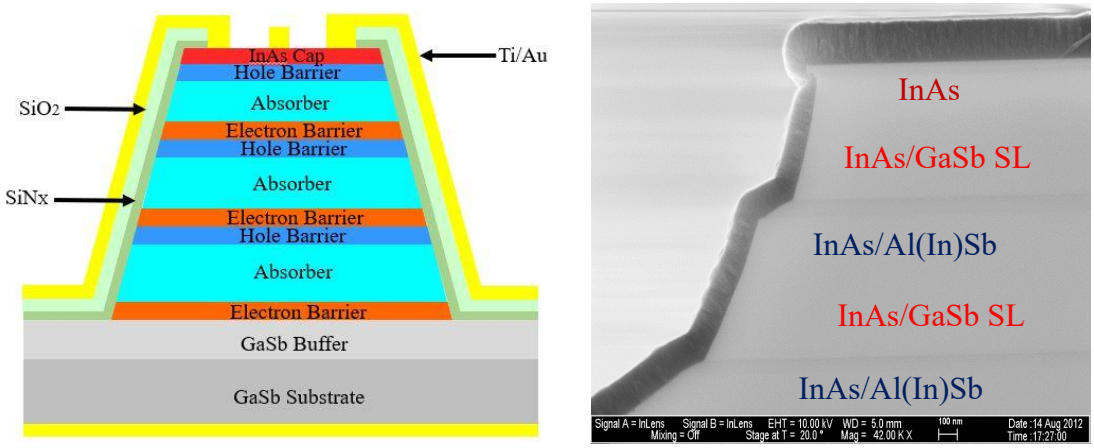

Figure 2-12: (a) The schematic of a processed ICTPV or ICIP device and (b) Cross-section scanning electron microscope image of a wet-etch ICTPV structure, the Figure is from [157].

Chapter 3: Limiting factors and efficiencies of narrow bandgap thermophotovoltaic cells

3.1 Background and motivation

In Chapter 1, the efficiency limits of TPV cells were calculated based on detailed balance theory, which however tends to be overestimated due to some unrealistic expectations. There are many theoretical works attempting to predict the efficiency limit of TPV cells. For example, in [49, 51], a prospective efficiency exceeding 30% was pointed out when the heat source is at 1000-2000 K, even without spectral control. For solar TPV, even a maximum efficiency of 85% was projected with full concentration of incident sunlight [55]. Realization of this extremely high efficiency requires that the incident light spectrum is perfectly tailored to the cell absorption spectrum and non-absorbed is recycled back to the heat source. At current stage, the highest reported TPV cell efficiencies at 300 K are 24% for a 0.6 eV InGaAs diode on InP [37] and 19.7% for a 0.53 eV GaInAsSb diode on GaSb [39], which were measured using a 950 °C broadband radiator with spectral control filters mounted on the front surface of the TPV cells. As for narrow bandgap TPV cells (E_g< 0.4 eV), the demonstrated efficiencies at 300 K are far below 10% (See table 1.2). Evidently, there is a large gap between the efficiencies of existing TPV cells and theoretical predictions, and little work has been dedicated to narrow bandgap TPV cells to clarify their efficiency limits. It is therefore necessary to have ongoing work to bridge the efficiency gap and to determine the practical efficiency limits as well.

Most of previous theoretical works assumed very ideal behaviors of carrier recombination and collection. Specifically, they assumed purely radiative recombination and an infinite diffusion length. However, in real devices, non-radiative recombination is often involved and even prevails, and carrier collection can be limited by a short diffusion

length. In this chapter, practical factors such a finite diffusion length (L) and absorption coefficient (α) are considered and their effects on conversion efficiency (η) are inspected. As examples, calculations are carried out for narrow bandgap InAs/GaSb T2SLs and quaternary GaInAsSb materials in several different scenarios under monochromatic light illumination. This narrow bandwidth light illumination can be accomplished through the use of spectral filters or selective emitters that can be made based on nanostructured materials and metamaterials [31-33]. The calculations start from single-absorber TPV cells and then are performed for multistage IC architecture to show how it can be used to improve the performance of narrow bandgap TPV cells.

3.2 Practical limitations on single-absorber TPV devices

3.2.1 Quantum efficiency and dark saturation current density

The conversion efficiency of a TPV device is intimately related to its output current and voltage. These two quantities are characterized by quantum efficiency QE and voltage efficiency η_V (defined as the ratio of open-circuit voltage eV_{oc} to the bandgap). Both QE and V_{oc} are largely ruled by dark saturation current density J_0, as well as minority carrier transport and lifetime τ. Therefore, QE and V_{oc} will be severely limited if the carrier lifetime and diffusion length are short and the J_0 is significant. As an example of such limitation, InAs/GaSb SL absorber with a bandgap of 0.29 eV will be first used for illustration purpose. At 300 K, the diffusion length and carrier lifetime are estimated to be 1.5 μm and 20 ns based on the experimental results of type-II InAs/GaSb infrared detectors [149-151, 158]. The conversion efficiency of a TPV device under monochromatic illumination is given by:

$$\eta = FF \cdot QE \cdot \frac{qV_{oc}}{h\nu} \tag{3-1}$$

where FF is the fill factor and ν is the frequency of incident photons. Hence, FF, QE and V_{oc} are the three main performance metrics that controls the desired conversion efficiency. Below, their respective behaviors are studied in narrow bandgap TPV devices. The frequency of incident photons also plays a role in affecting conversion efficiency, but is less significant than the above-mentioned three quantities, which will be described in Subsection 3.4.

The expression of QE for a single-absorber TPV device is given by Equation 2-4. Here the light is assumed to travel through the absorber in a direction opposite to the flow of minority carriers. Based on this equation, the calculated QE as a function of normalized absorber thickness (d/L) for different values of αL is shown in Figure 3-1. As can be seen, the QE peaks a at a certain value of d/L and falls off with further increasing the absorber thickness, irrespective of the value of αL. This common tendency of QE was identified due to the reduction of collection efficiency as the absorber thickness increases [159]. Particularly, for αL=0.45, the maximum QE is only 32%, which would significantly limit the conversion efficiency as will be shown later.

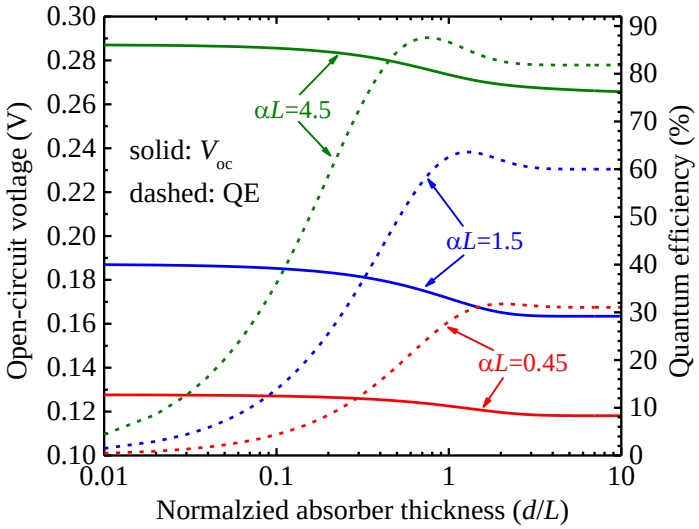

Figure 3-1: Calculated open-circuit voltage (solid) and quantum efficiency (dashed) as a function of normalized absorber thickness for different values of αL. The incident power density is assumed to be 50 W/cm^2.

The dark saturation current density is the pre-factor in standard diode equation and measures the recombination loss in PV devices. Normally, the open-circuit voltage is a logarithmic function of the ratio between photocurrent density and J_0. In solar cells, the thermal current density is sometimes ignored because it is low when the bandgap is relatively wide. In contrast, J_0 is orders of magnitude higher in TPV devices and therefore cannot be neglected. The value of J_0 can be calculated based on Equation 2-6 for the simple single-stage case. The thermal generation rate g_{th} in this equation for *p*-type doped absorbers can be written as: $g_{th}=n_0/\tau$, where n_0 is the electron concentration at thermal equilibrium. By replacing n_0 with n_i^2/p_0, thermal generation rate can be further written as: $n_i^2/\tau N_a$, where n_i and N_a are the intrinsic carrier concentration and doping concentration, respectively. Hence, a short carrier lifetime (e.g. 20 ns) will manifest itself as a high J_0, thus severely limiting the open-circuit voltage. An increase of carrier lifetime will naturally reconcile this issue and enhance QE as well since the diffusion length is increased with raised carrier lifetime. For example, if carrier lifetime is extended to 200 ns, on a

conservative estimate, the diffusion length will be increased is 5 μm, assuming the electron mobility (43 $cm^2 \cdot V^{-1} \cdot s^{-1}$) remains the same. In this scenario, the J_0 will be an order of magnitude lower and the QE will be appreciably improved.

Nevertheless, the J_0 is still much higher than the radiative limit set by the detailed balance theory [58]. In this fundamental limit, the dark saturation current density is given by:

$$J_0 = \frac{2\pi q}{h^3 c^2} \int_{E_g}^{\infty} \frac{n^2 (1 - e^{-\alpha d}) E^2}{e^{E/k_b T} - 1} \, dE \tag{3-2}$$

where n is refractive index. Here, several assumptions were made: the surface reflections and photon recycling effect [160-161] are ignored, and the radiative photons are assumed to have a single path and a solid angle of π. The term $(1\text{-}e^{-\alpha d})$ in Equation 3-2 describes incomplete absorption of photons due to the finite absorber thickness, compared to the full absorption for a blackbody. With ignoring recycling factor, the calculated radiative carrier lifetime is about 2.3 μs [See table 3-1]. As a result, the diffusion length is around 15 μm, assuming a constant electron mobility of 43 $cm^2 \cdot V^{-1} \cdot s^{-1}$. Based on Equation 2-6 and Equation 3-2, the calculated dark saturation density is shown in Figure 3-2 for three different carrier lifetimes. As can be seen, for τ =20 ns, J_0 is on the order of 0.1 A/cm^2, in agreement with the measurements for ICIPs [158]. This substantially high J_0 poses a difficulty in realizing a high open-circuit voltage. By comparison, in the radiative limit, J_0 is approximately two orders of magnitude lower. This implies that there is a still plenty room for improvement of performance for existing TPV devices based on InAs/GaSb SLs.

Table 3-1: Parameters used in calculation for InAs/GaSb superlattice.

Temperature and bandgap	T_{device}=300 K, E_g=0.29 eV
Effective mass	$m_e = 0.03m_0$, $m_h = 0.4m_0$
Effective density of states	N_c=1.3×10^{17} cm^{-3}, N_v=6.3×10^{18} cm^{-3}
Intrinsic carrier concentration	$n_i = \sqrt{N_c N_v}\exp\left(\frac{-E_g}{2k_bT}\right)$= 3.4×10^{15} cm^{-3}
***p*-type doping concentration in the absorber**	N_a=2.4×10^{16} cm^{-3}
Refractive index	n=3.5
Absorption coefficient:	α=3000 cm^{-1}
Radiative recombination coefficient [162]	$B = \frac{n^2}{n_i^2}\int_{\theta=0}^{\theta=\pi}\int_{\varphi=0}^{\varphi=2\pi}\int_{E=E_g}^{E=\infty}\alpha(E)\frac{2E^2}{h^3c^2}[exp\left(\frac{E}{k_bT}\right)-1]^{-1}sin\theta d\theta d\varphi dE$ B=1.75×10^{-11} cm^{-3}·s^{-1}
Actual lifetime	τ=20 ns, L=1.5 μm, **α*L*=0.45**
Electron mobility	μ_e=43 cm^2·V^{-1}·s^{-1}, calculated from L=1.5 μm and τ=20 ns.
Medium lifetime	τ=200 ns, L=5 μm, **α*L*=1.5**
Radiative lifetime α*L*=4.5	$\tau_{rad} = 1/BN_a$ = 2.3 μs (no photon recycling), L=15 μm,
Ultimate limit	L=15 μm, **α*L*=4.5**, V_{oc}=0.29 V

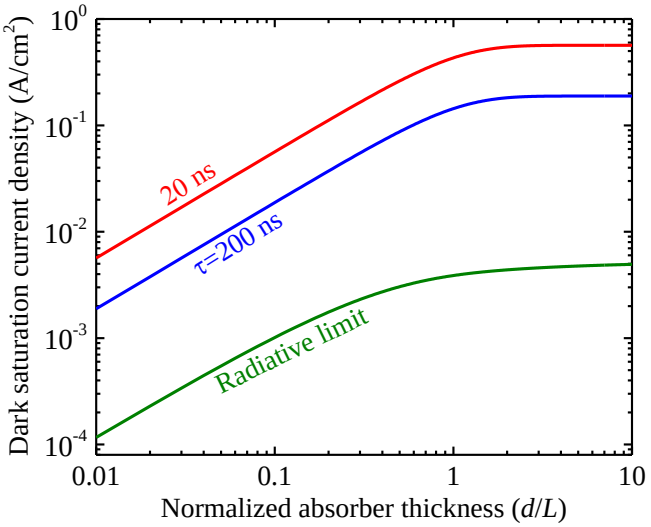

Figure 3-2: Calculated dark saturation current density as a function of normalized absorber thickness for a carrier lifetime of 20 ns, 200 ns and the radiative limit.

3.2.2 Open-circuit voltage and fill factor

The illuminated *J-V* characteristic needs to be known prior to calculating the open-circuit voltage and fill factor. The net current density flowing out from a TPV device under illumination is simply the superposition of the dark current density (J_d) and the photocurrent density (J_{ph}):

$$J = J_{ph} - J_0(e^{\frac{qV}{k_bT}} - 1) \tag{3-3}$$

where J_{ph} equates $e\mathrm{QE}\Phi_0$ and J_0 is given by Eq. (4) or Eq. (5) (for the radiative limit). The term J_0e^{qV/k_bT} stands for the injection current density under a forward bias, which is in the opposite direction of J_{ph} and thus can strongly affect the fill factor. Figure 3-3 shows the simulated *J-V* curves for different values of αL (0.45, 1.5 and 4.5). The diffusion lengths and carrier lifetimes are different but the absorption coefficient (~ 3000 cm^{-1}) is the same in the three scenarios as shown in Table 3-1. The incident power density P_{inc} was assumed to be 25 and 50 W/cm^2. In each case, the absorber thickness is the optimal value that maximizes the conversion efficiency. As shown in Figure 3-3, the simulated *J-V* curve is more square-like for larger αL, suggesting the increase of fill factor with αL. As can be seen in Figure 3-4, the FF decreases with d/L and is lower than 55% for αL=0.45, which is significantly lower than the 85% reported for high-quality crystalline Si and thin film GaAs solar devices. Likewise, the V_{oc} exhibit similar trends with d/L and is low when αL is small due to relatively high J_0. These two quantities (V_{oc} and FF) both increase with αL due to the decrease of J_0 as well as the increase of the QE. Raising the incident power density from 25 W/cm^2 to 50 W/cm^2 led to the insignificant enhancements of FF and conversion efficiency for each value of αL. Specifically, the FF (η) increases from 50% (6%), 58% (19%) and 54% (69%) to 53% (7%), 61% (23%) and 71% (59%) for αL equal to 0.45, 1.5

and 4.5, respectively. In the following analysis, the incident power density is set at a fixed value of 50 W/cm^2. Nevertheless, the fundamental insights gained in the analysis are expected to be applicable to lower incident power densities.

In practice, the goal of a 50 W/cm^2 incident power density is difficult to achieve for conventional TPV configurations, but is still feasible under some circumstances. For instance, adding a concentrator in a TPV system, analogous to concentration solar cells, can significantly enhance the incident power density. Another example is the PV device used in power beaming as the light is sent from a high-power laser source. In this case, the incident power density is likely to exceed 50 W/cm^2 for adequate power delivery. In addition, in the near filed transfer technology where the TPV device is placed in extreme proximity (typically < 100 nm) to the heat source (or radiator) [15-17], the incident power density of the device can be very high as well. On the other hand, the high incident power density can incur the high injection effect, as observed in a GaSb p-n junction near filed TPV cell [163]. Narrow bandgap TPV devices with low doping level may be also subject to this effect, but this is beyond the scope of this chapter.

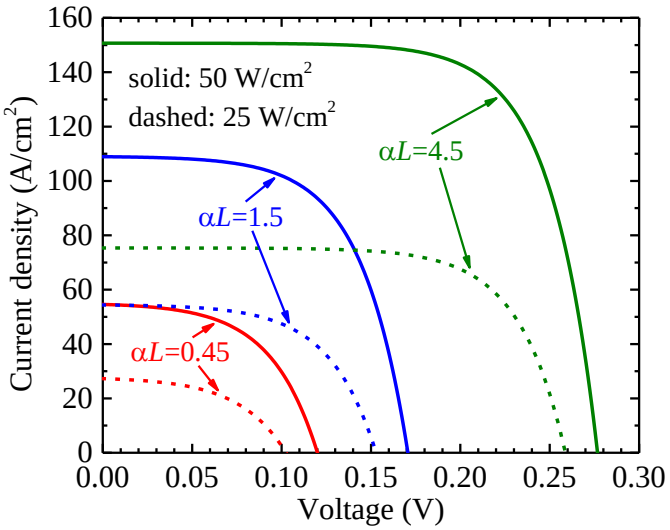

Figure 3-3: Simulated *J-V* curves for different values of αL and with incident power density of 25 and 50 W/cm^2.

Based on Equation 2-6 and Equation 3-3, the expression of open-circuit voltage can be written as:

$$V_{oc} = \frac{k_b T}{q} ln(\frac{\Phi_0 QE}{g_{th} L tanh(d/L)} + 1) \quad (3\text{-}4)$$

Under highly intensive illumination, the second term in the natural logarithm can be neglected, then the open-circuit voltage can be expressed as:

$$V_{oc} = \frac{k_b T}{q} ln\left(\frac{\Phi_0 QE\tau p_0}{N_c N_v L tanh(d/L)} e^{\frac{E_g}{k_b T}}\right) = \frac{E_g}{q} + \frac{k_b T}{q} ln\left(\frac{\Phi_0 QE\tau p_0}{N_c N_v L tanh(d/L)}\right) \quad (3\text{-}5)$$

Here, the well-known relationship for non-degenerate absorbers was used:

$$n_i^2 = N_c N_v e^{-E_g/k_b T} \quad (3\text{-}6)$$

where N_c (N_v) is the effective density of state for the conduction (valence) band of the absorbers (See Table 3-1). Based on Equation 3-5, the calculated open-circuit voltage for different values of αL (0.45, 1.5 and 4.5) is presented in Figure 3-1. As shown, the V_{oc} gradually decreases with the absorber thickness due to the sharper increase of J_o (as shown in Figure 3-2) than QE. As an example, the V_{oc} decreases from 0.128, 0.187 and 0.287 V to 0.118, 0.163 and 0.266 V while the normalized absorber thickness increases from 0.01 to 10 for αL of 0.45, 1.5 and 4.5, respectively. Hence, in practical device with αL=0.45, the V_{oc} seldom exceeds 0.13 V even at high incident power density, which sets a boundary (<0.45%) of the voltage efficiency. As the carrier lifetime increases via improvement of material quality, the V_{oc} can be increased substantially as shown in Figure 3-1 with a higher αL. The V_{oc} in the radiative limit is quite close to bandgap voltage, but never allowed to exceed it. This is because the amplified stimulated emission will be triggered when the separation of quasi-fermi levels for electrons and holes exceeds the bandgap. Such a process will further reduce the carrier lifetime thus increase the saturation dark current

density. In [164], unexpectedly, the value of V_{oc} was evaluated to be higher than bandgap voltage for a solar device under monochromatic light illumination. However, the calculation did not account the reduction in carrier lifetime. Below, based on Equation 3-5, a convincing argument is provided to support why $V_{oc} < E_g/q$.

Under steady state condition, the sweep-out of photo-generated electrons needs to be compensated by the absorption of photons. This signifies that the density of escaping photogenerated electrons equates $\Phi_0 QE/v$, where $v = L\tanh(d/L)/\tau$ represents the average escaping speed of photogenerated electrons. The upper limit of photo-generated electron density is the available density of states $N_c N_v/p_0$. Hence, based on Equation 3-5, V_{oc} is always lower than E_g/q. This implies that the carrier lifetime τ reduces with increasing Φ_0 in order to keep consistent with the upper limit.

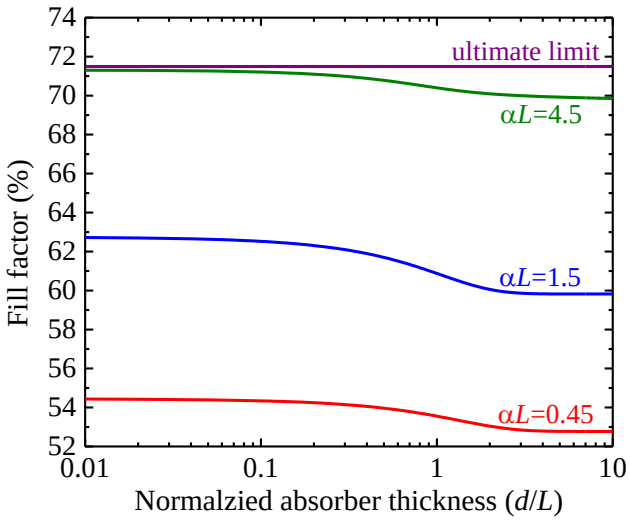

Figure 3-4: Calculated fill factor as a function of normalized absorber thickness for different values of αL. The incident power density is assumed to be 50 W/cm^2 except in the ultimate limit.

3.2.3 Conversion efficiency

The fact that V_{oc} is always lower than E_g/q offers an effective approach to evaluate

the ultimate limit of conversion efficiency for single-absorber devices. To do this, one needs to first define the ratio of the photon flux to the thermal flux as:

$$\xi = \frac{\Phi_0}{g_{th}L} \tag{3-7}$$

According to Equation 3-4, the maximum value of ζ is $\exp(-E_g/k_bT)\cdot\tanh(d/L)$/QE to keep V_{oc} lower than E_g/q. When ξ reaches this value at sufficiently high incident power density, the conversion efficiency will be stretched to its ultimate limit. This means the ultimate efficiency limit of a single-absorber device can be obtained by maximizing following equation with an optimal voltage:

$$\eta = [e^{E_g/k_bT} - (e^{qV/k_bT} - 1)] \cdot V/(e^{E_g/k_bT}E_g) \cdot QE \tag{3-8}$$

According to this equation, the ultimate efficiency equates the quantum efficiency multiplied by a factor of 0.71 for a 0.29 eV bandgap. The diffusion length in the ultimate limit will be assumed to be 15 μm, identical to the value in the radiative limit (See Table 3-1). In the ultimate limit, the fill factor remains constant with of d/L as shown in Figure 3-4. It should be emphasized that there are two approximations were made to derive Equation 3-8. First, the incident photon energy is precisely matched with the bandgap. Second, the illumination source has an ideal monochromatic spectrum with a shape of delta function. In practice, the incident photons should possess an energy higher than bandgap to excite electron-hole pairs. Thus, the first assumption would somewhat overestimate the conversion efficiency. The second assumption significantly simplifies the illumination source, which in fact does not make too much difference in conversion efficiency. For example, provided that the incident photon has Gaussian distribution with the central energy being 0.34 eV (50 meV higher than the bandgap) and a FWHM of 26 meV (equal to k_bT), the calculated conversion efficiency is 5.4% for αL=0.45 at the power density of

50 W/cm^2. This value of efficiency is slightly lower than the 5.6% calculated for the case with a perfect monochromatic light (delta function) at 0.34 eV.

Figure 3-5 shows the calculated conversion efficiency of single-absorber devices in different cases. As shown, the efficiencies in the radiative and ultimate limit are quite close to each other, especially at smaller d/L. The peak efficiencies are 59% and 63% in the radiative and ultimate limit, respectively. The vast gap between the radiative limit and the practical efficiency (αL=0.45) reveals a huge potential for improvement. To bridge this gap, the material quality needs to be greatly improved. For αL=0.45, the actual achievable efficiency is less than 7% as a directly result of low V_{oc} (Figure 3-1) and FF (Figure 3-4) that spring from a high J_0 with a short carrier lifetime (~ 20 ns). If, however, the carrier lifetime increases by an order of magnitude, the efficiency is possible to reach up to 23%. These results explicitly show that carrier lifetime is the key issue in narrow bandgap TPV devices. Besides, another important issue is the relatively low QE (< 32%) due to a small product of αL. The main tendency of conversion efficiency with d/L is resembles that of QE with d/L (Figure 3-1). That is, the conversion efficiency peaks at a certain absorber thickness, then slowly drops, and finally reaches a plateau value with further increasing absorber thickness. The maximum value of η occurs at an optimal d/L equal to 1.8, 1.1 and 0.7 for αL value of 0.45, 1.5 and 4.5, respectively, consistent with the order of the optimal d/L for maximum QE. Compared to the optimal d/L for maximum QE, the optimal d/L for maximum η is slightly lower due the decrease of V_{oc} and FF with increasing d/L.

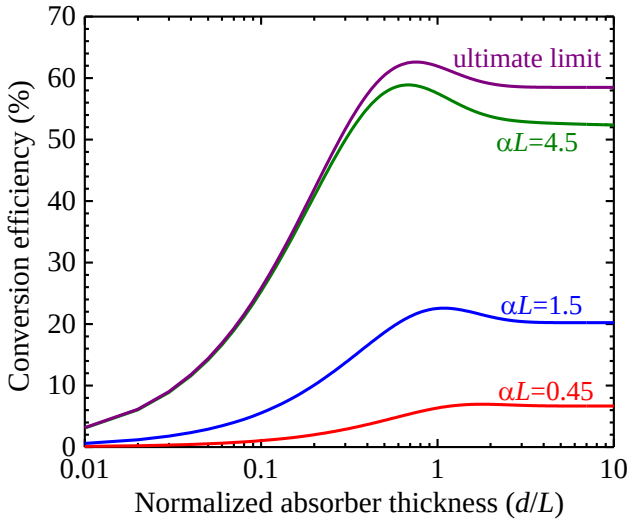

Figure 3-5: Calculated conversion efficiency vs normalized absorber thickness for different values of αL. The incident power density is assumed to be 50 W/cm^2 except for the ultimate limit.

Figure 3-6 shows the calculated conversion efficiency as a function of bandgap within 0.2-0.4 eV for single-absorber devices. In principle, the variation of bandgap should result in systematic changes in carrier lifetime. However, because of little relevant experimental data and uncertainties in carrier lifetime for InAs/GaSb SLs with different bandgaps, the carier lifetime, absorption coefficient and diffusion length are remained same for different bandgaps as given in Table 3-1. This assumption, together with same doping concentration, implies that the thermal generation is proportioanl to $e^{-Eg/kbT}$. Hence, a modest increase in bandgap will result in a large redcution in J_0 and significant increases in FF and votlage efficiency, eventually raising conversion efficiency sustantially as shwon in Figure 3-6. For example, for αL=0.45, the conversion efficiency is raised from 3% to 12% while the bandgap is increased from 0.2 eV to 0.4 eV.

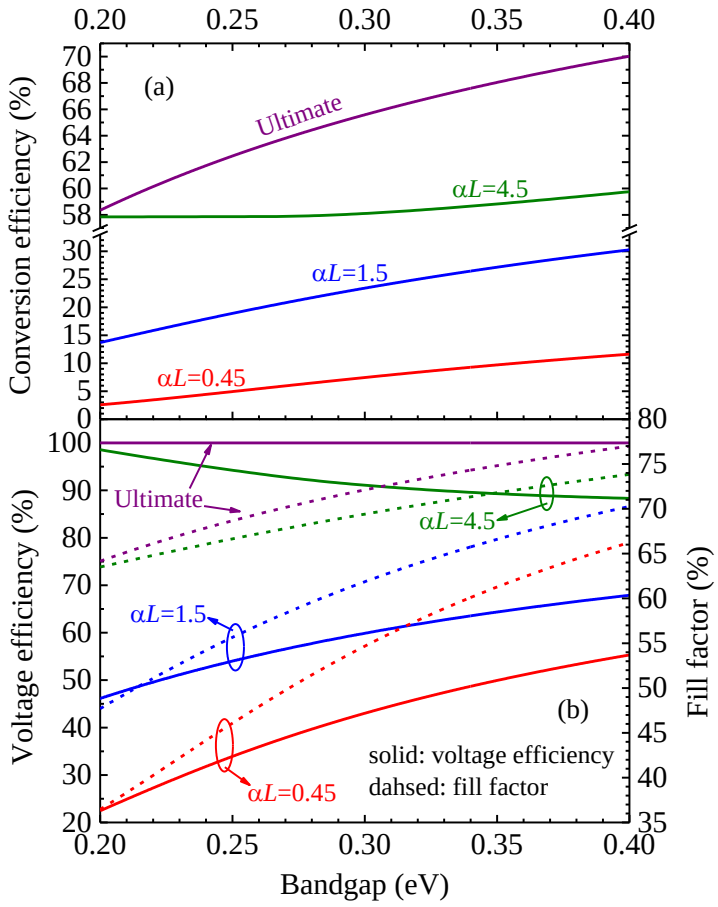

Figure 3-6: Calculated (a) conversion efficiency and (b) voltage efficiency and fill factor for αL=0.45, 1.5 and 4.5 and the ultimate efficiency limit as a function of bandgap. The incident power density is 50 W/cm^2 except for the ultimate limit.

In the radiative limit, the J_0 detemined by Equation 3-2 decreases with increasing bandgap, but at a slower rate than that for for αL=0.45 or 1.5. Consequently, the FF and V_{oc} increase gradually with bandgap, while the voltage efficiency decreases with bandgap as shown in Figure 3-6(b). Hence, in the radiative limit, the increase of conversion efficiency with bandgap is insignificant as it ranges between 58%-60%, as shown in Figure 3-6(a). Note that, in Equation 3-2, the absorption spectrum was assumed to have same shape but different take-off points for different bandgaps. The diffusion length in the radiative limit was still taken to be 1.5 μm for different bandgaps. In addition, the QE at the optimal absorber thickness is almost identical for different bandgaps. This means that

the maximum QE is purely decided by the value of αL and insensitive to the change of bandgap. Also, the small value of αL (0.45) in narrow bandgap materials serves as an obstacle to achieving a high conversion efficiency (<15% as shown in Figure 3-6) in single-absorber TPV devices.

3.3 Efficiency improvement in multistage TPV devices

3.3.1 Enhancement of open-circuit voltage

The structure and operation principle of ICTPV devices are described in Chapter 2. Figure 3-7 shows the chemical potentials (designated by the flat lines) across individual stages for an ICTPV device under illumination, which adds up to generate a high open-circuit voltage. Each stage in a multistage ICTPV device operates in the same manner as a single-absorber device. The equations in the preceding section can be directly applied to the individual stages in a multistage device. The net current flowing in the *m*th stage is given by:

$$J_m = \Phi_m QE_m - g_{th} L tanh(d_m/L)(e^{\frac{qV_m}{k_b T}} - 1) \quad (3\text{-}9)$$

where Φ_m is the incident flux on the *m*th stage, QE_m is the effective quantum efficiency given by Equation 2-5, V_m is the voltage across the *m*th stage, and d_m is the absorber thickness. The optimized multistage device is designed to have an equal photocurrent in each stage. This current matching condition is realized with an iterative process by varying the thickness of each stage so that the contribution of photocurrent from each is equal. The optimal absorber thicknesses are then found by selecting the photocurrent-matched absorber sequence that maximizes the output power.

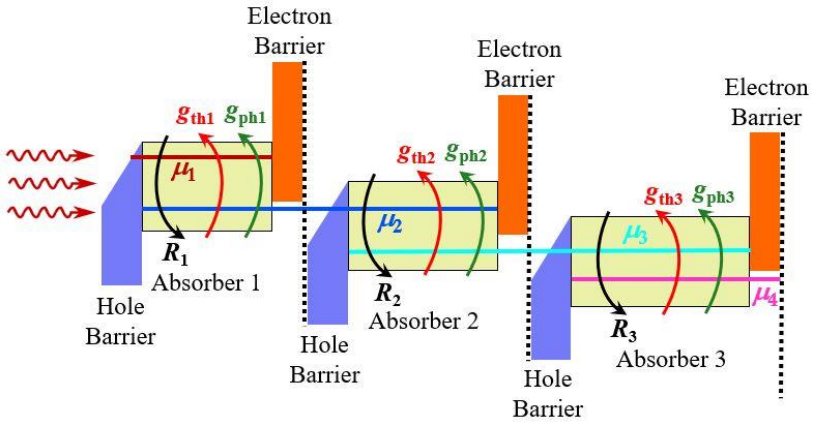

Figure 3-7: Schematic of a three-stage ICTPV device under forward voltage and illumination. Optical generation g_{phm}, thermal generation g_{thm} and recombination R_m, along with the chemical potentials μ_m in each stage are shown, where the index m denotes the stage ordinal. The flat quasi-Fermi levels (designated with μ_1, μ_2, μ_3 and μ_4) correspond to the case where the diffusion length is infinite.

Based on Equation 3-9, the *J*-*V* characteristic of a multistage TPV device is obtained by adding together the voltage across each stage:

$$V = \sum_{m=1}^{N_c} \frac{k_b T}{q} ln[\frac{\Phi_m QE_m - J}{g_{th} L tanh(d_m/L)} + 1] \quad (3\text{-}10)$$

Then the open-circuit voltage of a multistage device can be derived by setting J=0 in Equation 3-10. After correcting Φ^m with absorption in the upper stages, the expression of V_{oc} can be written as:

$$V_{oc} = \frac{k_b T}{q} [N_c ln(\xi) + \sum_{m=1}^{N_c} ln\left(\frac{QE_m}{\tanh(d_m/L)}\right) - \sum_{m=2}^{N_c} \sum_{i=1}^{m-1} \alpha d_i] \quad (3\text{-}11)$$

where ξ is the ratio of photon flux to thermal flux, defined by Equation 3-7. The third term on the right side of Equation 3-11 represents light attenuation. According to Equation 3-11, when ξ is substantially high, the V_{oc} of a multistage device is dominated by the first term in Equation 3-11 since the last two terms are negligible. This implies that the V_{oc} of a multistage device nearly scales with number stages when the photon flux to thermal flux ratio is very high. This speculation is confirmed by the calculations for the incident power

density of 50 W/cm^2 (corresponding to a minimum ξ of 305) as shown in Figure 3-8. The open-circuit voltage enhancement in this figure is the $V_{oc}(N_c)$ of the optimized multistage device normalized to the $V_{oc}(1)$ of the optimized single-absorber device. Note that, the parameters used in the calculation are same as those for single-absorber devices, as presented in Table 3-1. In different scenarios, the normalized open-circuit voltage almost scales with N_c. The slopes are only slightly lower than unity (indicated by the dashed purple line in Figure 3-8, i.e. $V_{oc}(N_c)/V_{oc}(1)=N_c$) due to light attenuation in the optically deeper stages. For example, the slope is about 0.9 for αL=0.45 and 0.95 for αL=1.5 and 4.5. This good consistent linear proportionality for a wide range of αL will lead to a universal enhancement of conversion efficiency in multistage ICTPV devices compared to single-absorber devices.

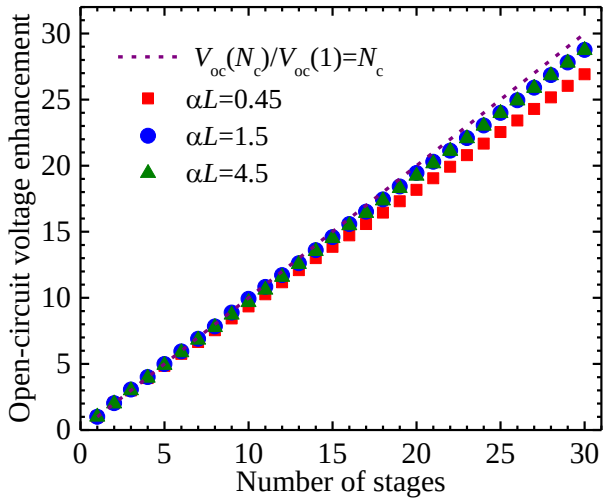

Figure 3-8: Calculated open-circuit voltage enhancement $V_{oc}(N_c)/V_{oc}(1)$ as a function of number of stages. The dashed purple line indicates $V_{oc}(N_c)/V_{oc}(1)=N_c$. In the calculations, αL was set at 0.45. 1.5 and 4.5. The incident power density is 50 W/cm^2.

3.3.2 Enhancement of conversion efficiency

Figure 3-9 shows the calculated conversion efficiency as a function of number of stages for different values of αL. The η is increased from 7%, 23% and 59% in a single-absorber structure to 17%, 33% and 68% in a multistage IC architecture for αL equal to 0.45, 1.5 and 4.5, respectively. Therefore, the η has a universal absolute increase of 9-10% regardless of the value of αL. In terms of relative change, it is more pronounced for small value of αL. For example, for αL=0.45, the η of multistage devices is more than twice that for single-stage cells. This can be explained by resorting to the preceding analysis. When ξ is high enough, the following equations hold: $V_{oc}(N_c)/V_{oc}(1)\approx N_c$ (Figure 3-8) and $FF(N_c)/FF(1)\approx 1$ according to Equation 3-9 and 3-11. Then efficiency enhancement in a multi-stage structure $\eta(N_c)/\eta(1)$ is approximated as:

$$\frac{\eta(N_c)}{\eta(1)} = \frac{QE(N_c)}{QE(1)} \cdot \frac{V_{oc}(N_c)}{V_{oc}(1)} \cdot \frac{FF(N_c)}{FF(1)} \approx \frac{N_c \cdot QE(N_c)}{QE(1)} \tag{3-12}$$

According to this equation, it is evident that the efficiency enhancement of a multistage device is essentially due to its increased particle conversion efficiency η_{part} that is defined as $N_c \cdot QE(N_c)$ for current-matched IC structures. Increasing the number of stages increases η_{part}, although it shortens the absorber thicknesses and reduces $QE(N_c)$. This explains why the η increases with the number of stages as shown in Figure 3-9. From Figure 3-1, QE(1) is low for small αL, hence the $\eta(N_c)/\eta(1)$ can be substantial. For large αL, QE(1) is relatively high, so the $\eta(N_c)/\eta(1)$ is less significant, but still exceeds unity. This manifestly shows how the multistage structures enhance through an increased particle efficiency with shortened individual absorbers for high collection of photo-generated carriers, which could otherwise be lost to recombination with a long single absorber.

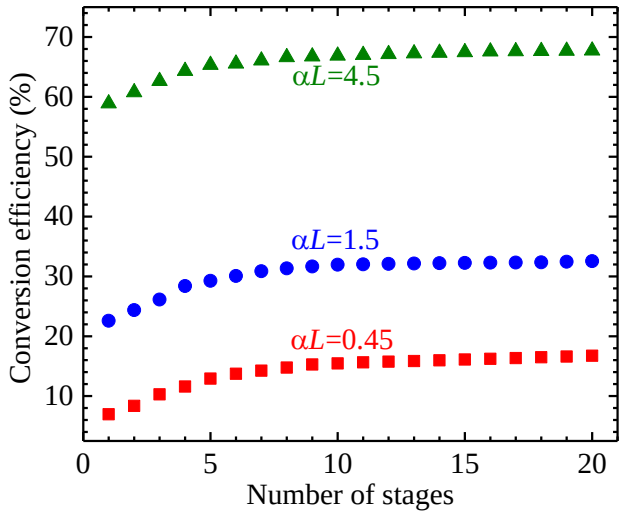

Figure 3-9: Calculated conversion efficiency for optimized multistage cells as a function of number of stages. The calculation is done for αL=0.45 1.5 and 4.5. The incident power density is 50 W/cm^2.

According to Equation 3-12, if $V_{oc}(N_c)/V_{oc}(1)=N_c$ and $N_c \cdot QE(N_c)=1$ (with sufficiently large number stages), the efficiency enhancement is equal to 1/QE(1). This maximum efficiency enhancement is calculated as a function of αL and is indicated by the solid purple curve in Figure 3-10. However, it is higher than the real efficiency enhancement as represented by the dashed olive curve in Figure 3-10, since $V_{oc}(N_c)/V_{oc}(1)$ is slightly lower than N_c in practical case (See Figure 3-8). Also displayed in Figure 3-10 are the calculated maximum efficiencies that can be achieved by single-absorber and multistage devices with two different bandgaps (*i.e.* 0.29 and 0.4 eV). The number of stages of the multistage devices is twenty, which is large enough to reach the plateau value of achievable efficiency (as shown in Figure 3-9). For the two different bandgaps, almost the same improvement is observed. When the bandgap is increased to 0.4 eV, it's possible to achieve a conversion efficiency of 30% with a multistage IC architecture even for a small αL value of 0.45. This elucidates that multistage IC architecture is an effective strategy to universally improve the device performance in a wide infrared spectral range.

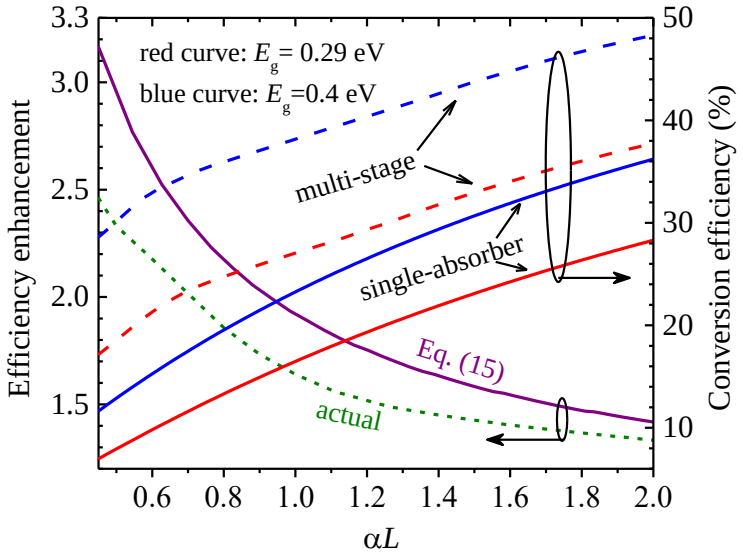

Figure 3-10: Calculated maximum conversion efficiency and conversion efficiency enhancement as a function of αL. The incident power density is 50 W/cm^2.

3.4 Performance of TPV devices under variable illumination sources

3.4.1 Single-absorber TPV cells

In the preceding two sections, the incident photon energy is set equal to bandgap, which inevitably overestimates the conversion efficiency to some degree. This is because, to excite electron-hole pairs, the photon energy needs to be higher than the bandgap. On the other hand, a high photon energy will escalate thermalization loss. Here, to evluate the dependence of device performance on incident photon energy, an energy-dependent absorption coefficient $\alpha(E)=1.9\times(h\nu-E_g)^{1/2}$ μm^{-1} is used, which matches well with that for quaternary $Ga_{0.44}In_{0.56}As_{0.5}Sb_{0.5}$ with a bandgap of 0.29 eV [165]. This bulk material has been employed as the absorbers in IC detectors and the pre-factor 1.9 μm^{-1} is assumed as the best fit to the experiment data [165]. Table 3-2 shows all the parameters used in the calculations for this $Ga_{0.44}In_{0.56}As_{0.5}Sb_{0.5}$ material, some of which are same with those for InAs/GaSb SL in Table 3-1.

Table 3-2: Parameters used in calculation for bulk $Ga_{0.44}In_{0.56}As_{0.5}Sb_{0.5}$.

Temperature and bandgap	T_{device}=300 K, E_g=0.29 eV
Effective mass	$m_e = 0.028m_0$, $m_h = 0.51m_0$
Density of states	N_c=1.2×10^{17} cm^{-3}, N_v=9.2×10^{18} cm^{-3}
Intrinsic carrier concentration	$n_i = \sqrt{N_c N_v}\exp\left(\frac{-E_g}{2k_bT}\right)$= 3.8×10^{15} cm^{-3}
***p*-type doping concentration in the absorber**	N_a=2.8×10^{16} cm^{-3}
Refractive index	n=3.5
Absorption coefficient:	$\alpha = 1.9 \times \sqrt{E - E_g}$ (μm^{-1})
Radiative recombination coefficient [29]	$B = \frac{n^2}{n_i^2}\int_{\theta=0}^{\theta=\pi}\int_{\varphi=0}^{\varphi=2\pi}\int_{E=E_g}^{E=\infty}\alpha(E)\frac{2E^2}{h^3c^2}\left[exp\left(\frac{E}{k_bT}\right)-1\right]^{-1}sin\theta d\theta d\varphi dE$ B=2.81×10^{-11} cm^{-3}·s^{-1}
Actual lifetime	τ=20 ns, L=1.5 μm
Electron mobility	μ_e=43 cm^2·V^{-1}·s^{-1}, calculated with L =1.5-μm and τ=20-ns.
Radiative lifetime	$\tau_{rad} = 1/BN_a$ = 1.3 μs (no photon recycling), L=12 μm

Figure 3-11 shows the calculated conversion efficiency of a single-absorber device as a function of incident wavelength for different diffusion lengths and under illumination at 50 W/cm^2. Note that the η at each wavelength and diffusion length is the maximum value with the optimal absorber thickness. Given a constant electron mobility of 43 cm^2·V^{-1}·s^{-1}, the diffusion length increases from 1.5 μm to 15 μm while the carrier lifetime is enhanced from 20 ns to 2.0 μs. For a long diffusion length, the QE is high (Figure 3-1) and the η reaches the maximum value at an incident photon energy that is closely matched with the bandgap. Conversely, when the diffusion length is short, the QE is low at a photon energy close to the bandgap, thus resulting in a low η. By increasing the energy of incident photons, the η can be improved since the absorption coefficient and QE is enhanced. This leads to a blue shift of the peak value of η as indicated by the black arrow in Figure 3-11. This result for a short diffusion length goes against the conventional view that the incident

photon energy should be very close to the bandgap for best conversion efficiency. However, based on above analyses, it is comprehensible from the perspective of the QE for narrow-bandgap TPV cells with small αL.

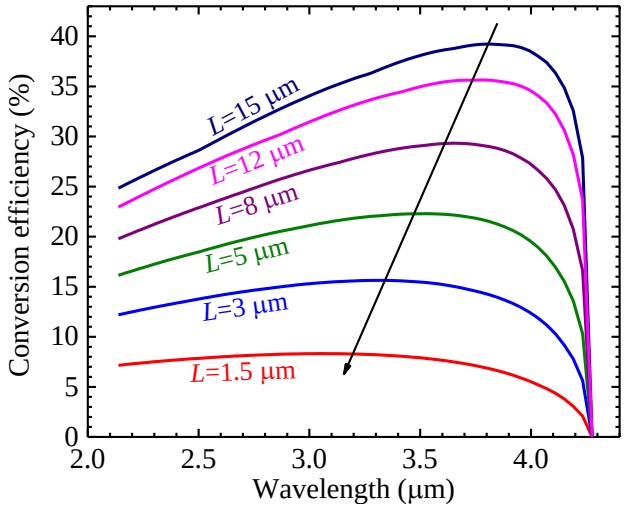

Figure 3-11: Calculated conversion efficiency of a GaInAsSb single-absorber device vs wavelength for various values of diffusion length. The incident power density is 50 W/cm^2.

3.4.2 Multistage ICTPV devices

As for multistage TPV cells, there is more flexibility to maximize the conversion efficiency under different incident photon energies because of the multiple adjustable parameters. Despite more complicated than the single-absorber structure, the multistage IC architecture offers an effective way of dealing with the diffusion length limitation and thus to maximize the η at a photon energy close to the bandgap. One important consideration in the design of a multistage TPV device is the photocurrent match between stages. If the current is mismatched, the QE decreases with incident photon energy, which can be partially caused by the light attenuation. Figure 3-12 shows the calculated η for four multistage structures. These structures have the optimal current matched absorbers that

were designed based on an absorption coefficient of α_0=3000 cm^{-1} (at a wavelength λ_0 of 4 μm, close to the cutoff wavelength of 4.3 μm) to maximize conversion efficiency. With the same number of stages, the individual absorber thicknesses differ considerably for different diffusion lengths. For example, for the 5-stage devices, the optimal absorber thickness sequence (nm) is 476/562/693/923/1567 and 603/733/941/1318/2225 for a diffusion length equal to 1.5 and 15 μm, respectively. The light attenuation is significant in the thick absorbers for the case of L=15 μm, therefore, there are dramatic reductions in the QE and η at short wavelengths. This explains why η of the 20-srage device with L=15 μm is even lower than that for L=1.5 μm at wavelengths shorter than 3 μm. These results illustrate the importance of retaining current match when selecting the illumination source for multistage devices.

In addition, the η of four devices peaks at a wavelength slightly shorter than λ_0, where the QE reaches its maximum with current match. This is because the open-circuit voltage and fill factor are both somewhat higher at a wavelength slightly shorter than λ_0. Alternatively, one can optimize the multistage structure based on the measured absorption coefficient at every given wavelength such that the η at each wavelength reaches the maximum value that is achievable by a multistage architecture. This is illustrated by the olive curves in Figure 3-12 for two diffusion lengths. The total absorber thickness of each optimized structure is about 8 μm for wavelength near the bandgap, and the number of stages for each structure is twenty. For example, for λ=4 μm and L=1.5 μm (represented by the solid olive curve in Figure 3-12), the optimal absorber thickness (nm) sequence is 148/156/165/174/183/194/206/220/236/254/276/301/332/370/419/483/573/711/960/175 with a total absorber thickness of about 8.1 μm. In contrast to single-absorber devices, the

maximum η of the optimized multistage devices always occurs at an incident photon energy very close to the bandgap, regardless of the magnitude of the diffusion length. This further validates the advantages and flexibility of the multistage architecture.

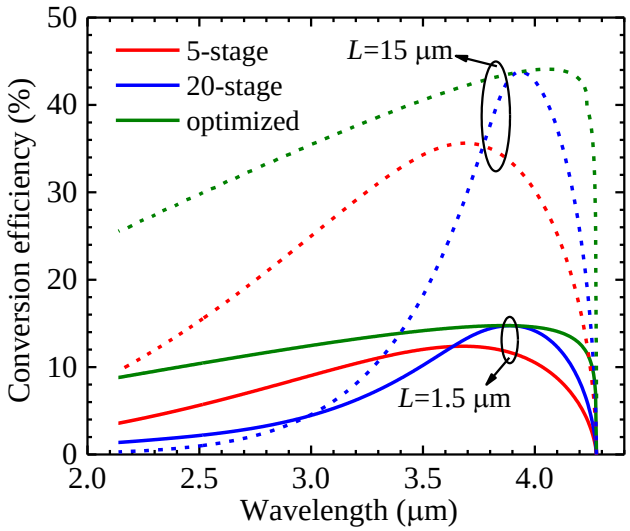

Figure 3-12: Calculated conversion efficiency for the 5- and 20-stage devices with L=1.5 μm (solid curves) and 15 μm (dashed curves). The absorbers were adjusted to be photocurrent matched with an absorption coefficient of 3000 cm^{-1}, corresponding to a wavelength of 4 μm. The calculated maximum efficiencies with optimized multi-stage structures at every wavelength are represented by the olive curves. The incident power density is 50 W/cm^2.

3.5 Summary and concluding remarks

To recapitulate, in this chapter, the efficiency limiting factors in narrow bandgap TPV cells are identified and how they affect the device performance is discussed. These factors are highly correlated with high dark saturation current density, short carrier lifetime, relatively small absorption coefficient and finite diffusion length. As an example, narrow-bandgap InAs/GaSb SLs are used to illustrate the specific impact of these factors on conversion efficiency and how the device performance can be improved by adjusting material parameters such as the product αL. One way to increase αL is to employ Ga-free

InAs/InAsSb SLs for absorbers with a relatively long carrier lifetime [166-167]. Furthermore, it is shown that multistage IC structure is capable to overcome the diffusion length limitation and achieve a particle conversion efficiency approaching 100%, therefore increasing the conversion efficiency by about 10% in a wide range of αL values and bandgaps. The enhancement of conversion efficiency with multistage IC structure is especially impressive for small values of αL, for which the conversion efficiency is more than double that in the single-absorber TPV devices. In addition, the entire structure's flexibility and other advantages of multistage structure offer the possibility to achieve maximum conversion efficiency with the incident photon energy close to the bandgap. Nevertheless, as with single-absorber TPV devices, the issues of relatively low fill factor and voltage efficiency ($=qV_{oc}/(N_cE_g)$ for IC structures) remain. These issues are directly related to the high dark saturation current density in narrow bandgap materials. To resolve them, an approach that can significantly increase the photocurrent without requiring a higher incident power density needs to be implemented, which should be one of future research focuses.

Chapter 4: Experimental comparison between single-absorber and multistage IC thermophotovoltaic devices

4.1 Background and motivation

In chapter 3, theoretical evidence and illustrated scenarios are presented to prove the advantage of multistage ICTPV devices over single-absorber TPV devices. Specifically, IC structures are shown to be capable to enhance the conversion efficiency by promoting the collection of photo-generated carriers. In this chapter, broad experimental proof is furnished to support the advantage of IC devices, especially in concerns of enhanced collection efficiency. Aside from InAs/GaSb T2SLs that are treated in Chapter 3, the advantage of IC structures is also true for other narrow bandgap materials since their diffusion length and absorption coefficient are limited as well. For example, the bulk InAs and InSb (either intrinsic or lightly doped) typically have α in the range of 1000-3000 cm^{-1} near bandgap. Their L can be several microns at room temperature but may be shortened significantly under strong illumination due to the high concentration of excess carriers.

The effects of small α and short L on single-absorber TPV performance are illustrated in Figure 4-1, where the calculated QE and collection efficiency (η_c) are plotted as functions of normalized absorber thickness (d/L). The calculation of QE is carried out based on Equation 2-4 without considering the surface reflection of light. The collection efficiency is defined as the ratio of collected carriers to absorbed photons and is equal to $QE/[1-\exp(-\alpha d)]$. For single-absorber devices, adequate absorption of incident light necessities a thick absorber, especially with a small α. However, if the diffusion length is short, QE will not increase further with absorber thickness after $d \approx L$ as shown in Figure 4-1(a). This is because some photogenerated carriers recombine before being collected and

the collection efficiency is reduced with absorber thickness. The reduction of collection efficiency with increasing d is more significant when $\alpha L<1$, as shown in Figure 4-1(a). Also, for $\alpha L>1$, the QE peaks at a certain finite absorber thickness, because the collection probability (defined by Equation 2-1) of photogenerated carriers is reduced with absorber thickness. A high collection efficiency (>90%) can be obtained only when the absorber is thinner than the diffusion length (or thinner than $0.6L$ for $\alpha L<1$) as shown in Figure 4-1(a). In addition, the open-circuit voltage, defined by Equation 3-4, is reduced with a limited collection efficiency. This is illustrated by the open-circuit voltage factor $VF=\ln[QE/\tanh(d/L)]$ in Figure 4-1(b), where the dotted curves are calculated assuming complete collection of carriers while solid curves are based on the calculated QE in Figure 4-1(a) with a limited collection efficiency. As can be seen, comparatively, VF is decreased considerably with a limited collection efficiency especially when $\alpha L<1$ and $d>L$. For instance, for $\alpha L=0.35$ and $d=3L$, VF is decreased by 0.91, resulting in a reduction of V_{oc} by 24 mV at 300 K. Hence, the considerably reduced VF coupled with the limited QE due to the finite diffusion length will result in a poor conversion efficiency when αL is less than unity.

In this chapter, a comparative study of three TPV devices is presented to experimentally confirm the advantage of multistage architecture, as well as to examine how different configurations affect device performance. One of the three devices has single-absorber structure while the others are three- and five-stage IC devices. The bandgap of the InAs/GaSb T2SLs in these devices is about 0.2 eV at 300 K, which is the narrowest bandgap ever reported so far in TPV cells.

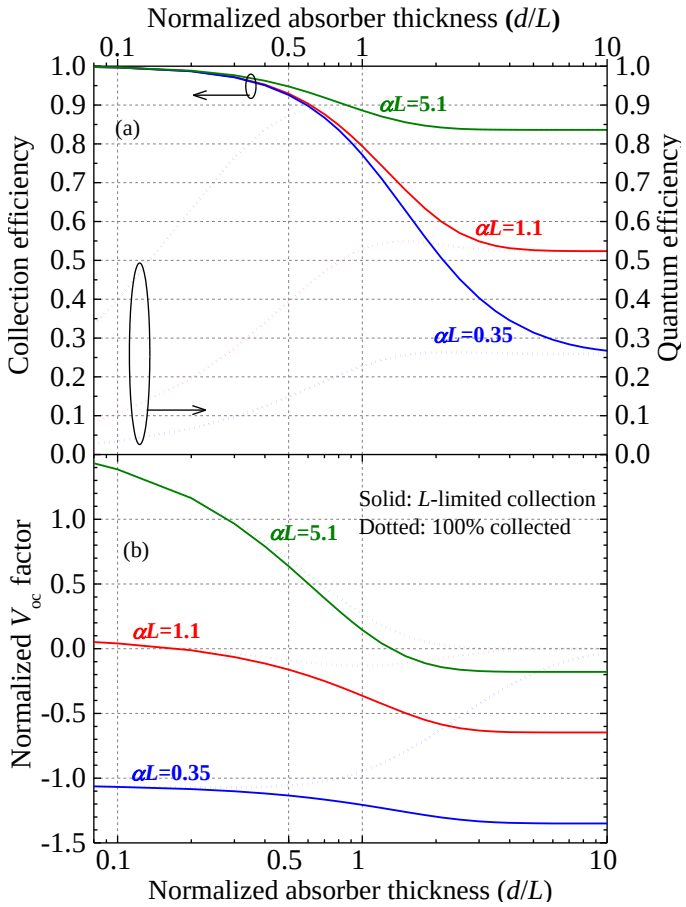

Figure 4-1: (a) Calculated quantum efficiency and collection efficiency, and (b) open-circuit voltage factor as a function of normalized absorber thickness for several values of αL. VF initially decreases with increasing d/L due to the nearly linear increase of dark current when d/L is small.

4.2 Device structure, growth and fabrication

The three TPV structures are grown by GENxplor MBE system (Figure 2-11) on nominally undoped *p*-type GaSb (001) substrates. In the three structures, each period of the SL absorber is composed of four layers: InSb (1.2 Å), InAs (20.5 Å), InSb (1.2 Å) and GaSb (25.1 Å). The two thin InSb layers were inserted to balance the tensile strain of the InAs layer [168]. The absorbers in the three structures are *p*-type doped to 2.6×10^{16} cm^{-3}. In the two multistage structures, the individual absorber thickness was increased in the optically deeper stages to achieve current match between stages by compensating for light

attenuation. The current-matched absorbers were deigned based on the absorption coefficient of 3000 cm^{-1} for a monochromatic light source and the assumption of full collection of photo-generated carriers. The absorber thickness for the 1-stage device is 2.31 μm. The 3-stage device has a total absorber thickness equal to that of the 1-stage device with the discrete individual thicknesses of 624, 749 and 936 nm from surface to the substrate. The individual absorber thicknesses in the 5-stage device are 360, 408, 480, 576 and 696 nm, and the total absorber thickness is 2.52 μm, slightly longer than the 1- and 3-stage devices. The electron barriers in the three devices were made of four digitally GaSb/AlSb QWs with GaSb well thicknesses of 33/43/58/73 Å. The hole barriers consist of eight digitally graded InAs/AlSb QWs with the InAs well thicknesses (in Å) of 32/34/36/40/45/52/60/71. The schematic layer structures of the three devices are shown Figure 4-2. After MBE growth, square mesa devices with edge lengths ranging from 50 to 1000 μm are processed by using conventional contact lithography and wet etching. For passivation, two layers composed of Si_3N_4 followed by SiO_2 are used for improving overall stress management and minimizing pin holes. Finally, Ti/Au contacts are deposited by sputtering, and then the devices are mounted on heat sinks and wire bonded for characterization.

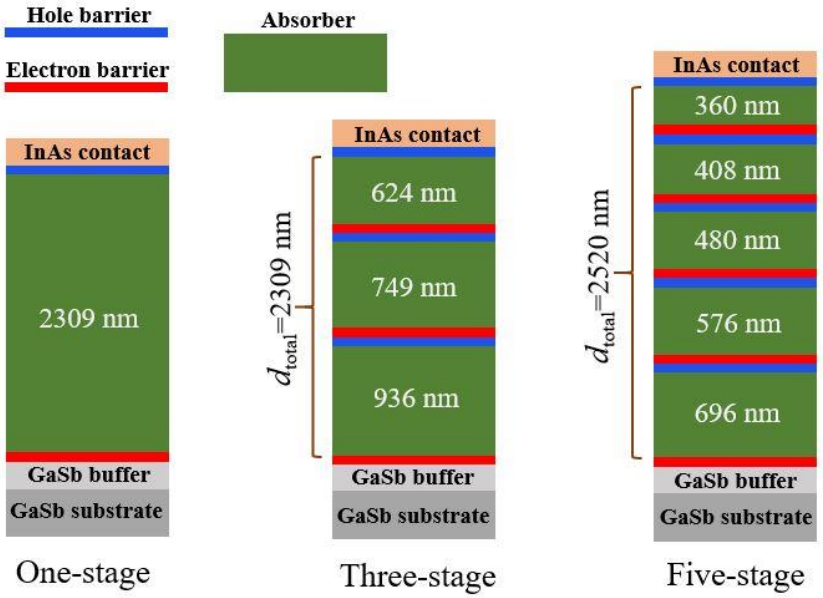

Figure 4-2: Schematic layer structures of the three TPV devices with one, three and five stages.

4.3 Device characterizations and discussions

4.3.1 Quantum efficiency

The QEs of the three devices were measured using a FTIR spectrometer and a calibrated blackbody radiation source with a temperature of 800 K and a 2π field of view (FOV). The blackbody source had an aperture of 0.76 cm and was placed at 30 cm from the device. Figure 4-3 shows the calibrated QE spectra at 300 and 340 K for the representative 0.2×0.2 mm^2 devices processed from the three wafers. Because of current continuity in multistage IC structure, the device QE is decided by the stage with weakest response, therefore the measured QE reflects the actual device performance and is more meaningful than the effective QE for any individual stages. As can be seen in Figure 4-3, at 300 K, the 1- and 3-stage devices have a 100% cutoff wavelength of 5.5 μm, which corresponds to a bandgap of 225 meV. By comparison, the 5-stage device has a slightly

longer 100% cutoff wavelength of 5.8 μm with the SL absorber bandgap estimated to be 214 meV. Since the QE is roughly proportional to the individual absorber thickness, the 5-stage device with thinnest individual absorbers has the lowest QE, while the 1-stage device with a 2.31-μm absorber has the highest QE among the three devices. For example, at λ=4 μm and T=300 K, the QEs are 29.5%, 12.0%, and 8.8% for the 1-, 3- and 5-stage devices, respectively. As the temperature in increased to 340 K, the QEs of the 1- and 3-stage devices were decreased, while the QE of the 5-stage device was nearly unchanged. Also, the decline of QE with temperature for the 1-stage device is more pronounced than the 3-stage device. For example, at λ=4 μm, the QE was reduced to 23.6% for the 1-stage device, compared to a small reduction to 11.3% for the 3-stage device at 340 K. The QEs were reduced because the diffusion length was shorter at a higher temperature, leading to a smaller collection efficiency as illustrated in Figure 4-1. This speculation is further proved by the bias dependence of the QE at λ=4 μm for the three devices as shown in Figure 4-4.

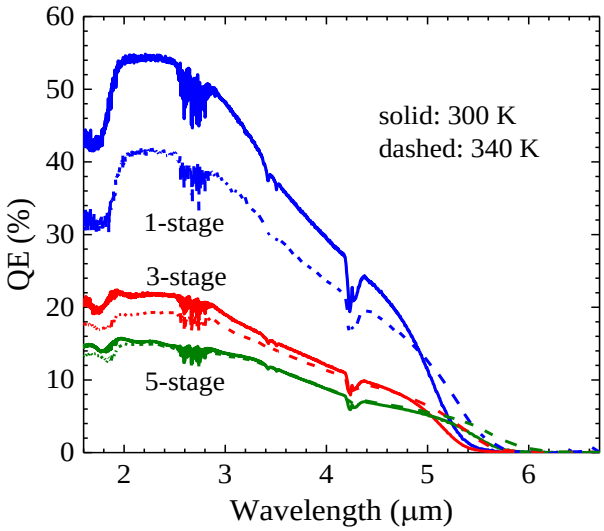

Figure 4-3: Measured QE spectra of 1-, 3- and 5-stage devices at 300 and 340 K.

As can be seen in Figure 4-4, for the 1-stage and 3-stage devices, a reverse bias is required to achieve the saturation (or maximum) value of QE with complete collection of photo-generated carriers at 300 K. This is because the diffusion length is either shorter than or comparable to the absorber thicknesses in the 1- and 3-stage devices. Hence, at zero bias, some of the photo-generated carrier recombine during transport paths and do not contribute to photocurrent. At higher temperature (e.g. 340 K), the diffusion length is even shorter, consequently, a larger reverse bias is required to saturate the QE for the 1- and 3-stage devices. By comparison, the diffusion length has much less impact on the 5-stage device since its individual absorbers are much thinner. Also, the saturation values of QE for all the devices are higher at 340 K since the absorption coefficient is enhanced due to the bandgap narrowing with rising temperature. Thanks to the thickest absorber, the 1-stage device has the highest QE among the three devices. However, this highest QE does not necessarily result in the best performance among the three devices when they operate at a forward bias voltage.

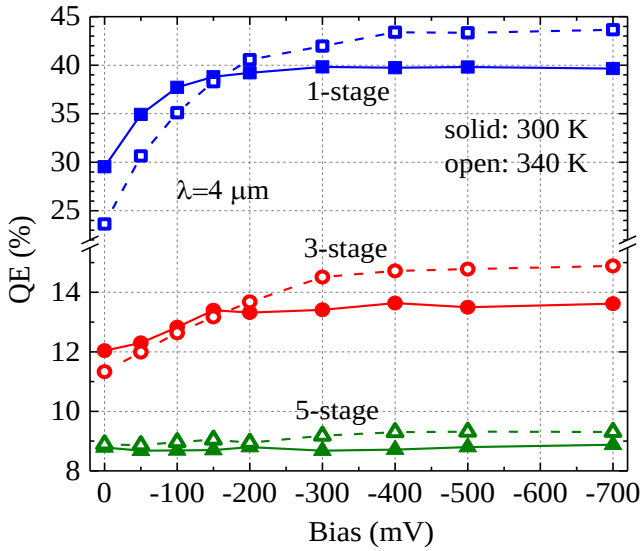

Figure 4-4: Voltage dependent QE at 4 μm for the three devices, where different vertical scales are used in the top and bottom portions to better show variations.

4.3.2 Particle conversion efficiency

As pointed out in Chapter 3, instead of QE, a more proper figure of merit for multistage TPV device is the particle conversion efficiency PCE [169-170]. It is defined as the sum of effective QEs in individual absorbers and is equal to $N_c \times$QE for a current-matched configuration. At λ=4 μm and T=300 K, current match condition is nearly fulfilled based on the measured absorption coefficient (3159 cm^{-1} for 1- and 3-stage devices and 3470 cm^{-1} for the 5-stage device) from the transmission measurement. Hence, the PCE at zero bias is 29.5%, 36.0%, and 44% for the 1-, 3- and 3-stage devices at 300 K, respectively. The highest PCE for the 5-stage device among them agrees with the projected high collection efficiency due to thin individual absorbers. In principle, the value of PCE can be increased up to maximum 69% (estimated by subtracting the 31% reflection loss from the top surface) by adding more stages to fully absorb the incident photons. Also, adding an anti-reflection coating onto the surface can raise the PCE beyond 69%.

In theory, the effective QE in the *N*th stage of a multistage ICTPV device can be calculated based on Equation 2-5. Based on Equation 2-5, together with the measured absorption coefficient and QE, the diffusion length was extracted to be about 1.5 μm at 300 K for the three devices. Evidently, at λ=4 μm, the product of absorption coefficient and diffusion length (αL) is smaller than unity in the three devices. Consequently, according to Figure 4-1, the individual absorber thicknesses need to be shorter than 0.6L in order to achieve a collection efficiency higher than 90%. The 1-stage device has an absorber thickness that is about 1.5 times of the diffusion length and thus it has the lowest collection efficiency at zero bias (~60% as illustrated in Figure 4-1). In comparison, the individual absorbers in the 5-stage device are thinner than 0.6L, thus resulting in a collection

efficiency over 90% and the highest PCE at zero bias as discussed above.

4.3.3 Illuminated *J-V* curve and open-circuit voltage

In the lighted current density-voltage (*J-V*) measurement, a type-II IC laser (ICL) was employed to illuminate the three devices. The narrow emission spectrum of the ICL reproduced the characteristics of a selective emitter (or a narrow-band filter), which is usually included in a TPV system to minimize the thermalization and below-bandgap losses. Both experimental and theoretical efforts were devoted to nanostructured materials for efficient narrowband emissivity near 4 μm or longer wavelengths [32-33]. These studies reinforce the feasibility and applicability of narrow bandgap TPV devices. During the lighted *J-V* measurement, the IC laser was cooled down to ~80 K and continuously delivered high output power at an emission wavelength near 4.2 μm (See inset in Figure 4-5(b)). This emission wavelength corresponds to a photon energy of 295 meV that is 70-80 meV higher than the bandgap of the three TPV devices at 300 K. Hence, there is some thermalization loss (20-27%) from above-bandgap photons. Nevertheless, at laser emission wavelength, current match was almost satisfied in the 3- and 5-stage devices. The PV characteristics of the three devices were studied at different incident power densities simply by adjusting the injection current of the laser. The measured *J-V* curves at 300 K under a medium level of illumination from the ICL are shown in Figure 4-5(a). The incident power density P_{inc} was about 19 W/cm^2, which was assessed through the connection between QE and J_{sc} as expressed by the following equation:

$$P_{inc} = \frac{1.24 J_{sc}}{\lambda_{laser} QE} \tag{4-1}$$

where λ_{laser} is the laser emission wavelength. This simple and effective method to estimate

incident power density allows to circumvent the difficulties associated with the nonuniform and divergent beam of the edge emitting ICL laser.

Also displayed in Figure 4-5(a) are the series resistance (R_s) corrected *J-V* curves and the ideal curves that were plotted in the same manner with [171]. Or rather, the ideal *J-V* curve is the superposition of dark current density and the maximum photocurrent density (J_{phmax}), where the photo-generated carriers are completely collected. The magnitude of J_{phmax} is the difference between the saturated current densities at a reverse bias under dark and illuminated conditions. For example, at T=300 K and P_{inc}=19 W/cm^2, the saturation value of current density under illuminated (dark) condition was 25.3 (2.9), 9.1 (1.1) and 5.9 (0.9) A/cm^2 for the 1-, 3- and 5-stage devices, respectively. Therefore, the corresponding J_{phmax} is 22.4 (1-stage), 8.0 (3-stage) and 5.0 A/cm^2 (5-stage), proportional to their individual absorber thicknesses. At the same incident power density, the J_{sc} values are 9.2 A/cm^2, 6.7 A/cm^2, and 4.9 A/cm^2 for the 1-, 3- and 5-stage devices, respectively. These values of J_{sc} are higher than J_{phmax} values for the three devices, primarily due to incomplete collection of photo-generated carriers particularly in the 1-stage device. Even though the J_{sc} is highest in the 1-stage device, its PCE and collection efficiency are lowest, which results in the lowest conversion efficiency described in next subsection. The high current in the 1-stage device also results in a significant Ohmic loss in series resistance, as reflected by the notable shift between the R_s-corrected and measured *J-V* curves. Instead, the R_s-corrected *J-V* curves for the 3- and 5-stage devices almost coincide with the measured *J-V* curves due to the relatively lower currents.

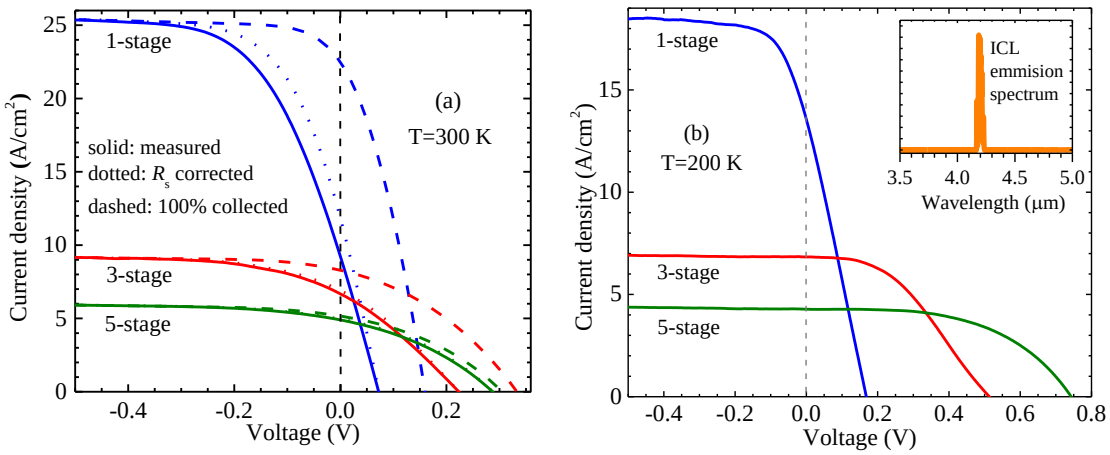

Figure 4-5: (a) Current-voltage characteristics of the three devices at 300 K under a medium illumination level where the incident power density was about 19 W/cm^2. The solid, dotted and dashed curves correspond to the measured, R_s corrected and ideal cases, respectively. (b) Current-voltage characteristics of the three devices at 200 K under the same level of illumination as in (a). The inset shows the emission spectrum of the ICL.

The primary reason for the low collection efficiency in the 1-stage device at 300K was because the diffusion length was shorter than absorber thickness. This can be further confirmed by examining the behaviors at a low temperature where the diffusion length should be longer. Figure 4-5(b) shows the measured *J*-*V* curves of the three devices at 200 K under the same illumination level as in Figure 4-5(a) from the ICL. As shown, for the 3- and 5-stage devices, the onset of current saturation occurs at a certain forward voltage rather than a reverse voltage. This suggests that complete collection of photogenerated carriers was achieved under a forward voltage and the diffusion length was increased significantly beyond the absorber thicknesses in the 3-and 5-stage devices. The increased diffusion length also improved the collection efficiency (~72% at zero bias) in the 1-stage device, although it was still below 100% since the diffusion length was shorter than the absorber thickness (2.31 μm). Also, because of the reduced dark saturation current (orders of magnitude lower than the photocurrent), the V_{oc} was appreciably higher for the three

devices at 200 K. On the other hand, at 200 K, the J_{phmax} under this illumination level dropped to 18.5, 6.9 and 4.4 A/cm^2 for the 1-, 3- and 5-stage devices, respectively. This is because the absorption coefficient decreased due to bandgap widening at lower temperatures.

Aside from a higher collection efficiency compared to the single-stage device, the multistage IC structure can also create a V_{oc} far exceeding the individual absorber bandgap. For example, at T=200 K and P_{inc}=19 W/cm^2, the measured V_{oc} was 170 (1-stage), 513 (3-stage) and 745 meV (5-stage), corresponding to a voltage efficiency of 67%, 68% and 63%, respectively. As the temperature increased to 300 K, the V_{oc} at the same illumination level dropped to 72 (1-stage), 223 (3-stage) and 287 meV (5-stage) with a corresponding voltage efficiency of 32%, 33% and 27%, respectively. Presumably, the slightly lower voltage efficiency in the 5-stage device was due to the narrower bandgap and poorer material quality, which collectively resulted in a much higher thermal generation rate (about two times higher as estimated in Subsection 4.4.2) than in the 3-stage devices at 300 K. Specifically, the V_{oc} could be reduced by ~90 mV (amplified by about 5 times with five cascade stages [169-170]) due to the doubling of the thermal generation rate. On the same account, the V_{oc} of the 5-stage was lower than the 3-stage device in the ideal case as well. In addition, the V_{oc} and voltage efficiency increased when the incident power density was enhanced. For example, at T=300 K and P_{inc}=36 W/cm^2 (highest illumination level available from the ICL), the measured V_{oc} was 85, 271 and 371 mV for the 1-, 3- and 5-stage devices, respectively.

4.3.4 Fill Factor and conversion efficiency

Figure 4-6 shows the measured V_{oc}, *FF*, maximum output power density (P_{max}), and conversion efficiency (η) as functions of incident power density at 300 K for the three devices. At the maximum incident power density (36 W/cm^2), the *FF* was 25%, 28% and 38% for the 1-, 3- and 5-stage devices, respectively. Throughout the whole range of incident power density, the 1-stage device had the lowest *FF* due to the lowest collection efficiency and a greater series resistance loss, while the 5-stage device had the highest *FF* because of the highest collection efficiency. Under the highest illumination level, the maximum output power was harvested at a voltage of 43, 136 and 226 meV for the 1-, 3- and 5-stage devices, respectively. At this voltage, the extracted collection efficiencies (See Figure 4-7) were about 29% (1-stage), 53% (3-stage) and 87% (5-stage). If, however, the photogenerated carriers were fully collected as in the ideal case, the *FF* would increase to 32%, 36% and 39% for the 1-, 3- and 5-stage devices, respectively. From this point of view, the 5-stage device with thin absorbers is nearest to the ideal case for maximum output power. The *FF*s of the 1- and 3-stage devices were also observed to peak at a certain incident power density and then fall off with further increasing the incident optical power. This behavior was possibly related to the larger current and the resulting higher Ohmic losses in series resistances. In contrast, the *FF* of the 5-stage device exhibited a monotonic rise with increasing incident power. The *FF*s of the three devices were considerably lower than the typical values (~60-70%) of TPV cells with bandgaps of 0.5-0.6 eV [5], but they are reasonable for narrow bandgap (~0.2 eV) TPV cells with un-optimized structures.

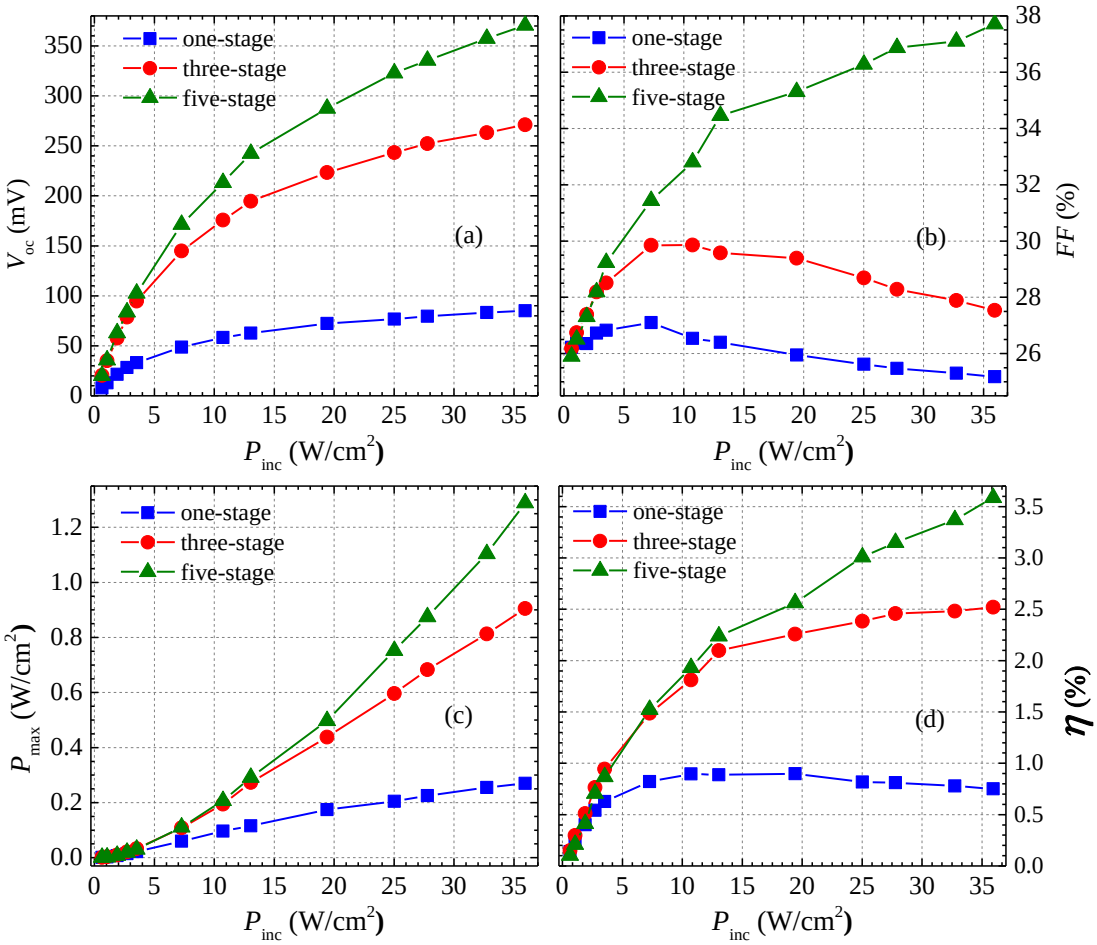

Figure 4-6: (a) Open-circuit voltage, (b) fill factor, (c) maximum output power density and (d) conversion efficiency as a function of incident power density for the three devices at 300K.

The maximum conversion efficiencies at 300 K are 0.9% (1-stage), 2.5% (3-stage) and 3.6% (5-stage) as shown in Figure 4-6(d). The 5-stage device attained the highest power efficiency thanks largely to the efficient collection of photogenerated carriers. This unambiguously verifies the advantage of multistage IC structures with thin individual absorbers for narrow bandgap TPV cells. The main reason for the relatively low conversion efficiency in the three devices was because the dark current was significant in such a narrow band gap (~0.2 eV) structure. Other factors include the contact resistances, some thermalization loss (20-27%), surface reflection (31%), as well as incomplete absorption

(~50%) due to insufficient thick total absorber (≤2.52 μm). At lower illumination levels (P_{inc}<5 W/cm^2), the conversion efficiency of the 5-stage device was slightly lower than the 3-stage device due to the narrower bandgap and the higher thermal generation rate, as will be given in Subsection 4.4.2. For example, at P_{inc}=3.5 W/cm^2, the conversion efficiency was respectively 0.94% and 0.88% for the 3- and 5-stage devices, although the V_{oc} of the 5-stage device was somewhat higher than the 3-stage device (103 vs. 95 mV). In fact, the conversion efficiencies of the two multistage devices can be further enhanced by increasing the incident power, as the conversion efficiencies have not yet saturated even at 36 W/cm^2. This can be accomplished with built-in lenses on the device surface and by exploring the photonic structure or metamaterial. In contrast, the conversion efficiency of the 1-stage device dropped by about 16% after saturation, which is consistent with the trend of *FF* with incident power. In addition to *FF*, the increased Ohmic losses at higher incident power in the 1-stage device provided another mechanism for reducing the conversion efficiency after saturation. In contrast, for the 3-stage device, the rapid increase of V_{oc} overcame the decrease of *FF* with increasing incident power, and the Ohmic loss in the 3-stage device was lower than in the 1-stage device. Consequently, similar trends of conversion efficiency and V_{oc} were observed for the 3-stage device. Table 4-1 summarizes the PV performance characteristics and related parameters for the representative devices from the three wafers. These data collectively show the capabilities and advantages of multistage ICTPV devices, and the limitation of the single-stage TPV devices.

Table 4-1: Summary of the PV performance and the related parameters of representative devices (0.2×0.2 mm^2) from the three ICTPV wafers at 300 K. The maximum efficiencies shown in the table for the 3- and 5-stage devices are obtained at a maximum incident power density of 36 W/cm^2.

Device	η_c (0) (%)	J_{sc} (A/cm^2)	J_{phmax} (A/cm^2)	V_{oc} (mV)	FF (%)	P_{max} (W/cm^2)	Maximum η (%)	R_s (Ω)
1-stage	40	12.9	40.8	85	25	0.27	0.9	4.9
3-stage	76	12.2	15.7	271	28	0.91	2.5	4.6
5-stage	95	9.3	9.7	371	38	1.29	3.6	4.7

4.4 Extraction of some important performance related parameters

4.4.1 Voltage-dependent collection efficiency

In Figure 4-5(a), there is a common characteristic for the three devices, namely a shift between the measured and ideal *J-V* curves. This shift is particularly striking for the 1-stage device, significantly reduces for the 3-stage device, and almost disappears for the 5-stage device. The implies that the collection efficiencies and the photocurrents in the three devices are voltage-dependent, and the illuminated *J-V* curves do not comply with the usual superposition principle [7]. This voltage-dependent characteristic has been reported for solar cells made of Silicon [172-174], CdS/CdTe [171, 175-176], CdS/$CdInSe_2$ [177-178] and GaAs [173]. In thses solar cells, the voltage-dependent characteristic mainly arises from the variation of the electrical field in the depletion region when the applied external voltage is changed. By comparison, the diffusion process plays a more important role in ICTPV structures.

The voltage-dependent collection efficiency η_c (V) can be obtained through the approach described in [171, 174, 178]. This approach relies on two assumptions: First, the photocurrent density can be written as the J_{phmax} times η_c (V): J_{ph} (V)= $J_{phmax} \cdot \eta_c$ (V).

Second, the dark current density is assumed to remain unchanged at different incident power densities [171, 174, 178]. Applying this approach to the current three devices, the η_c(V) can be expressed as:

$$\eta_c(V) = \frac{J_2(V) - J_1(V)}{J_{2phmax} - J_{1phmax}} \quad (4\text{-}2)$$

where J_1(V) and J_2(V) are the current densities at two different incident power densities, and $J_{1\text{phmax}}$ and $J_{2\text{phmax}}$ are the corresponding maximum photocurrent densities. For each device at 300 K, four *J*-*V* curves were selected at incident power densities of 19, 13, 7 W/cm^2 and the dark condition to extract η_c(V) as shown in Figure 4-7(a). As can be seen, the extracted η_c(V) from different pairs of *J*-*V* data does not exactly overlap for the 1- and 3-stasge devices. This suggests that the dark current might change with the incident power density, which can be partially explained by large number of photo-generated excess carriers shortening the carrier lifetime. Another possibility was the small variation of device temperature (<1 K according to the estimated thermal resistance for IC structures [179] and incident power), which may affect the dark injection current contribution, especially at high incident power densities. For this reason, the *J*-*V* pairs at relatively low incident power densities were used to extract η_c(V) as shown in Figure 4-7(a). However, this effect somehow becomes insignificant when the individual absorbers are thin, as evidenced by the almost overlapped η_c(V) profiles with different pairs of incident power densities for the 5-stage device. Another factor is the surface leakage due to imperfect passivation and active surface stages on the etched sidewalls, which will be discussed in Subsection 4.4.4. Note that the possible variations of the diffusion length due to the small change of temperature (<1 K) under different incident power densities should be negligible, since the QE would only differ by at most 0.15% with a 1 K deviation at 4.25 μm as shown

Figure 4-3. The temperature variation for a larger size device might be larger under intensive illumination, but still can be addressed with effective thermal dissipation through a heat sink. For example, based on the previously extracted data for IC structures [179], the specific thermal resistance (R_{sth}) for a device with side dimension of 1 mm is lower than 100 K·cm^2/kW. An incident power density of 36 W/cm^2 would increase the device's temperature by at most 3.6 K (with effective heat conduction through the substrate to a heat sink) compared to its temperature in the dark.

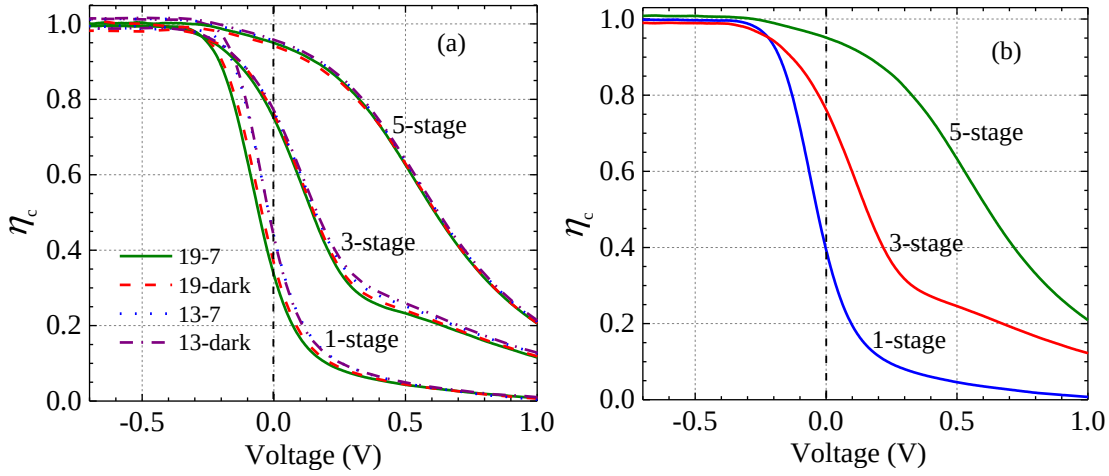

Figure 4-7: (a) Voltage dependence of collection efficiency derived from Equation 4-2 using four different pairs of *J-V* data at 300 K for the three devices. The numbers in the legend indicate the incident power densities under different illumination levels. (b) Average collection efficiency over the four pairs in (a).

For ease of comparison, the average of the four η_c (V) curves in Figure 4-7(a) is plotted in Figure 4-7(b). As shown, the 5-stage device had the highest average η_c (V), while the 1-stage device had the lowest average η_c (V) among the three devices. At zero bias, the η_c (0) was 40%, 76% and 95% for the 1-, 3- and 5-stage devices, respectively. For the 1-stage device, at least 80% of the photo-generated carriers were not collected at forward bias (>0.1 V), as reflected by the small η_c (V) (<0.2). This small η_c (V) severely penalized the fill factor and conversion efficiency as discussed in Subsection 4.3.4. The extracted η_c

(0) was substantially smaller than the theoretical projection (~60%) shown in Figure 4-1(a), especially for the 1-stage device. This was likely caused by the shutting of surface leakage as mentioned earlier. As shown in Figure 4-10, there is significant surface leakage in dark condition especially in the 1-stage device. Likewise, under illuminated condition, large number of photogenerated carriers could leak through the rough sidewalls, thus reducing the collection efficiency. At this moment, why the 1-stage device had most notable surface leakage is not fully understood, and it is worth exploring in the further research.

4.4.2 Thermal generation rate and carrier lifetime

The relatively low conversion efficiencies (<5%) in the three devices were primarily due to the high dark current density associated with the high thermal generation rate (g_{th}) and a relatively short carrier lifetime (τ) in narrow bandgap InAs/GaSb T2SL absorbers. As will be described in Chapter 6, there is a simple and effective method to extract thermal generation rate and carrier lifetime in IC structures. This method is particularly suitable for multistage IC devices since their dark current densities usually exhibit clear and large linear regions at reverse bias [158]. In this method, the g_{th} is first found from the intercept of the linear fitting of dark current at large reverse bias [158]. The carrier lifetime then can be calculated from the g_{th} based on the equation:

$$g_{th} = \frac{n_i^2}{N_a \tau} \tag{4-3}$$

where n_i is the intrinsic carrier concentration and N_a is the *p*-type doping concentration. The intrinsic carrier concentration is given by:

$$n_i = 2\left(\frac{2\pi k_b T}{h^2}\right)^{1.5}(m_e m_h)^{0.75} T^{1.5} e^{-E_g/2k_b T} \quad (4\text{-}4)$$

where m_e and m_h are the electron and hole effective masses, taken to be $0.03m_0$ (m_0 is electron mass) and $0.4m_0$, respectively. Based on Equation 4-4, the calculated intrinsic carrier concentrations at 300 K were 1.15×10^{16} (1- and 3-stage) and1.44×10^{16} (5-stage) cm^{-3}. From the linear fitting of dark current density, the thermal generation rate at 300 K was found to be 3.81×10^{22}, 4.55×10^{22} and 8.35×10^{22} $cm^{-3}\cdot s^{-1}$ for the 1-, 3- and 5-stage devices, respectively. Based on Equation 4-3, the carrier lifetime at 300 K was calculated to be 134 (1-stage), 113 (3-stage) and 89 (5-stage) ns. Compared to the 1- and 3-stage devices, the shorter carrier lifetime and higher thermal generation rate in the 5-stage device are ascribed to its narrower bandgap (214 meV vs. 225 meV) and poorer material quality (with somewhat more defects and larger perpendicular lattice mismatch). In addition, both g_{th} and τ are very strong functions of temperature in the three devices, as shown in Figure 4-8. The sharp decrease of carrier lifetime with temperature is likely due to the growing prevalence of Auger processes linked with bandgap narrowing of the SL absorber at high temperatures. The thermal generation rate in the three devices is many orders of magnitude higher than those in solar cells. For example, for a crystalline Si solar cell, the N_a and τ at 300 K are normally in the ranges of 10^{15}-10^{16} cm^{-3} [7] and 0.1-1 ms [180-181], respectively. Therefore, the g_{th} is estimated to be 2.25×10^{7}-2.25×10^{9} $cm^{-3}\cdot s^{-1}$, about 13-15 orders of magnitude lower than that in the current three ICTPV devices. Evidently, reducing the g_{th} either by increasing carrier lifetime or cooling down the device, even by one order of magnitude, will boost the conversion efficiency of ICTPV devices.

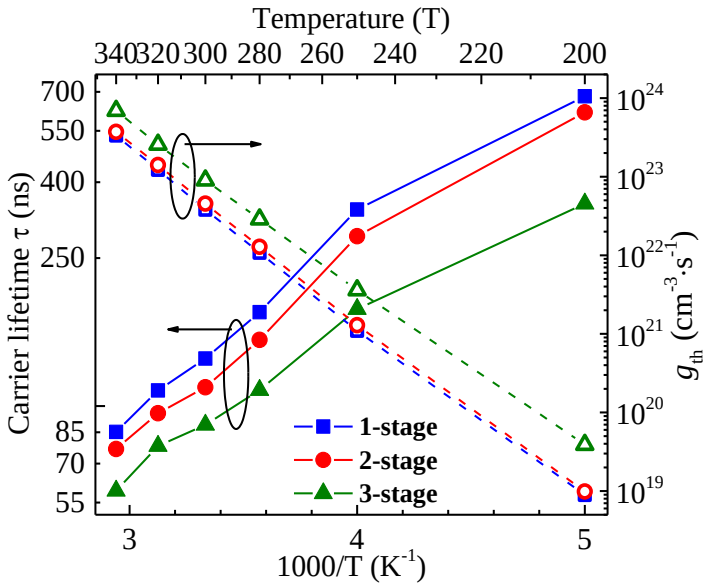

Figure 4-8: The thermal generation rate and minority carrier lifetime for the 1-, 3- and 5-stage devices at high temperatures.

4.4.3 Series resistance

As identified in Subsection 4.4.1, the photocurrents in the three devices were voltage dependent. This voltage-dependent characteristic creates significant complexities when extracting the series resistance R_s using illuminated *J-V* curves. Even with a relatively weak voltage dependence of photocurrent, the series resistance extracted based on a generalized *Suns*-V_{oc} method could be somewhat overestimated [182]. Hence, to avoid the complexity caused by the voltage-dependent photocurrent, the series resistance of the three devices were extracted from the dark condition based on the following equation [174, 178]:

$$R_s = \lim_{1/I \to 0}(dV/dI) \tag{4-5}$$

Figure 4-9 shows the plots of *dV*/d*I* under dark conditions, as well as the extracted series resistances for the three devices. The R_s was acquired by finding the intercept of *dV/dI* vs. 1/*I*. The extracted series resistances were respectively 4.9, 4.6 and 4.7 Ω for the 1-, 3- and 5-stag devices, which were close to each other. This implies that the series resistances in

the three devices were mainly from the contacts and wires, while the resistances between cascade stages can be ignored due to the smooth carrier transport in the type-II broken-gap heterostructure.

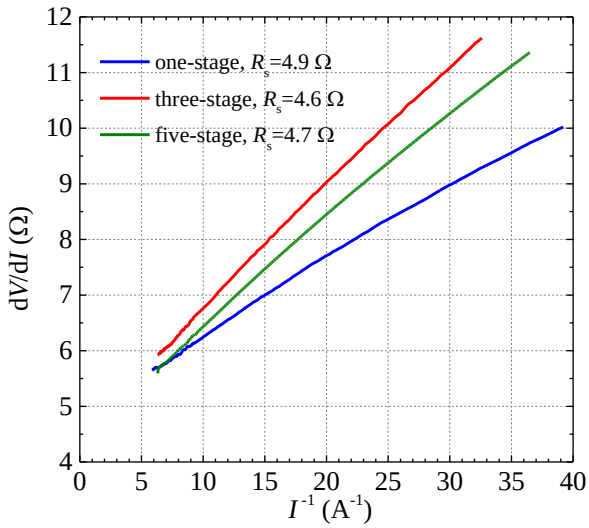

Figure 4-9: *dV/dI* data to obtain series resistance at 300 K, which was found from the intercept of *dV/dI*.

4.4.4 Surface leakage

Surface leakage has been a long-standing issue for III-V based, especially T2SL based, infrared devices [183]. Various passivation techniques were developed for T2SL detectors with varying degree of reliability and effectiveness [184]. In principle, under dark condition, the effect of surface leakage can be quantified through the linear fitting between P/A and 1/R_0A [185]:

$$\frac{1}{R_0 A} = \left(\frac{1}{R_0 A}\right)_{bulk} + \frac{1}{\rho_{sw}}\left(\frac{P}{A}\right) \tag{4-6}$$

where ρ_{sw} is the device sidewall resistivity, and P and A are the device area and perimeter. Figure 4-10 shows the size dependence of R_0A, along with the ρ_{sw} obtained through above fitting for the three devices at 300 K. For the 200×200 μm^2 devices, the R_0A values were

0.02 (1-stage), 0.11 (3-stage) and 0.18 Ω.cm^2 (5-stage). Hence, surface leakage contributed to 74%, 62% and 48% of the total dark current for the 1-, 3- and 5-stage devices, respectively. For devices with larger sizes, the surface leakage affects the dark current to a lesser degree. However, the larger size device has a relatively low R_0 (e.g. only 26 Ω for the 0.5×0.5 mm^2 device from the 1-stage wafer at 300 K), which makes it difficult to accurately extract the device QE. Hence, to optimize the tradeoff, the 0.2×0.2 mm^2 devices with comparatively high R_0 in the three wafers were selected for device analysis.

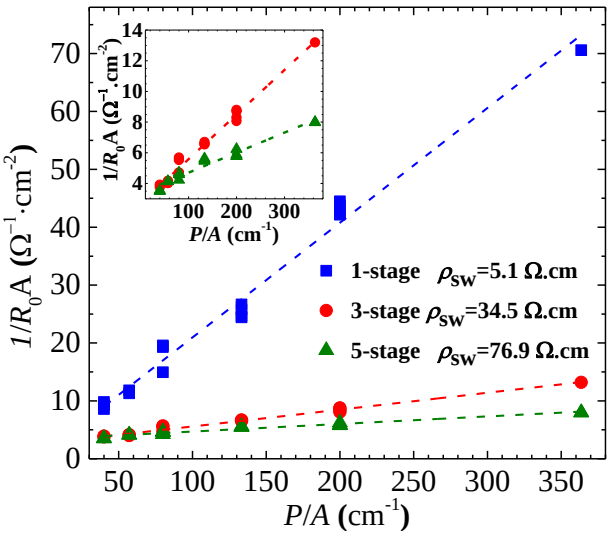

Figure 4-10: Size dependent R_0A for the three devices at 300 K. The sidewall resistivity was smallest for the one-stage device.

4.5 Summary and concluding remarks

In this chapter, rigorous experimental justifications of the advantage of multistage ICTPV devices over conventional single-absorber devices are presented. This is done by a comparative study of three narrow bandgap (~0.2 eV) TPV devices with a single-absorber and multistage IC structures. It is shown that the performance of a single-absorber TPV cell with T2SL absorbers is mainly limited by the small collection efficiency associated with a relatively short diffusion length (1.5 μm at 300 K). Instead, multistage IC structure

is proven to be capable of overcoming the diffusion length limitation and achieving a collection efficiency of about 100% for photogenerated carriers. Consequently, the open-circuit voltage, fill factor and conversion efficiency are greatly improved compared to the single-absorber TPV structure. At current stage, although the demonstrated room-temperature conversion efficiency (3.6%) is relatively low, there is still great room for further improvement. Possible ways to improve the efficiency include increasing the total absorber thickness, adding an anti-reflection coating onto the surface, attaching a back reflector, as well as reducing the contact resistance. The fundamental limitation of a high dark current in narrow bandgap absorbers can be overcome by applying an even stronger optical illumination. This will increase the conversion efficiency since the η in multistage ICTPV devices has not yet saturated as shown in Figure 4-6(d). Alternatively, these narrow bandgap TPV devices can be cooled down to lower temperatures with substantially reduced dark current density and increased power efficiency for applications such as in space (e.g. Jupiter and Saturn missions) where the environment temperature is well below 300 K.

Chapter 5: Interband cascade thermophotovoltaic devices with more stages

5.1 Background and motivation

Unlike the Esaki tunnel junctions routinely used in multijunction solar cells [13, 14], type-II broken-gap heterostructures are used to connect adjacent cascade stages in IC structures so that the interband tunneling is smooth and the electrical resistances between stages are negligible. As often implemented in ICLs, many stages (>20) can be concatenated together without impacting carrier transport. Hence, for ICTPV cells, many IC stages are desirable to maximize the absorption of incident light and produce a high open-circuit voltage for optimizing power efficiency. However, in contrast to ICLs where the light is generated inside the active cascade stages, each stage in an ICTPV cell sees a different intensity due to the absorption in preceding stages. Consequently, to satisfy the current match condition between cascade stages for optimized device operation, the absorber thickness in the optically deeper stages is increased based on the absorption coefficient. In practice, if there are many stages in an ICTPV cell, the deviation of exact current match condition due to the variation of material parameters can be significant. Also, ICTPV cells are relatively complex structures that are very vulnerable to the instable growth conditions, thus the material quality may differ vastly from structure to structure. In this chapter, the effects of current mismatch and material quality will be identified and quantified in four ICTPV devices with different number of stages and absorber thickness.

In addition, in Chapter 4, the better device performance in the 5-stage compared to the 1- and 3-stage devices implies that IC structure with more stages should be preferred. This inference is also in accordance with other experimental data of ICTPV cells [157, 182, 186-188] and the theoretical projection in Chapter 3. Hence, another purpose of this chapter

is to examine this inference with ICTPV devices with many stages. Note that these ICTPV cells were designed for achieving a better understanding of the underlying physics rather than reaching optimized device performance. At current stage, the conversion efficiencies of ICTPV cells do not reach respected levels, and they are not comparable with those achieved from the TPV cells with relatively wide bandgaps [36-42], as shown in Table 5-1. This is because the conversion efficiency of an ICTPV device is primarily limited by a significantly high dark saturation current density J_0 associated with the narrower bandgap and a short carrier lifetime. In Chapter 4, it has been shown that although the IC structure is able to overcome the limitations of a short diffusion length and low absorption coefficient in conventional single-stage TPV cells, the issues of low fill factor and voltage efficiency that result from the high J_0, remain in narrow bandgap ICTPV cells even under monochromatic illumination with high incident power density, as shown in Table 5-1.

Table 5-1: Summary of ICTPV devices that have been reported so far.

N_c	Temperature (K)	E_g (eV)	V_{oc} (V)	Illumination Source	P_{inc} (W/cm^2)	η (%)	Ref.
7	80	0.24	1.11	Blackbody @ 1323 K	0.67	NA	100
7	80	0.31	1.68	Blackbody @ 1323 K	0.23	4.3	189
7	300	0.24	0.65	ICL emitting @ 4.3 μm	19	2.1	190
3	300	0.23	0.18	ICL emitting @ 4.3 μm	7	NA	157
3	300	0.39	0.80	ICL emitting @ 2.81 μm	130	9.6	182
5	300	0.23	0.37	ICL emitting @ 4.2 μm	36	3.6	187
6	300	0.23	0.52	ICL emitting @ 4.2 μm	21	4.1	191

5.2 Device structure, growth and fabrication

The four structures were grown using GENxplor MBE system on nominally undoped *p*-type GaSb (001) substrates. The first two structures have six and seven stages and were grown earlier. The other two structures have substantially increased stages (sixteen and twenty-three) and were grown a year later after the system maintenance. Hence, the growth conditions and material qualities can be somewhat different between the two sets of structures. The absorbers in the four structures were made of InAs/GaSb T2SLs and each period of the SL consist of four layers: InSb (1.2 Å), InAs (20.5 Å), InSb (1.2 Å) and GaSb (25.1 Å). The purpose of including the two InSb layers is to balance the tensile strain of the InAs layer [168]. The absorbers in the four structures were *p*-type doped to 2.6×10^{16} cm^{-3}. The schematic layer diagram of the four structures are shown in Figure 5-1, and the individual absorber thicknesses are presented in Table 5-2. As can be seen, the individual absorbers in the 16- and 23-stage structures are much thinner than in the 6- and 7-stage devices. Conversely, the total absorber thicknesses in the 16- and 23-stage structures are thicker compared to those in the 6- and 7-stage ones. The electron and hole barriers in the four structures were identical to those in the three devices described in Chapter 4. After the MBE growth, the wafers are processed into square mesa devices with dimensions ranging from 50 to 1000 μm by using standard contact UV photolithography and wet-chemical etching. A RF-sputter deposited two-layer passivation (Si_3N_4 then SiO_2) is used for minimizing pin holes and improving overall stress management, and then the Ti/Au layers are sputter deposited for top and bottom contacts. Finally, the devices were mounted on heat sinks and wire bonded for characterization.

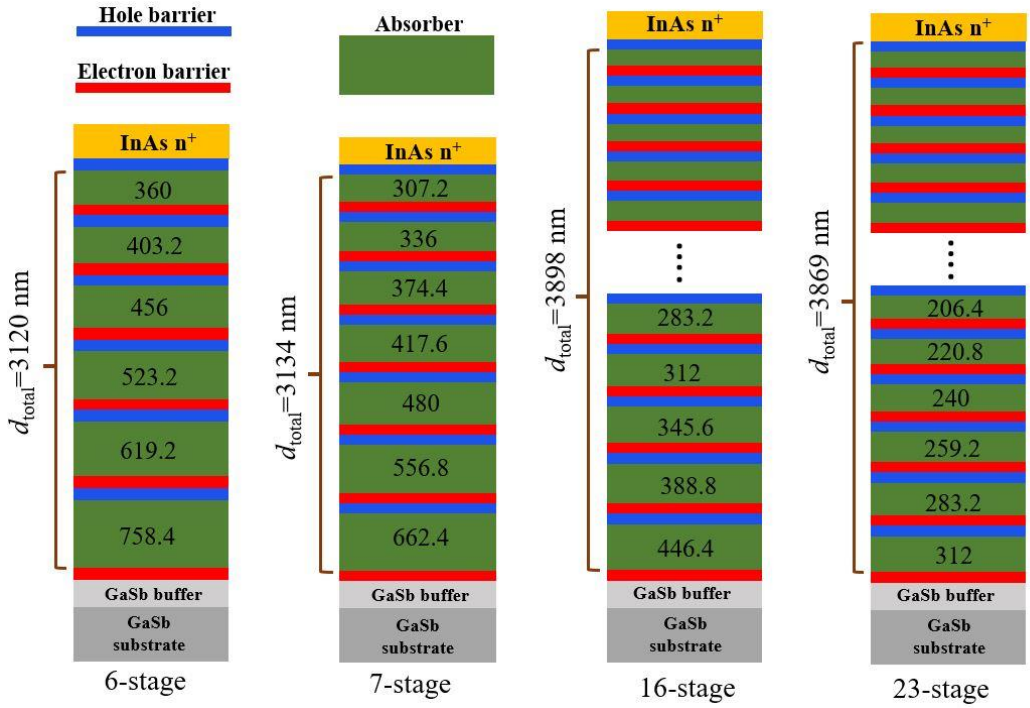

Figure 5-1: Schematic layer structure of the four TPV devices with six, seven, sixteen and twenty-three stages.

Table 5-2: Individual and total absorber thicknesses for the four IC TPV structures.

Device	Individual absorber thickness (nm)	d_{total} (μm)
6-stage	360/403.2/456/523.2/619.2/758.4	3.12
7-stage	307.2/336/374.4/417.6/480/556.8/662.4	3.13
16-stage	144/153.6/158.4/168/177.6/187.2/196.8/211.2/225.6/240/259.2/283.2/312/345.6/388.8/446.4	3.90
23-stage	96/100.8/105.6/110.4/115.2/120/124.8/129.6/134.4/139.2/144/148.8/158.4/168/172.8/182.4/196.8/206.4/220.8/240/259.2/283.2/312	3.87

5.3 Energy conversion efficiency

The energy conversion efficiency η of the four TPV structures was investigated under the illumination from an IC laser. The narrow emission spectrum of the IC laser is analogous to a selective emitter that would be included in a TPV system to reduce the thermalization and below-bandgap losses. During the experiment, the laser was cooled to

80 K and continuously emitted at a wavelength near 4.2 μm (photon energy is 295 meV) as shown in the inset within Figure 5-2(a). The output power of the laser can be controlled by adjusting the injection current, thereby the performance of the four devices was investigated under different incident power densities. Figure 5-2(a) shows the measured illuminated *J*-*V* characteristics at 300 K for representative 200×200 μm^2 devices from the four wafers. The incident power density of 17 W/cm^2 was assessed through the connection between quantum efficiency and short-circuit current density J_{sc}, as expressed by Equation 4-1. As can be seen in Figure 5-2(a), the short-circuit current density decreases with number of stages N_c, primarily due to reduced optical absorption in individual stages with thinner absorbers. Conversely, the open-circuit voltage increases with the number of stages, since it is proportional to N_c when the individual stages are connected in series, as stated by Equation 3-11. For example, at T=300 K and P_{inc}=17 W/cm^2, the J_{sc} was 4.4, 3.2, 1.3 and 1.0 A/cm^2, while the V_{oc} was 350, 518, 910 and 1461 meV for the 6-, 7-, 16- and 23-stage devices, respectively. The trade-off of J_{sc} for V_{oc} with increasing the number of stages can in principle be beneficial for improving the conversion efficiency in many cases, according to the previous experimental results [157, 182, 186-188]. However, such benefit may not always be demonstrated, as will be discussed in the analysis of the characteristics of the current four devices.

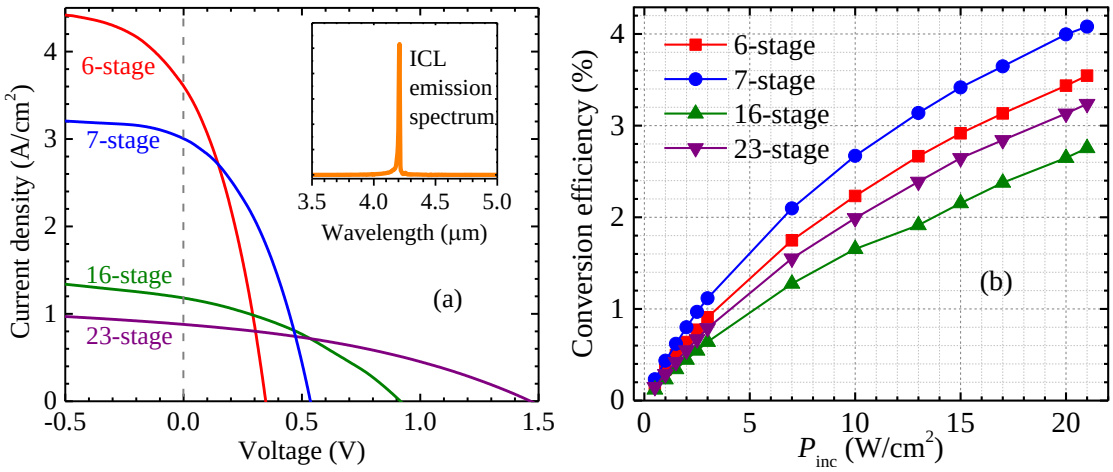

Figure 5-2: (a) Illuminated current density-voltage characteristics for the representative 200×200 μm^2 devices from the four wafers at 300 K and at an incident power density of 17 W/cm^2. The inset shows the emission spectrum of the IC laser used as the illumination source, (b) Conversion efficiency as a function of incident power density for the four devices at 300 K.

Figure 5-2(b) shows the energy conversion efficiencies as a function of incident power density for the four devices at 300 K. As shown, the four devices can be arranged as 7-, 6-, 23- and 16-stage devices according to their η values, from best to worst. For example, at the maximum incident power density (~21 W/cm^2) available from the illumination of the IC laser, the η is 3.5%, 4.1%, 2.7% and 3.3% for the 6-, 7-, 16- and 23-stage devices, respectively. As theoretically illustrated in Chapter 3, the efficiency of ICTPV cells should monotonically increase with the number of stages. This is because the particle conversion efficiency (η_{part}), a more appropriate figure of merit for ICTPV devices, is enhanced as the number of stages increases [169-170]. However, the results of the current four devices indicate that the device performance in terms of η is better with fewer cascade stages (6 and 7) than with more stages (16 and 23. This goes counter with the theoretical forecasting in Chapter 3 and the previous experimental results [157, 182, 186-188]. Nevertheless, the η was higher with more stages for devices grown in the same

campaign. For example, the device performance is better for the 7-stage compared to the 6-stage, and for the 23-stage compared to the 16-stage. Give that the four devices have nominally identical absorber and barrier structures, what causes the different device performances between the two sets? One possible factor is that the current mismatch is more significant in the 16- and 23-stage devices compared to the 6- and 7-stage devices. Another possible cause is that the 16- and 23-stage devices have poorer material quality than the 6- and 7-stage devices, since the two sets of structures were grown in different campaigns. In the following sections, the two possible factors will be inspected and quantified through the analysis of detailed device characteristics such as dark current density, carrier lifetime and quantum efficiency.

5.4 Device characterization and analysis

5.4.1 Dark current density and carrier lifetime

The dark current density-voltage (J_d-V) characteristics of the four devices were measured using a Keithley 2636A source meter. During the measurement, the device was put in a cryostat for temperature control between 78 to 340 K, and a top copper shield was used to block background radiation from the environment. The measured dark current densities at 300 K for the representative 200×200 μm^2 devices from the four wafers are shown in Figure 5-3(a). As shown, the J_d decreases with number of stages due to the reduced thermal generated carriers in thinner individual absorbers [141]. Also, the J_d in the four devices is orders of magnitude higher than in conversional solar cells made of Si and GaAs, which severely limits the device performance of these TPV cells. This is mainly due to their narrow bandgaps that are 0.22-0.25 eV at 300 K as estimated from the 100% cutoff

wavelength of the quantum efficiency spectra [see Figure 5-4(a)]. From the measured dark current, the carrier lifetime (τ), an important indicator of material quality, can be extracted. As will be described in Chapter 6, a simple and effective method to extract carrier lifetime is to apply a linear fit of the dark current density at large reverse bias and first obtain the thermal generation rate g_{th}. This approach is particularly useful for multistage IC devices since their dark current densities usually have a large linear region under reverse bias, as shown in Figure 5-3(b) for the four TPV devices. There is an explicit linear relationship between current density and voltage at reverse bias starting from -2 V. The linear fittings of current density with good accuracy from -4 to -2 V are indicated by the dashed lines in Figure 5-3(b). Based on Equation 6-4, the thermal generation rate at 300 K acquired from the intercept of the linear fitting is 6.6×10^{22}, 4.3×10^{22}, 9.6×10^{22} and 7.9×10^{22} $cm^{-3}s^{-1}$ for the 6-, 7-, 16- and 23-stage devices, respectively. The shunt resistance obtained from the slope of the linear fitting is 10547 (6-stage), 21258 (7-stage), 29294 (16-stage) and 63459 Ω (23-stage).

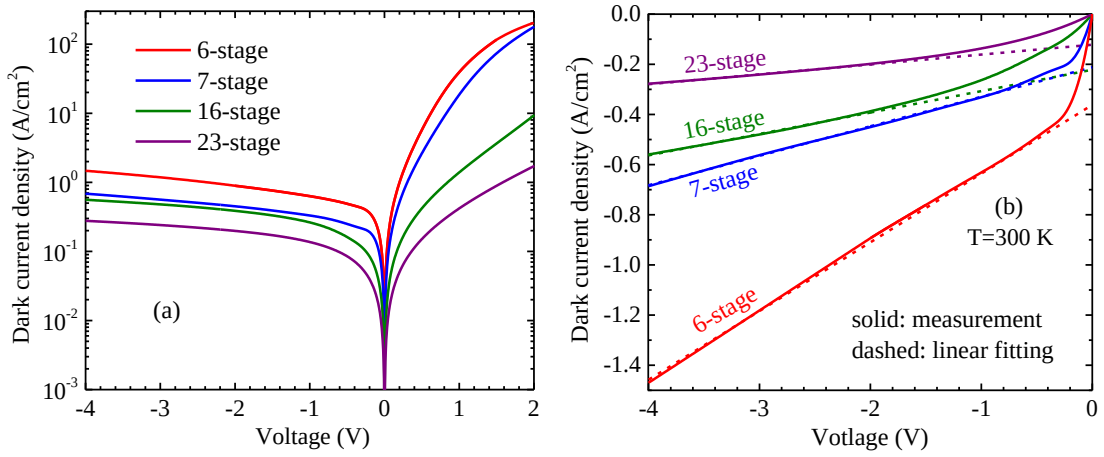

Figure 5-3: (a) Dark current density for the representative 200×200 μm² devices from the four wafers at 300 K, (b) Linear fitting (dashed lines) of dark current density at reverse voltage for the four devices at 300 K.

With the extracted g_{th}, the minority carrier lifetime can be calculated according to Equation 4-3. The carrier lifetime is determined by the comprehensive effect of the radiative, Auger and SRH processes. Usually, based on experimental results in literature [158, 192-193], Auger and SRH processes are dominant in InAs/GaSb T2SLs. The intrinsic carrier concentration at 300 K is calculated to be 1.21×10^{16} (6-stage), 9.9×10^{15} (7-stage), 8.3×10^{15} (16-stage) and 7.6×10^{15} (23-stage) cm^{-3}, according to Equation 4-4. Finally, based on Equation 4-3 and the obtained g_{th} values, the extracted carrier lifetime at 300 K is 86, 88, 28, 28 ns for the 6-, 7-, 16- and 23-stage devices, respectively. Compared to the 16- and 23-stage devices, the longer carrier lifetime in the 6- and 7-stage devices suggests their better material quality. This agrees with higher activation energies E_a (213 and 217 eV between 200 and 340 K) for the 6- and 7-stage devices than that (204 and 207 eV) for the 16- and 23-stage devices. The activation energies were extracted from the temperature dependence of the zero-bias resistance. These values of E_a are 50%-100% of the zero-temperature bandgap values (~ 275-302 meV), which implies a non-negligible contribution of the SRH process to the dark current. The variations of material quality and the corresponding contributions to the SRH process among the four TPV wafers result in different carrier lifetimes, which ultimately affects the TPV device performance that will be quantified in Section 5-5.

5.4.2 Quantum efficiency and current mismatch

In the quantum efficiency measurement, a fourier transform infrared spectrometer (FTIR) was used to measure the relative spectra response. The calibrated QE spectrum was obtained by measuring the device's photocurrent, while it was illuminated by chopped radiation from a standard blackbody source (800 K). The measured QE spectra of the four

devices at 300 K are shown in Figure 5-4(a). The 100% cutoff wavelength where the QE fast turns on is 5.6, 5.3, 5.1 and 5.0 μm, corresponding to a bandgap of 221, 234, 243 and 248 meV at 300 K for the 6-, 7-, 16- and 23-stage devices, respectively. The bandgap difference results from variations in MBE growth conditions, although the SL absorbers in each device were designed to have identical compositions and period. The difference is more outstanding between devices grown in different campaigns. As shown in Figure 5-4(a), the QE decreases with number of stages due to the reduced optical absorption in in thinner individual absorbers. For example, at T=300 K and λ=4.2 μm, the QE is 6.46%, 5.41%, 2.31% and 1.57% for the 6-, 7-, 16- and 23-stage devices, respectively. Figure 5-4(b) shows the measured bias dependence of the QE at 300 K and at the same wavelength. As shown, the devices with more stages and thinner absorbers tend to have weaker bias dependences of QE. The QEs of the 6-, 7- and 16-stage devices slightly increase with reverse bias, while the QE of the 23-stage device is nearly a constant value. Specifically, the QE changes from 6.46%, 5.41%, 2.31% and 1.57% to 7.03%, 5.66%, 2.37% and 1.58%, while the reverse bias is increased from 0 mV to -700 meV for the 6-, 7-, 16- and 23-stage devices, respectively. The moderate degree of bias dependence for the QEs is due to the relatively thin individual absorbers compared to the conventional TPV structure with a single thick absorber. This leads to the unique advantage of high collection efficiency of photogenerated carriers, as described in Chapter 4.

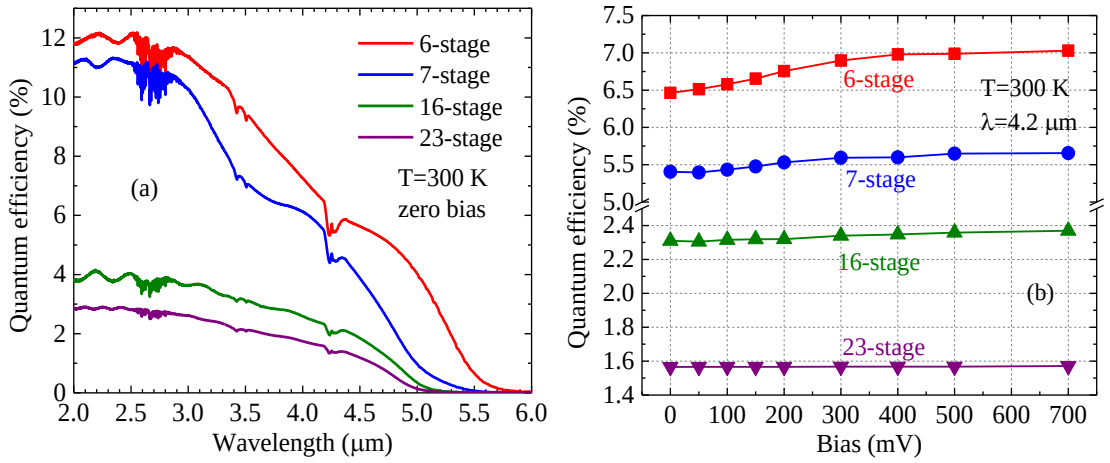

Figure 5-4: (a) Quantum efficiency spectra of the four devices at 300 K and (b) Bias dependence of quantum efficiency for the four devices at 300 K and at the wavelength of 4.2 μm.

In theory, provided that the absorption coefficient (α) and diffusion length (L) are known, the effective QE in each stage of an IC device can be calculated from Equation 2-5 in the diffusion limited case. At 300 K, the measured absorption coefficient at 4.2 μm is 2984, 2643, 2334 and 2200 cm^{-1} for the 6-, 7-, 16- and 23-stage devices, respectively. Based on Equation 2-5, the calculated effective QE at 4.2 μm in each stage of the four devices is shown in Figure 5-5(a). In the calculation, the diffusion length was assumed to be 1.5 μm for the 6- and 7-stage devices, while it was taken to be 0.7 μm for the 16- and 23-stage devices. These values of L were adopted to achieve close agreement with the experimental results. As can be seen, the calculated effective QEs of the 7-stage device are nearly equal in each stage and are quite close to the measured device QE. Contrarily, the calculated effective QEs of the 6-, 16- and 23-stage devices are mismatched between stages. In this scenario, as will be described in Chapter 7, an electrical gain will be delivered across the device to ensure current continuity and will enhance the device's QE to the average value over all stages [194]. On average, the effective QE is 6.65%, 2.42% and 1.63% for the 6-, 16- and 23-stage devices, respectively. These values are well matched

with the measured device QEs with an error less than 5%. This also indirectly verifies the appropriateness of the values used for the diffusion lengths for these devices. Compared to the 16- and 23-stage devices, the longer diffusion length for the 6- and 7-stage devices agrees with their longer carrier lifetime. In addition, the mismatch of effective QE is less significant in the 6-stage device than in the 16- and 23-stage devices. For example, the minimum (maximum) of the effective QEs is 6.39% (6.90%), 2.20% (2.69%), 1.38% (1.95%) in the 6-, 16- and 23-stage devices, corresponding to a mismatch of 8% (6-stage), 22% (16-stage), 41% (23-stage) in their QEs.

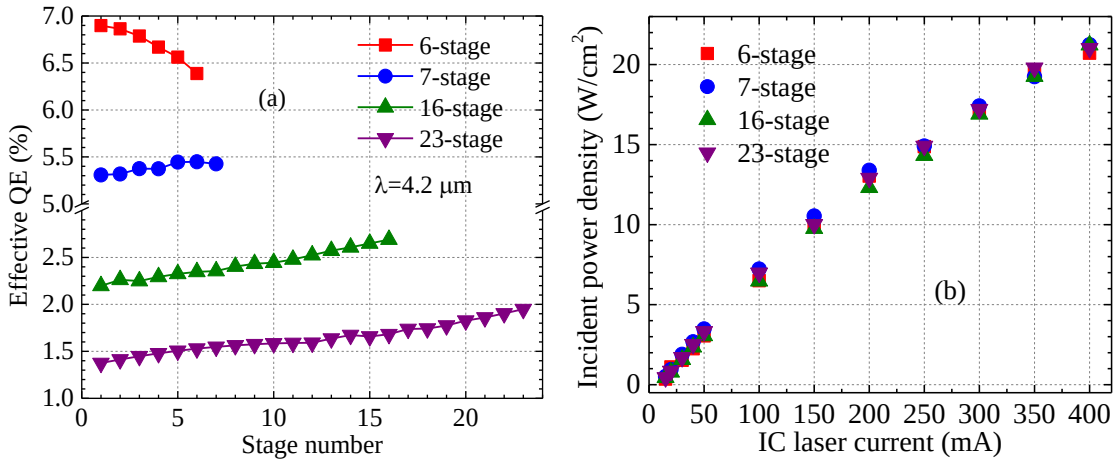

Figure 5-5: (a) Calculated effective quantum efficiency based on Equation 2-5 in each stage of the four devices, (b) Calculated incident power density vs IC laser current based on Equation 4-1 for the four devices.

The direct result of current mismatch in these multistage devices is the reduction of their photocurrents, which are decided by the stage with the minimum effective QE. From Figure 5-5(a), the photocurrent was determined by the last stage in the 6-stage device, while it was decided by the first stage in the 16- and 23-stage devices. This statement is tenable when the photocurrent is dominant in the device under intense illumination from the IC laser, which can be validated through the assessed incident power densities on the four

devices. A simple and effective method to assess P_{inc} is based on the relationship between J_{sc} and QE (at laser emission wavelength), as expressed by Equation 4-1. Note that, the QE in Equation 4-1 should be the minimum effective QE in the individual stages. According to this equation, the calculated P_{inc} as a function of the IC laser current is shown in Figure 5-5(b). As can be seen, the calculated values of P_{inc} onto the four devices are close to each other. This is anticipated since they were illuminated by the same IC laser, even with some possible experimental uncertainties due to alignment. The good consistency of the P_{inc} also validates the above-mentioned statement that there was no electrical gain in the four devices when they were illuminated by the IC laser. Based on this commonality, the effect of current (or effective quantum efficiency) mismatch between stages on device performance will be quantified in Subsection 5.5.2.

5.4.3 Collection efficiency of photogenerated carriers

As described in Chapter 4, a special feature of some ICTPV devices is that the photocurrent is voltage dependent. But this feature is likely to be less notable for devices with thinner individual absorbers and more stages. It would be interesting to examine this feature in the 16- and 23-stage devices which have even more stages and thinner individual absorbers. This can be done by comparison between the 100% collected and the measured *J-V* curves. At T=300 K and P_{inc}=17 W/cm^2, the 100% collected and the measured *J-V* curves for the four devices are shown in Figure 5-6(a). As mentioned in Chapter 4, the 100% collected *J-V* curve refers to the ideal case where the photogenerated carriers are completely collected. It can be plotted in the same manner as in [171] and is the superposition of the dark current density and the maximum photocurrent density J_{phmax}. The magnitude of J_{phmax} is the difference between the saturated current densities under dark

and illuminated conditions. As can be seen in Figure 5-6(a), there are noticeable shifts between the ideal and the measured *J-V* curves for the 6- and 7-stage devices. This means that the photocurrents (or the collection efficiencies) in the two devices are voltage dependent. In contrast, for the 16- and 23-stage devices, the ideal and the measured *J-V* curves almost overlap with each other. This indicates that the collection efficiencies in the two devices are close to unity as well as being voltage independent.

The collection efficiency η_c in the four devices can be extracted based on Equation 4-2 whose validity relies on two assumptions, as mentioned in Subsection 4.4.1. For each of the four devices, the *J-V* data at four different illumination levels were chosen for subtraction to make a fair comparison. It was found that, although not presented here, the extracted η_c using different *J-V* data pairs overlap each other. This verifies the assumption that the dark current density and collection efficiency remain almost unchanged at under different illumination levels. In particular, the extracted η_c based on Equation 4-2 using *J-V* data at incident power densities of 7 and 17 W/cm^2 is shown in Figure 5-6(b). As can be seen, the η_c in the 6- and 7-stage devices decreases dramatically with forward voltage. In contrast, the η_c is always close to unity in the 16- and 23-stage devices throughout the forward voltage range of interest. At this moment, this difference of η_c between ths two sets of devices is not fully understood. Presumably, one factor is that the photocurrent in the 16- and 23-stage devices is determined by the first stage [Figure 5-5(a)] with an absorber that is much thinner than the one in the last stage of the 6- and 7-stage devices. This factor along with more stages (to share forward voltage) could contribute to the nearly 100% collection efficiency in the 16- and 23-stage devices. This phenomenon may need further investigation in the future.

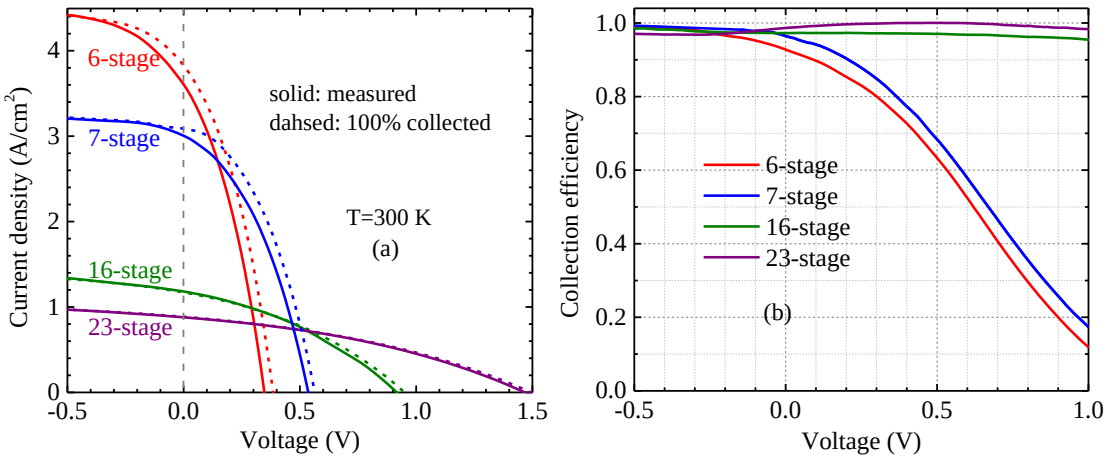

Figure 5-6: (a) The measured and the 100% collected *J-V* curves for the four devices at 300 K and at the incident power density of 17 W/cm^2, (b) Extracted collection efficiency at 300 K based on Equation 4-2 using *J-V* data under incident power densities of 7 and 17 W/cm^2 for the four devices.

5.5 Quantification of the effects of the performance limiting factors

5.5.1 Effect of collection efficiency

In the preceding section, the 16- and 23-stage devices are identified to have poor material quality and more severe current mismatch that that the 6- and 7-stage devices. On the other hand, the collection efficiency was higher in the 16- and 23-stage devices compared to the 6- and 7-stage devices. Table 5-3 summaries the three factors and characteristics, and some important performance-related parameters at 300 K. In this section, the effects of the three performance limiting factors will be quantified.

Table 5-3: Summary of device characteristics and some important performance-related parameters for the four devices at 300 K.

	E_g (meV)	n_i (cm^{-3})	g_{th} (cm^{-3}s^{-1})	R_{shunt} (Ω)	τ (ns)	L (μm)	η	Current mismatch	η_c-Voltage dependence
6-stage	221	1.21×10^{16}	6.6×10^{22}	10547	86	1.5	3.5%	mild	substantial
7-stage	234	9.9×10^{15}	4.3×10^{22}	21258	88	1.5	4.1%	none	substantial
16-stage	243	8.3×10^{15}	9.6×10^{23}	29294	28	0.7	2.7%	severe	insensitive
23-stage	248	7.6×10^{15}	7.9×10^{23}	63459	28	0.7	3.3%	severe	insensitive

Among the three factors, the effect of voltage dependent collection efficiency is simplest to quantify. This can be done through a comparison between the measured η and the ideally collected case, as shown in Figure 5-7. As shown, at the maximum incident power density, the η was 4.4% and 4.6% in the ideal case for the 6- and 7-stage devices, respectively. This corresponds to a 0.9% (6-stage) and 0.5% (7-stage) increase relative to the actual measured values. The more significant increase for the 6-stage device is due to the lower collection efficiency than in the 7-stage device. Also, the increase of η was less appreciable at the lower incident power density. This occurs because the operating voltage at the maximum output power was smaller at the lower incident power density. From Figure 5-6(b), the collection efficiency at the operating voltage is higher for the lower incident power density. For example, at P_{inc}=17 W/cm^2, the η was increased from the measured 3.1% and 3.7% to the ideal 3.8% and 4.1%, corresponding to a 0.7% and 0.4% increase for the 6- and 7-stage devices, respectively.

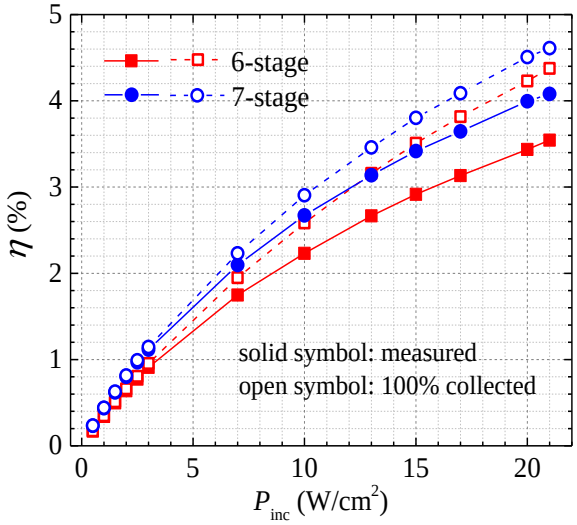

Figure 5-7: Comparison of the measured η and the ideal η in the 100% collected case at 300 K for the 6- and 7-stage devices.

5.5.2 Effect of current mismatch

As for the current mismatch, it is commonly recognized as a serious problem in PV arrays. For example, it can even cause localized heating of the cell and possible cell damage, which is known as hot-spot heating [195-196]. By comparison, although current mismatch between stages is significant in the 16- and 23-stage devices, but far from being able to cause any substantial damage or heating issues in a single stage when under intense illumination. The direct negative impact of current mismatch in ICTPV devices is the reduction of photocurrent. According to Equation 2-5, current mismatch in an IC structure can result from the deviation of either the absorption coefficient or diffusion length from the original reference values that were used to design current-matched absorbers. Comparatively, the deviation of α is more prone to occur in practice and has a greater impact on the calculated effective QE. Hence, here only the deviation of α will be considered. In addition, the voltage dependence of collection efficiency in the 6- and 7-stage devices should not be ignored. In this regard, the effect of current mismatch can be quantified by decoupling the photocurrent and dark current densities. Proceeding in this way, the illuminated *J-V* relation can be expressed as:

$$J\,(V) = J_{sc}\,\eta_c/\eta_c(0) - J_d(V) = P_{inc}QE\,\eta_c/\eta_c(0) - J_d(V) \qquad (5\text{-}1)$$

where η_c is shown in Figure 5-6(b) and $\eta_c\,(0)$ is the collection efficiency at zero voltage. As previously emphasized, the QE in Equation 5-1 should be the minimum effective QE in individual stages and can be calculated from Equation 2-5. For direct connection to actual devices, the J_d (V) in Equation 5-1 was replaced by the experimental data for the four devices. With these specifications, the effect of the deviation of α and consequential current mismatch will only be embodied in J_{sc} and QE in Equation 5-1.

The calculated J_{sc} and η as functions of α based on Equation 5-1 are shown in Figure 5-8. In the calculation, the incident power density was taken to be 17 W/cm^2, and the diffusion length was assumed to be 1.5 μm for the 6- and 7-stage devices and 0.7 μm for the 16- and 23-stage devices. The kinks in the calculated J_{sc} and η curves correspond to the condition where the effective QE is perfectly matched between stages. This occurs at an α of 2687 (6-stage), 2721 (7-stage), 2849 (16-stage) and 3061 cm^{-1} (23-stage). As can be seen in Figure 5-8, the J_{sc} and η of the 16- and 23-stage devices peak at the current-matched condition, while the J_{sc} and η in the 6- and 7-stage devices slightly increase when α passes the current-matched condition with further increases. This is because the total absorbers in the 6- and 7-stage devices are relatively thin so that the higher absorption coefficient will increase absorption of photons and enhance the photocurrent. In contrast, the total absorbers of the 16-and 23-stage devices are much thicker than the 6- and 7-stage devices, so the light attenuation (and thus the current-mismatch) is more dominant in the optically deeper stages. The circles in Figure 5-8 represent the calculated J_{sc} and η with the measured α. As can be seen, the 16- and 23-stage devices depart far more from the current-matched condition than the 6- and 7-stage devices. At the current-matched condition, the calculated η is 3.0%, 3.9%, 3.4% and 4.5% for the 6-, 7-, 16- and 23-stage devices, respectively. This corresponds to a difference of 0.1% (6-stage), 0.2% (7-stage), 1.0% (16-stage) and 1.7% (23-stage) compared to the actual measured η. The impact of current mismatch is comparable at different incident power densities. For example, at P_{inc}=21 W/cm^2, the calculated η at the current-matched condition is 3.43%, 4.29%, 3.85%, 5.08%, corresponding to a difference of 0.11%, 0.21%, 1.1%, 1.84% compared to the actual obtained η for the 6-, 7-, 16- and 23-stage devices, respectively.

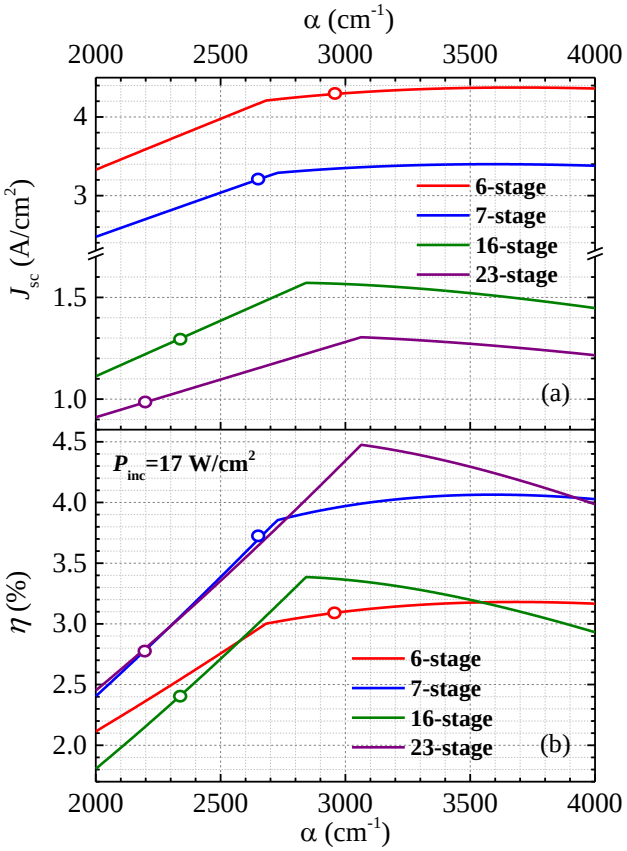

Figure 5-8: Calculated (a) short-circuit current density and (b) conversion efficiency based on Equation 5-1 as a function of absorption coefficient at incident power density of 17 W/cm^2 for the four devices.

5.5.3 Effect of material quality

Lastly, regarding the effect of material quality, it can be quantified through the variation of carrier lifetime τ, an important parameter for material quality. The variation of τ brings corresponding variations of thermal generation and dark saturation current density [197], which can significantly affect the fill factor and open-circuit voltage [197], consequently making a substantial impact on conversion efficiency. The effect of material quality can be evaluated based on a diffusion limited model as described in detail in Chapter 3. In this model, the *J-V* characteristic of the device is given by Equation 3-10. Based on Equation 3-10, the calculated conversion efficiency as well as the measurement are shown in Figure

5-9. In the calculation, the carrier lifetime was assumed to be 28 and 87 ns, close to the extracted values shown in Table 5-3. As can be seen, the calculated η using the extracted carrier lifetime was higher than the measured value for all the four devices. This is mainly because the extracted lifetime was somewhat overestimated due to the occurrence of the SRH process. For the 6- and 7-stage devices, this is also due to the voltage dependence of collection efficiency that was instead ignored in the calculation. Nevertheless, the calculations based on Equation 2-5 evidently indicate the considerable impact of carrier lifetime on device performance. As shown in Figure 5-9, there is a distinct gap between the calculated conversion efficiencies with different values of carrier lifetime. For example, for τ=28 ns and P_{inc}=17 W/cm^2, the calculated η was 2.2% (6-stage), 2.6% (7-stage), 3.1% (16-stage) and 3.3% (23-stage). However, as the carrier lifetime increased to 87 ns, the calculated η at the same P_{inc} was 4.1%, 4.6%, 5.3% and 5.4% for the 6-, 7-, 16- and 23-stage devices, respectively. This corresponds to an efficiency increase of 1.9% (6-stage), 2.0% (7-stage), 2.2% (16-stage) and 2.1% (23-stage). Clearly, this increase is much more significant than those due to the eliminations of voltage-dependent collection efficiency and current mismatch. Therefore, the material quality plays the most important role among the three factors. If carrier lifetime is kept the same, the η is higher in the 16- and 23-stage devices than in the 6- and 7-stage devices, even though the current mismatch is more significant in the 16- and 23-stage devices. In this respect, given comparable material quality, ICTPV devices with more stages and thinner absorbers are advantageous, consistent with previous experimental results [157, 182, 186-188]. When the current mismatch is minimized, ICTPV devices will have further conversion efficiency with more stages.

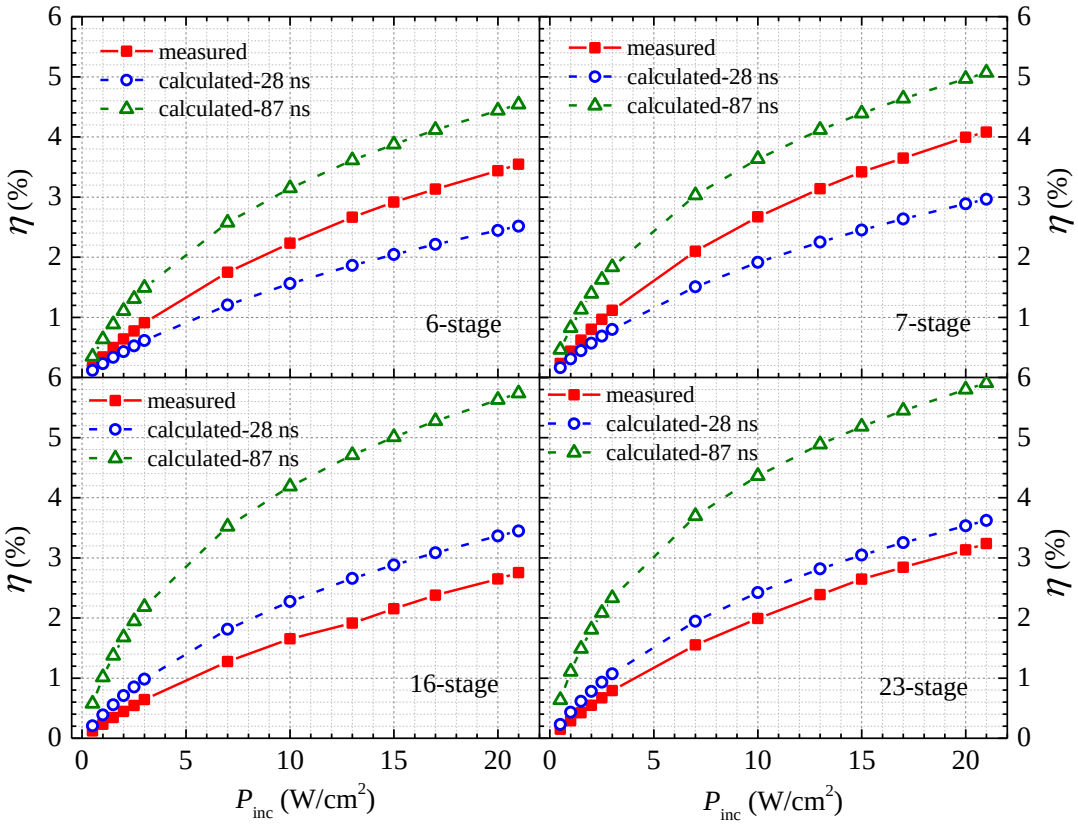

Figure 5-9: Calculated conversion efficiency based on Equation 3-10, along with measurement for the four devices. For each of the four devices, the carrier lifetime used in the calculation was 27 and 87 ns.

5.6 Summary and concluding remarks

This chapter deals with detailed characterization and performance analysis of two sets of four narrow bandgap (~0.22-0.25 eV at 300 K) ICTPV devices. The four ICTPV devices have increased number of stages compared to the three devices in Chapter 4. With different numbers of stages and individual absorber thicknesses, it was shown that current mismatch between stages could be significant with more stages due to the variation of absorption coefficient. On the other hand, the collection efficiency of photogenerated carriers can be much improved with thinner individual absorbers and more stages. Also, the carrier lifetime was extracted from dark current density to evaluate the material quality.

The extracted shorter carrier lifetime, together with substantial current mismatch, explains the lower conversion efficiencies in the 16- and 23-stage devices compared to that in the 6- and 7-stage devices. Furthermore, the effects of material quality, current mismatch and collection efficiency on device performance are quantified. The quantitative analysis shows that the material quality has the most significant impact on the device performance among the three factors. This indicates the importance of good material quality and its consistency for realizing efficient IC TPV devices. This conclusion also challenges the inference put forward in Section 5.1 as more cascade stages may not succeed to improve device performance if the material quality is poor.

Chapter 6: Carrier lifetime in mid wavelength interband cascade devices

6.1 Introduction

Starting from this chapter, experimental studies of IC structure for infrared detector will be presented. The operation principle and theoretical background of IC infrared photodetectors (ICIPs) are reviewed in Chapter 2. Specifically, the noise reduction and detectivity enhancement in multistage detectors compared to single-absorber detectors are detailed in Chapter 2. These advantages enable ICIPs to operate at high temperatures with decent detectivity, as has been manifested in experiment [99, 137, 151, 199]. Nevertheless, at the current stage, ICIPs does not outperform the state-of-art HgCdTe detectors in the MWIR regime. For example, at 300 K, the detectivity of an ICIP with a cutoff wavelength of 4.3 μm is close to 1×10^9 Jones [151], slightly lower than the claimed $\geq 3.0\times10^9$ Jones for an uncooled photovoltaic HgCdTe detector with similar cutoff wavelength (~4 μm) [91]. This is partially because the carrier lifetime in InAs/GaSb T2SLs is lower than in the HgCdTe materials, although the Auger reduction is theoretically projected to be suppressed in T2SLs [128-130]. For example, the reported lifetimes are 30-100 ns in MWIR T2SLs [200-203], and 10-55 ns for LWIR T2SLs [192-193, 201, 204], which are mainly limited by SRH recombination. Speculatively, the origin of the recombination centers is ascribed to the presence of gallium, as the gallium-free InAs/InAsSb SLs possess much longer radiative-dominated lifetimes (e.g. >400 ns or 9 μs at 77 K) [166-167]. Because of the shorter lifetime, the dark current densities in InAs/Ga(In)Sb T2SLs detectors are generally higher than the benchmark known as “Rule 07” [205] for MCT materials.

In this chapter, a simple and effective electrical method is developed to the extract

carrier lifetime in InAs/GaSb T2SLs. This method differs from the frequently used optical methods based on time- or frequency-domain photoluminescence (PL) measurements [192, 200-201, 204]. These optical methods are mainly focused on low temperatures (<200 K), while the developed method can extract lifetime in a wide range of temperature, especially at high temperatures (e.g. 300 K and above). There have been a few studies on carrier lifetime using different approaches, such as measuring photoconductive response and modeling dark current characteristics of T2SL detectors [206-209]. However, as with the optical methods, these approaches fail to work at high temperatures. Sometimes, a more meaningful carrier lifetime that is different from the recombination lifetime needs to be realized and extracted. For example, for a photodiode that is operated under a reverse bias, the generation lifetime is more relevant to the device performance and could be far longer than the recombination lifetime, depending on the defect energy level as discussed for Si-based devices [210]. In practical devices, carrier lifetime is often a mixture of various mechanisms (See Figure 6-1), which are challenging to separate.

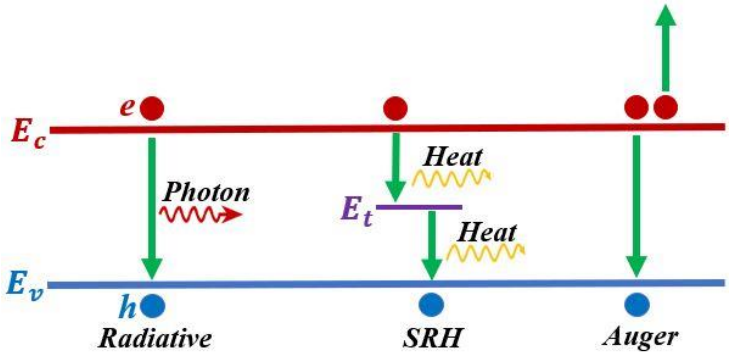

Figure 6-1: Radiative and non-radiative recombination processes in semiconductors.

The carrier lifetime in IC devices (QCDs) is lower than MCT materials. However, compared to the other cascade device family ─ quantum cascade (QC) devices, it can be much longer. QC devices (QCDs) operate based on intersubband transitions within the

same band (e.g. the conduction band). This contrasts to IC devices (ICDs) that are based on the interband transitions between the conduction and valence band. This fundamental difference in carrier transport results in distinct carrier lifetimes and device performances, especially at high temperatures. For example, the lifetime in QCDs is in the picosecond range due to fast phonon scattering, while ICDs have a nanosecond lifetime scale due to Auger and SRH recombination. Like IC devices, QC family include QC lasers and QC detectors. Although QC structures were also proposed and simulated theoretically for PV cells [211-212], none have been reported experimentally. The two families of devices are both based on quantum-engineered layer structures, and they nearly went through a parallel rapid evolution, especially in lasers [70-73]. However, they were often discussed and presented separately but seldom compared with their counterparts. There is particularly no evaluation or comparison based on a unified figure of merit to fairly describe their characteristics with different device functionalities. In this chapter, the saturation current density J_0 is identified as the common figure of merit. A semi-empirical model is employed to extract the J_0 from many QCDs and ICDs published in literature and some of unpublished ICDs.

6.2 Carrier lifetime in mid-wavelength ICIPs

6.2.1 Device structure, growth and fabrication

The seven devices presented in this section have ICIP structures with different numbers of stages (N_c) and absorber thicknesses. They were grown using a GENxplor MBE system on nominally undoped *p*-type GaSb (001) substrates. Table 6-1 presents the individual absorber thicknesses of the seven ICIPs in order from the surface to substrate. For

convenience, they are denoted as 1S-1040, 1S-2340, M3S-312, M6S-312, N8S-312, M12S-156 and N16S-156, where "M" and "N" stand for current-matched and noncurrent-matched configurations, respectively. As mentioned in Chapter 2, the individual absorbers in current-matched ICIPs are designed thicker in the optically deeper stages to ensure equal photocurrent in each stage. In contrast, the individual absorber thicknesses in a non-current-matched ICIP are made identical. For the current-matched ICIPs studied in the section, the individual absorber thicknesses were designed based on the absorption coefficient of 3000 cm^{-1} and the assumption of complete collection of photogenerated carriers. 1S-1040, 1S-2340, M3S-312, M6S-312 and N8S-312 were grown earlier as descried in [151], while M12S-156 and N16S-156 were grown in a later growth campaign (just after system maintenance) with possibly varied conditions and material qualities. The seven detectors have identical electron and hole barriers as described in [151]. The absorbers in the seven detectors consist of InAs/GaSb/Al(In)Sb/GaSb *M*-shape SLs [104, 134-135] with layer thicknesses of 27/15/815 Å, respectively. The GaSb layers in the SLs were *p*-type doped to 5.1×10^{16} cm^{-3} for all the seven detector structures. The average doping concentration in the SLs is estimated to be 2.4×10^{16} cm^{-3} according to the ratio of the GaSb thickness over the SL period. Upon this doping level, the carrier transport in the absorbers is expected to be determined by the dynamics of minority electrons. The bandgap of the absorbers was designed with a cutoff wavelength (λ_c) near 4.3 μm at 300 K, which closely matched the observed 100% cutoff wavelengths for devices made from the seven wafers, implying good control of layer thicknesses and alloy compositions during MBE growth.

The important design and material parameters such as surface defect density and perpendicular (⊥) lattice mismatch of the seven wafers are summarized in Table 6-1. After the MBE growth, the wafers were processed into square mesa devices with dimensions from 50 to 1000 μm using standard contact UV photolithography followed by wet-chemical etching. A two-layer passivation (Si_3N_4 then SiO_2) was RF sputter deposited to improve overall stress management and minimize pin holes. Sputter deposited Ti/Au layers provided top and bottom contacts. Finally, the devices were mounted on heat sinks and wire bonded for characterization.

Table 6-1: Summary of the design and material parameters of the seven wafers.

Wafer	Absorber thickness (nm)	# of stage	d_{total} (μm)	Doping (cm^3)	λ_c (μm)	Defect (cm^{-2})	Lattice mismatch
1S-1040	1040	1	1. 04	2.4×10^{16}	4.4	6.0×10^{3}	-0.09%
1S-2340	2340	1	2.34	2.4×10^{16}	4.4	5.0×10^{4}	~0
M3S-312	312/344.5/383.5	3	1.04	2.4×10^{16}	4.3	2.0×10^{4}	-0.027%
M6S-312	312/344.5/383.5/435.5/507/604.5	6	2.59	2.4×10^{16}	4.3	2.0×10^{4}	-0.10%
N8S-312	312×8	8	2.50	2.4×10^{16}	4.3	5.0×10^{4}	-0.08%
M12S-156	156/169/182/195/208/227.5/247/273/299/331.5/370.5/422.5	12	3.08	2.4×10^{16}	4.3	4.4×10^{4}	0.051%
N16S-156	156×16	16	2.49	2.4×10^{16}	4.3	4.3×10^{4}	0.065%

6.2.2 Dark current density

The dark current density-voltage (J_d-V) characteristics of the seven ICIPs were measured at various temperatures. Figure 6-2 (a) and (b) shows the measured J_d at 250 and 300 K for the representative 400×400 (1S-1040 and 1S-2340) and 500×500 (other five wafers) μm^2 devices made from the seven wafers. As shown, at reverse voltage, the seven

devices in the ascending order of J_d are N16S-156, M12S-156, N8S-312, M6S-312, M3S-312, 1S-1040 and 1S-2340. This sequence is precisely in the descending order of number of stages or increasing order of absorber thickness. This is because ICIPs with more stages and thinner individual absorbers are better able to suppress the dark current. Given carrier transport is diffusion limited, according to Equation 2-6 and 2-7, the dark current density in the m_{th} stage of an ICIP can be written as:

$$J_{d,m} = eg_{th}Ltanh(d_m/L)(e^{eV_m/k_bT} - 1) \quad (6\text{-}1)$$

where V_m is the applied voltage across the m_{th} stage and d_m is the individual absorber thickness of the m_{th} stage. Here, the parasitic series resistance R_s and shunt resistance R_{shunt} are ignored. The voltage drop across each stage equates V/N_c in a noncurrent-matched ICIP with identical absorbers. However, in a current-matched ICIP, to ensure dark current continuity, the V_m will be smaller in an optically deeper stage with a thicker individual absorber. Based on Equation 6-1, given a similar cutoff wavelength and minority carrier lifetime, the dark current density at the same voltage will be lower in ICIPs with more stages and thinner individual absorbers. This essentially agrees with the measured J_d-V characteristics of the seven ICIPs as shown in Figure 6-2 (a) and (b).

However, at large reverse voltage where all the carriers are swept out from the absorbers [213-214], a more appropriate equation for dark current density is given by:

$$J_d = eg_{th}d_1 + \frac{V - J_d R_s A}{R_{shunt} A} \quad (6\text{-}2)$$

Because the cascade stages are connected in series, the dark current density is decided by the stage with the thinnest individual absorber (i.e. the first stage). The second term on the right side of Equation 6-2 represents the average leakage current density with a constant shunt resistance. Hence, from Equation 6-2, there is a liner relationship between current

density and voltage at large reverse voltage, which forms the important basis to extract thermal generation rate and carrier lifetime.

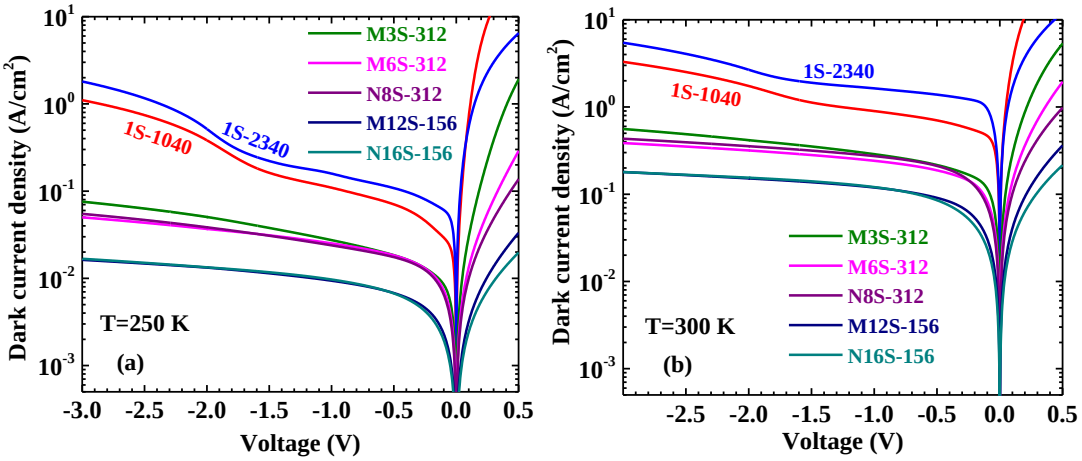

Figure 6-2: Dark current density versus applied voltage for the seven devices at (a) 250 K and (b) 300 K.

6.2.3 Contribution of SRH process to dark current

When carrier transport is affected by the SRH process, the description based on Equation 6-1 is prone to errors. In contrast, Equation 6-2 can account for combined effects of various mechanisms. Inclusion of Auger and SRH mechanisms gives a thermal generation rate that is expressed as [213-214]:

$$g_{th} = \frac{n_i^2}{N_a \tau_A} + \frac{n_i^2}{(N_a + n_i)\tau_{SRH}} = \frac{n_i^2}{N_a \tau} \qquad \text{(6-3 a)}$$

$$\frac{1}{\tau} = \frac{1}{\tau_A} + \frac{N_a}{(N_a + n_i)} \frac{1}{\tau_{SRH}} \approx \frac{1}{\tau_A} + \frac{1}{\tau_{SRH}} \qquad \text{(6-3 b)}$$

where τ_A represents the carrier lifetime due to the Auger mechanism and τ_{SRH} is the SRH carrier lifetime. The approximation made in Equation 6-3(b) is valid if the doping concentration N_a is much higher than the intrinsic carrier concentration n_i. Therefore, one can first extract g_{th} from Equation 6-2 and then calculate the carrier lifetime τ from

Equation 6-3, which covers various transport mechanisms and is more accurate than Equation 6-1.

The contribution of SRH process in the seven devices can be indirectly assessed by the activation energy E_a. Based on the temperature dependence of R_0A [See Figure 6-3(a)], the E_a in a temperature range of 200-340 K was 256, 252, 258, 254, 249, 256, 253 meV for 1S-1040, 1S-2340, M3S-312, M6S-312, N8S-312, M12S-156 and N16S-156, respectively. These values of E_a were smaller than their bandgaps (~288 meV) at room temperature and about 75% of the zero-temperature bandgap $E_g(0)$ (~329 meV). This means that the SRH processes were involved in the carrier transport besides the diffusion process [215]. The bandgaps of the seven devices were estimated from the 100% cutoff wavelengths in their responsivity spectra, which were very close at every temperature of interest and two were presented in [151]. Particularly, the temperature dependence of the bandgap for M3S-312, as well as the Varshni fitting, are presented in Figure 6-3(b).

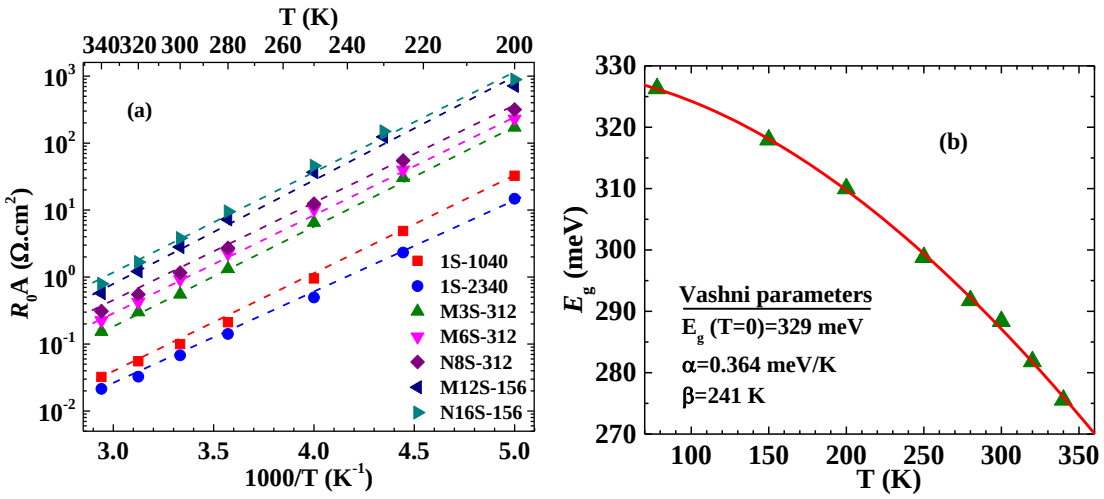

Figure 6-3: (a) R_0A of the seven devices in the temperature range of 200-340 K. (b) Temperature dependence of bandgap for M3S-312. The fitting Varshni parameters for the device are shown.

6.2.4 Linear fitting of dark current density

Since the carrier transport is affected by the SRH process, Equation 6-2 is preferably used to extract g_{th} for the seven devices at higher temperatures, which is simpler with assuming constant parasitic resistances. The feasibility and validity of constant parasitic resistances are supported by the observed linear relationship of current density with voltage as shown in Figure 6-4. There are obvious linear regions of J_d for the five multi-stage devices at large reverse bias starting from -1.5 V. This behavior was also observed at other higher temperatures for the five devices. For the two single-stage devices, their current density-voltage curves exhibited linear characteristics between about -1.5 and -0.3 V as well. However, the current density increased sharply with reverse bias voltage after -1.5 V, which was likely triggered by a substantial electric field in the absorber region and the consequential tunneling of carriers through the bandgap. This is because the entire voltage is applied exclusively on the single stage, while the multistage ICIPs have multiple unipolar barriers to share and withstand the voltage. In this sense, this method of extracting the thermal generation rate is particularly well suited for multistage ICIPs where the linearity can be ensured in a wide range of reverse voltage.

Based on Equation 6-2, the thermal generation rate for the seven devices can be extracted by linearly fitting the dark current density at larger reverse voltages with the rearranged equation:

$$J_d = \left(-eg_{th}d_1 + \frac{V}{R_{shunt}A}\right)/\left(1 + \frac{R_s}{R_{shunt}}\right) \quad (6\text{-}4)$$

The lines that were linearly fit to the experimental data for the seven devices at 300 K are shown in Figure 6-4. The linear fits were performed between -3 and -1.5 V for the five multistage devices for good accuracy. By comparison, the linear fits for the two single-

stage devices were done in the voltage range of -1.5 to -0.3 V to circumvent the effect of substantial tunneling of carriers as previously mentioned.

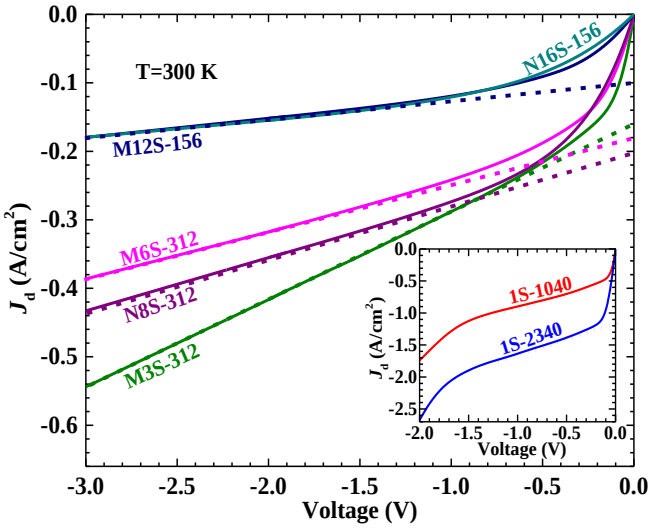

Figure 6-4: Linear fitting (dashed) and experimental measurements (solid) of the dark current density at reverse bias voltage for the five multistage devices at 300 K. The inset shows the corresponding results of the two single-stage devices at 300 K.

6.2.5 Estimated thermal generation rate and carrier lifetime

Based on Equation 6-4, the thermal generation rate at 300 K found from the intercept of the fitted line with the vertical axis was 3.1×10^{22} (1S-1040), 3.2×10^{22} (1S-2340), 3.2×10^{22} (M3S-312), 3.6×10^{22} (M6S-312) and 4.0×10^{22} cm^{-3}/s (N8S-312, M12S-156 and N16S-156). Simultaneously, the shunt resistance obtained from slope of a fitted curve was 1449, 1192, 3338, 5639, 5054, 13343 and 13361 Ω for 1S-1040, 1S-2340, M3S-312, M6S-312, N8S-312, M12S-156 and N16S-156, respectively. The R_s was extracted from the differential resistance at large forward voltage, and was less than 10 Ω at 300 K. Since R_s was at least two orders of magnitude smaller than R_{shunt}, the term R_s/R_{shunt} in Equation 6-4 can be ignored when extracting the thermal generation rate in the seven devices.

With the extracted g_{th}, the minority carrier lifetime can then be calculated from Equation 6-3 in which the intrinsic carrier concentration is given by Equation 4-4. At 300 K, the calculated electron and hole effective masses of the T2SLs using a two-band $k \cdot p$ model were $0.049m_0$ and $0.48m_0$, respectively. Note that the electron effective mass scales linearly with the temperature-dependent bandgap according to Kane's model [216]. At 300 K, the calculated intrinsic carrier concentration was 4.1×10^{15} cm^{-3}, one order of magnitude lower than the doping concentration in the absorbers. At a lower temperature (e.g. 200 K), the calculated n_i was 7.8×10^{13} cm^{-3} and the Fermi energy E_F was 4.5 k_bT higher than the valence band edge E_v, implying that Equation 4-4 was still valid for the seven devices. Hence, the extraction of carrier lifetime was carried out at 200-340 K.

Based on Equation 4-4 and 6-3, along with the extracted thermal generation rate, the minority carrier lifetime at 300 K was estimated to be 22.9 (1S-1040), 22.1 (1S-2340), 22.3 (M3S-312) 19.7 (M6S-312), 17.8 (N8S-312), 17.8 (M12S-156) and 17.8 ns (N16S-156). In the same manner with 300 K, the carrier lifetimes and thermal generation rates at other higher temperatures were also obtaine as shown in Figure 6-5. For the seven devices at 200-340 K, the extracted τ was ranges between 167 and 8.5 ns depending on the material quality, and monotonically decreased with increasing temperature. For example, compared to M12S-312 and N16S-312 (which were grown later in a different growth campaign), the longer τ in M3S- is due to the better material and crystal structure quality (Table 6-1). For the same reason, the lifetime of 1S-1040 was longer than that of 1S-2340. Also, the extracted carrier lifetimes were similar between the two single-stage devices and the five multistage devices. This supports the validity and feasibility of the developed method for non-cascade photodetectors. At temperatures higher than 200 K, the extracted carrier

lifetime was somehow shorter than the values (of 135-108 ns between 200 and 300 K) that were stated in [217] for T2SL ICIPs (with a cutoff wavelength near 5 μm) based on the fitting of the J_d-V curve to an equation similar to Equation 6-1. Also, the carrier lifetimes exhibited a rapid decrease with increasing temperature, which was close to an exponential relationship especially in the temperature range of 250-340 K. For instance, for M6S-312, the carrier lifetime decreased from 132 ns to 10.6 ns while the temperature was increased from 200 to 340 K. This dependence of lifetime on temperature was quite different from the previous results obtained by optical and other electrical methods [192-193, 208], which follow a $T^{-1/2}$ law determined by the SRH mechanism [218]. Analogous to R_0A, an effective "activation energy" of ~150 meV was extracted for the seven devices at 250-340 K, confirming an exponential relationship with inverse temperature (1/T). The sharp decrease of the carrier lifetime with increasing temperature can be attributed to the growing dominance of the Auger processes associated with the bandgap narrowing of the SL absorber at high temperatures. The similar effect of Auger process has been analyzed by others for InAs/InAsSb T2SLs [219-220]. Overall, the developed method to extract carrier lifetime include contributions from various transport mechanisms such as Auger and SRH processes as indicated in Equation 6-3, which should be effective in broader contexts and closer to actual devices.

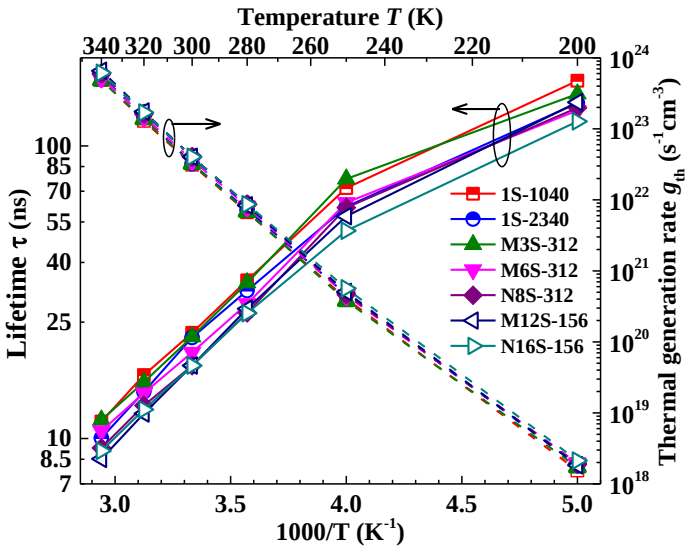

Figure 6-5: The thermal generation rate and minority carrier lifetime for the five multistage and two single-stage devices at high temperatures.

6.3 Interband cascade devices vs quantum cascade devices

6.3.1 Device structures

As estimated in the preceding section, the lifetime in IC devices (ICDs) has a tens of nanosecond timescale at 300 K. This should be much longer than the intersubband transitions occurring on a time scale of picosecond in QC devices (QCDs). It is generally known that the relatively much longer carrier lifetime in ICDs has resulted in a significantly lower threshold current density (J_{th}) and power consumption in ICLs at room temperature (RT) compared to in QCLs. This has been demonstrated for a wide IR spectral region (2.7-6 μm) [73, 221]. Since the lasers normally operate under forward bias, the *J*-*V* characteristics under reverse bias for extracting J_0 are not readily available for QCLs. Hence, the analysis of QCDs is mainly concentrated on RT QC detectors reported in the literature [83-84, 96, 222-224]. Some ICDs included here are IC laser structures that were reported previously [115, 120, 179, 225-226], while the others are IC light emitting devices

(LEDs). The active regions of all these ICDs consist of an asymmetric "W" quantum well (QW) [227] with two InAs electron QW layers on both sides of the GaInSb hole QW layer. The ICDs have numbers of cascade stages (N_c) ranging from 6 to 15. Besides, ICDs with InAs/Ga(In)Sb T2SL absorbers that were designed as detectors and TPV cells are also included here [137, 151, 159, 199, 228-231]. They will be denoted by "ICD_SL" to differentiate from those having QWs in the active regions. Most of the ICDs were processed into square mesa type devices as well as several broad area IC lasers.

6.3.2 Semi-empirical model for dark current density

In cascade devices, there is a potential barrier region formed between two ends of adjacent cascade stages, since the electronic states near the two ends lie at a low energy level on one end and a high energy level on the other. If a forward bias (positive on the high energy end) is applied to a cascade stage, the number of available carriers being able to overcome the potential barrier from the low energy end to the high energy end is increased exponentially with the bias voltage. Consequently, the forward current density will have an exponential increase with the bias voltage. Conversely, at reverse voltage, the current density approximates to a constant (J_0) value since the number of carriers that can move from the high energy end does not increase with the reverse bias voltage. Hence, semi-empirically, the current density-voltage (J_d-V) characteristic in a cascade device with identical stages can be described by:

$$J_d\ (V) = J_0\left(e^{qV/N_c k_b T} - 1\right) \tag{6-5}$$

Qualitatively, this expression resembles the standard diode equation for a p-n junction. Equation 6-5 can be derived from a fundamental level with lengthy mathematical

manipulations, as described in detail in [141] for ICDs and in [232-234] for QCDs. The approach offered here grasps the main feature in cascade devices and offers a simple way to derive Equation 6-5 for current-voltage characteristics in complicated cascade structures. This approach has not been documented before should be beneficial in helping promote a better understanding of complex cascade devices.

It has been shown that the value of J_0 is proportional to the carrier concentration and inversely proportional to carrier lifetime that can be affected by various scattering mechanisms such as defects, doping, phonons and Auger recombination. This relationship has been explored to extracted carrier lifetime in ICIPs as described in the preceding section. From Equation 6-5, the R_0A of a cascade device can be obtained as:

$$R_0 A = \frac{N_c k_b T}{q J_0} \tag{6-6}$$

In theory, the values of J_0 for ICDs and QCDs can be extracted by fitting the measured J_d-V curves to Equation 6-5. However, in an actual device, the parasitic series and shunt resistance (R_s and R_{shunt}) are often presented. Considering these factors, the J_d-V curve of a cascade device should be fitted to a modified equation:

$$J_d\,(V) = J_0\left(e^{q(V-R_s A J_d)/N_c k_b T} - 1\right) + \frac{V - R_s A J_d}{R_{shunt} A} \tag{6-7}$$

6.3.3 Saturation current densities for cascade devices

From Equation 6-7, the three parameters, J_0, R_{shunt} and R_s, can be extracted through the least-square fitting method. In the fits, the values of R_{shunt} and R_s were kept in the range of 10^3-10^4 and 1-10 Ω, respectively. As an example, Figure 6-6 shows the measured J_d-V curves and fitting results for a large area (400 μm×400 μm) eight-stage ICD (wafer R083) [115] and a fifty-stage QCD (110 μm×110 μm) [96] at 300 K. The two devices have the

identical transition energy ΔE of 0.23 eV in the active region at 300 K, which was the bandgap for the ICD or the energy separation of the two involved conduction subbands for the QCD. As shown in Figure 6-6, the magnitude of J_d is at least an order of magnitude lower in the ICD than in the QCD. This difference is ascribed to the comparatively much longer carrier lifetimes in the ICD. Also, the least-square fittings based on Equation 6-7 were in excellent agreement with measurements, supporting the validity of the semi-empirical model. Specifically, the extracted J_0 (R_{shunt}) obtained from the fitting procedure is 0.017 A/cm^2 (5945 Ω) and 1.8 A/cm^2 (6772 Ω) for the eight-stage ICD and fifty-stage QCD, respectively. The other fitting parameter R_s is 5 Ω for the ICD, and 7 Ω for the QCD with a smaller device area.

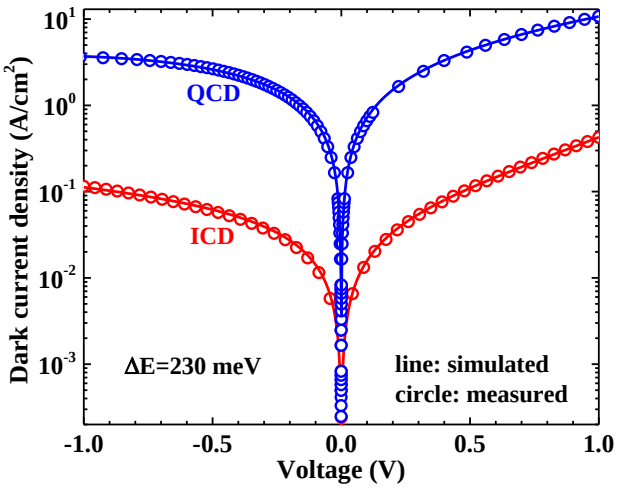

Figure 6-6: The measured and fitted J_d-V curves for an 8-stage ICD and a 50-stage QCD at 300 K. The ICD and QCD were mentioned in [115] (wafer R083) and [96], respectively.

Aside from the two devices, the least-square fitting was also performed for other ICDs [83-84, 96, 222-224] and QCDs [115, 120, 179, 225-226]. The extracted values of J_0 at 300 K for these ICDs and QCDs are presented in Figure 6-7. As can be seen, the value of J_0 is more than one order of magnitude lower in ICDs than in QCDs with similar ΔE.

This distinction of extracted J_0 implies the significant effect of carrier lifetime on transport current, consistent with threshold behavior in laser performance for a wide infrared spectral region mentioned earlier. Also, Figure 6-6 shows that J_0 tends to increase exponentially with decreasing ΔE for both ICDs and QCDs. It should be commented that ICDs are more susceptible to surface leakage currents due to the existence of surface states in their bandgap. Hence the extracted J_0 in Figure 6-7 might be more overestimated for ICDs than for QCDs. Since there is considerable variation in device area, the product of resistance and area is a more appropriate quantity as used effectively in Equation 6-7. In general, the value of $R_{shunt}A$ extracted from fitting is smaller for QCDs compared to ICDs. However, the ratio of $R_{shunt}A$ to R_0A is generally higher in QCDs than in ICDs, which suggests the relatively lower percentage of surface leakage in QCDs than in ICDs. Moreover, the material qualities and fabrication technologies may differ greatly between different groups

Overall, the extracted values of J_0 are much lower in ICDs than in QCDs. This not only manifests substantial difference of threshold current density in lasers between the two families, but also yields considerable differences in detector and PV device performance as will be discussed later. The vast gap of J_0 between ICDs and QCDs is fundamentally attributed to their distinctive carrier lifetimes since J_0 is inversely proportional to the lifetime. In ICDs, Auger and SRH (through defects) processes are the main scattering mechanisms. In QCDs, longitudinal optical (LO) phonon scattering prevails and is fast (in ps or shorter) between and within the conduction subbands. With interband transitions, the carrier lifetime is in the nanosecond range, about three orders of magnitude slower than for phonon scattering. The extracted J_0 is much lower in ICDs than in QCDs, which unambiguously proves the much longer lifetime in ICDs than QCDs.

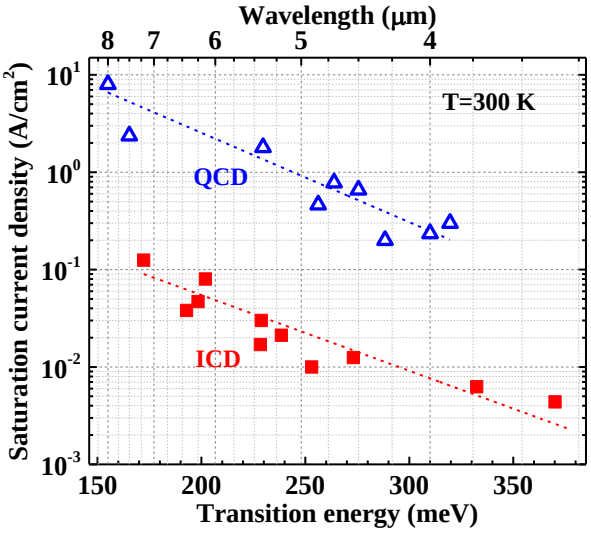

Figure 6-7: The extracted values of J_0 for ICDs and QCDs at 300 K. Some ICDs have been described previously in [83-84, 96, 222-224], while others are from our unpublished studies. The QCDs are from [115, 120, 179, 225-226].

6.3.4 Effect of J_0 on the performances of detectors

The saturation current density J_0 is a measure of Johnson noise in a photodetector. The R_0A contained in Equation 6-6 is also reflected in the specific detectivity D^*. As described in Subsection 1.3.4, D^* is essentially a measure of signal to noise ratio ─ the most important figure of merit for photovoltaic photodetectors operating at zero bias. The expression of D^* is given by Equation 1-8 where R_i is the responsivity. Figure 6-8(a) shows the measured peak R_i for ICDs and QCDs at 300 K. In addition to some of the ICDs presented in Figure 6-7, another two ICDs (devices A and B) [136] and ICD_SLs from [137, 151, 199, 229-231] are also included in Figure 6-8 (a) and (b). As shown in Figure 6-8(a), the peak R_i is generally higher in ICDs than in QCDs and is especially high in ICD_SLs with enhanced absorption in SL absorbers. The lower R_i in QCDs is partly because of the low escape probability that is proportional to the carrier lifetime [65, 83] for QCDs, while this value is close to unity for ICDs with the much longer lifetime [99].

Another factor might be the polarization selection rule for intersubband transitions in conduction band QWs [65, 79], which prohibits the absorption of normal incident light in QCDs. This problem in QCDs is typically mitigated by making facets made by polishing at an angle of 45^{o} to the growth direction. In addition, an improved responsivity can be achieved for intersubband photodetectors by using a photonic metamaterial to enhance the light-matter interaction. This was demonstrated in a QWIP detector with photoconductive gain near 9 μm at RT [236]. in which the responsivity (~0.2 A/W) is comparable to those in ICD_SLs as shown in Figure 6-8(a). However, due to substantial noise with a high dark current density, its detectivity D^* (~2.8×10^7 Jones) is about one order of magnitude lower than that in ICD_SLs with similar ΔE as shown in Figure 6-7(b).

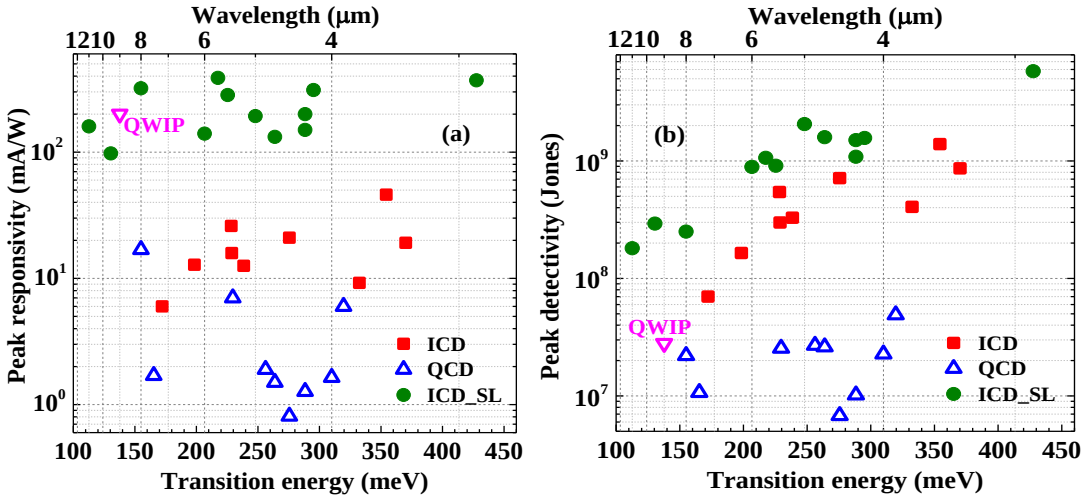

Figure 6-8: Measured peak (a) responsivities and (b) detectivities for ICDs, ICD_SLs and QCDs at 300 K. In addition to some of the ICDs presented in Figure 6-6, two ICDs (devices A and B) [136] and all ICD_SLs from [137, 151, 199, 229-231] are included. One QWIP is from [236].

From Equation 1-8 and 6-6, the John-noise limited D^* is inversely proportional to the square root of J_0. Figure 6-8(b) shows the measured peak D^* values at 300 K for the considered ICDs and QCDs. As can be seen, the values of D^* are almost one order of magnitude higher for ICDs than for QCDs. At 300 K, the achieved D^* in most QCDs is less

than 3×10^7 Jones mainly because of a high J_0, while most D^* values for ICDs are higher than 1×10^8 Jones and some even exceed 1×10^9 Jones. Also, the difference of D^* between ICDs and QCDs is more significant than the difference in R_i between the two families. This arises from more than one order of magnitude lower J_o in ICDs than in QCDs, although the number of cascade stages N_c (<15) in ICDs is less than in QCDs (≥30). If they had the same N_c, the value of D^* would be increasingly higher in ICDs than in QCDs.

According to Equation 1-8 and 6-6, D^* is proportional to the square root of the number of stages if R_i remains unchanged. This is roughly correct when individual absorbers are only made of a pair QWs and kept thin, and the total absorber thickness does not cause a substantial light attenuation [99]. Conversely, when the light absorption is significant in individual absorbers (e.g. especially in ICD_SLs), the attenuation of light intensity along the propagation direction needs to be considered in evaluating the R_i [141, 194, 232]. In this scenario, the D^* for a non-current matched cascade device (e.g. with identical absorbers) will reach a maximum value at a finite N_c as discussed in [141, 194]. This is particularly true for ICD_SLs where SLs are used as active absorbers to enhance absorption and responsivity for attaining the highest value of D^* among all devices, as shown in Figure 6-8. Nevertheless, compared to ICDs, the additional increase in D^* in ICD_SLs is not as appreciable as the boost in the peak R_i. This is because the J_o is much higher in ICD_SLs with thicker SL absorbers than in ICDs. Nevertheless, with two adjustable parameters, the SL absorber thickness and the number of stages, ICD_SLs can be optimized with more flexibilities to improve D^* at high temperatures [141, 194].

In addition, if the detector has a voltage rather than a current output, one can define its responsivity as the ratio of output voltage to power [9]. Analogous to *p*-*n* diodes,

neglecting shunt and series resistances, the net current density J in ICDs and QCDs (with identical stages) under light illumination can be approximately written as:

$$J = J_0\left(e^{qV/N_c k_b T} - 1\right) - J_{ph} \tag{6-8}$$

where the photocurrent density J_{ph} is simply presumed to be bias independent. In an actual device, the photocurrent may be bias dependent as described in Chapter 4 and 5 for some ICTPV devices. Based on Equation 6-8, the open-circuit voltage V_{oc} for a cascade device can be expressed as:

$$V_{oc} = \frac{N_c k_b T}{q} ln\left(\frac{J_{ph}}{J_0} + 1\right) \tag{6-9}$$

Hence from this equation one can see that the lower J_0, the higher V_{oc} would be.

Also, when the photocurrent is significantly lower than the dark current, which is generally true in the detection of weak light at high temperatures. In this case, Equation 6-9 can be approximated to first order as:

$$V_{oc} = \frac{N_c k_b T}{q} \frac{J_{ph}}{J_0} \tag{6-10}$$

which is linearly proportional to the number of stages and the ratio of photocurrent and saturation current densities. Therefore, if the detector output is voltage, more stages and a lower saturation current density will benefit the device performance. According to Figure 6-7 and 6-8, the voltage responsivity will be much higher in ICDs than in QCDs. The is due to the higher photocurrent (proportional to responsivity) and the much lower J_0 in ICDs compared to QCDs. Overall, in terms of either current or voltage responsivity, ICDs will maintain the advantages over QCDs.

6.3.5 Effect of J_0 on the performances of photovoltaic cells

As for photovoltaic cells to convert light into electricity, the saturation current density J_0 remains an important parameter to evaluate device performance. As mentioned in Chapter 1, the relatively low transition energy ΔE in the active region makes ICDs and QCDs more appropriate for TPV applications where the heat source temperatures are generally at 1000-2000 K. In fact, TPV cells based on IC structures have been experimentally demonstrated with high V_{oc} that far exceeded the single bandgap value, showing the cascade effect [159, 182, 190-191]. In contrast, TPV cells based on QC structures have not been reported experimentally, possibly due to high values of J_0 in QCDs. Based on Equation 6-10 and the data in Figure 6-7 and 6-8, the open-circuit voltage V_{oc} can be calculated for cascade devices under light illumination at an incident power density P_{inc}. Assuming P_{inc}=1 W/cm^2, about ten times the average of solar radiation at the surface of the earth, and the radiation peaks at the response wavelength (with spectral control in a TPV system) for ICDs and QCDs so that $J_{ph}=R_i \cdot P_{inc}$, the V_{oc} is estimated and plotted in Figure 6-9 for the devices presented in Figure 6-8. As can be seen, the QCDs have a very modest V_{oc} (<3 mV) due to a high J_0 even with many stages (≥30). This may explain why QC TPV cells have not been demonstrated in experiment so far. In contrast, the values of V_{oc} for the ICDs are considerably higher (more than an order of magnitude in most cases) than for QCDs. This mainly stems from the much lower J_0 in ICDs than in QCDs (Figure 6-7). Combined with the higher photocurrent density as indicated in Figure 6-8(a), the IC structure is more advantageous than the QC structure for TPV applications. Note that, despite the much higher R_i, the V_{oc} for ICD_SLs is similar with those for ICDs because of the higher J_0 in ICD_SLs. However, with higher R_i and J_{ph}, ICD_SLs will have

a higher output power and conversion efficiency if they have the same number of cascade stages.

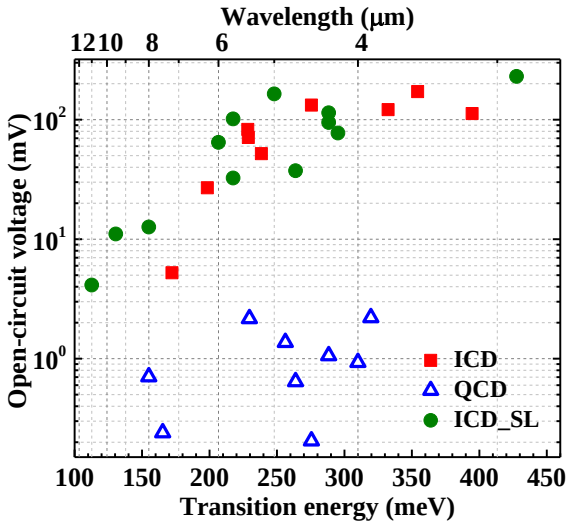

Figure 6-9: Estimated V_{oc} at 300 K for the ICDs, ICD_SLs and QCDs shown in Figure 6-8.

6.4 Summary and concluding remarks

In this chapter, firstly, an electrical method is developed to extract thermal generation rate and minority carrier lifetime in in T2SL-based ICIPs. This method is more general and considers the parasitic shunt and series resistances existed in practical devices. It can also cover various transport mechanisms such as Auger and SRH processes. Based on this method, the carrier lifetime at high temperatures (200-340 K) was evaluated to be between 8.5 and 167 ns, depending on the material quality. The extracted carrier lifetime displayed a different temperature dependence from those previously obtained by other methods for T2SL detectors, especially at high temperature range. Speculatively, such a temperature dependence may be related to the growing dominance of the Auger process at high temperatures. This method should also be applicable to detectors with other barrier configurations, such as nBn, XBn and CBIRD [67, 81-82].

Secondly, the fundamental difference in carrier lifetime between ICDs and QCDs is manifested by the saturation current density J_0. By comparing and analyzing available ICD and QCD data, it is shown that J_0 can be used as a unified figure of merit to describe both interband and intersubband cascade structures in terms of their device functionalities. The significance of J_0 on detector and PV cell performances was illustrated by comparing the measured detectivity and the estimated open-circuit voltage, respectively. The extracted values of J_0 are more than one order of magnitude lower in ICDs than in QCDs with similar transition energies. This result, in combination with the discussion of the consequences of J_0 on device performance, clearly revealed the advantages of IC configurations over intersubband QC configurations based on the same framework. The overall picture for both QCDs and ICDs sheds light from the perspective of a united figure of merit, which will offer instructive guidance and stimulation to the future development of both ICDs and QCDs. It is worth pointing out that both ICDs and QCDs have their respective merits. For example, QCDs are based on more mature material systems. The epitaxial growth and the device processing technologies are well-established. Consequently, at the present stage, QCDs can have better uniformity as well as less surface leakage and higher output power for lasers. Hence, both QCDs and ICDs will coexist for various applications with different requirements.

Chapter 7: Long wavelength interband cascade infrared photodetectors

7.1 Introduction

In Chapter 6, a new method was developed to extract the carrier lifetime in mid-wavelength ICIPs and a common figure of merit (closely related to carrier lifetime) was proposed to evaluate the performances of IC and QC devices. In this chapter, further understandings in the operations and behaviors of ICIPs are presented. All the devices included in this chapter operate in the LWIR band. However, the fundamental principles revealed in this chapter are also suitable to ICIPs working in other spectral regions. Compared to conventional single-absorber structures, the multistage configuration of ICIPs provides more degrees of freedom for optimizing device performance. On the other hand, this also complicates the design process and requires a more comprehensive understanding of multiple factors in order to optimize device performance. For example, ICIPs can be divided into two groups: current-matched ICIPs [142, 231, 237-239] where the photocurrent is designed to equal in all stages, and noncurrent-matched ICIPs [99, 137, 198-199, 240-241] with identical stages, as shown in Figure 7-1. In a current-matched ICIP, the absorbers in the optically deeper stages are made thicker to achieve an equal photocurrent in all stages. This relies on the precise knowledge of material absorption coefficients, which may vary with temperature and increase the difficulty in implementation at different operating temperatures. By comparison, in a noncurrent-matched ICIP, the individual absorber thicknesses are designed to be identical in each stage. It's simpler to implement but has a possible drawback of substantially reduced responsivity due to light attenuation, especially with relatively thick absorbers [99, 141].

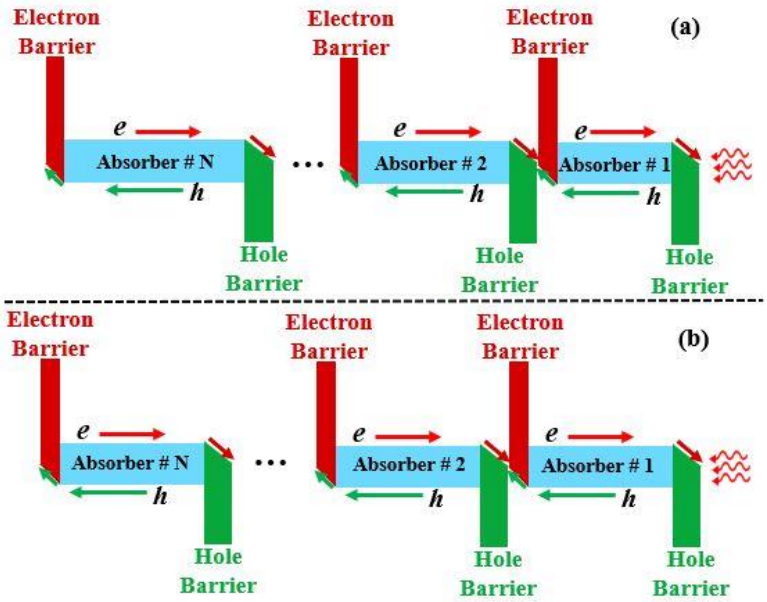

Figure 7-1: Schematic illustration of the multi-stage ICIP with (a) regular and (b) reverse configurations. The two configurations can be realized by reversing the growth order of layers in one structure without changing the light illumination direction.

Although these two groups of ICIPs have been explored independently, they have not been studied together in the same framework. To identify and understand their specific features and differences in device performance, a comparative study of the electrical and optical properties of several ICIPs with both absorber designs are presented in this chapter. Electrical gains significantly exceeding unity are observed from noncurrent-matched ICIPs. To further examine the preliminary findings on electrical gain and to better understand how noncurrent-matched ICIPs can be designed for optimized device performance, additional three ICIPs with varied absorber thicknesses and number of cascade stages are studied and a theory is developed to quantitatively explain the electrical gain. As will be discussed in detail in the Section 7.3, a reasonable agreement is obtained between theoretical calculations and experimental results.

7.2 Current matched ICIPs vs noncurrent-matched ICIPs

7.2.1 Device structure, growth and fabrication

The two sets of four ICIP structures included in this section were designed to target the LWIR region (8-12 μm) with a reverse illumination configuration [142, 239]. The four structures have different numbers of stages and variations of individual absorber thicknesses, but they have identical electron and hole barriers and the same InAs/GaSb SL composition. Each period (60 Å) of the SL absorber are made of layers: InSb (1.9 Å), InAs (31 Å), InSb (1.9 Å) and GaSb (25.2 Å). The two thin InSb layers were inserted to balance the strain from the InAs layer [168]. The absorbers in the four structures were *p*-doped to 2.6×10^{16} cm^3 so that the electrons were the minority carriers. The electron barriers consist of four GaSb/AlSb QWs with GaSb well thicknesses of 33/43/58/73 Å. The hole barriers are seven digitally graded InAs/GaSb QWs and the InAs well thicknesses therein are 48/50/52/55/58/62/70 Å.

Set #1 includes two current-matched ICIP structures called Mat.-8S and Mat.-12S. They have eight and twelve cascade stages, respectively. Mat.-8S was fabricated from wafer S#4-8 that was described in detail in [239]. Mat.-12S is made up of 12 stages with absorber thicknesses of 180, 192, 210, 228, 246, 264, 282, 306, 336, 366, 396, and 432 nm, from the surface to the substrate (the direction of light illumination). Set #2 has two noncurrent-matched ICIP structures, NMat.-16S and NMat.-20S, with sixteen and twenty cascade stages, respectively. NMat.-16S has sixteen discrete identical stages with the individual absorber thickness (222 nm) equal to that of the first-stage absorber in Mat.-8S. NMat.-20S has twenty discrete identical stages with each absorber thickness (180 nm) equal to that of the first absorber of Mat.-12S. The total absorber thickness in these four

ICIP structures is 2.29 μm (Mat.-8S), 3.44 μm (Mat.-12S), 3.55 μm (NMat.-16S), and 3.60 μm (NMat.-20S). Table 7-1 summarizes the design parameters, along with some key material properties including cutoff wavelength λ_c, bandgap E_g and activation energy E_a for the four ICIPs.

Table 7-1: Summary of material and design parameters for the four devices.

Device	Absorber type	# of stages	Total thickness (μm)	100% λ_c (μm)	E_g (meV) at 0K	E_a (meV) 78-125K	E_a (meV) 150-250K
NMat.-20S	Identical	20	3.60	9.5	188	43	160
Mat.-12S	Current-matched	12	3.44	11.0	174	45	155
NMat.-16S	Identical	16	3.55	11.1	172	64	160
Mat.-8S	Current-matched	8	2.29	11.0	175	45	155

The four ICIP structures were grown by molecular beam epitaxy (MBE) on *p*-type GaSb substrates that were nominally undoped. After the MBE growth, the wafers were processed into deep-etched square mesa devices with dimensions from 50 to 1000 μm using conventional contact UV photolithography and wet etching. A RF-sputter deposited two-layer passivation (Si_3N_4 then SiO_2) was used for improving overall stress management and minimizing pin holes, and sputter deposited Ti/Au layers were used for top and bottom contacts. Finally, the devices were mounted on heat sinks and wire bonded for characterization.

7.2.2 Electrical properties

Electrical and optical properties of devices from these wafers were determined through measurements of dark current density-voltage (J_d-V) characteristics and photo-response spectra. From the measured J_d-V curves, the R_0A were extracted for the four

representative devices as shown in Figure 7-2 at a wide temperature range. This allows to obtain the activation energies by fitting R_0A (1/T) to the following equation:

$$R_0A = CT^b e^{E_a/k_bT} \tag{7-1}$$

where b and E_a are the two fitting parameters. In principle, the parameter b is expected to be 1.5 if the dark current density scales with n_i (SRH limited) and 3 if it scales with n_i^2 (diffusion limited). The extracted E_a values are shown in Table 7-1, where q=0 was used at 78-125 K and q=2 was used at 150-250 K. From the extracted E_a, the carrier transport in these devices at high temperatures (>150 K) is diffusion limited. This is because the extracted E_a is nearly equal to their zero-temperature bandgaps E_g (T=0), which can be determined by fitting E_g (T) to the Varshni formula:

$$E_g\ (T) = E_g\ (T = 0) - \frac{\alpha T^2}{\beta + T} \tag{7-2}$$

where α and β are the Varshni parameters. The evaluated Eg (T=0) based on Equation 7-2 was 188, 174, 172 and 165 meV for NMat.-20S, Mat.-12S, NMat.-16S and Mat.-8S, respectively.

The diffusion limited carrier transport can be further examined by comparing the experimentally extracted R_0A with the theoretical projections of a diffusion transport model, which is given by Equation 2-8. According to this equation, R_0A is larger for detectors with more cascade stages, but lower for detectors with thicker absorbers. This feature is corroborated by Figure 7-2, where the values of R_0A for NMat.-20S and NMat.-16S are higher than Mat.-12S and Mat.-8S thanks to the larger number of stages and the thinner individual absorbers for all stages. Note that the thermal generation rate in Equation 2-8 is given by Equation 4-3, which implies that it scales with e^{-E_g/k_bT}.

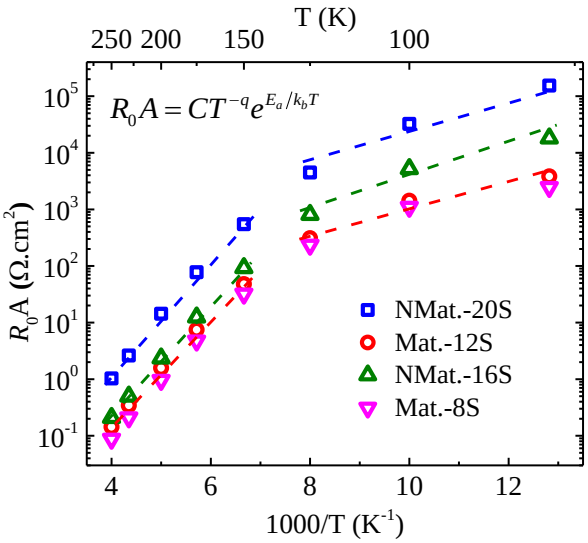

Figure 7-2: Extracted R_0A of the four representative devices at various temperatures.

Based on Equation 2-8, the ratio of R_0A between NMat.-20S (NMat.-16S) and Mat.-12S (Mat.-8S) can be obtained from:

$$\frac{R_0A_{NMat.-20S}}{R_0A_{Mat.-12S}} = \frac{\sum_m^{NMat.-20S}(\tanh d_m/L)^{-1}}{\sum_m^{Mat.-12S}(\tanh d_m/L)^{-1}} e^{\Delta E_g/k_bT} \quad (7\text{-}3\ a)$$

$$\frac{R_0A_{NMat.-16S}}{R_0A_{Mat.-8S}} = \frac{\sum_m^{NMat.-16S}(\tanh d_m/L)^{-1}}{\sum_m^{Mat.8S}(\tanh d_m/L)^{-1}} e^{\Delta E_g/k_bT} \quad (7\text{-}3\ b)$$

where ΔE_g is the bandgap variation between two devices. Here, the diffusion length and carrier lifetime were assumed to be same for the four wafers, which is reasonable because they were designed with nominally identical SL absorber periods and grown in a close time interval. Since the cutoff wavelength of NMat.-20S was shorter than the other three devices that had a nearly equal bandgap, one needs to account the bandgap difference between NMat.-20S and Mat.-12S in Equation 7-3(a), while ΔE_g can be neglected for NMat.-16S and Mat.-8S in Equation 7-3(b). Based on Equation 7-3, the calculated ratios of R_0A as a function of diffusion length at 300 K are shown in Figure 7-3. As can be seen, if the diffusion length far exceeds absorber thickness, the two R_0A ratios approach a saturation value of 6.44 and 2.50 for $R_0A_{\text{NMat.-20S}}/R_0A_{\text{Mat.-12S}}$ and $R_0A_{\text{NMat.-16S}}/R_0A_{\text{Mat.-8S}}$, respectively.

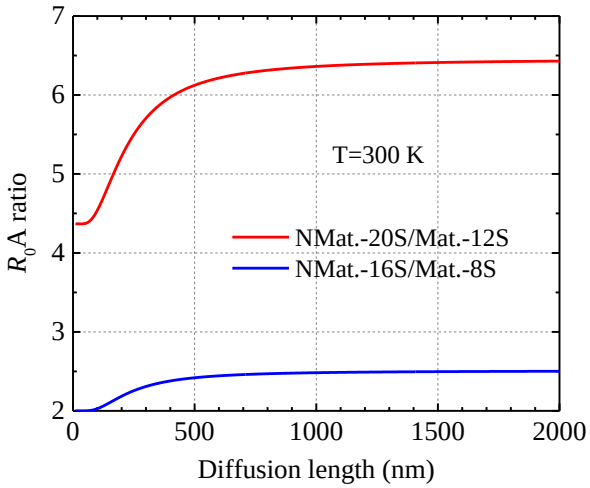

Figure 7-3: The theoretical R_0A curves at T=300K. The device dark current was dominated by the diffusion process at this temperature.

Table 7-2 shows the experimentally obtained R_0A ratios and the theoretically calculated R_0A ratios by assuming the diffusion length is appreciably longer than the individual absorber thickness (i.e. $L \gg d_m$). The variations in the calculated values of $R_0A_{NMat.-20S}/R_0A_{Mat.-12S}$ with temperature resulted from the exponential term $\exp[\Delta E_g/(k_bT)]$ in Equation 7-3, where ΔE_g was determined from the experimental data with certain uncertainty. The experimentally obtained values used in Table 7-2 are for bulk R_0A, obtained by excluding the surface leakage contribution based on Equation 4-6. The non-monotonic temperature dependence of the theoretical and experimentally extracted R_0A ratios may be caused by the uncertainty of ΔE_g as mentioned above. Nevertheless, as shown in Table 7-2, the experimentally extracted R_0A ratios are in good agreement with theoretical calculations at these high temperatures, confirming the diffusion limited carrier transport. This also implies that the diffusion length is indeed longer than the individual absorber thicknesses, though there may be minor inaccuracies in experimental data related to variations of their bandgaps and parasitic series resistances. From Table 7-2 and Figure 7-3, it can be inferred that the diffusion length in the four devices is finite, but probably longer

than 500 nm at 300 K.

Table 7-2: Theoretical calculated and experimental extracted values of R_0A ratios at high temperatures.

T (K)	280	300	320
$(R_0A_{NMat.-20S}/R_0A_{Mat.-12S})_{measured}$	6.2	6.1	6.3
$(R_0A_{NMat.-20S}/R_0A_{Mat.-12S})_{theory}$	6.3	6.4	6.4
$(R_0A_{NMat.-16S}/R_0A_{Mat.-8S})_{measured}$	2.4	2.5	2.3
$(R_0A_{NMat.-16S}/R_0A_{Mat.-8S})_{theory}$	2.5	2.5	2.5

7.2.3 Responsivity

The optical response of the ICIPs was collected using a FTIR spectrometer and then calibrated with a 600 K blackbody source (aperture diameter of 0.762cm) with a 2π field of view (FOV). Due to efficient carrier collection in these ICIPs with thin individual absorbers, the photocurrent is insensitive to bias voltage. The zero-bias responsivity spectra of the four representative devices at 200-300 K are shown in Figure 7-4. As can be seen, the current-matched ICIPs have higher responsivities than the noncurrent-matched ICIPs at all temperatures of interest. The responsivity of the noncurrent-matched ICIPs was only about 60% of that obtained from the corresponding current-matched ICIPs with the same absorber thickness (180 or 222 nm) in the first stage. This relation is exemplified in Table 7-3, where the value of R_i was taken at 7 μm for NMat.16S, Mat.12S and Mat.8S ICIPs, and at 5 μm for NMat.-20S since its cutoff wavelength was about 2 μm shorter than other three detectors. These data clearly evidence the necessity of current match for optimal responsivity, and substantial light attenuation in the optically deeper stages. This conclusion can be further examined and illustrated by considering the temperature dependence of responsivity, as shown in Figure 7-5.

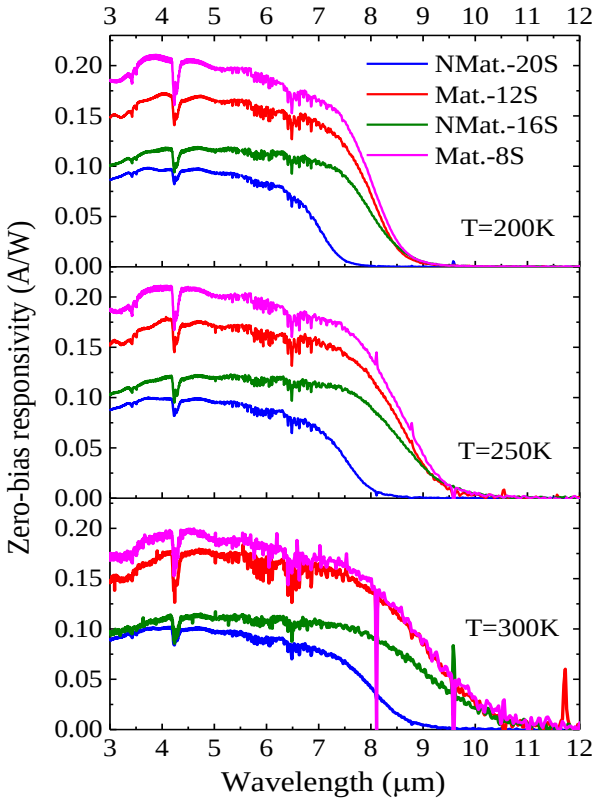

Figure 7-4: Zero-bias responsivity spectra for the four devices at different temperatures.

Table 7-3: Experimentally obtained ratio of responsivity for ICIPs at different temperatures.

T (K)	200	250	280	300	320
$R_0A_{NMat.-20S}/R_0A_{Mat.-12S}$	0.66	0.62	0.63	0.61	0.63
$R_0A_{NMat.-16S}/R_0A_{Mat.-8S}$	0.63	0.61	0.62	0.59	0.57

As shown in Figure 7-5, the responsivities of the four devices exhibited similar trends with temperature as they peaked at certain temperatures and then fell off with further increasing temperature. The observed trends were linked with variations of absorption coefficient, diffusion length, and current match with temperature. As discussed earlier, the diffusion length (>500 nm at 300 K) was likely longer than or comparable to individual absorber thicknesses throughout the entire temperature range of interest. Accordingly, the

collection of photogenerated carriers would not be affected in these ICIPs at various temperatures. Hence, the temperature dependence of responsivity resulted mainly from the increase of absorption coefficient due to bandgap narrowing at higher temperatures and the consequential change in current match. In other words, the responsivity initially increased with enhanced absorption as the temperature was raised, and then decreased when the more substantial light attenuation in the optically deeper stages began to disrupt the current match. This was more significant for devices with relatively thick absorbers. For instance, since the first-stage absorber of Mat.-8S and NMat.-16S is thicker (222 nm) than that (180 nm) of Mat.-12S and NMat.-20S, their responsivities peaked at lower temperatures (280 and 250 K) compared to the peak locations (300 and 320 K) for Mat.-12S and NMat.-20S. This fact once again demonstrates the existence of substantial light attenuation and the need of current match in achieving optimal responsivity. Note that the cutoff wavelength of NMat.-20S was much shorter than the other three devices and approached 7 μm at low temperatures. Thus, the light absorption (and attenuation) was small at this wavelength. This yielded a relatively rapid increase of the corresponding responsivity with temperature up to 280 K and the peak at 320 K, as shown in Figure 7-5.

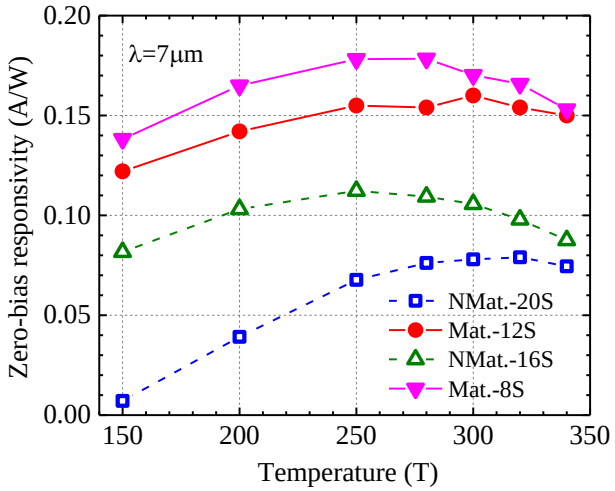

Figure 7-5: Temperature-dependent responsivity of the four devices at 7 μm.

7.2.4 Electrical gain

To perform a further quantitative analysis of current-matched and noncurrent-matched ICIPs, the absorption coefficients of the SL absorbers were measured at room temperature as shown in Figure 7-6. Based on the measured absorption coefficient, the evaluated responsivity was much lower than the values in Figure 7-4 for noncurrent-matched ICIPs, indicating possible electrical gain (*G*) exceeding unity. Theoretically, the responsivities of current-matched and noncurrent-matched ICIPs are expressed as [242]:

$$R_i(\lambda)\frac{1.24}{\lambda} = (1-R)(1-e^{-\alpha d_1})G \quad \text{(7-4 a)}$$

$$R_i(\lambda)\frac{1.24}{\lambda} = (1-R)e^{-(N_c-1)\alpha d_1}(1-e^{-\alpha d_1})G \quad \text{(7-4 b)}$$

where R is the from surface reflectance taken to be 0.31 for an InAs cap layer, and d_1 is the absorber thickness in the first stage. Only the first stage was considered in Equation 7-4(a) for the current matched ICIPs owing to an equal photocurrent in every stage. All stages were considered with Equation 7-4(b) for noncurrent-matched ICIPs because the photocurrent is the smallest in the last stage. According to Equation 7-4, the electrical gain can be estimated from the measured responsivities and absorption coefficients for the four devices.

Figure 7-6 shows the estimated electrical gain at room temperature for the four devices. As can be seen, the electrical gain for the ICIPs exceeds the unity when the absorption coefficient is higher than a certain value (e.g. >1500 cm^{-1}). As the absorption coefficient further increases at the higher photon energies, *G* increases for noncurrent-matched ICIPs, but remains nearly unchanged in current-matched ICIPs. This is because the enhanced absorption at a larger photon energy attenuates the light intensity in the last stage, which then necessities a large electrical gain to maintain current continuity. In

contrast, in first stage of the current-matched ICIPs, the increase of electrical gain is not required since the photocurrent is highest among all the stages. Also, to maintain current continuity, the electrical gain is required to be higher in ICIPs with thinner absorbers to make up for a shorter absorption length. This is revealed in Figure 7-6, where the *G* is higher in Mat.-12S than Mat.-8S, and is higher in NMat.-20S compared to NMat.-16S when the photon energy is higher than 0.2 eV. Note that the value of *G* could vary greatly in different cascade stages with substantial light attenuation. Gain exceeding unity was also observed in single-absorber T2SL detectors (>5) [242] and in other MWIR ICIPs [151, 165], although the mechanism was not fully understood. The underlying mechanism and the relevant theory of electrical gain in ICIPs will be described in detail in Section 7.3.

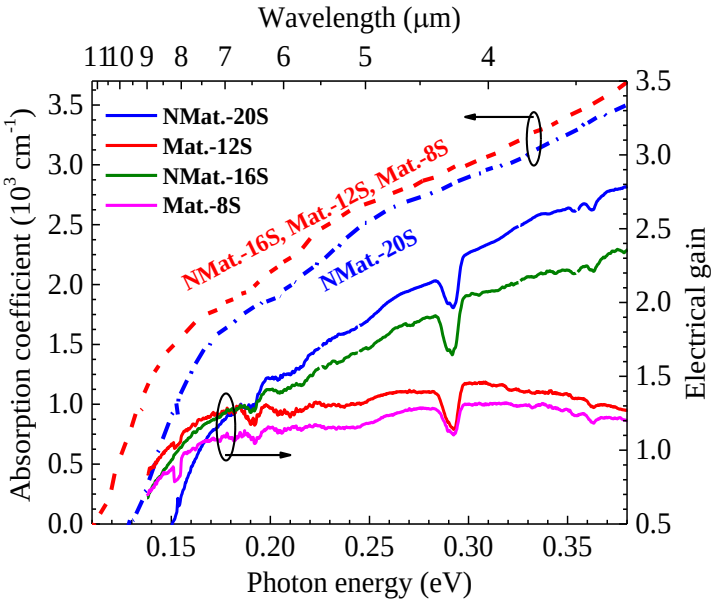

Figure 7-6: Absorption coefficient and electrical gain at room temperature. The dips near 4.2 μm in the gain curves were due to CO_2 absorption in the response spectra.

7.2.5 Johnson-noise limited detectivity

Overall, the generated electrical gain in ICIPs can partly compensate for the light attenuation in an optically deeper stage. As such, the responsivity in noncurrent-matched

ICIPs can be appreciable although not as impressive as in the current-matched ICIPs. Given much higher R_0A (Figure 7-2) and suppressed noise as shown in cleaner response spectra (Figure 7-4), noncurrent-matched ICIPs may achieve detectivities comparable to current-matched ICIPs. Also, due to substantial electrical gain, perfect current match is not a must in ICIPs, which offers great flexibility in design and practical implementation.

Based on the measured responsivity and R_0A, the estimated Johnson-noise limited detectivities for the four devices are presented in Figure 7-7. The general advantage provided by ICIPs with more stages (theoretically discussed in Chapter 2) can be seen from the maximum values of D^* for NMat.-20S. For example, at 250K, the Johnson-noise-limited D^* at λ=7 μm (with a FOV of 2π) were 6.05×10^8, 5.12×10^8, 4.51×10^8 and 4.56×10^8 Jones for NMat.-20S, Mat.-12S, NMat.-16S and Mat.-8S, respectively. At a higher temperature (e.g. 300K), the corresponding Johnson-noise limited D^* are 2.40×10^8 (NMat.-20S), 1.77×10^8 (Mat.-12S), 1.48×10^8 (NMat.-16S) and 1.40×10^8 (Mat.-8S) Jones. These values of D^* significantly exceeds the claimed value (e.g. $\geq 4.0\times10^7$ Jones with a FOV between $\pi/2$ and 2π) for commercial uncooled MCT detectors [91]. The significantly higher D^* for NMat.-20S was partially due to the relatively shorter cutoff wavelength compared to the other three devices. Nevertheless, with a similar cutoff wavelength, the D^* of NMat.-16S is slightly higher than Mat.-8S with same first-stage absorber thickness, even though the responsivity is lower in NMat.-16S. Hence, in terms of detectivity, noncurrent-matched ICIPs with appropriate designs can have comparable or even better performance over current-matched ICIPs. In fact, there is still room for improvement of the performance for noncurrent-matched ICIPs. When the stages of an ICIP are made identical, there is a tradeoff between reduced signal and suppression of noise with increasing stages. Adding

more stages to a noncurrent-matched ICIP reduces the thermal noise, but also compromises the signal current, due to light attenuation in the optically deeper stages. Hence, an optimized number of cascade stages may exist for maximizing D^* based on the absorption coefficient and absorber thickness [141]. If, however, the electrical gain is considered, the optimal number of stages will change as discussed in next section.

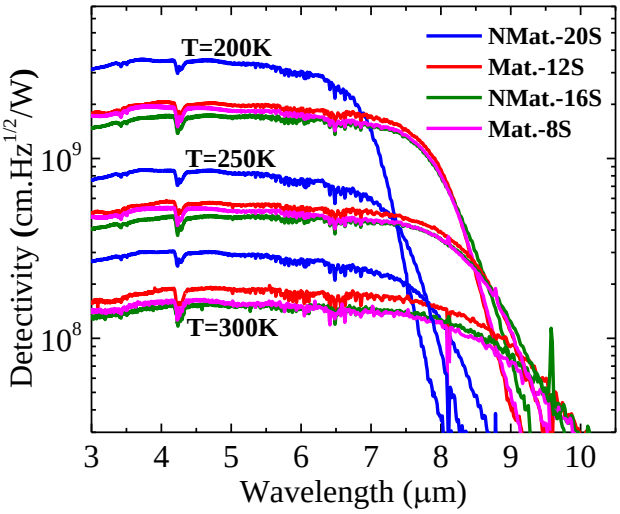

Figure 7-7: Johnson-noise limited D^* spectra of the four devices at various temperatures.

7.3 A comprehensive study of electrical gain in ICIPs

7.3.1 Device structure, growth and fabrication

To fully unlock the mechanism and theory of the electrical gain observed in ICIPs, apart from the two ICIP structures (NMat.-16S and NMat.-20S) in the preceding section, another three noncurrent-matched structures are studied and compared in this section,. Hence, there are in total five noncurrent-matched ICIPs quoted in this section. The three structures were grown using GENxplor MBE system on nominally-undoped *p*-type GaSb (001). The electron barriers, the hole barriers, the InAs/GaSb SL composition and the doping concentration in them are the same with those in NMat.-16S and NMat.-20S.

However, they have different numbers of stages and variations of individual absorber thicknesses. The three structures have 15, 23 and 28 cascade stages, and the corresponding individual absorber thicknesses are 180, 180 and 150 nm, respectively. For convenience, the three structures are denoted as I15S-180, I23S-180 and I28S-150. Also, for consistency, NMat.-16S and NMat.-20S are designated afresh here as I16S-222 and I20S-180, respectively. In the notations, the "I" indicates the identical-stage design. The total absorber thicknesses are 2.70 (I15S-180), 3.55 (I16S-222), 3.60 (I20S-180), 4.14 (I23S-180) and 4.20 μm (I28S-150). The absorption is insignificant in the electron and hole barriers, since they are composed of semiconductor QWs with bandgaps that are much wider than the absorber bandgap.

Table 7-4 summarizes key design and material parameters, including defect density and perpendicular (⊥) lattice mismatch of the five wafers, which have comparable material and crystal structural quality. After the MBE growth, the wafers were processed into square mesa devices with dimensions from 50 to 1000 μm using standard contact UV photolithography followed by wet-chemical etching. A RF-sputter deposited two-layer passivation (Si_3N_4 then SiO_2) was used to improve overall stress management and minimize pin holes. Sputter deposited Ti/Au layers provided top and bottom contacts. Finally, the devices were mounted on heat sinks and wire bonded for characterization.

Table 7-4: Summary of the design and material parameters of the five wafers.

Device	# of stages	Individual thickness (nm)	SL periods	Total thickness (μm)	Defect density (cm^{-2})	⊥ lattice mismatch
I15S-180	15	180	30	2.70	5.5×10^4	-0.394%
I16S-222	16	222	37	3.55	5.0×10^4	0.043%
I20S-180	20	180	30	3.60	3.3×10^4	0.061%
I23S-180	23	180	30	4.14	6.4×10^4	-0.378%
I28S-150	28	150	25	4.20	4.7×10^4	-0.369%

7.3.2 Responsivity

The optical response of the ICIPs was characterized following the same procedure described in the beginning of Subsection 7.2.23. The calibrated responsivities of representative devices (200×200 μm^2) from the five wafers at 200-300 K are shown in Figure 7-8(a). As shown, at 300 K, I15S-180, I23S-180 and I28S-150 have a nearly identical cutoff wavelength (10.6 μm), which is longer than for I20S-180 (9.5 μm) but slightly shorter than for I16S-222 (11.1 μm). As descried in the Section 7.2, the responsivities of these ICIPs are relatively small due to the thin individual absorbers, especially for noncurrent-matched ICIPs because of light attenuation. On the other hand, the shot and Johnson noises are suppressed for thinner individual absorbers and a larger number of cascade stages. As shown in Figure 7-8(a), the responsivity spectra for the five ICIPs at high temperatures are low but clear. Although the spectra were red shifted with temperature due to bandgap narrowing, the peak responsivity was either nearly unchanged or raised slightly (<10%) with increasing temperature. This is because the light absorption and attenuation in multiple stages limit the maximal value of QE and increasing the absorption coefficient beyond a certain value does not enhance QE, as shown in Figure 7-

8(b) for the five devices.

In general, the QE of a noncurrent-matched ICIP is determined by the last stage with minimum number of photogenerated carriers, as expressed by Equation 7-4(b). The calculated QEs for the five devices as a function of absorption coefficient are shown in Figure 7-8(b). The quite small values (<1.8%) agree with the relatively low responsivities shown in Figure 7-8(a). Also, the order of the calculated QEs of the five devices is nearly the same as for the measured responsivities. The peak values of QEs are1.75%, 1.64%, 1.30%, 1.13% and 0.92% that occur at an absorption coefficient of 3527, 2737, 2567, 2287 and 2119 cm^{-1} for I15S-180, I16S-222, I20S-180, I23S-180 and I28S-150, respectively. This is because of a tradeoff between the light absorption and attenuation in the last individual stage. From Equation 7-4(b), for a given absorption coefficient, it is anticipated that the device with thinner individual absorbers and thicker total absorber will have a smaller QE, and thus a lower responsivity. For instance, with similar cutoff wavelengths, the responsivity of I28S-150 is lower than I23S-180 and I28S-180 at each temperature of interest. Specifically, at T=300 K and λ=7 μm, the responsivity of I15S-180, I23S-180 and I28S-150 is 0.098, 0.078 and 0.065 A/W, respectively. Note that the lower responsivity in I28S-150 does not necessarily result in a lower detectivity since it also relies on the noise as will be discussed later.

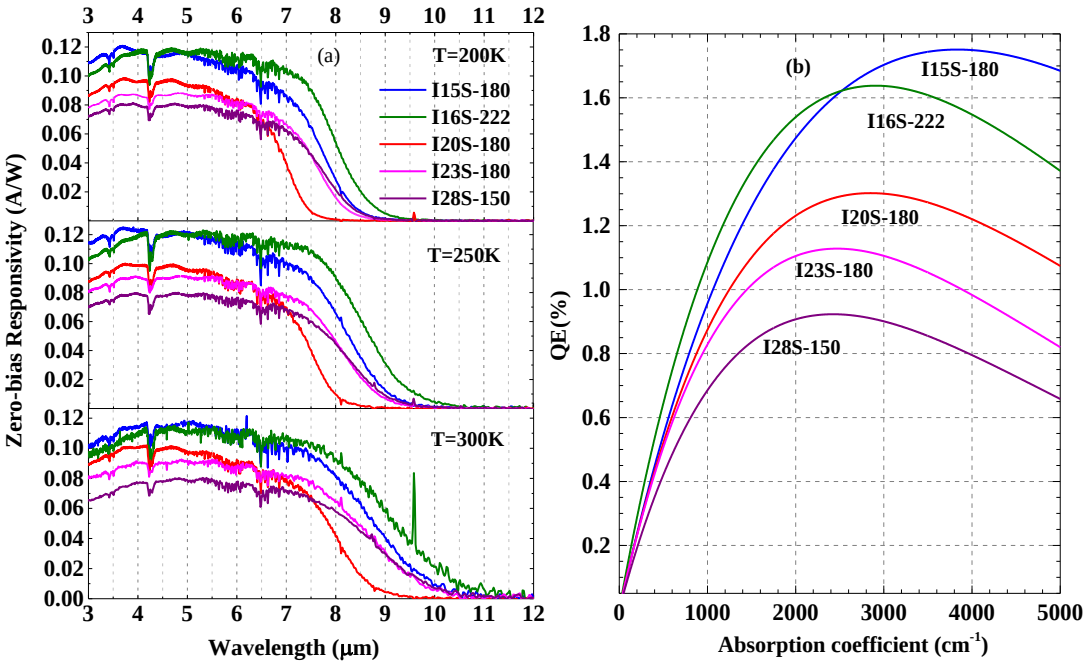

Figure 7-8: (a) Zero-bias responsivity spectra for the five devices at different temperatures. (b) Theoretically calculated external quantum efficiency of the five devices vs. absorption coefficient.

As mentioned above, there is a tradeoff between light attenuation and absorption related to the last stage in a noncurrent-matched ICIP. This is revealed by the trends of the calculated QE with absorption coefficient for the five devices. As can be seen in Figure 7-8(b), the calculated QE curves of the five devices exhibit similar and nearly parallel patterns with increasing absorption coefficient. They all peak at a certain absorption coefficient and then fall off with further increases. Although the individual absorbers of I16S-222 are thicker than I15S-180, the calculated QE of I16S-222 was smaller when the absorption coefficient exceeds 2600 cm^{-1}, due to more substantial light attenuation in the last stage of I16S-222. This explains the measured lower responsivity of I16S-222 compared to I15S-180 at shorter wavelengths (e.g. < 4 μm). In the opposite case where the light absorption had a greater effect than the attenuation in the last stage, the responsivity

of I16S-222 was higher than I15S-180, as manifested in the longer-wavelength region. Note that the analyses have not accounted for the effect of electrical gain on responsivity. In fact, in this context, the responsivity of a device follows the same sequence as the photocurrent in the last stage, which will be discussed in the Subsection 7.3.5.

7.3.3 Electrical gain

Like the devices described in Section 7.2, the estimated responsivities with the measured absorption coefficient for the five devices are smaller than the values shown in Figure 7-8. This means that the electrical gain (G) exceeds unity in the five ICIPs. Based on Equation 7-4(b), the G can be extracted from the experimentally measured absorption coefficient and responsivities. Figure 7-9 shows the estimated G, along with the measured absorption coefficients at room temperature. The electrical gain of the five noncurrent-matched ICIPs exhibits a monotonic increase with absorption coefficient and when the absorption coefficient is higher than a certain value (e.g. 1500 cm^{-1}), the electrical gain exceeds unity. For I23S-180 and I28S-150, G can be as high as ~4 at an absorption coefficient of 4800 cm^{-1}, which is expected to compensate for more significant light attenuation when the absorption is increased. Thanks to the high G, the Johnson-noise limited detectivity of the two devices can exceed that of I15S-180 at 300 K, as will be discussed in Subsection 7.3.7.

Equation 7-4(b) states that the electrical gain in noncurrent-matched ICIPs is to compensate for the attenuation of incident light in the last stage due to absorption in the preceding stages. Hence, the G needs to be higher in ICIPs with thinner individual absorber and thicker total absorber to make up for the shorter absorption length and larger attenuation in the last stage. This inference from a physical viewpoint agrees with the

estimated *G* for the five devices. As shown Figure 7-9, the five devices in ascending order of *G* are I15S-180, I16S-222, I20S-180, I23S-180 and I28S-150. This sequence is exactly in ascending order of the total absorber thickness. The higher *G* in I28S-150 compared to the other four devices was also partially because of a shorter absorption length with a thinner individual absorber. In addition, the *G* was slightly higher in I16S-222 compared to I15S-180 because there was more substantial light attenuation in the last stage of I16S-222, even though the thicker individual absorbers enabled more light absorption in the last stage. Accordingly, although both light attenuation and absorption in the last stage were relevant, the attenuation outweighed the absorption in the five devices when determining *G*. In fact, the *G* differs between stages in a noncurrent matched ICIP due to different light attenuations. The optically deeper stages have higher *G* to compensate for the more significant light attenuation. Consequently, the *G* depends on the number of cascade stages and is not the same for all stages.

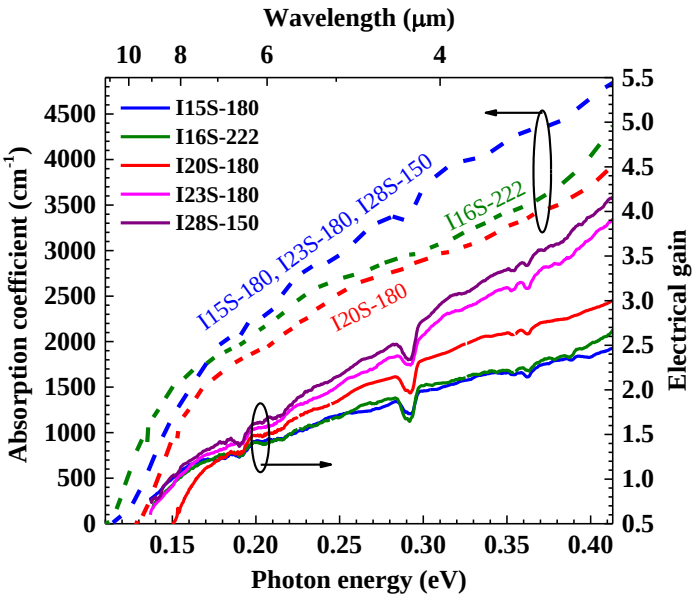

Figure 7-9: Absorption coefficient and electrical gain at room temperature. The dips near 4.2 μm in the gain curves were due to CO_2 absorption in the response spectra.

7.3.4 Underlying mechanism of electrical gain

As initially proposed in Refs. [141], the electrical gain in ICIPs stems from the adjustment of the electric potential over every cascade stage to maintain current continuity. In a noncurrent-matched ICIP, since the light is partially absorbed in the preceding stages and attenuates along the propagation direction, the number of photogenerated carriers (or the photocurrent) will not be the same in each stage. To fulfil the same current flow in each stage, the large photocurrent in the front stages (near the top surface), must be counterbalanced by an injection current induced by a forward electric potential. Contrarily, the small photocurrent in the back stages (near the bottom) must be supplemented by a thermal generation current resulted from a reverse electric potential. The total electric potential over all of stages equates zero or the external voltage if a bias is applied on the device. At high temperatures, the thermal generation current is high and therefore significant gain can be obtained in the back stages, as illustrated in the current five devices. In next subsection, a theory is developed to quantitatively describe the measured photocurrent and the electric potentials over each stage in these ICIPs.

As per Planck's law and standard theories for barrier detectors [141, 244], the photocurrent in the *m*th stage (I_{phm}) of a noncurrent-matched ICIP receiving the radiation from a standard blackbody is given by:

$$I_{ph} = \frac{2\pi q A_{opt}}{h^3 c^2}\left(\frac{r_a}{d_{sd}}\right)^2 \int_{E_g}^{\infty} QE_m \left(\frac{E^2}{e^{E/k_b T_{bb}}} - \frac{E^2}{e^{E/k_b T_{amb}}}\right) dE \qquad (7\text{-}5\ \text{a})$$

$$QE_m = (1-R)T_{win} e^{-(m-1)\alpha d} QE_d \qquad (7\text{-}5\ \text{b})$$

$$QE_d = \frac{\alpha L}{1-(\alpha L)^2} \times \left[\tanh(d/L) + \frac{\alpha L \exp(-\alpha d)}{\cosh(d/L)} - \alpha L\right] \qquad (7\text{-}5\ \text{c})$$

where A_{opt} is the optical area of the device, r_{a} is the radius of the aperture of the blackbody

source, d_{sd} is the distance between the blackbody source and the device, E_g is the bandgap of the absorber, QE_m is the effective quantum efficiency in the mth stage, T_{bb} is the blackbody temperature (set to 600 K), T_{amb} is the ambient temperature (~297 K), E is the photon energy, T_{win} (~0.7) is the transmittance of the cryostat window (ZnSe), and QE_d is the individual quantum efficiency, which is equal in each stage. The collection probability of photogenerated carriers is imbedded in Equation 7-5(b) and Equation 7-4(b) corresponds to the limiting case of Equation 7-5(b) where the diffusion length is much longer than the individual absorber thickness, leading to complete collection of photo-generated carriers. As mentioned before, the responsivities of the five devices have weak bias dependence. This conveys that the photo-generated carriers are efficiently collected in the five devices due to thin individual absorbers. Hence, there is no essential difference between the two equations, and the choice of diffusion length (typically <2 μm at room temperature) is inconsequential to the calculation of QE_m; here L_n was taken to be 0.7 μm. The optical loss due to the reflection of cryostat window was considered during the calibration of responsivity, hence Equation 7-5(b) only accounts for reflectance at the top surface of the device. Based on Equation 7-5, the calculated photocurrent in each stage of the five devices at room temperature is shown in Figure 7-10(a). As shown, the calculated individual photocurrent decreases with stage number, in agreement with the attenuation of light intensity. The first stage is unaffected by light attenuation, therefore the photocurrent in this stage only depends upon the absorption coefficient and individual absorber thickness. Among the five devices, I16S-222 has the highest photocurrent in the first stage since it has the thickest individual absorber. The I20S-180 device has the lowest first-stage photocurrent because it has the largest bandgap. Additionally, the order of the five devices,

in ascending photocurrent in the last stage, is nearly consistent with the order according to the responsivity spectra [Figure 7-8(a)]. As will be illustrated later, the signal current in the context of electrical gain, follows the same sequence as well. The calculated photocurrents of I15S-180 and I23S-180 overlap as expected, because they have the same individual absorber thickness, cutoff wavelength, and absorption coefficient.

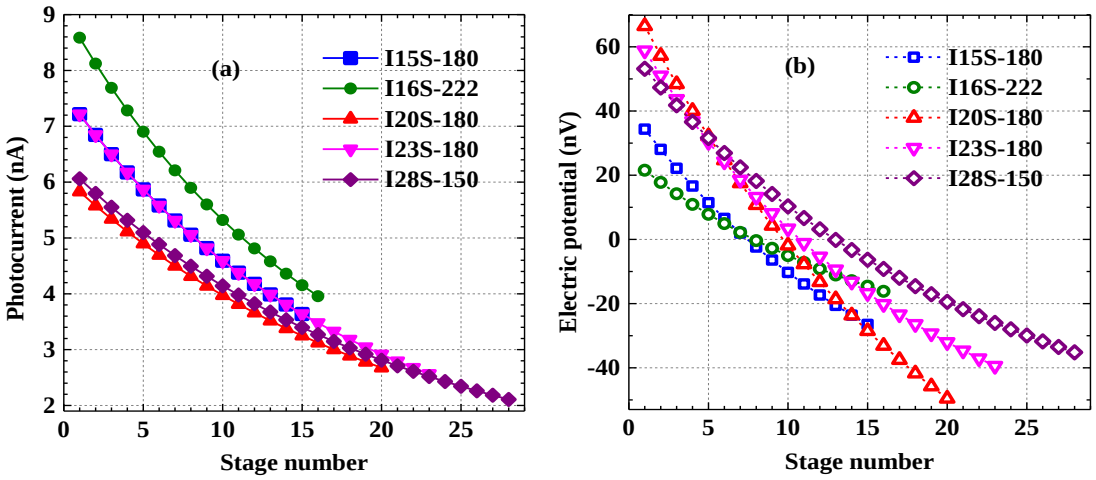

Figure 7-10: Theoretically calculated photocurrent based on Equation 7-5 and (b) electric potential calculated based on Equation 7-7 for each stage of the five devices at room temperature.

7.3.5 Net effect of electrical gain

Based on the mechanism discussed above, with electrical gain, the signal current I_s can be expressed as:

$$I_s = I_{ph1} - I_0\left(e^{qV_1/k_bT} - 1\right) = I_{phm} - I_0\left(e^{qV_m/k_bT} - 1\right) \qquad (7\text{-}6)$$

where I_0 is the saturation dark current, which is identical in each stage for a noncurrent-matched ICIP, and V_m is the electric potential across the mth stage. At zero external bias, the sum of the electric potential across each stage is zero: $V_1+V_2+\cdots+V_{Nc-1}+V_{Nc}=0$. At high temperatures, I_0 is much higher than the photocurrent, thus the magnitude of the electric

potential will be quite small and a first-order approximation in V_m can be used. Equation (7-6) plus the condition of zero total electrical potential, to the first-order approximation, leads to the expression of V_m:

$$V_m = \frac{1}{N_c}\frac{k_bT}{qI_0}\left(N_cI_{phm} - \sum_{i=1}^{N_c} I_{phi}\right) \tag{7-7}$$

where *i* denotes the stage number. Based on this equation, the calculated electric potential across each stage at room temperature for the five devices is shown in Figure 7-10(b). As can be seen, the individual electric potential is very small as it ranges from several to tens of nV. Hence, the first-order approximation is appropriate when estimating the signal current in the five ICIPs. In a certain stage, the electric potential shifts from positive to negative. This means that the electrical gain is above unity in the subsequent stages.

By replacing V_m with Equation 7-7, the signal current in Equation 7-6 can be modified to:

$$I_s = I_{phm} - I_0\left(e^{qV_m/k_bT} - 1\right) \xrightarrow{first\ order} I_{phm} - I_0\frac{qV_m}{k_bT}$$

$$= I_{phm} - \frac{qI_0}{k_bT}\frac{1}{N_c}\frac{k_bT}{qI_0}\left(N_cI_{phm} - \sum_{i=1}^{N_c} I_{phi}\right) = \sum_{i=1}^{N_c}\frac{I_{phi}}{N_c} \tag{7-8}$$

This equation states that the signal current in a noncurrent-matched ICIP will be the average of the photocurrents in each stage, provided that the dark current is much higher than the photocurrent. The net effect of electrical gain is to raise the signal current from the minimum photocurrent in the last stage to the average photocurrent over all the stages. Figure 7-11 shows the calculated and the measured signal currents for the five devices in a temperature range of 200-300 K. The calculations agree well with the experimental values for the five devices, considering some inaccuracies and uncertainties in the absorption coefficients and possible underestimates for I16S-222 at high temperatures with a small

resistance. Also, the device sequences according to the calculated last-stage photocurrents [Figure 7-10(a)], and the calculated and measured signal currents have almost the same order. The theory predicts that the photocurrent should increase with temperature, since the number of photogenerated carriers increases due to bandgap narrowing. However, for I16S-222 and I15S-180, the measured photocurrent slightly decreased while the device temperature was raised from 280 to 300 K. This was probably caused by an error from the small resistances or other factors that have not been understood yet, which deserve future investigation.

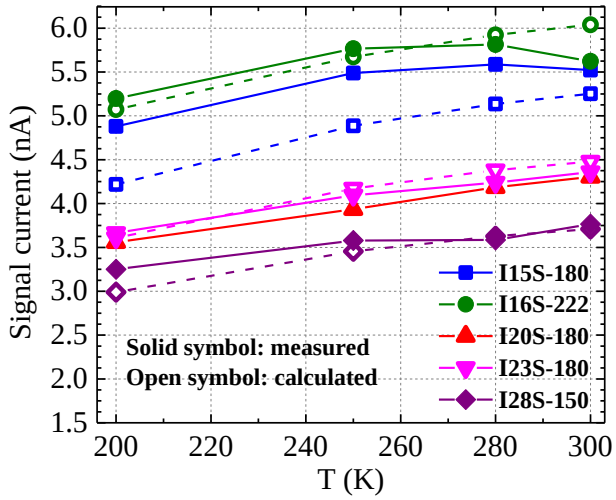

Figure 7-11: Theoretically calculated and experimentally measured signal current for the five devices.

Thanks to the electrical gain, the signal current is enlarged. Likewise, the spectral responsivity is enhanced and can be expressed by the average value of QE_m in each stage:

$$R_i(\lambda) = \frac{\lambda}{1.24}(1-R)\left[QE_d + e^{-\alpha d}QE_d + \cdots + e^{-(N_c-1)\alpha d}QE_d\right]/N_c$$

$$= \frac{\lambda}{1.24}\frac{(1-R)QE_d\left(1-e^{-N_c\alpha d}\right)}{N_c\left(1-e^{-\alpha d}\right)} \quad (7\text{-}9)$$

This expression of R_i (λ) can be further simplified for ICIPs with thin absorbers. The QE_d in the numerator can be canceled with the term ($1\text{-}e^{-ad}$) in the denominator when the

photogenerated carriers are fully collected. Therefore, this equation indicates that, for noncurrent-matched ICIPs with thin absorbers, R_i (λ) should monotonically increase with absorption coefficient at high temperatures. This is consistent with the calculated temperature dependence of the signal current as shown in Figure 7-11. However, when α is large at a photon energy well above the bandgap, the exponential term $\exp(-N_c \alpha d)$ in the numerator in Equation 7-9 is small and negligible. Consequently, the R_i (λ) reaches its saturation value, as observed in Figure 7-8(a) where the peak responsivities are almost insensitive to temperature.

Based on Equation 7-9, the simulated responsivity spectra for I20S-180 and I23S-180 at 250 K are shown in Figure 7-12. Also displayed are the calculations without considering the gain, experimental results with the regular mode of the IR source (inside the Nicolet 8700 FTIR spectrometer) and experimental results with a standard blackbody radiation source (model IR-563 from Infrared Systems Development Corporation) at 800 and 1200 K. In comparison with the regular theory without the gain, the calculation based on Equation 7-9 agrees much better with the experimental results. However, there are some deviations from the experimental results at high photon energies. Also, the real responsivity spectrum depends on the light source, while the calculated responsivity cannot express this feature. The effect of the light source is significant when it radiates more photons at high energies, which is evidenced by the higher responsivity at short wavelengths measured with the IR source (which has more high energy photons than the 1200 K blackbody source) and with the blackbody source at different temperatures. This means that the gain spectrum has some dependence on the incident photon distribution and the real response spectrum might not exactly follow with Equation 7-9, especially when the incident light

has a broad energy distribution with a large percentage of high energy photons. One interpretation of this phenomenon is that larger electrical gains are required to compensate for the increasing light attenuation at high photon energies and it turns out to be more dominant with the increased proportion of high energy photons.

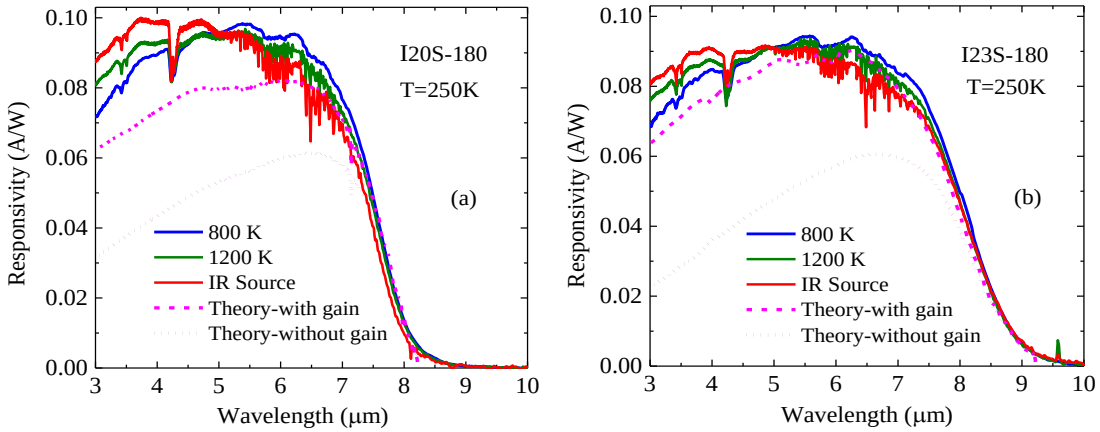

Figure 7-12: Theoretical and experimental responsivity spectra for two devices at 250 K with the IR source and a standard blackbody radiation source at 800 and 1200 K.

7.3.6 Electrical characteristics

The electrical properties of the ICIPs were characterized at 78-340 K. The measured dark current densities at -50 mV and the R_0A of the five devices are shown in Figure 7-13. At 300 K, the J_d at -50 mV was 0.95, 1.46, 0.32, 0.56and 0.43 A/cm^2 for I15S-180, I16S-222, I20S-180, I23S-180 and I28S-150, respectively. These values of J_d are nearly two orders of magnitude lower than that (50-70 A/cm^2) stated by the "Rule 07" for HgCdTe detectors [244]. Table 7-5 presents the activation energies extracted from the temperature dependence of R_0A, along with the zero-temperature bandgaps for the five devices. For I16S-222 and I20S-18, the carrier transport is diffusion limited since the activation energies approach the zero-temperature bandgaps. In contrast, for the other three devices, the extracted E_a is 50%-100% of zero-temperature bandgap, suggesting the involvement of

both the diffusion and the SRH processes in carrier transport. As can be seen in Table 7-5, the relatively larger perpendicular lattice mismatch may lead to a somewhat poorer material quality for these three devices compared to I16S-222 and I20S-180. Theoretically, given diffusion-limited carrier transport, the R_0A of a noncurrent-matched ICIP can be expressed by Equation 2-9. This equation indicates that, with a similar cutoff wavelength, the noncurrent-matched ICIP with more stages and thinner individual absorber will have a larger R_0A. This correlation is directly proved by the ascending order of R_0A of I15S-180, I23S-180 and I28S-150, although the carrier transport was partially affected by the SRH process. With similar cutoff wavelengths at 300 K, I28S-150 had the largest R_0A (1.12×10^{-1} $\Omega.cm^2$), followed by I23S-180 (8.43×10^{-2} $\Omega.cm^2$) and then I15S-180 (4.78×10^{-2} $\Omega.cm^2$). The largest R_0A (1.48×10^{-1} $\Omega.cm^2$ at 300 K) of I20S-180 among the five devices was ascribed to the shortest cutoff wavelength. On the same account, the R_0A (3.15×10^{-2} $\Omega.cm^2$ at 300 K) of I16S-222 was smallest, as a result of the longest cutoff wavelength as well as the thickest individual absorber among the five devices.

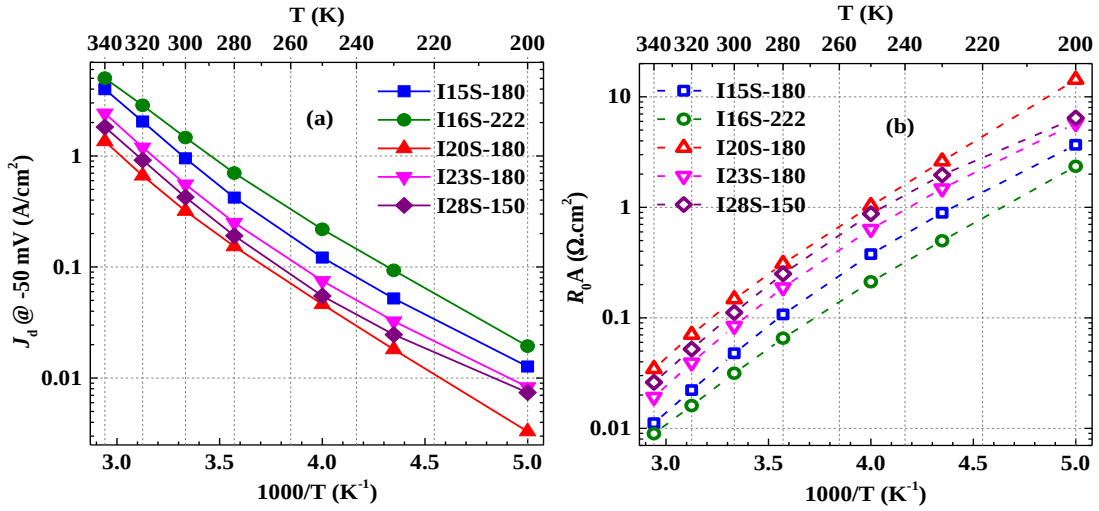

Figure 7-13: Arrhenius plot of dark current density (measured at -50 mV) and R_0A of the five devices in the temperature range of 200-340 K.

Table 7-5: Comparison of electrical parameters of the five ICIPs.

	I15S-180	I16S-222	I20S-180	I23S-180	I28S-150
R_0A ($\Omega.cm^2$) @ 200 K	3.68	2.35	14.30	5.76	6.43
R_0A (10^{-2} $\Omega.cm^2$) @ 300 K	4.78	3.15	14.8	8.43	11.2
E_g (meV) @ 0 K	176	172	188	174	174
E_a (meV) 150-250 K	132	160	160	132	102

7.3.7 Johnson-noise limited detectivity

The estimated Johnson-noise limited detectivities for the five devices are shown in Figure 7-14. Because of significant electrical gain, in terms of detectivity, these noncurrent-matched ICIPs can outperform the commercially viable uncooled HgCdTe detectors with a similar cutoff wavelength. For instance, at T=250 K, the Johnson-noise limited D^* values (for λ=7 μm and a FOV of 2π) were 5.34×10^8 (I15S-180), 4.41×10^8 (I16S-222), 5.91×10^8 (I20S-180), 5.28×10^8 (I23S-180) and 5.45×10^8 (I28S-150) Jones. At a higher temperature (e.g. 300 K), the corresponding Johnson-noise limited D^* were 1.66×10^8, 1.46×10^8, 2.37×10^8, 1.84×10^8 and 1.87×10^8 Jones, for I15S-180, I16S-222, I20S-180, I23S-180 and I28S-150, respectively. By comparison, the stated D^* (FOV between π/2 and 2 π) for commercial uncooled MCT detectors is about 4.0×10^7 Jones [91]. The significantly higher D^* of I20S-180 was partially due to the relatively shorter cutoff wavelength than the other four devices. By the same token, the lowest D^* of I16S-222 was partly because of the longest cutoff wavelength among the five devices. With similar cutoff wavelengths, despite the lower responsivities, the D^* of I23S-180 and I28S-150 are slightly higher than that of I15S-180 at 300 K, due to the larger R_0As of these two devices than that of I15S-180 (Table 7-5). The Johnson-noise limited D^* (λ=7 μm) and the 100% cutoff wavelength (at 300 K) for the five devices are summarized in Table 7-6.

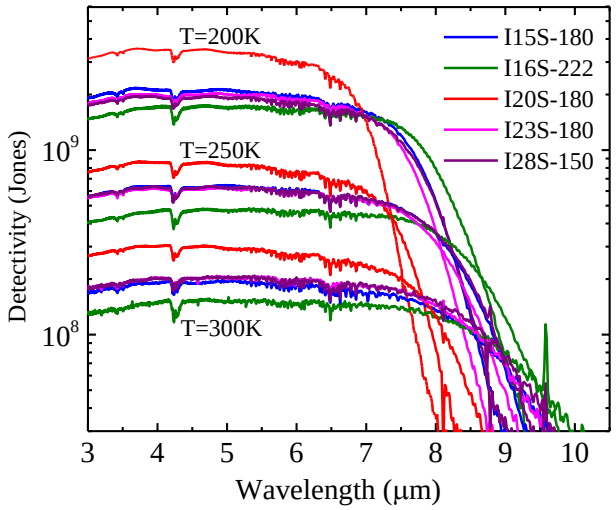

Figure 7-14: Johnson-noise limited D^* spectra of the five devices at various temperature.

Table 7-6: Comparison of D^* at λ=7 μm, along with the 100% cutoff wavelengths at 300 K, for the five devices.

	I15S-180	I16S-222	I20S-180	I23S-180	I28S-150
100% cutoff (μm) @ 300 K	10.6	11.1	9.5	10.6	10.6
D^* (10^8 Jones) @ 250 K	5.34	4.41	5.91	5.28	5.45
D^* (10^8 Jones) @ 300 K	1.66	1.46	2.37	1.84	1.87

In fact, there is still room for improvement of D^* in noncurrent-matched ICIPs. As mentioned in Section 7.2, the tradeoff between reduced signal and suppressed noise as the number of stages increases implies that there is an optimal number of stages that maximizes D^* based on the absorption coefficient. The optimal number depends on the electrical gain is considered or not since it alleviates the signal current compromise. If G is accounted, according to Equation 7-9, the R_i (λ) will be equal to the average value of all the stages. If, however, the gain is excluded, the R_i (λ) will be determined by the value of the last stage. In [141] and [245], the optimizations of D^* ignored the effect of G and consequently the optimized D^* (and corresponding N_c) was underestimated.

If the electrical gain is considered, based on Equation 2-9 and 7-9, the Johnson-noise limited detectivity of a noncurrent-matched ICIP can be estimated by the following equation:

$$D^* = \frac{\lambda}{hc}\frac{QE_d[1-\exp(-N_c\alpha d)]}{\sqrt{N_c}[1-\exp(-\alpha d)]\sqrt{4g_{th}L\tanh(d/L)}} \tag{7-10}$$

where QE_d is the individual quantum efficiency and is given by Equation 7-5(c). The calculated D^* as a function of the number of stages for different individual absorber thicknesses are shown in Figure 7-15. Both cases are considered, where the gain is included or excluded. In the calculation, the absorption coefficient was taken to be 2000 cm^{-1}, closely corresponding to λ=7 μm (Figure 7-9), and the diffusion length was assumed to 0.7 μm. As can be seen in Figure 7-15, the calculated D^* peaks at a certain number of stages and then decreases with more stages, as anticipated from the tradeoff between signal and noise mentioned above. However, with certain individual absorber thickness, the D^* peaks at a higher value and at a larger number of stages when the gain is considered. For instance, for d=0.5L, the calculated optimal number of stages is 18 when the gain is considered, while it is 7 when the gain is ignored. This is consistent with the previous statement that the gain alleviates the effect of light attenuation, thus bringing an upward shift of the optimal number of stages. It was also reflected by a modest drop of D^* after the peak value, as distinguished from the sharp decrease in the case without the gain. Adding many stages in a noncurrent-matched ICIP could make D^* approach zero if the gain is absent. However, this could occur only at a significantly larger number of stages if the gain is included. The peak value of D^* is raised by about 40% with the gain for each given absorber thickness. But, in both cases, the peak D^* has a weak dependence on the absorber thickness, especially when the absorber in each stage is made thin.

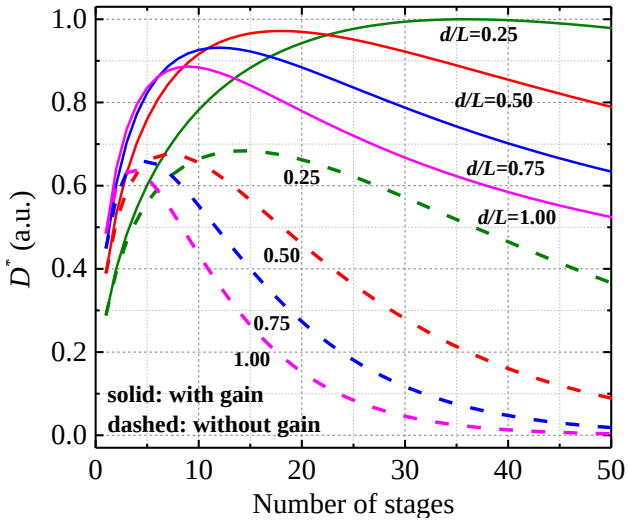

Figure 7-15: Detectivity derived from Equation 7-10 versus the number of stages with various ratios of the individual absorber thickness to the diffusion length (*d*/*L*), which are labeled near the curves in the two cases.

7.4 Summary and concluding remarks

In this chapter, a comparative study of four LWIR ICIPs with current-matched and noncurrent-matched configurations is presented. It is demonstrated that current match is necessary to maximize the utilization of absorbed photons for optimal responsivity. The reduced responsivity in noncurrent-matched ICIPs is correlated with light attenuation in the optically deeper stages. Based on the extracted R_0As for these LWIR ICIPs, the diffusion length is evaluated to be longer or comparable to 0.5 μm at various temperatures of interest. In addition, electrical gain above unity is observed, which is more substantial in noncurrent-matched ICIPs for maintaining current continuity. The significant electrical gain enabled an appreciable responsivity in noncurrent-matched ICIPs, although still not comparable with current-matched ICIPs. This, combined with the large R_0A, resulted in Johnson-noise limited detectivities (>1.4×10^8 Jones at 300 K) comparable to or even better than in current-matched ICIPs.

To fully explain the observed electrical gain, additional three noncurrent-matched structures are included and studied, which shows that the electrical gain commonly exists in noncurrent-matched ICIPs. Furthermore, a theory is developed to quantitatively explain the electrical gain in ICIPs. The calculations based on this theory exhibit good agreement with experimental results. Also, on this basis, insights and guidance to optimize the Johnson-noise limited detectivities in noncurrent-matched ICIPs are provided. This theory on electrical gain should also be applicable to other types of multistage photodetectors such as QWIPs [65, 78] and QCDs [83, 84]. This is because, even with distinctive transition mechanisms from ICIPs, these types of multistage detectors are also limited by light attenuation in the optically deeper stages, especially when the total absorbers are made thick. Likewise, the electric potential across each stage in QWIPs and QCDs will be self-adjusted to maintain current continuity and electrical gain will supplement the photocurrent in the optically deeper stages.

Chapter 8: Concluding notes and future work

8.1 Dissertation summary

The aim of this dissertation research was to identify and understand specific factors that affect narrow bandgap TPV cell performance and investigate how interband cascade (IC) structures can improve thermophotovoltaic (TPV) cells and infrared detectors, as well as to gain further understanding of relevant device physics and operations. IC devices are unique because of their multistage and multifactor nature in design, which was made feasible largely thanks to the type-II broken gap alignment between InAs and GaSb. For example, electron inter-stage transport profits much from this alignment as it enables the smooth transition of electrons from the valence band in GaSb layer to the conduction band in InAs layer without any considerable resistance. Through this process, electrons recycle themselves between stages with a transport path that consists of a series of interband excitation and collection events.

A consequence of the multistage strategy is the reduction of quantum efficiency (or photocurrent) due to the fact that multiple photons are required for an electron to traverse between the contacts. Nevertheless, the quantum efficiency is no longer an appropriate measurement for multistage structures where the particle conversion efficiency is more appropriate and is higher in IC devices. The multistage design uses thin absorbers in all stages to ensure efficient collection of photogenerated carriers before they recombine; while utilizing multiple stages to absorb incident photons to the maximal extent. This results in advantages such as enhanced open-circuit voltage and suppressed noise in ICTPV cells and IC infrared photodetectors (ICIPs), respectively. Ultimately, these advantages

enable the higher conversion efficiency and detectivity in multistage ICTPV cells and ICIPs compared to conventional single-absorber TPV cells and detectors.

In chapter 3, compelling theoretical arguments are provided to underpin the advantages of multistage ICTPV devices over single-absorber TPV devices. This chapter begins with the identifications of the limiting factors that have driven low efficiencies in single-absorber TPV devices. These factors are closely integrated with the high dark saturation current density, short carrier lifetime, small absorption coefficient and limited diffusion length. Their impact on conversion efficiency was illustrated in T2SL based TPV devices in view of several scenarios with different values of αL. It is shown that the multistage IC structure can eliminate the diffusion length limitation that affects single-absorber devices. As such, the particle conversion efficiency can approach 100%, and the conversion efficiency can be increased by about 10% in a wide range of αL values and bandgaps.

In chapter 4, a fair amount of experimental evidence is presented to illustrate and confirm the theoretically projected advantage of multistage ICTPV devices. This is done by a comparative study of three narrow bandgap (~0.2 eV at 300 K) TPV devices with a single stage, and three and five cascade stages. Based on the measured quantum efficiency (QE), the diffusion length is extracted to be ~1.5 μm at 300 K, which severely limited the collection efficiency of photogenerated carriers in the single-absorber device (<20%). Instead, the extracted collection efficiency in multistage devices approach 100%, thus its conversion efficiency is greatly improved compared single-absorber TPV devices (3.6% vs 0.9%).

Chapter 5 deals with the detailed characterization and performance analysis in narrow bandgap (0.22-0.25 eV at 300 K) multistage ICTPV devices with increased number of stages (i.e. 6, 7, 16, and 23 stages). It is found that current mismatch between stages could be significant with more stages due to the variation of absorption coefficient. In contrast, the collection efficiency of photogenerated carriers can be much improved with thinner individual absorbers and more stages. Also, the carrier lifetime is extracted from the dark current density to evaluate the material quality. Moreover, the effects of material quality, current mismatch and collection efficiency on device performance are quantified. The quantitative analysis shows that the material quality has the most significant impact on the device performance among the three factors.

Starting from Chapter 6, experimental studies of IC structures for infrared photodetection are provided. In this chapter, a novel and simple method is developed to extract the thermal generation rate and minority carrier lifetime in in T2SL-based ICIPs. This method is more general and can cover various transport mechanisms such as Auger and SRH processes. Based on this method, the carrier lifetime at high temperatures (200-340 K) is extracted to be 8.5-167 ns, which turns out to be affected by the material and structural quality. The exponential temperature dependence of carrier lifetime was speculated due to the growing dominance of the Auger process at high temperatures. In addition, in this chapter, fundamental difference in carrier lifetime between IC devices (ICDs) and quantum cascade devices (QCDs) is apparent from the saturation current density J_0. The extracted values of J_0 are more than one order of magnitude lower in ICDs than in QCDs with similar transition energies. Also, it is shown that J_0 can be used as a common figure of merit to describe cascade structures in terms of the device

functionalities. The significance of J_0 on detector and PV cell performances was revealed by the measured detectivity and the estimated open-circuit voltage, respectively.

Chapter 7 attempts a comparative study of four LWIR ICIPs with current-matched and noncurrent-matched configurations. The cutoff wavelength of these ICIPs is around 11 μm at 300 K. It is formally shown that current match is necessary to maximize the utilization of absorbed photons for optimal responsivity. Also, the reduced responsivity in noncurrent-matched ICIPs is strongly linked with the light attenuation in the optically deeper stages. These ICIPs feature a substantial electrical gain, especially for noncurrent-matched configurations. The significant electrical gain boosts the responsivity in noncurrent-matched ICIPs, although it is still less than that in the current-matched ICIPs. This, combined with the large R_0A, results in Johnson-noise limited detectivities (>1.4×10^8 Jones at 300 K) comparable to that in current-matched ICIPs. The values of detectivity in these LWIR ICIPs are better than that (~4.0×10^7 Jones) for uncooled state-of-the-art MCT detectors with similar cutoff wavelengths. Hence, ICIPs can be positioned to be a prospective candidate for replacing the commercially available MCT detectors in the LWIR regime.

In Chapter 7, to gain an exhaustive understanding of the observed electrical gain, three additional LWIR noncurrent-matched ICIPs are studied to allow a possible-in-depth comparison. The study shows that the electrical gain universally exists in noncurrent-matched ICIPs. Furthermore, a theory is developed to quantitatively elucidate the electrical gain in ICIPs. The calculations based on this theory exhibit good agreement with experimental results. On such a basis, insights and guidance to optimize the Johnson-noise limited detectivities in noncurrent-matched ICIPs are provided.

8.2 Future works

As repeatedly stated in Chapter 3, 4, and 5, in the current phase, the relatively low conversion efficiency in ICTPV devices is primarily due to the high saturation dark current density coupled with a short carrier lifetime and narrow bandgap. Hence, grand structural modifications or/and improvements in material quality are required. Otherwise for the normal ICTPV structure with current InAs/GaSb SL materials, an attractive energy efficiency would continue to be an unrealistic goal. The reduced dark current with increased carrier lifetime will be equally beneficial for detector performance as the dominating thermal noise is reduced. From this perspective, several means for objectively reducing the dark current can be employed alone or in combination. For example, to increase carrier lifetime, one feasible direction to pursue is to replace the InAs/GaSb SL absorbers with gallium free InAs/InAsSb SLs with a relatively longer carrier lifetime. This would be somewhat challenging with zero experience in incorporating this type of SL and IC scheme together. The difficulty also lies in the possible substantial strain released from the InAsSb layers in the SL.

Alternatively, one can improve the performance from the perspective of raising photocurrent rather than reducing the dark current. This relies on a special technique to enhance the light absorption, such as using plasmonic structures for achieving strong light focusing at a certain wavelength [246-247]. Plasmons can create very strong local fields around particle and can be guided along the interface in the form of traveling wave, known as a surface plasmon-polariton. The enhanced absorption can only occur at the plasmonic resonance wavelength, resulting in extremely narrow response spectra of the integrated IC devices. For ICTPV cells, this would require an optimal spectral match between the

radiation spectrum of the selective emitter (or filter) and the plasmonic resonance. However, for ICIPs, this feature would restrict them to applications in only very limited areas.

In addition, other issues in IC devices are not fully resolved at this moment. From the extracted activation of energy, the SRH process is identified to affect the dark current in the form of G-R current, whose occurrence can only be in the depletion region. In the quasi-neutral absorber region in IC structures, the current arising from the SRH process essentially is still diffusion current. This goes counter to the ideal situation where depletion regions are fully eliminated in IC devices since no p-n junction exists therein. It would be meaningful to locate the depletion regions and remove them from IC devices, and eventually to reduce the dark current. Another not fully appreciated problem is the significant surface leakage, especially in IC devices with relatively small sizes as discussed in Chapter 4. The ongoing fabrication research of IC devices is mainly dedicated to dielectric passivation (SiO_2 and SiN_x) to improve the surface quality, which however seems to be less than ideal. Other passivation techniques such as MBE regrowth of a wide-bandgap semiconductor layer and deposition of a sulfide-based layer can be explored as well to reduce the dark current. In addition, as raised in Chapter 4, the surface leakage tends to cause less additional dark current in IC devices with more stages. This conflicts with the larger resistance with more stages and consequentially more shunting current through the parallel surface path, which needs to be understood in the future as well.

Another interesting subject of further investigation is the voltage dependent collection efficiency of photogenerated carriers in ICTPV devices under laser illumination. All the ICTPV devices in this dissertation have this feature in common. The remaining gap

about this subject is to theoretically simulate the collection efficiency while acknowledging the effect of the applied external voltage. Specifically, one needs to build a reliable mathematical model that can accurately describe the transport of electrons through the diffusion process under an electric filed. In addition, future effort needs to be directed toward explaining the observed exceptionally high collection efficiency for IC devices with many stages (e.g. the 16- and 23-stage devices in Chapter 5). This result is intuitively not surprising since more stages consume the applied voltage. However, it also might be that the model used to extract collection efficiency (Equation 4-2) has limited power in ICTPV devices with many stages as it is based on two idealized assumptions. Hence, additional factors need to be considered in the future to improve the model's performance.

Finally, research into improving the source and spectral shaping technology is ongoing, but not in the MWIR regime. A good selective emitter that is able to convert the radiation emitted from a broadband source to a narrow spectral band make the spectral splitting approach unnecessary. However, there is a lack of effort into the development of selective emitters whose radiation spectrum would match with the response of ICTPV devices. Therefore, a reasonable next step in ICTPV research may be to utilize absorbers with different bandgaps in order to achieve spectral splitting. This can be useful only if the radiation received by the cell has a broadband spectral distribution. Because there are already many inherent losses in a TPV system, this may be the most promising path towards an efficient system.

References

[1] J. Byrnes, "*Unexplored Ordnance Detection and Mitigation*," Springer, 2009.

[2] OxMachina, available: https://medium.com/0xmachina/applying-infrared-thermography-for-coronavirus-screening-ee5b2dc8a6cb

[3] C. L. DeBellis, M. V. Scotto, L. Fraas, J. Samaras, R. C. Watson, S. W. Scoles, "Component Development for 500watt Diesel Fueled Portable Thermophotovoltaic (TPV) Power Supply," *AIP Conference Proceedings*, **460**, p. 362, 1999.

[4] T. J. Coutts, "A review of progress in thermophotovoltaic generation of electricity", *Renewable and Sustainable Energy Review*, **3**, pp. 77-184, 1999.

[5] T. Bauer, "*Thermophotovoltaics: Basic Principles and Critical Aspects of System Design*," Springer, 2011.

[6] J. Zhao, A. Wang, M. A. Green, "19.8% efficient "honeycomb" textured multicrystalline and 24.4% monocrystalline silicon solar cells," *Applied Physics Letters*, **73**, p. 1991, 1998.

[7] J. Nelson, "*The Physics of Solar Cells*," Imperial College Press, 2003.

[8] O. Nesher, S. Elkind, A. Adin, I. Nevo, A. B. Yaakov, S. Raichshtain, et al., "Digital cooled InSb detector for IR detection," *SPIE Proceedings*, **5074**, Infrared Technology and Applications, 2003.

[9] A. Rogalski, "*Infrared detectors*," CRC Press Inc, 2010.

[10] N. K. Dhar, R. Dat, A. K. Sood, "*Advances in Infrared Detector Array Technology*," IntechOpen, 2012.

[11] M. A. Khalighi, M. Uysal, "Survey on Free Optical Communication: A Communication Theory Perspective," *IEEE Communications Surveys & Tutorials*, **16**, pp. 2231-2258, 2014.

[12] R. E. Nelson, "A brief history of thermophotovoltaic development," *Semiconductor Science and Technology*, **18**, p. S141, 2003.

[13] M. Yamaguchi, T. Takamoto, K. Araki, N. Ekins-Daukes, "Multi-junction III-V solar cells: current status and future potential," *Solar Energy*, **79**, pp. 78-85, 2005.

[14] R. R. King, D. C. Law, K. M. Edmondson, C. M. Fetzer, G. S. Kinsey, H. Yoon, et al., "40% efficienct metamorphic GaInP/GaInAs/Ge multijunction solar cells," *Applied Physics Letters*, **90**, p. 183516, 2007.

[15] J. E. Raynolds, "Enhanced electro-magnetic energy transfer between a hot and cold body at close spacing due to evanescent fields," *Proceedings of the 4th NREL*

conference on thermophotovoltaic generation of electricity, American Institute of Physics, pp. 49-57, 1999.

[16] M. D. Whale, E. G. Cravalho, "Modeling and Performance of Microscale Thermophotovoltaic Energy Conversion Devices," *IEEE Transactions on Energy Conversion*, **17**, p.130, 2002.

[17] M. Laroche, R. Carminati, J.-J. Greffet, "Near-Field Thermophotovoltaic Energy Conversion", *Journal of Applied Physics*, **100,** p. 063704, 2006.

[18] L. M. Fraas, J. E. Avery, H. X. Huang, R. U. Martinelli, "Thermophotovoltaic system configurations and spectral control," *Semiconductor Science and Technology*, **18**, pp. 165–173, 2003.

[19] O. M. Nielsen, L. R. Arana, C. D. Baertsch, K. F. Jensen, M. A. Schmidt, "Thermophotovoltaic micro-generator for portable power applications," *12th International Conferences on Solid-State Sensors, Actuators and Microsystems*, **1**, pp. 714–717, 2003.

[20] W. R. Chan, P. Bermel, R. C. N. Podgurski, C. H. Marton, K. F. Jensen, J. J. Senkevich, et al., "Toward high-energy-density, high-efficiency, and moderate-temperature chip-scale thermophotovoltaics," *Proceedings of the National Academy of Sciences of the United States of America*, **110**, pp. 5309–5314, 2013.

[21] B. Bitnar, W. Durisch, J. C. Mayor, H. Sigg, H .R. Tschudi, G. Palfinger, et al., "Record electricity-to-gas power efficiency of a silicon solar cell based TPV system," *Proceedings of the 5th conference on thermophotovoltaic generation of electricity*, American Institute of Physics, pp 18–28, 2003.

[22] L. Fraas, J. Samaras, J. Avery, L. Minkin, "Antireflection coated refractory metal matched emitters for use with GaSb thermophotovoltaic generators," *Proceedings of the 28th IEEE photovoltaic specialists conference*, pp 1020–1023, 2000.

[23] B. Wernsman, R. R. Siergiej, S. D. Link, R. G. Mahoeter, M. N. Palmisano, R. J. Wehrer, et al., "Greater than 20% radiant heat conversion efficiency of a thermophotovoltaic radiator/module system using reflective spectral control," *IEEE Transactions of Electronic Devices*, **51**, pp. 512–515, 2004.

[24] D. Wilt, D. Chubb, D. Wolford, P. Magari, C. Crowley, "*Thermophotovoltaics for space power applications," Proceedings of the 7th world conference on thermophotovoltaic generation of electricity*, American Institute of Physics, pp 335–345, 2007.

[25] A. Datas, C. Algora, "Development and experimental evaluation of a complete solar thermophotovoltaic system," *Progress of Photovoltaics: Research and Applications*, **21**, pp.1025–1039, 2013.

[26] C. Ungaro, S. Gray, M. Gupta, "Solar thermophotovoltaic system using

nanostructures," *Opt. Express*, **23**, pp. A1149–A1156, 2015.

[27] W. Yang, S. Chou, C. Shu, H. Xue, Z. Li, "Research on micro-thermophotovoltaic power generators with different emitting materials," *Journal of Micromechanics and Microengineering*. **15**, p. S239, 2005.

[28] K. Qiu, A. Hayden, E. Entchev, "TPV power generation system using a high temperature metal radiant burner," *AIP Conference Proceedings*, **890**, pp. 27–36, 2007.

[29] M. G. Krishna, M. Rajendran, D. R. Pyke, A. K. Bhattacharya, "Spectral emissivity of ytterbium oxide-based materials for application as selective emitters in thermophotovoltaic devices," *Solar Energy Materials and Solar Cells*, **59**, pp. 337–348, 1999.

[30] W. Tobler, W. Durisch, "Plasma-spray coated rare-earth oxides on molybdenum disilicide–high temperature stable emitters for thermophotovoltaics," *Applied Energy*, **85**, pp. 371–383, 2008.

[31] S. Molesky, C. J. Dewalt, Z. Jacob, "High temperature epsilon-near-zero and epsilon-near-pole metamaterial emitters for thermophotovoltaics", *Optical Express*, **21**, pp. A96-A110, 2013.

[32] C. Argyropoulos, K. Q. Le, N. Mattiucci, G. D'Aguanno, A. Alù, "Broadband absorbers and selective emitters based on plasmonic Brewster metasurfaces", *Physics Review B*, **87**, p. 205112, 2013.

[33] P. Nagpal, S. E. Han, A. Stein, D. J. Norris, "Efficient Low-Temperature Thermophotovoltaic Emitters from Metallic Photonic Crystals", *Nano Lett.* **8** (10), pp. 3238–3243, 2008.

[34] R. M. Swanson, "Silicon photovoltaic cells in thermophotovoltaic energy conversion," *1978 International Electron Devices Meeting*, pp. 70-73, 1978.

[35] Fernández J, Dimroth F, Oliva E, Hermle M, Bett AW, "Back-surface Optimization of Germanium TPV Cells," *Proceeding of the 7th world conference on thermophotovoltaic generation of electricity*, pp. 190–197, 2007.

[36] O. V. Sulima, A. W. Bett, "Fabrication and simulation of GaSb thermophotovoltaic cells," *Solar Energy Materials and Solar Cells*. **66**, pp. 533-540, 2001.

[37] B. Wernsman, R. G. Mahorter, R. Siergiej, S. D. Link, R. J. Wehrer, S. J. Belanger, P. Fourspring, S. Murray, F. Newman, D. Taylor, T. Rahmlow, "Advanced thermophotovoltaic devices for space nuclear power systems," *AIP Conference Proceedings*, **746**, p. 1441, 2005.

[38] R. S. Tuley, J. M. S. Orr, R. J. Nicholas, D. C. Rogers, P. J. Cannard, S. Dosanjh, "Lattice-matched InGaAs on InP thermophotovoltaic cells," *Semiconductor*

Science and Technology, **28**, p. 015013, 2012.

[39] M. W. Dashiell, J. F. Beausang, H. Ehsani, G. Nichols, D. M. Depoy, L. R. Danielson, et al, "Quaternary InGaAsSb Thermophotovoltaic Diodes," *IEEE Transactions on Electron Devices*, **53**, p. 2879, 2006.

[40] C. A. Wang, H. K. Choi, S. L. Ransom, G. W. Charache, L. R. Danielson, D. M. DePoy, "High-quantum-efficiency 0.5 eV GaInAsSb/GaSb thermophotovoltaic devices," *Applied Physics Letters*, **75**, p. 1305, 1999.

[41] V. Sundaram, S. Saban, M. Morgan, W. Horne, B. Evans, J. Ketterl, *et al.*, "GaSb based ternary and quaternary diffused junction devices for TPV applications," *AIP Conference Proceedings*, **401**, pp. 105-115, 1997.

[42] P. Dutta, J. Borrego, H. Ehsani, G. Rajagopalan, I. Bhat, R. Gutmann, *et al.*, "GaSb and $Ga_{1-x}In_xSb$ thermophotovoltaic cells using diffused junction technology in bulk substrates," *Fifth Conference on Thermophotovoltaic Generation of Electricity*, pp. 392-401, 2003.

[43] K. J. Cheetham, P. J. Carrington, N. B. Cook, A. Krier, "Low bandgap GaInAsSbP Pentanary thermophotovoltaic diodes", *Solar Energy Materials and Solar Cells*, **95**, pp. 534-537, 2011.

[44] M. Mauk, O. Sulima, J. Cox, R. Mueller, "Low-bandgap (0.3 to 0.5 eV) InAsSbP thermophotovoltaics: assessment for open-circuit voltage improvements," *3rd World Conference on Photovoltaic Energy Conversion, 2003.*

[45] A. Krier, M. Yin, A.R.J. Marshall, and S.E. Krier, "Low Bandgap InAs-Based Thermophotovoltaic Cells for Heat-Electricity Conversion", *Journal of Electronic Materials*, **45**, p. 2826, 2016.

[46] Q. Lu, X. Zhou, A. Krysa, A. Marshall, P. Carrington, C-H. Tan, A. Krier, "InAs thermophotovoltaic cells with high quantum efficiency for waste heat recovery applications below 1000 °C", *Solar Energy Materials and Solar Cells*, **179**, p. 334, 2018.

[47] D. Cakiroglu, J. Perez, A. Evirgen, C. Lucchesi, P. Chapuis, T. Taliercio, E. Tournié, R. Vaillon, "Indium antimonide photovoltaic cells for near-field thermophotovoltaics," *Solar Energy Materials and Solar Cells*, **203**, p. 110190, 2019.

[48] X-L. Zhang, A-B. Huang, C-Y. Tian, Y. Wang, Yi-Yi Lou, "Thermophotovoltaic generation of electricity with $InAs_{0.91}Sb_{0.09}$ device", *IEEE Transactions on Electron Devices*, **65**, p. 4429, 2018.

[49] T. J. Coutts, J. S. Ward, "Thermophotovoltaic and Photovoltaic Conversion at High-Flux Densities," *IEEE Transactions on Electron Devices*, **46**, pp. 2145-2153, 1999.

[50] P. F. Baldasaro, J. E. Raynolds, G. W. Charache, D. M. DePoy, C. T. Ballinger, T. Donovan and J. M. Borrego, "Thermodynamic analysis of thermophotovoltaic efficiency and power density tradeoffs", *Journal of Applied Physics*, **89**, pp. 3319-3327, 2001.

[51] G. D. Cody, "Theoretical maximum efficiencies for thermophotovoltaic devices," *Proceedings of the 4th NREL Conference on Thermophotovoltaic Generation of Electricity*, American Institute of Physics, pp. 58-67, 1999.

[52] L. D. Woolf, "Optimum efficiency of single and multiple bandgap cells in thermophotovoltaic energy conversion," *Solar Cells*, **19**, pp. 19–38, 1986.

[53] M. W. Wanlass, K. A. Emery, T. A. Gessert, G. S. Horner, C. R. Osterwald, T. J. Coutts, "Practical considerations in tandem cell modelling," *Sol Cells*, **27**, pp. 191–204, 1989.

[54] A. Caruso, G. Piro, "Theoretical efficiency of realistic solar cells intended for thermophotovoltaic applications," *Sol Cells*, **19**, pp. 123–130, 1986

[55] N. P. Harder, P. Würfel, "Theoretical limits of thermophotovoltaic solar energy conversion." *Semiconductor Science and Technology*, **18**, pp.151–157, 2003.

[56] R. L. Bell, "Concentration ratio and efficiency in thermophotovoltaics," *Solar Energy*, **23**, pp. 203–210, 1979.

[57] V. Badescu, "Thermodynamic theory of thermophotovoltaic solar energy conversion," *Applied Physics*, **90**, pp. 6476–6486, 2001.

[58] W. Shockley, H. J. Queisser, "Detailed balance limit of efficiency of *p-n* junction solar cells," *Journal of Applied Physics*, **32**, p. 510, 1961.

[59] T. H. Johnson, "Lead Salt Detectors and Arrays PbS and PbSe," *SPIE Proceedings*, **0443**, Infrared Detectors, 1983.

[60] J. Werner, M. Oehme, M. Schmid, M. Kaschel, A. Schirmer, E. Kasper, et al. "Germanium-tin p-i-n photodetectors integrated on silicon grown by molecular beam epitaxy," *Applied Physics Letters*, **98**, p. 061108, 2011.

[61] D. N. Hall, R. S. Aikens, R. Joyce, T. W. McCurnin, "Johnson Noise Limited Operation of Photovoltaic InSb Detectors," *Applied Optics*, **14**, pp. 450-453, 1975.

[62] F. Shepherd, A. Yang, "Silicon Schottky Retinas for Infrared Imaging," *IEDM Technical Digest*, pp. 310–13, 1973.

[63] A. Rogalski, "HgCdTe infrared detector material: history, status and outlook," *Reports on Progress in Physics*, **68**, p. 2267, 2005.

[64] A. Lacaita, F. Zappa, S. Cova, P. Lovati, "Single-photon detection beyond 1 μm:

performance of commercially available InGaAs/InP detectors," *Applied Optics*, **35**, pp. 2986-2996, 1996.

[65] H. Schneider, H. C. Liu, "Quantum Well Infrared Photodetectors," Springer, 2007.

[66] H. C. Liu, M. Gao, J. McCaffrey, Z. R. Wasilewski, S. Fafard, "Quantum dot infrared photodetectors," *Applied Physics Letters*, **78**, p. 79, 2000.

[67] S. Maimon and G. W. Wicks, "nBn detector, an infrared detector with reduced dark current and higher operating temperature," *Applied Physics Letters*, **89**, p. 151109, 2006.

[68] D. L. Smith and C. Mailhiot, "Proposal for strained type II superlattice infrared detectors," *Journal of Applied Physics*, **62**, p. 2545, 1987.

[69] HITRAN Database, available: https://www.cfa.harvard.edu/hitran/

[70] J. Faist, F. Capasso, D. L. Sivco, C. Sirtori, A. L. Hutchinson, A. Y. Cho, "Quantum Cascade Laser," *Science*, **264**, pp. 553-556, 1994.

[71] J. Faist, "*Quantum Cascade Lasers*," Oxford University Press, 2013.

[72] R. Q. Yang, "Interband Cascade (IC) Lasers," in *Semiconductor lasers: Fundamentals and applications*. A. Baranov. E. Tournie (EDs). Woodhead Publishing, Chap. 12, 2013.

[73] I. Vurgaftman, R. Weih, M. Kamp, J. R. Meyer, C. L. Canedy, C. S. Kim, M. Kim, W. W. Bewley, C. D. Merritt, J. Abell, S. Höfling, "Interband cascade lasers," *Journal of Physics D: Applied Physics*, **48**, p. 123001, 2015.

[74] E. L. Dereniak, G. D. Boreman, "*Infrared Detectors and Systems*," Wiley, 1996.

[75] P. W. Kruse, "*Uncooled Thermal Imaging: Arrays, Systems, and Applications*," SPIE Press, 2001.

[76] A. Rogalski, "History of infrared detectors," *Opto-Electronics Review*, **20**, pp. 270-308, 2012.

[77] Hope-Wish, available: http://hpthermalcamera.com/cooled-vs-uncooled-thermal-cameras-long-range-surveillance/

[78] B. F. Levine, "Quantum-well infrared photodetectors," *Journal of Applied Physics*, **74**, p. R1, 1993.

[79] R. Q. Yang, J. M. Xu, M. Sweeny, "Selection rules of intersubband transitions in conduction-band quantum wells," *Physics Review B*, **50**, p. 7474, 1994.

[80] A. Yoshizawa, H. Tsuchida, "A 1550 nm Single-Photon Detector Using a Thermoelectrically Cooled InGaAs Avalanche Photodiode," *Japanese Journal of*

Applied Physics, **40**, p. 200, 2001.

[81] P. Klipstein, "XBn barrier photodetectors for sensitivity and high operating temperature infrared sensors," *SPIE proceedings*, **6940**, p. 69402U, 2008.

[82] D. Z.-Y. Ting, C. J. Hill, A. Soibel, S. A. Keo, J. M. Mumolo, J. Nguyen, et al., "A high-performance long wavelength superlattice complementary barrier infrared detector", *Appllied Physics Letter*, **95**, p. 023508, 2009.

[83] F. R. Giorgetta, E. Baumann, M. Graf, Q. Yang, C. Manz, K. Köhler, H. E. Beere, D. A. Ritchie, E. Linfield, A. G. Davies, et al., "Quantum Cascade Detectors," *IEEE Journal of Quantum Electronics*, **45**, p. 1039, 2009.

[84] P. Reininger, B. Schwarz, H. Detz, D. MacFarland, T. Zederbauer, A. M. Andrews, W. Schrenk, O. Baumgartner, H. Kosina and G. Strasser, "Diagonal-transition quantum cascade detector," *Applied Physics Letters*, **105**, p. 091108, 2014.

[85] J. F. Klem, J. K. Kim, M. J. Cich, G. A. Keeler, S. D. Hawkins, T. R. Fortune, "Mesa-isolated InGaAs photodetectors with low dark current," *Applied Physics Letters*, **95**, p. 031112, 2009.

[86] J. Masek, A. Ishida, H. Zogg, C. Maissen, S. Blunier, "Monolithic Photovoltaic PbS-on-Si Infrared-Sensor Array," *IEEE Electron Device Letters*, **11**, pp. 12-14, 1990.

[87] V. Kasiyan, Z. Dashevsky, C. M. Schwarz, M. Shatkhin, E. Flitsiyan, L. Chernyak, et al., "Infrared detectors based on semiconductor p-n junction of PbSe," *Applied Physics Letters*, **112**, p. 086101, 2012.

[88] R-M. Lin, S-F. Tang, S-C. Lee, C-H. Kuan, G-S. Chen, T-P. Sun, et al., "Room Temperature Unpassivated InAsp-i-n Photodetectors Grown by Molecular Beam Epitaxy," *IEEE Transactions on Electron Devices*, **44**, pp. 209-213, 1997.

[89] A. G. Foyt, W. T. Lindley, J. P. Donnelly, "n-p junction photodetectors in InSb fabricated by proton bombardment," *Applied Physics Letter*, **16**, p. 335, 1970.

[90] H. Shao, W. Li, A. Torfi, D. Moscicka, W. I. Wang, "Room-Temperature InAsSb Photovoltaic Detectors for Mid-Infrared Applications," *IEEE Photonics Technology Letters*, **18**, pp. 1756-1758, 2006.

[91] Catalogue, Vigo System S.A.

[92] A. M. Hoang, G. Chen, A. Haddadi, S. Abdollahi Pour, M. Razeghi, "Demonstration of shortwavelength infrared photodiodes based on type-II InAs/GaSb/AlSb superlattices," *Applied Physics* Letters, **100**, p. 211101, 2012.

[93] S. A. Pour, E. K. Huang, G. Chen, A. Haddadi, B.-M. Nguyen, M. Razeghi, "High operating temperature midwave infrared photodiodes and focal plane arrays based

on type-II InAs/GaSb superlattices," *Applied Physics* Letters, **98**, p. 143501, 2011.

[94] A. Haddadi, G. Chen, R. Chevallier, A. Hoang, and M. Razeghi, "InAs/$InAs_{1-x}Sb_x$ type-II superlattices for high performance long wavelength infrared detection," *Applied Physics* Letters, **105**, p. 121104, 2014.

[95] A. Haddadi, G. Chen, R. Chevallier, A. M. Hoang, and M. Razeghi, "InAs/InAs1−xSbx type-II superlattices for high performance long wavelength infrared detection," *Applied Physics Letter*, **105**, p. 121104, 2014.

[96] T. Dougakiuchi, K. Fujita, T. Hirohata, A. Ito, M. Hitaka and T. Edamura, "High photoresponse in room temperature quantum cascade detector based on coupled quantum well design," *Applied Physics Letter*, **109**, p. 261107, 2016; Erratum, **110**, p. 109902, 2017.

[97] P. Reininger, B. Schwarz, H. Detz, D. MacFarland, T. Zederbauer, A. M. Andrews, W. Schrenk, O. Baumgartner, H. Kosina and G. Strasser, "Diagonal-transition quantum cascade detector," *Applied Physics Letter*, **105**, p. 091108, 2014.

[98] R. Q. Yang, "Infrared laser based on intersubband transitions in quantum wells," *Superlattices and Microstructures*, **17**, pp. 77-83, 1995.

[99] R. Q. Yang, Z. Tian, Z. Cai, J. F. Klem, M. B. Johnson, H. C. Liu, "Interband-cascade infrared photodetectors with superlattice absorbers," *Journal of Applied Physics*, **107,** p. 054514, 2010.

[100] R. Q. Yang, Z. Tian, J. Klem, T. D. Mishima, M. B. Santos, M. B. Johnson, "Interband cascade photovoltaic devices", *Applied Physics Letters*, **96**, p. 063504, 2010.

[101] R. Q. Yang, J. M. Xu, "Bound and quasibound states in leaky quantum wells," *Physics Review B*, **46**, p. 6969, 1992.

[102] R. Q. Yang, J. M. Xu, "Leaky quantum wells: a basic theory and application," *Canadian Journal of Physics*, **70**, p. 1153, 1992.

[103] L. Esaki, L. L. Chang, E. E. Mendez, "Polytype superlattices and multi-heterojunctions", *Japanese Journal of Applied Physics*, **20**, p. L529, 1981.

[104] B. M. Nguyen, D. Hoffman, P. Y. Delaunay, M. Razeghi, "Dark current suppression in type II InAs/GaSb superlattice long wavelength infrared photodiodes with M-structure barrier", *Applied Physics Letters*, **91**, p. 163511, 2007.

[105] I. Vurgaftman, E. H. Aifer, C. L. Canedy, J. G. Tischler, J. R. Meyer, J. H. Warner, et al., "Graded band gap for dark-current suppression in long-wavelength infrared W-structure type-II superlattice photodiodes," *Applied Physics Letters*, **89**, p. 121114, 2006.

[106] O. Salihoglu, A. Muti, K. Kutluer, T. Tansel, R. Turan, Y. Ergun, A. Aydinli, "N" structure for type-II superlattice photodetectors, *Applied Physics Letters*, **101**, p. 073505, 2012.

[107] L. F. Luo, R. Beresford, W. I. Wang, "Resonant tunneling in AlSb/InAs/AlSb double-barrier heterostructures," *Applied Physics Letters*, **53**, p. 2320, 1988.

[108] E. R. Brown, J. R. Söderström, C. D. Parker, L. J. Mahoney, K. M. Molvar, T. C. McGill, "Oscillations up to 712 GHz in InAs/AlSb resonant-tunneling diodes," *Applied Physics Letters*, **58**, p. 2291, 1991.

[109] J. Devenson, R. Teissier, O. Cathabard, A. N. Baranov, "InAs-based quantum cascade lasers," *SPIE Proceedings*, **6909**, p. 69090U, 2008.

[110] C. Cathabard, R. Teissier, J. Devenson, J. C. Moreno, A. N. Baranov, "Quantum cascade lasers emitting near 2.6 μm," *Applied Physics Letters*, **96**, p. 141110, 2010.

[111] D. Z. Garbuzov, H. Lee, V. Khalfin, R. Martinelli, J. C. Connolly, G. L. Belenky, "2.3-2.7-μm room temperature CW operation of InGaAsSb-AlGaAsSb broad waveguide SCH-QW diode lasers," *IEEE Photonics Technology Letters*, **11**, pp. 794-796, 1999.

[112] J. G. Kim, L. Shterengas, R. U. Martinelli, G. L. Belenky, D. Z. Garbuzov, W. K. Chan, "Room-temperature 2.5 μm InGaAsSb/AlGaAsSb diode lasers emitting 1 W continuous waves," *Applied Physics Letters*, **81**, p. 3146, 2002.

[113] D. L. Partin, "Lead salt quantum well diode lasers," *Superlattices and Microstructures*, **1**, pp. 131-135, 1985.

[114] Z. Shi, M. Tacke, A. Lambrecht, H. Böttner, "Midinfrared lead salt multi-quantum-well diode lasers with 282 K operation," *Applied Physics Letters*, **66**, p. 2537, 1995.

[115] R. Q. Yang, L. Li, L. Zhao, Y. Jiang, Z. Tina, H. Ye, et al., "Recent progress in development of InAs-based interband cascade lasers," *SPIE Proceedings*, **8640**, p. 86400Q, 2013.

[116] J. Scheuermann, R. Weih, M. von Edlinger, L. Nähle, M. Fischer, J. Koeth, et al., "Single-mode interband cascade lasers emitting below 2.8 μm," *Applied Physics Letters*, **106**, p. 161103, 2015.

[117] M. Kim, C. L. Caney, W. W. Bewley, C. S. Kim, J. R. Lindle, J. Abell, et al., "Interband cascade laser emitting at λ=3.75 μm in continuous wave above room temperature," *Applied Physics Letters*, **92**, p. 191110, 2008.

[118] W. W. Bewley, C. L. Canedy, C. S. Kim, M. Kim, C. D. Merritt, J. Abell, *et al.*, "Continuous-wave interband cascade lasers operating above room temperature at λ = 4.7-5.6 μm," *Optics Express*, **20**, pp. 3235-3240, 2012.

[119] L. Li, Y. Jiang, R. Q. Yang, T. D. Mishima, M. B. Santos, M. B, Johnson, "Low-threshold InAs-based interband cascade lasers operating at high temperatures," *Applied Physics Letters*, **106**, p. 251102, 2015.

[120] S. M. Rassel, L. Li, Y. Li, R. Q. Yang, J. A. Gupta, X. Wu, et al., "High temperature and low-threshold interband cascade lasers at wavelengths longer than 6 μm," *Optical Engineering*, **57**, p. 011021, 2017.

[121] S. Höfling, R. Weih, M. Dallner, J. Scheuermann, M. V. Edlinger, L. Nähle, et al., "Mid-Infrared (~2.8 μm to ~7.1 μm) interband cascade lasers," *SPIE Proceedings*, **9550**, p. 95599F, 2015.

[122] Z. Tian, R. Q. Yang, T. D. Mishima, M. B. Santos, M. B. Johnson, "Plasmon-waveguide interband cascade lasers near 7.5 μm," *IEEE Photonics Technology Letter*, **21**, pp. 1588–190, 2009.

[123] Z. Tian, L. Li, Y. Hao, R. Q. Yang, T. D. Mishima, M. B. Santos, and M. B. Johnson, "InAs-based interband cascade lasers with emission wavelength at 10.4 μm," *Electronics Letters*, **48**, p. 113, 2012.

[124] R. Q. Yang, L. Li, W. Huang, S. M. Rassel, J. A. Gupta, X. Wu, et al., "InAs-Based Interband Cascade Lasers," *IEEE Journal of Selected Topics in Quantum Electronics*, **25**, p. 1200108, 2019.

[125] R. Q. Yang, C. J. Hill, K. Mansour, Y. Qiu, A. Soibel, R. E. Muller, et al., "Distributed feedback mid-infrared interband cascade lasers at thermoelectric cooler temperatures," *IEEE Journal of Selected Topics in Quantum Electronics*, **13**, pp. 1074–1078, 2007.

[126] I. Vurgaftman, W. W. Bewley, C. L. Canedy, C. S. Kim, M. Kim, C. D. Merritt, et al., "Rebalancing of internally generated carriers for mid-infrared interband cascade lasers with very low power consumption," *Nature Communications*, **2**, p. 585, 2011.

[127] G. A. Sai-Halasz, R. Tsu, L. Esaki, "A new semiconductor superlattice," *Applied Physics Letters*, **30**, p. 651, 1977.

[128] E. R. Youngdale, J. R. Meyer, C. A. Hoffman, F. J. Bartoli, C. H. Grein, P. M. Young, et al., "Auger lifetime enhancement in InAs-$Ga_{1-x}In_xSb$ superlattices," *Applied Physics Letter*, **64**, p. 3160, 1994.

[129] H. Mohseni, V. I. Litvinov, M. Razeghi, "Interface-induced suppression of the Auger recombination in type-II INAs/GaSb superlattices," *Physics Review B*, **58**, p. 15378, 1998.

[130] D. R. Rhiger, "Performance comparison of long-wavelength infrared type II superlattice devices with HgCdTe," *Journal of Electronic Materials*, **40**, pp. 1815–1822, 2011.

[131] C. M. Ciesla, B. N. Murdin, C. R. Pidgeon, R. A. Stradling, C. C. Phillips, M. Livingstone, et al., "Suppression of Auger recombination in arsenic-rich $InAs_{1-x}Sb_x$," *Journal of Applied Physics*, **80**, p. 2994, 1996.

[132] B. Tang, Y. Q. Xu, Z. Q. Zhou, R. T. Hao, G. W. Wang, Z. W. Ren, and Z. C. Niu, "GaAs Based InAs/GaSb Superlattice Short Wavelength Infrared Detectors Grown by Molecular Beam Epitaxy,"*Chinese Physics Letters*, **26**, p. 028102, 2009.

[133] A. M. Hoang, G. Chen, A. Haddadi, S. A. Pour, and M. Razeghi, "Demonstration of shortwavelength photodiodes based on type-II InAs/GaSb/AlSb superlattices," *Applied Physics Letter*, **100**, p. 211101, 2012.

[134] B.-M. Nguyen, M. Razeghi, V. Nathan, G. J. Brown, "Type-II M structure photodiodes: an alternative material design for mi-wave to long wavelength infrared regions," *SPIE Proceedings*, **6479**, p. 64790S, 2007.

[135] B. M. Nguyen, D. Hoffman, P. Y. Delaunay, E. K. Huang, M. Razeghi, J. Pellegrino, "Band edge tunability of *M*-structure for heterojunction design in Sb based type II superlattice photodiodes," *Applied Physics Letter*, 93, p. 163502, 2008.

[136] J. V. Li, R. Q. Yang, C. J. Hill, S. L. Chuang, "Interband cascade detectors with room temperature photovoltaic operation," *Applied Physics Letter*, **86**, p. 101102, 2005.

[137] Z. Tian, R. T. Hinkey, R. Q. Yang, D. Lubyshev, Y. Qiu, J. M. Fastenau, et al., "Interband cascade infrared photodetectors with enhanced electron barriers and p-type superlattice absorbers," *Journal of Applied Physics*, **111**, p. 024510, 2012.

[138] V. Andreev, V. Khvostikov, V. Kalinovsky, V. Lantratov, V. Grilikhes, V. Rumyantsev, et al., "High current density GaAs and GaSb photovoltaic cells for laser power beaming," 3rd World Conference on Photovoltaic Energy Conversion, pp. 761-764, 2003.

[139] E. Oliva, F. Dimroth, A. W. Bett, "GaAs converter for high power densities of laser illumination," *Progress in Photovoltaic: Research and Applications*, **16**, pp. 289-295, 2008.

[140] C. Donolato, "A reciprocity theorem for charge collection," *Applied Physics Letter*, **46**, pp. 270-272, 1985.

[141] R. T. Hinkey, R. Q. Yang, "Theory of Multiple-Stage Interband Photovoltaic Devices and Ultimate Performance Limit Comparison of Multiple-Stage and Single-Stage Interband Infrared Detectors," *Journal of Applied Physics*, **114**, p. 104506, 2013.

[142] H. Lotfi, L. Lei, L. Li, R. Q. Yang, J. C. Keay, M. B. Johnson, et al., "High-temperature operation of interband cascade infrared photodetectors with cutoff

wavelengths near 8 μm," *Optical Engineering*, **54,** p. 063103, 2015.

[143] B. Satpati, J. B. Rodriguez, A. Trampert, E. Tournié, A. Joullié, P. Christol, "Interface analysis of InAs/GaSb superlattice grown by MBE," *Journal of Crystal Growth*, **301-302**, pp. 889-892, 2007.

[144] Z.-B Tian, E. A. Plis, R. T. Hinkey, S. Krishna, "Influence of composition in InAs/GaSb type-II superlattices on their optical properties," *IEEE Electronics Letters*, **50**, pp. 1733-1734, 2014.

[145] Y. Livneh, P. C. Klipstein, O. Klin, N. Snapi, S. Grossman, A. Glozman, et al., "k.p model for the energy dispersions and absorption spectra of InAs/GaSb type-II superlattices," *Physics Review B*, **86**, p. 235311, 2012.

[146] I. Vurgaftman, G. Belenky, Y. Lin, D. Donetsky, L. Shterengas, G. Kipshidze, et al., "Interband absorption strength in long-wave infrared type-II superlattices with small and large superlattice periods compared to bulk materials," *Applied Physics Letters*, **108**, p. 222101, 2016.

[147] H. Mohseni, E. Michel, J. Sandoen, M. Razeghi, "Growth and characterization of InAs/GaSb photoconductors for long wavelength infrared range," *Applied Physics Letters*, **71**, p. 1403, 1997.

[148] R. Rehm, M. Walther, J. Schmitz, F. Rutz, J. Fleibner, R. Scheibner, et al., "InAs/GaSb superlattices for advanced infrared focal plane arrays," *Infrared Physics and Technology*, **52**, pp. 344-347, 2009.

[149] Y. Wei, A. Hood, H. Yau, A. Gin, M. Razeghi, M. Z. Tidrow, et al., "Uncooled operation of type-II InAs/GaSb superlattice photodiodes in the midwavelength infrared range", *Appl. Phys. Lett*. **86**, p. 233106, 2005.

[150] J. V. Li, C. J. Hill, J. Mumolo, S. Gunapala, S. Mou, and S-L. Chuang, "Midinfrared type-II InAs/GaSb superlattice photodiodes toward room temperature operation" *Applied Physics Letters*, **93**, p. 163505, 2008.

[151] L. Lei, L. Li, H. Lotfi, H. Ye, R. Q. Yang, T. D. Mishima, et al., "Mid-wavelength interband cascade infrared photodetectors with superlattice absorbers and gain", *Optical Engineering*, **57**, p. 011006, 2018.

[152] R. Rehm, M. Walther, J. Schmitz, F. Rutz, J. Fleibner, R. Scheibner, et al., "InAs/GaSb superlattices for advanced infrared focal plane arrays," *Infrared Physics and Technology*, **52**, pp. 344-347, 2009.

[153] H. Lotfi, L. Li, L. Lei, H. Ye, S. M. S. Rassel, Y. Jiang et al., "High-frequency operation of a mid-infrared interband cascade system at room temperature," *Applied Physics Letters*, **108**, p. 201101, 2016.

[154] Y. Chen, X. Chai, Z. Xie, Z. Deng, N. Zhang, Y. Zhou, "High Speed Mid-Infrared

Interband Cascade Photodetector Based on InAs/GaSb Type-II Superlattice", *IEEE Journal of Lightwave Technology*, **38**, pp. 939-945, 2019.

[155] A. Y. Cho, J. R. Arthur, "Molecular beam epitaxy," *Progress in Solid State Chemistry*, **10**, pp. 157-191, 1975.

[156] M. A. Herman, H. Sitter, "*Molecular Beam Epitaxy: Fundamentals and Current Status*," Springer, 2012.

[157] H. Ye, H. Lotfi, L. Li, R. T. Hinkey, R. Q. Yang, L. Lei, et al., "Multi-stage interband cascade photovoltaic devices with a bandgap of 0.23 eV operating above room temperature," *Chinese Science Bulletin*, **59**, pp. 950-955, 2014.

[158] W. Huang, L. Li, L. Lei, Jeremy A. Massengale, H. Ye, Rui Q. Yang, et al., "Minority carrier lifetime in mid-wavelength interband cascade infrared photodetectors," *Applied Physics Letters*, **112**, p. 251107, 2018.

[159] W. Huang, L Lei, L. Li, J. A. Massengale, R. Q. Yang, T. D. Mishima, et al., "Enhanced collection efficiencies and performance of interband cascade structures for narrow bandgap semiconductor thermophotovoltaic devices," *Journal of Applied Physics*, **124**, p. 023101, 2018.

[160] P. Asbeck, "Self-absorption effects on the radiative lifetime in GaAs–GaAlAs double heterostructures," *Journal of Applied Physics*, **48**, p. 820, 1977.

[161] A. Marti, J. L. Balenzategui, R. F. Reyna, "Photon recycling and Schockley's diode equation," *Journal of Applied Physics*, **82**, p. 4067, 1997.

[162] W. van Roosbroeke, W. Shockley, "Photon-radiative recombination of electrons and holes in germanium," *Physical Review*, **94**, p. 1558, 1954.

[163] E. Blandre, P-O. Chapuis, R. Vaillon, "High-injection effects in near-filed thermophotovoltaic devices," *Scientific Report*, **7**, p. 15860, 2017.

[164] M. A. Green, "Limiting Photovoltaic Monochromatic Light Conversion Efficiency," *Progress in Photovoltaic: Research and Applications*, **9**, p. 257, 2001.

[165] L. Lei, L. Li, H. Lotfi, Y. Jiang, R. Q. Yang, M. B. Johnson, "Mid-wave interband cascade infrared photodetectors banded on GaInAsSb absorbers," *Semiconductor Science and Technology*, **31**, p. 105014, 2016.

[166] E. H. Steenbergen, B. C. Connelly, G. D. Metcalfe, H. Shen, M. Wraback, D. Lubyshev, et al., "Significantly improved minority carrier lifetime observed in a long-wavelength infrared III-V type-II superlattice cmprised of InAs/InAsSb," *Applied Physics Letters*, **99**, p. 251110, 2011.

[167] B. V. Olson, E. a. Shaner, J. K. Kim, J. F. Klem, S. D. Hawkins, L. M. Murray, et al., "Time-resovled optical measurements of minority carrier recombination in a

mid-wave infrared InAsSb alloy and InAs/InAsSb superlattice," *Applied Physics Letters*, **101**, p. 092109, 2012.

[168] H. Ye, L. Li, H. Lotfi, L. Lei, R. Q. Yang, J. C. Keay, et al., "Molecular beam epitaxy of interband cascade structures with InAs/GaSb supperlattice absorbers for long-wavelength infrared detection," *Semiconductor Science and Technology*, **30**, p. 105029, 2015.

[169] R. T. Hinkey, R. Q. Yang, "Theoretical comparison of performance of limits of single- and multiple-stage photovoltaic devices," *Semiconductor Science and Technology*, **30**, p. 015013, 2015.

[170] W. Huang, R. Q. Yang, "Limiting factor and efficiencies of narrow bandgap single-absorber and multi-stage interband cascade thermophotovoltaic cells under monochromatic light illumination," *Journal of Applied Physics*, **126**, p. 045714, 2019.

[171] S. Hegedus, D. Desai, C. Thompson, "Voltage dependent photocurrent collection in CdTe/CdS solar cells," *Progress of Photovoltaics: Research and Applications*, **15**, pp. 587-602, 2017.

[172] R. Crandall, "Modeling of thin film solar cells: uniform field approximation," *Journal of Applied Physics*, **54**, pp. 7176-7186, 1983.

[173] X. X. Liu, J. R. Sites, "Solar-cell collection efficiency and its variation with voltage," *Journal of Applied Physics*, **75**, pp. 577-581, 1994.

[174] S. S. Hegedus, "Current-voltage analysis of a-Si and a-SiGe solar cells including voltage-dependent photocurrent collection," *Progress of Photovoltaics: Research and Applications*, **5**, pp. 151-168, 1997.

[175] D. A. Fardig, J. E. Phillips, "Characterization of CdTe/CdS Solar Cells," *Proceedings of 22nd IEEE Photovoltaic Specialists Conference*, pp. 1146-1150, 1991.

[176] S. M. Arnab, M. Z. Kabir, "Modeling of the effects of charge transport on voltage-dependent photocurrent in ultrathin CdTe solar cells," *Journal of Vacuum Science and Technology A*, **31**, p. 061201, 2013.

[177] M. Eron, A. Rothwarf, "Effects of a voltage-dependent light-generated current on solar cell measurements: $CuInSe_2$/Cd(Zn)S," *Applied Physics Letters*, **44**, pp. 131-133, 1984.

[178] J. Phillips, J. Titus, D. Hoffman, "Determining the voltage dependence of the light generated current in CuInSe2-based solar cells using I-V measurements made at different light intensities," *Proceedings of 26th IEEE Photovoltaic Specialists Conference*, pp. 463-466, 1997.

[179] R. Q. Yang, C. J. Hill, L. E. Christensen, C. R. Webster, "Mid-IR type-II interband cascade lasers and their applications," *SPIE Proceedings*, **5624**, pp. 413-422, 2005.

[180] R. Häcker, A. Hangleiter, "Intrinsic upper limits of the carrier lifetime in silicon," *Journal of Applied Physics*, **75**, p. 7570, 1994.

[181] A. Cuevas, D. Macdonald, "Measuring and interpreting the lifetime of silicon wafers," *Solar Energy*, **76**, pp. 255-262, 2004.

[182] H. Lotfi, L. Li, L. Lei, R. Q. Yang, J. F. Klem, M. B. Johnson, et al., "Narrow-bandgap interband cascade thermophotovoltaic cells," *IEEE Journal of Photovoltaics*, **7**, pp. 1462-1468, 2017.

[183] M. Kinch, "*State-of-the-Art Infraed Detector Technology*," SPIE Press, 2014.

[184] E. A. Plis, M. N. Kutty, S. Krishna, "Passivation tehcniques for InAs/GaSb strained layer superlatccies detectors," *Laser & Photonics Reviews*, **7**, p. 45, 2013.

[185] H. K. Chung, M. A. Rosenberg, P. H. Zimmermann, "Origin of 1/f noise observed in $Hg_{0.7}Cd_{0.3}Te$ variable area photodiode arrays," *Journal of Vacuum Science and Technology A*, **3**, p. 189, 1985.

[186] R. Q. Yang, H. Lotfi, L. Li, R. T. Hinkey, H. Ye, J. F. Klem, et al., "Quantum-engineered interband cascade photovoltaic devices," *SPIE Proceedings*, **8993**, p. 899310, 2014.

[187] W. Huang, L Lei, L. Li, J. A. Massengale, R. Q. Yang, T. D. Mishima, at al., "Enhanced collection efficiencies and performance of interband cascade structures for narrow bandgap semiconductor thermophotovoltaic devices," *Journal of Applied Physics*, **124**, p. 023101, 2018.

[188] W. Huang, L. Li, J. A. Massengale, R. Q. Yang, T. D. Mishima, M. B. Santos, "Investigation of Narrow Bandgap Interband Cascade Thermophotovoltaic Cells," *SPIE Proceedings*, **10913**, p. 1091317, 2019.

[189] R. T. Hinkey, Z. Tian, S. M. Rassel, R. Q. Yang, J. F. Klem, M. B. Johnson, "Interband cascade photovoltaic devices for conversion of mid-infrared radiation," *IEEE Journal of Photovoltaics*, **3**, p. 745, 2013.

[190] H. Lotfi, R. T. Hinkey, L. Li, R. Q. Yang, L. Lei, M. B. Johnson, et al., "Narrow-bandgap photovoltaic devices operating at room temperature and above with high open-circuit voltage," *Applied Physics Letters*, **102**, p. 211103, 2013.

[191] W. Huang, J. A. Massengale, Y. Lin, L. Li, R. Q. Yang, T. D. Mishima, M. B. Santos, "Performance analysis of narrow-bandgap interband cascade thermophotovoltaic cells," *Journal of Physics D: Applied Physics*, **53**, p. 175104, 2020.

[192] B. C. Connelly, G. D. Metcalfe, H. Shen, M. Wraback, "Direct minority carrier lifetime measurements and recombination mechanism in long-wave infrared type-II superlattices using time-resolved photoluminescence," *Applied Physics Letters,* **97**, p. 251117, 2010.

[193] D. Wang, D. Donetsky, S. Jung, G. Belenky, "Carrier lifetime measurements in long-wave infrared InAs/GaSb superlattices under low excitation conditions", *Journal of Electronic Materials*, **41**, pp. 3027–3030, 2012.

[194] W. Huang, L. Li, L. Lei, J. A. Massengale, R. Q. Yang, T. D. Mishima, et al., "Electrical gain in interband cascade infrared photodetectors", *Journal of Applied Physics*, **123**, p. 113104, 2018.

[195] M. M. Alkaisi, N. A. Aldawody, "Factors affecting the hot spot efficacy in photovoltaic arrays," *Solar Cells*, **28**, pp. 11-17, 1990.

[196] D. Roche, H. Outhred, R. J. Kaye, "Analysis and Control of Mismatch Power Loss in Photovoltaic Arrays," *Progress in Photovoltaic: Research and Applications*, **3**, pp. 115-127, 1995.

[197] W. Huang, S. Rassel, L. Li, J. Massengale, R. Q. Yang, T. D. Mishima, et al., "A Unified Figure of Merit for Interband and Intersubband Cascade Devices," *Infrared Physics and Technology*, **96**, p. 298, 2019.

[198] Z. Tian, S. E. Godoy, H. S. Kim, T. Schuler-Sandy, J. A. Montoya, S. Krishna, "High operating temperature interband cascade focal plane arrays," *Applied Physics Letters*, **105**, p. 051109, 2014.

[199] N. Gautam, S. Myers, A.V. Barve, B. Klein, E.P. Smith, D.R. Rhiger, L.R. Dawson, and S. Krishna, "High operating temperature interband cascade midwave infrared detector based on type-II InAs/GaSb strained layer superlattice," *Applied Physics Letters*, **101**, p. 021106, 2012.

[200] D. Donetsky, S. P. Svensson, L. E. Vorobjev, G. Belenky, "Carrier lifetime measurements in short-period InAs/GaSb strained-layer superlattice structures," *Applied Physics Letters*, **95**, p. 212104, 2009.

[201] D. Donetsky, G. Belenky, S. Svensson, S. Suchalkin, "Minority carrier lifetime in type-2 InAs-GaSb strained-layer superlattices and bulk HgCdTe materials," *Applied Physics Letters*, **97**, p. 052108, 2010.

[202] L. M. Murray, K. S. Lokovic, B. V. Olson, A. Yildirim, T. F. Boggess, J. P. Prineas, "Effects of growth rate variations on carrier lifetime and interface structure in InAs/GaSb superlattices," *Journal of Crystal Growth*, **386**, p. 194, 2014.

[203] B. Klein, N. Gautam, E. Plis, T. Schuler-Sandy, T. J. Rotter, Sanjay Krishna, "Carrier lifetime studies in midwave infrared type-II InAs/GaSb strained layer superlattice," *Journal of Vacuum Science & Technology B*, **32**, p. 02C101, 2014.

[204] S. Bandara, P. Maloney, N. Baril, J. Pellegrino, M. Tidrow, "Doping dependence of minority carrier lifetimes in long-wave Sb-based type-II superlattice infrared detector materials," *Optical Engineering*, **50**, p. 061015, 2011.

[205] D. R. Rhiger, "Performance of Comparison of Long-Wavelength Infrared Type II superlattice Devices with HgCeTe," *Journal of Electronic Materials*, **40**, p. 1815, 2011.

[206] Q. K. Yang, C. Pfahler, J. Schmitz, W. Pletschen, F. Fuchs, "Trap cneters and minority carrier lifetimes in InAs/(GaIn)Sb superlattice long wavelength photodetectors," *SPIE Proceedings*, **4999**, p. 448, 2003.

[207] J. Pellegrino, R. DeWames, "Minority carrier lifetime characteristics in type II InAs/GaSb LWIR superlattice $n^+\pi p^+$ photodiodes," *SPIE Proceedings*, **7298**, p. 72981U, 2009.

[208] M. Delmas, J. B. Rodriguez, P. Christol, "Electrical modeling of InAs/GaSb superlattice mid-wavelength infrared pin photodiode to analyze experimental dark current characteristics," *Journal of Applied Physics*, **116**, p. 113101, 2014.

[209] C. Cervera, K. Jaworowicz, H. Aït-Kaci, R. Chaghi, J.B. Rodriguez, I. Ribet-Mohamed, et al., "Temperature dependence performances of InAs/GaSb superlattice photodiode," *Infrared Physics and Technology*, **54**, p. 258, 2011.

[210] D. K.Schroder, "The Concept of Generation and Recombination Lifetimes In Semiconductors," *IEEE Transactions on Electron Devices*, **29**, p. 1336, 1982.

[211] J. Yin, R. Paiella, "Multiple-junction quantum cascade photodetectors for thermophotovoltaic energy conversion," *Opt. Express*, **18**, p. 1618, 2010.

[212] J. Yin, R. Paiella, "Limiting performance analysis of cascaded interband/intersubband thermophotovoltaic devices," *Applied Physics Letters*, **98**, p. 041103, 2011.

[213] M.A. Kinch, F. Aqariden, D. Chandra, P-L Liao, H.F. Schaake, H.D. Shih, "Minority Carrier Lifetime in p-HgCdTe," *Journal of Electronic Materials*, **34**, p. 880, 2005.

[214] A. Rogalski, P. Martyniuk, M. Kopytko, "InAs/GaSb type-II superlattice infrared detectors: Future prospect," *Applied Physics Reviews*, **4**, p. 031304, 2017.

[215] G. Marre, B. Vinter, V Berger, "Strategy for the design of a non-cryogenic quantum infrared detector," *Semiconductor Science and Technology*, **18**, p. 284, 2003.

[216] E. O. Kane, "*Semiconductors & Semimetals*," chapter 3, vol. **1**, New York: Academic, 1966.

[217] K. Hackiewicz, P. Martyniuk, J. Rutkowski, A. Kowalewski, "Calculation of dark

current in interband cascade type-II infrared InAs/GaSb superlattice detector," *Acta Physica Polonica A*, **132**, p. 1415, 2017.

[218] R. K. Ahrenkiel, "*Semiconductors and Semimetals*," R. K. Ahrenkiel and M. S. Lundstrom (ETs), **39**, pp. 39–150, New York: Academic, 1993.

[219] B. V. Olson, E. A. Shaner, J. K. Kim, J. F. Klem, S. D. Hawkins, M. E. Flatté, et al., "Identification of dominant recombination mechanism in narrow-bandgap InAs/InAsSb type-II superlattices and InAsSb alloys," *Applied Physics Letters*, **103**, p. 052106, 2013.

[220] L. Hőglund, D. Z. Ting, A. Khoshakhlagh, A. Soibel, C. J. Hill, A. Fisher, et al., "Influenence of radiative and non-radiative recombination on the minority carrier lifetime in the midewave infrared InAs/InAsSb supperlatices," *Applied Physics Letters*, **103**, p. 221908, 2013.

[221] I. Vurgaftman, W. W. Bewley, C. D. Merritt, C. L. Canedy, M. V. Warren, C. S. Kim, et al., "Sensitive Chemical Detection with Distributed Feedback Interband Cascade Lasers", *Encyclopedia of Analytical Chemistry*, John Wiley & Sons, Ltd., 2016.

[222] S.-Q. Zhai, J.-Q. Liu, K. Ning, F.-Q. L, L. Li, L.-J. Wang, et al., "Strin-composed InP-based InGaAs/InAsAs Quantum Cascade Infrared Detectors for 3~5 μm Atmospheric Window," *SPIE Proceedings*, **8193**, p. 81931X, 2011.

[223] X. Wang, J. Liu, S. Zhai, F. Liu, Z. Wang, "Room temperature quantum cascade detector operating at 4.3 μm," *Journal of Semiconductors*, **35**, p. 104009, 2014.

[224] P. Reininger, T. Zederbauer, B. Schwarz, H. Detz, D. MacFarland, A. M. Andrews, et al., "InAs/AlAsSb based quantum cascade detector," *Applied Physics Letters*, **107**, p. 081107, 2015.

[225] T. Dougakiuchi, K. Fujita, T. Hirohata, A. Ito, M. Hitaka, T. Edamura, "High photoresponse in room temperature quantum cascade detector based on coupled quantum well design," *Applied Physics Letters*, **109**, p. 261107, 2016; Erratum, **110**, p. 109902, 2017.

[226] Y. Jiang, L. Li, R. Q. Yang, J. A. Gupta, G. C. Aers, E. Dupont, et al., "Type-I interband cascade lasers near 3.2 μm," *Applied Physics Letters*, **106**, p. 041117, 2015.

[227] Y. Li, L. Li, W. Huang, R. Q. Yang, J. A. Gupta, X. Wu, "Low-threshold InAs-based interband cascade lasers near 6.3 μm," *14th International Conference on Mid-IR Optoelectronics: Materials and Devices MIOMD-XIV*, 2018.

[228] J. R. Meyer, C. A. Hoffman, F. J. Bartoli, L. R. Ram-Mohan, "Type-II quantum-well lasers for the mid-wavelength infrared," *Applied Physics Letters*, **67**, p. 757, 1995.

[229] Z.-B. Tian, T. Schuler-Sandy, S. Krishna, “Electron barrier study of mid-wave infrared interband cascade photodetectors,” *Applied Physics Letters*, **103**, p. 083501, 2013.

[230] H. Lotfi, L. Lei, L. Li, R. Q. Yang, J. C. Keay, M. B. Johnson et al., “High-temperature operation of interband cascade infrared photodetectors with cutoff wavelength near 8 μm”, *Optical Engineering*, **54**, p. 063103, 2015.

[231] H. Lotfi, L. Li, L. Lei, Y. Jiang, R.Q. Yang, J.F. Klem, et al., "Short-wavelength interband cascade infrared photodetectors operating above room temperature", *Journal of Applied Physics*, **119**, p. 023105, 2016.

[232] W. Huang, L. Lei, L. Li, J. A. Massengale, R. Q. Yang, T. D. Mishima, et al., “Current-matching versus non-current-matching in long wavelength interband cascade infrared photodetectors,” *Journal of Applied Physics*, **122**, p. 083102, 2017.

[233] C. Koeniguer, G. Dubois, A. Gomez, V. Berger, “Electronic trnasport in quantum cascade strucutures at equilibrium,” *Physics Review B*, **74**, p. 235325, 2006.

[234] A. Buffaz, A. Gomez, M. Carras, L. Doyennette, V. Berger, “Role of subband occupancy on electronic transport in quantum cascade detectors,” *Physics Review B*, **81**, p. 075304, 2010.

[235] A. Delga, L. Doyennette, M. Carras, V. Trinite, P. Bois, “Johnson and shot noises in intersubband detectors,” *Applied Physics Letters*, **102**, p. 163507, 2013.

[236] D. Palaferri, Y. Todorov, A. Bigioli, A. Mottaghizadeh, D. Gacemi, A. Calabrese, et al., “Room-temperature nine-μm-wavelength photodetctors and GHz-frequency heterodyne receivers,” *Nature*, **556**, pp. 85-88, 2018.

[237] H. Lotfi, L. Li, H. Ye, R. T. Hinkey, L. Lei, R. Q. Yang, et al., “Interband cascade infrared photodetectors with long and very-long cutoff wavelengths,” *Infrared Physics and Technology*, **70**, p. 162, 2015.

[238] Y. Zhou, J. Chen, Z. Xu, L. He, “High quantum efficiency mid-wavelength interband cascade infrared photodetectors with one and two stages,” *Semiconductor Science and Technology*, **31**, p. 085005, 2016.

[239] L. Lei, L. Li, H. Ye, H. Lotfi, R. Q. Yang, M. B. Johnson, et al., “Long wavelength interband cascade infrared photodetectors operating at high temperatures,” *Journal of Applied Physics*, **120**, p. 193102, 2016.

[240] W. Pusz, A. Kowalewski, P. Martyniuk, W. Gawron, E. Plis, S. Krishna, et al., “Mid-wavelength infrared type-II InAs/GaSb superlattice interband cascade photodetectors,” *Optical Engineering*, **53**, pp. 043107-043107, 2014.

[241] Z. Tian, S. Krishna, “Mid-Infrared Interband Cascade Photodetectors With

Different Absorber Designs," *IEEE Journal of Quantum Electronics*, **51**, pp. 1-5, 2015.

[242] A. Soibel, D. Z. Ting, C. J. Hill, M. Lee, J. Nguyen, S. A. Keo, et al., "Gain and noise of high-performance long wavelength superlattice infrared detectors," *Applied Physics Letters*, **96**, p. 111102, 2010.

[243] M. B. Reine, A. K. Sood, T. J. Tredwell, "*Semiconductors and Semimetals*," R. K. Willardson and A. C. Beer (ETs), Vol. **18**, p. 201, Academic: New York, 1981.

[244] W. E. Tennant, ""Rule 07" Revisited: Still a good Heuristic Predictor of p/n HgCdTe Photodiode Performance?," *Journal of Electronic Materials*, **39**, p. 1030, 2010.

[245] Klaudia Hackiewicz, Jaroslaw Rutkowski, Piotr Martyrium, Tetina Manyk, "Calculation of optimal absorber thickness in interband cascade type-II infrared InAs/GaSb super lattice photodetectors," *SPIE Proceedings*, **10433**, p. 104330Z, 2017.

[246] S. A. Maier, "*Plasmonics: fundamentals and applications*," Springer, 2007.

[247] R. Stanley, "Plasmonics in the mid-infrared," *Nature photonics*, **6**, pp. 409-411, 2012.

Appendix A: Publications list

Refereed journal articles

[1] **W. Huang**, J. A. Massengale, Y. Lin, L. Li, R. Q. Yang, T. D. Mishima, M. B. Santos, "Performance analysis of narrow-bandgap interband cascade thermophotovoltaic cells", Journal of Physics D: Applied Physics **53**,175104 (2020).

[2] **W. Huang,** R. Q. Yang, "Limiting Factors and Efficiencies of Narrow Bandgap Thermophotovoltaic Cells under Monochromatic Light Illumination", Journal of Applied Physics **126**, 045714 (2019)

[3] **W. Huang**, S. M. Rassel, L. Li, J. A. Massengale, H. Ye, R. Q. Yang, T. D. Mishima, M. B. Santos, "A unified figure of merit for interband and intersubband cascade devices", Infrared Physics and Technol. **96**, 298 (2019)

[4] **W. Huang**, L. Lei, L. Li, J. A. Massengale, H. Ye, R. Q. Yang, T. D. Mishima, M. B. Santos, "Enhanced collection efficiencies and performances of interband cascade structures for narrow bandgap semiconductor thermophotovoltaic devices", Journal of Applied Physics **124**, 023101 (2018)

[5] **W. Huang**, L. Li, L. Lei, J. A. Massengale, R. Q. Yang, T. D. Mishima, M. B. Santos, "Electrical gain in interband cascade infrared photodetectors", Journal of Applied Physics **123**, 113104 (2018)

[6] **W. Huang**, L. Li, L. Lei, J. A. Massengale, H. Ye, R. Q. Yang, T. D. Mishima, M. B. Santos, "Minority carrier lifetime in mid-wavelength interband cascade infrared photodetectors", Applied Physics Letters **112**, 251107 (2018)

[7] **W. Huang**, L. Lei, L. Li, J. A. Massengale, R. Q. Yang, T. D. Mishima, M. B. Santos, "Current-matching versus non-current-matching in long wavelength interband cascade infrared photodetectors", Journal of Applied Physics **122**, 083102 (2017)

[8] Y. Lin, J. A. Massengale, **W. Huang**, R. Q. Yang, T. D. Mishima, M. B. Santos, "Examination of the durability of interband cascade lasers against structural variations", Journal of Infrared and Millimeter Waves, **39**, 137-141, (2020)

[9] R. Q. Yang, L. Li, **W. Huang**, S. M. Rassel, J. A. Gupta, A. Bezinger, X. Wu, S. G. Razavipour, G. C. Aers, "InAs-based Interband Cascade Lasers", IEEE Journal of Selected Topics in Quantum Electronics, **25**, 1200108 (2019)

[10] L. Lei, **W. Huang**, J. A. Massengale, H. Ye, H. Lotfi, R. Q. Yang, T. D. Mishima, M. B. Santos, M. B. Johnson, "Resonant tunneling and multiple differential conductance features in long wavelength interband cascade infrared photodetectors", Applied Physics Letters, **111**, 113504 (2017)

Conference presentations and proceedings

[1] **W. Huang**, R. Q. Yang, "Efficiencies and limiting factors of narrow bandgap thermophotovoltaic cells", talk 11275-36 at Physics, Simulation, and Photonic Engineering of Photovoltaic Devices IX at SPIE. Photonics West, San Francisco, California, Feb. 1-6, 2020

[2] **W. Huang**, L. Li, J. A. Massengale, R. Q. Yang, T. D. Mishima, M. B. Santos, "Multistage Interband Cascade Thermophotovoltaic Devices with ~0.2 eV Bandgap", at Photovoltaic Specialists Conference, Chicago, Illinois, June16-21, 2019

[3] **W. Huang**, L. Li, J. A. Massengale, R. Q. Yang, T. D. Mishima, M. B. Santos, **"**Investigation of narrow bandgap interband cascade thermophotovoltaic cells", talk 10913-42 at Physics, Simulation, and Photonic Engineering of Photovoltaic Devices VIII at Photonics West, San Francisco, CA, Feb. 2-7, 2019 (in Proc. SPIE. **10913**, 1091317)

[4] J. A. Gupta, X. Wu, G. C. Aers, Y. Li, L. Li, **W. Huang**, R. Q. Yang, **"**Low-threshold InAs-based interband cascade lasers with room-temperature emission at 6.3 μm" (**Invited**), talk 10939-33 at Novel In-Plane Semiconductor Lasers XVIII at Photonics West, San Francisco, CA, Feb. 2-7, 2019

[5] **W. Huang**, S. Rassel, L. Li, J. Massengale, Y. Li, R. Q. Yang, T. D. Mishima, M. B. Santos, "A Unified Figure of Merit for Interband and Intersubband Cascade Devices", at 14th International Conference on Mid-IR Optoelectronics: Materials and Devices MIOMD-XIV (MIOMD 2018), Flagstaff, AZ, Oct. 7-10, 2018

[6] **W. Huang**, L. Lin, L. Li, J. Massengale, R. Q. Yang, T. D. Mishima, M. B. Santos, "Collection Efficiency and Device Performance in Narrow Bandgap Thermophotovoltaic Cells Based on Interband Cascade Structures", at 14th International Conference on Mid-IR Optoelectronics: Materials and Devices MIOMD-XIV (MIOMD 2018), Flagstaff, AZ, Oct. 7-10, 2018

[7] Y. Li, L. Li, **W. Huang**, R. Q. Yang, J. A. Gupta, X. Wu, G. Aers, "Low-threshold InAs-based Interband Cascade Lasers near 6.3 μm", at 14th International Conference on Mid-IR Optoelectronics: Materials and Devices MIOMD-XIV (MIOMD 2018), Flagstaff, AZ, Oct. 7-10, 2018

[8] J. A. Gupta, A. Bezinger, S.G. Razavipour**,** X. Wu, G. C. Aers, Y. Li, L. Li, **W. Huang**, R. Q. Yang, "Long-Wavelength InAs-based Interband Cascade Lasers Grown by MBE", paper TuM6 at 34th North American Conference on Molecular Beam Epitaxy (NAMBE 2018), Banff, Canada, Sept. 30-Oct. 5, 2018

[9] **W. Huang**, L. Li, L. Lei, J. A. Massengale, H. Ye, R. Q. Yang, T. D. Mishima, M. B. Santos, "Carrier Lifetime in Mid-Infrared Type-II Superlattice Photodetectors",

at 31th Annual Conference of the IEEE Photonics Society, Reston, VA, Sept. 30-Oct. 4, 2018

[10] R. Q. Yang, **W. Huang**, L. Li, L. Lei, J. A. Massengale, T. D. Mishima, and M. B. Santos, "Gain and resonant tunneling in interband cascade IR photodetectors" (**Invited**), talk 10543-13 at Quantum Sensing and Nanophotonic Devices XV at Photonics West, San Francisco, CA, Jan. 27- Feb.1, 2018 (in *Proc. SPIE*. **10540**, 105400E)